AD-A126 396 FINAL TECHNICAL REPORT ON CONTRACT N00014-81-C-0010 1 1/3
OCTOBER 1980-30 SEPTEMBER 1982(U) WOODS HOLE
OCEANOGRAPHIC INSTITUTION MA J A WHITEHEAD MAR 83
UNCLASSIFIED WHOI-83-11 N00014-81-C-0010 F/G 8/3 NL

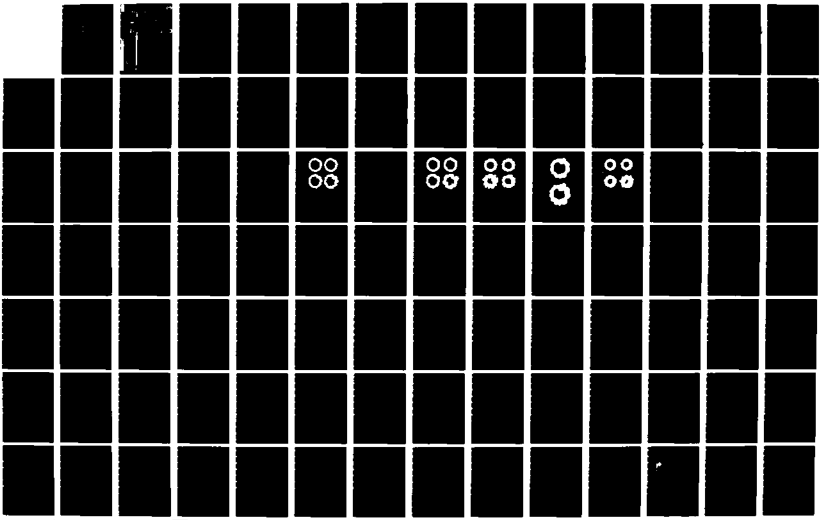

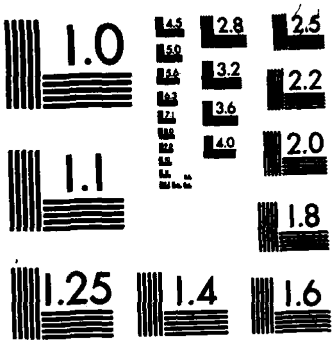
1.0
1.1
1.25
1.4
1.6
1.8
2.0
2.2
2.5
2.8
3.2
3.6
4.0
4.5
5.0
5.6
6.3
7.1

MICROCOPY RESOLUTION TEST CHART
NATIONAL BUREAU OF STANDARDS-1963-A

(12)

WHOI-83-11

Woods Hole Oceanographic Institution

AD A126396

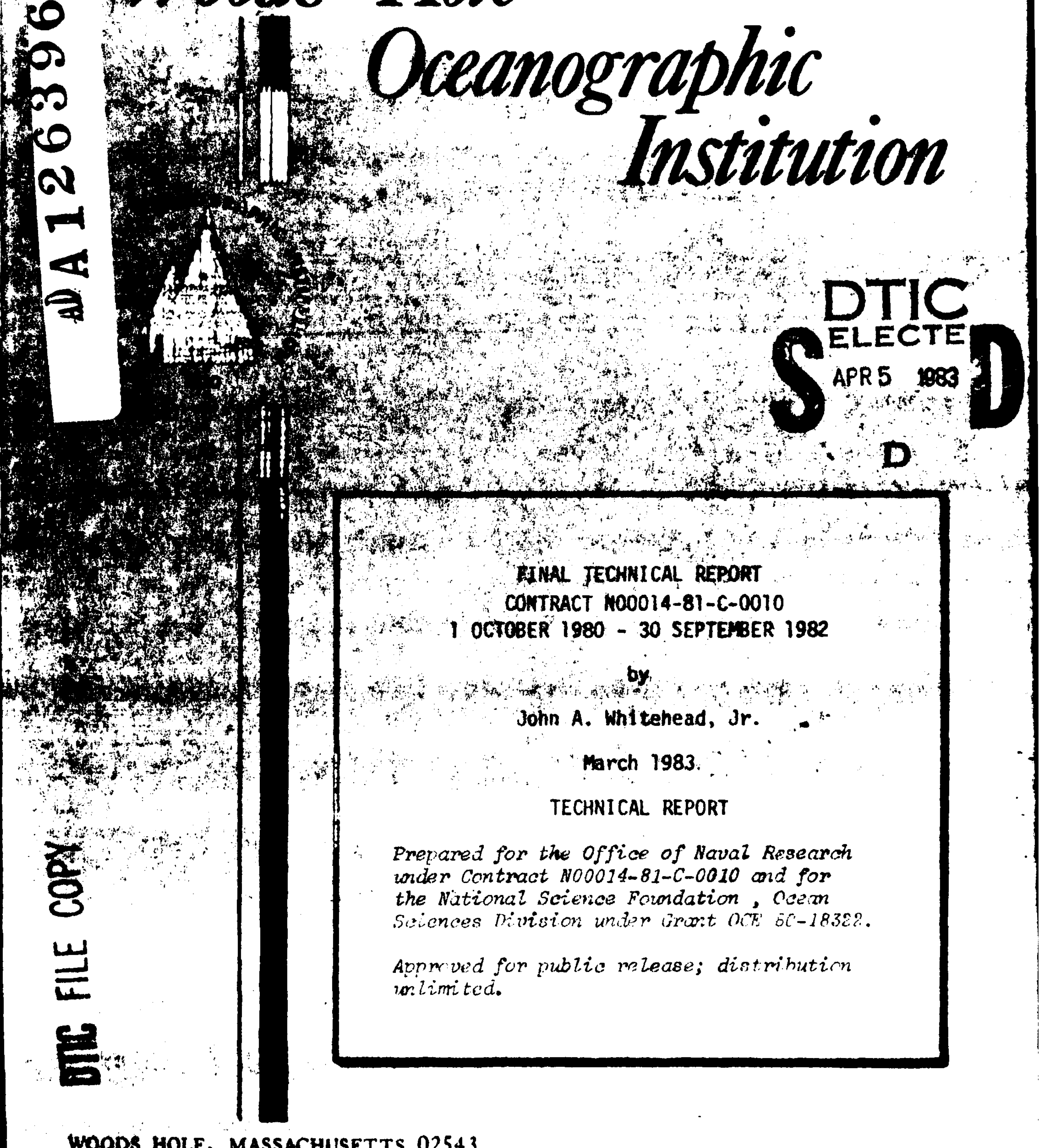

DTIC
ELECTE
APR 5 1983
S D
D

FINAL TECHNICAL REPORT

CONTRACT N00014-81-C-0010
1 OCTOBER 1980 - 30 SEPTEMBER 1982

by

John A. Whitehead, Jr.

March 1983

TECHNICAL REPORT

Prepared for the Office of Naval Research under Contract N00014-81-C-0010 and for the National Science Foundation , Ocean Sciences Division under Grant OCE 80-18322.

Approved for public release; distribution unlimited.

DTIC FILE COPY

WOODS HOLE, MASSACHUSETTS 02543

UNCLASSIFIED 3/83

SECURITY CLASSIFICATION OF THIS PAGE (*When Data Entered*)

REPORT DOCUMENTATION PAGE	**READ INSTRUCTIONS BEFORE COMPLETING FORM**

1. REPORT NUMBER
WHOI-83-11 ✓

2. GOVT ACCESSION NO.
AD-A126396

3. RECIPIENT'S CATALOG NUMBER

4. TITLE (*and Subtitle*)
FINAL TECHNICAL REPORT
CONTRACT N00014-81-C-0010
1 OCTOBER 1980 — 30 SEPTEMBER 1982

5. TYPE OF REPORT & PERIOD COVERED
Technical

6. PERFORMING ORG. REPORT NUMBER
WHOI-83-11

7. AUTHOR(s)
John A. Whitehead, Jr.

8. CONTRACT OR GRANT NUMBER(s)
N00014-81-C-0010
OCE 80-18322

9. PERFORMING ORGANIZATION NAME AND ADDRESS
Woods Hole Oceanographic Institution
Woods Hole, Massachusetts 02543

10. PROGRAM ELEMENT, PROJECT, TASK AREA & WORK UNIT NUMBERS

11. CONTROLLING OFFICE NAME AND ADDRESS
NORDA/National Space Technology Laboratory
Bay St. Louis, MS

12. REPORT DATE
March 1983

13. NUMBER OF PAGES
206

14. MONITORING AGENCY NAME & ADDRESS(*if different from Controlling Office*)

15. SECURITY CLASS. (*of this report*)
Unclassified

15a. DECLASSIFICATION/DOWNGRADING SCHEDULE

16. DISTRIBUTION STATEMENT (*of this Report*)
Approved for public release; distribution unlimited.

17. DISTRIBUTION STATEMENT (*of the abstract entered in Block 20, if different from Report*)

18. SUPPLEMENTARY NOTES
This report should be cited as: Woods Hole Oceanog. Inst. Tech. Rept. WHOI-83-11.

19. KEY WORDS (*Continue on reverse side if necessary and identify by block number*)
1. Rotating
2. Density
3. Current

20. ABSTRACT (*Continue on reverse side if necessary and identify by block number*)
Please see reverse side.

DD FORM 1 JAN 73 1473 EDITION OF 1 NOV 65 IS OBSOLETE
S/N 0102-014-6601

UNCLASSIFIED 3/83

SECURITY CLASSIFICATION OF THIS PAGE (*When Data Entered*)

20.

Laboratory, theoretical and numerical research was conducted into the structure and stability of baroclinic non-linear currents in a rotating fluid. A rotating version of the dam-break problem in which a density current is generated after a barrier has been removed was studied.

Theoretical studies of the stability of a free isolated baroclinic jet whose free surface in cross-section intersects the water surface at two points by Griffiths, Killworth and Stern (1982) was undertaken. Killworth and Stern (1982) showed that a coastal density current in a rotating system is unstable to downstream wave disturbances when the mean potential vorticity increases towards the (vertically-walled) coast and when the mean current vanishes there.

Paldor, in his Ph.D. Thesis, used Rayleigh integral to prove that an unbounded geostrophic front of uniform potential vorticity is stable with respect to small perturbations of arbitrary wavelength. Stern and Paldor (1983) used extremum concepts to analyze large amplitude disturbances in a boundary layer shear flow with an inviscid and longwave theory.

Accession For
NTIS GRA&I ☒
DTIC TAB ☐
Unannounced ☐
Justification

By
Distribution/
Availability Codes
Dist | Avail and/or Special
A

DTIC
COPY
INSPECTED
2

WHOI-83-11

FINAL TECHNICAL REPORT
CONTRACT N00014-81-C-0010
1 OCTOBER 1980 - 30 SEPTEMBER 1982

by

John A. Whitehead, Jr.

WOODS HOLE OCEANOGRAPHIC INSTITUTION
Woods Hole, Massachusetts 02543

March 1983

TECHNICAL REPORT

Prepared for the Office of Naval Research under Contract N00014-81-C-0010 and for the National Science Foundation, Ocean Science Division under Grant OCE 80-18322.

Reproduction in whole or in part is permitted for any purpose of the United States Government. This report should be cited as: Woods Hole Oceanog. Inst. Tech. Rept. WHOI-83-11.

Approved for public release; distribution unlimited.

Approved for Distribution: N.P. Fofonoff
N. P. Fofonoff, Chairman
Department of Physical Oceanography

TABLE OF CONTENTS

	Page Number
ABSTRACT	2
INTRODUCTION	3
LIST OF REFEREED PAPERS	5
APPENDICES	6
Ageostrophic Instability of Ocean Currents	343-377
Instabilities on Density-Driven Boundary Currents and Fronts	1-28
Linear Stability and Stable Modes of Geostrophic Fronts	1-43
The Intrusion of a Density Current Along the Coast of a Rotating Fluid	237-265
Large Amplitude Long Waves in a Shear Flow	1-55
Laboratory Models of Circulation in Shallow Seas	583-595

Abstract

Laboratory, theoretical and numerical research was conducted into the structure and stability of baroclinic non-linear currents in a rotating fluid. A rotating version of the dam-break problem in which a density current is generated after a barrier has been removed was studied. The speed of the current and its width and depth were measured by Whitehead (1981) and more extensively by Stern, Whitehead, and Lien Hua (1982), who report the experiments and compare the results to theory. Properties of a limiting bore solution for rotation density currents predicted earlier by Stern are incorporated into the above theory to predict the speed of the nose of the current. Experiments are described in which the current width is measured to be in reasonable agreement with the theory.

Theoretical studies of the stability of a free isolated baroclinic jet whose free surface in cross-section intersects the water surface at two points by Griffiths, Killworth and Stern (1982) was undertaken. The waves permit the release of both kinetic and potential energy. They can have rapid growth rates, the e-folding time for waves on a current with zero potential vorticity being close to one-half of a rotation period. Experiments with a current of buoyant fluid at the free surface of a lower layer were also conducted. The current was observed to be always unstable.

Killworth and Stern (1982) showed that a coastal density current in a rotating system is unstable to downstream wave disturbances when the mean potential vorticity increases towards the (vertically-walled) coast and when the mean current vanishes there. Other new instability modes were also found which do not require the potential vorticity extremum of quasi-geostrophic theory.

Paldor, in his Ph.D. thesis, used Rayleigh integral to prove that an unbounded geostrophic front of uniform potential vorticity is stable with respect to small perturbations of arbitrary wavelength. Stern and Paldor (1983) used extremum concepts to analyze large amplitude disturbances in a boundary layer shear flow with an inviscid and longwave theory. It was found that initially weak horizontal convergences were concentrated and amplified in time.

Introduction

Laboratory, theoretical and numerical research was conducted into the structure and stability of baroclinic non-linear currents in a rotating fluid. A rotating version of the dam-break problem in which a density current is generated after a barrier has been removed was studied. The rotation causes the current to lean against the right-hand wall (looking downstream for counter-clockwise rotation) and turbulent eddies are detrained to the side rather than vertically. The speed of the current and its width and depth were measured by Whitehead (1981) and more extensively by Stern, Whitehead, and Lien Hua (1982), who report the experiments and compare the results to a theory which is a modification of the Benjamin theory of a non-rotating density current. Properties of a limiting bore solution for rotation density currents predicted earlier by Stern are incorporated into the above theory to predict that the speed of the nose of the current would be 1.58 $(g^*h)^{1/2}$, and the width of the current would be 0.42 $(g^*h)^{1/2}\ f^{-1}$, where g^* is reduced gravity, h is depth of the current upstream of the nose, and f is the Coriolis parameter. Experiments are described in which the current width is measured to be in reasonable agreement with the theory. The velocity of the highest Reynolds number flows studies may also be approaching the predicted values, although the lower Reynolds number flows go more slowly.

Theoretical studies of the stability of a free isolated baroclinic jet whose free surface in cross-section intersects the water surface at two points by Griffiths, Killworth and Stern (1982) was undertaken. The analysis includes the influence of vanishing depth and large inertial effects at the edge of the current and shows that such currents are always unstable to linearized perturbations even when there is no extremum in the potential vorticity profile. The waves permit the release of both kinetic and potential energy. They can have rapid growth rates, the e-folding time for waves on a current with zero potential vorticity being close to one-half of a rotation period.

Experiments with a current of buoyant fluid at the free surface of a lower layer were also conducted, and the observations compared with the computed mode of maximum growth rate for a flow with a uniform potential vorticity. The current was observed to be always unstable, but, contrary to the predicted behavior of the one-layer coupled mode, the dominant length scale of growing disturbances was independent of current width. When the current was sufficiently narrow compared with the Rossby deformation radius, disturbances have the structure predicted by the one-layer theory.

Killworth and Stern (1982) showed that a coastal density current in a rotating system is unstable to downstream wave disturbances when the mean potential vorticity increases towards the (vertically-walled) coast and when the mean current vanishes there. Other new instability modes were also found which do not require the potential vorticity extremum of quasi-geostrophic theory. The instabilities release mean kinetic energy and mean potential energy as well, though an increase of the latter can occur under certain circumstances.

Paldor, in his Ph.D. thesis at the University of Rhode Island, and in a text prepared for publication (Paldor, 1983), used Rayleigh integral to prove that an unbounded geostrophic front of uniform potential vorticity is stable with respect to small perturbations of arbitrary wavelength. The front was bounded by a motionless fluid. The ageostrophic theory developed in his study yielded a stable, near-inertial, long-trapped mode. Recent oceanic observations of the increase in the energy of the inertial peak in the vicinity of fronts support the existence of this inertial trapped mode. In addition, the theory yielded a geostrophic mode which is expected to become unstable when the potential vorticity is not uniform.

Stern and Paldor (1983) used similar extremum concepts to analyze large amplitude disturbances in a boundary layer shear flow with an inviscid and longwave theory. It was found that initially weak horizontal convergences were concentrated and amplified in time, thereby increasing the maximum normal velocity until it becomes comparable with the horizontal velocity. The longwave theory is applied to two-dimensional disturbances, then generalized to three-dimensional motions. The effect of an initial spanwise divergence is such as to rationalize the initial vorticity assumed in the two-dimensional model.

Refereed Papers for Contract N00014-81-C-0010

Griffiths, R. W., P. D. Killworth and M. E. Stern (1982). Ageostrophic instability of ocean currents. J. Fluid Mech., 117: 343-377.

Killworth, P. D. and M. E. Stern (1982). Instabilities on density-driven boundary currents and fronts. Geophys. Astrophys. Fluid Dyn., 22: 1-28.

Paldor, N. (1983) Linear stability and stable modes of geostrophic fronts. Ph.D. Thesis, July, 1981, University of Rhode Island, Kingston, RI.

Paldor, N. (1983) Linear stability and stable modes of geostrophic fronts. Geophys. Astrophys. Fluid Dyn., (accepted).

Stern, M. E., J. A. Whitehead, and B. Lien Hua (1982). The intrusion of a density current along the coast of a rotating fluid. J. Fluid Mech., 123: 237-265.

Stern, M. E. and N. Paldor (1983). Large amplitude long waves in a shear flow. Physics of Fluids, accepted.

Whitehead, J. A., Jr. (1981). Laboratory models of circulation in shallow seas. Phil. Trans. Roy. Soc. London A, 302: 583-595.

APPENDICES

J. Fluid Mech. (1982), *vol.* 117, *pp.* 343–377
Printed in Great Britain

Ageostrophic instability of ocean currents

By R. W. GRIFFITHS, PETER D. KILLWORTH
Department of Applied Mathematics and Theoretical Physics,
Silver Street, Cambridge CB3 9EW, England

AND MELVIN E. STERN
Graduate School of Oceanography, University of Rhode Island,
Kingston, RI 02881, U.S.A.

(Received 9 April 1981 and in revised form 17 September 1981)

We investigate the stability of gravity currents, in a rotating system, that are infinitely long and uniform in the direction of flow and for which the current depth vanishes on both sides of the flow. Thus, owing to the role of the Earth's rotation in restraining horizontal motions, the currents are bounded on both sides by free streamlines, or sharp density fronts. A model is used in which only one layer of fluid is dynamically important, with a second layer being infinitely deep and passive. The analysis includes the influence of vanishing layer depth and large inertial effects near the edges of the current, and shows that such currents are always unstable to linearized perturbations (except possibly in very special cases), even when there is no extremum (or gradient) in the potential vorticity profile. Hence the established Rayleigh condition for instability in quasi-geostrophic models, where inertial effects are assumed to be vanishingly small relative to Coriolis effects, does not apply. The instability does not depend upon the vorticity profile but instead relies upon a coupling of the two free streamlines. The waves permit the release of both kinetic and potential energy from the mean flow. They can have rapid growth rates, the *e*-folding time for waves on a current with zero potential vorticity, for example, being close to one-half of a rotation period. Though they are not discussed here, there are other unstable solutions to this same model when the potential vorticity varies monotonically across the stream, verifying that flows involving a sharp density front are much more likely to be unstable than flows with a small ratio of inertial to Coriolis forces.

Experiments with a current of buoyant fluid at the free surface of a lower layer are described, and the observations are compared with the computed mode of maximum growth rate for a flow with a uniform potential vorticity. The current is observed to be always unstable, but, contrary to the predicted behaviour of the one-layer coupled mode, the dominant length scale of growing disturbances is independent of current width. On the other hand, the structure of the observed disturbances does vary: when the current is sufficiently narrow compared with the Rossby deformation radius (and the lower layer is deep) disturbances have the structure predicted by our one-layer model. The flow then breaks up into a chain of anticyclonic eddies. When the current is wide, unstable waves appear to grow independently on each edge of the current and, at large amplitude, form both anticyclonic and cyclonic eddies in the two-layer fluid. This behaviour is attributed to another unstable mode.

1. Introduction

There have been many studies of the stability of stratified shear flows in a rotating fluid. Apart from Kelvin–Helmholtz instabilities, most studies have concentrated upon quasi-geostrophic models, in which inertial forces are small compared with Coriolis forces. These studies reveal two fundamental types of instabilities. The first of these takes place in a one-layer fluid. The resulting (barotropic) instability is driven by the horizontal shear of the basic flow, and requires an extremum in the profile of potential vorticity (i.e. absolute vorticity divided by depth). Although potential energy may be released by the instability, it is necessary that kinetic energy of the mean flow be released. The second type of instability takes place in a two-layer fluid (or, of course, a continuously stratified one). This instability, usually called baroclinic instability (cf. Pedlosky 1964), can occur without the release of mean kinetic energy but does require the release of mean potential energy that was stored in the density field. Again, a necessary condition for instability is that the gradient of potential vorticity changes sign somewhere within the fluid.

Models in which inertial forces are assumed to be much smaller than the Coriolis forces are appropriate for large-scale motions in the ocean and atmosphere, but do not provide a good description of many smaller-scale motions, such as the instabilities of density fronts in the ocean, where inertial forces can be comparable with Coriolis forces. By a 'front' we refer to the situation where a density surface intersects an upper or a lower boundary (such as the ocean surface or bottom). For this situation the conservation of potential vorticity by fluid columns aligned parallel to the axis of rotation, along with the vanishing layer depth, suggests that the fluid vorticity near the front may be comparable to the background (planetary) vorticity. Motions will then be strongly influenced by inertial forces. However, there have been very few studies (Orlanski 1968) of instabilities at density fronts because of the complexity of including the ageostrophic terms.

In this paper we want to study the situation in which the same density surface has two intersections with the same boundary (i.e. there are two fronts present). Such a situation occurs whenever buoyant water forms a narrow current at the ocean surface (away from coastal boundaries) or when dense water flows in a narrow stream over the ocean bottom under the influence of buoyancy forces. One such case is the flow of cold, dense Norwegian Sea water through the Denmark Strait and along the sloping bottom south of the strait (Worthington 1969; Mann 1969; Smith 1976). Coriolis forces are able to inhibit any slumping of the buoyant fluid in the direction perpendicular to the direction of flow and, at the same time, the presence of a cross-stream bottom slope prevents the current from curving to its right. We show here that the presence of two free streamlines, at the intersections of the density interface with the bottom on each side of the current, gives rise to another mechanism for instability. This mechanism operates even when only one layer of fluid (the current itself) is present, and instability does not depend critically upon the details of the potential vorticity profile.

Because we are particularly interested in the possibility that a *single* layer of fluid can be unstable, we consider a current flowing beneath a deep second layer which is stationary and passive. We show that a long rectilinear current bounded by two free streamlines and adjacent to a sloping (or horizontal) boundary is (almost) always unstable. Normal-mode perturbations with finite downstream wavelengths lead to the

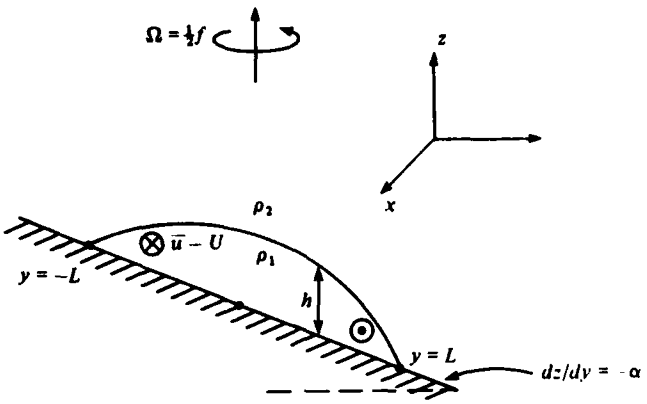

FIGURE 1. The configuration for the one-layer problem considered in this paper.

exponential growth of a combination of meandering and varicose modes.† This combination leads to release of kinetic and potential energy from the original flow. For a current with zero potential vorticity, the wavelength with maximum growth rate is predicted to be 7·9 times the deformation radius based on the maximum depth of the current, and the maximum growth rate gives an *e*-folding time of 0·57 rotation periods.

For a general vorticity distribution, it is shown that instability will always occur for sufficiently long waves whether or not the traditional Rayleigh criterion is satisfied, provided only that the undisturbed relative vorticity does not vanish at points where the flow velocity is equal to the phase velocity of growing disturbances. This kind of instability relies upon a coupling between the two edges of the current. It is therefore likely to continue to contribute to the energy release from sufficiently narrow currents when there are two layers of finite depth and where baroclinic two-layer instability may be important. As a particularly useful example (and one that may give a reasonable description of oceanic and laboratory currents – at least up to the single-layer assumption) we next consider flows with a finite but uniform potential vorticity and describe the exact numerical solution of the eigenvalue problem. In this case the radius of deformation and the current width are independent length scales. When all lengths are non-dimensionalized by the deformation radius we find that the downstream length scale of the most rapidly growing disturbance increases, while its growth rate decreases, with increasing current width.

The very unstable nature of a current with two free streamlines is demonstrated by laboratory experiments. A narrow current of buoyant fluid was produced at the free surface of a deep lower layer by floating a layer of fresh water on top of a salt solution between two axisymmetric cylindrical walls in a rotating system. When the walls were withdrawn, gravitational collapse produced a narrow annular flow with approximately uniform potential vorticity. Coupled disturbances, with a structure that was very similar to that predicted, appeared on the two fronts when the initial half-width of the current was less than twice the initial Rossby radius. The flow rapidly developed into

---

† It can also be shown that in the limit of very large downstream length scales variations of current width will give rise to a purely meandering instability. This meandering mode will grow linearly with time (Griffiths 1980).

a chain of anticyclonic eddies. The preferred downstream length scale of disturbance was 7·4 ± 1·3 times the radius of deformation for the state of geostrophic balance and was independent of current width. For narrow currents the observed length scale and structure of the instabilities can be explained by the present theory, but the model does not explain the instability that is observed when the current is wide. In that case a second mode of instability appeared to occur on each independent density front. This second mode may well require an active second layer, or else it may be the manifestation of another unstable solution to the equations for a single-layer fluid. This other unstable solution occurs on each front independently and will be discussed in another paper.

2. The stability problem

Governing equations

We consider the configuration in figure 1, in which a fluid of uniform density ρ_2 flows beneath an infinite fluid of density $\rho_1 < \rho_2$, against a uniformly sloping bottom whose (constant) gradient in the y-direction is $-\alpha$. The undisturbed flow is taken to be parallel to the x-axis. Assuming no flow in the upper layer, and that α is small enough for the hydrostatic assumption to hold, the momentum and continuity equations are

$$u_t + uu_x + vu_y - fv = -g'h_x, \tag{2.1}$$

$$v_t + uv_x + vv_y + f(u-U) = -g'h_y, \tag{2.2}$$

$$h_t + (uh)_x + (vh)_y = 0, \tag{2.3}$$

where (u,v) are the (x,y)-components of velocity, t represents time, f is the Coriolis parameter and $g' = g(\rho_2-\rho_1)/\rho_2$ is the reduced gravity. The velocity U, given by

$$U = g'\alpha f^{-1}, \tag{2.4}$$

is the constant x-component of flow induced by the sloping bottom and will often play the role of a mean advecting current. Equations (2.1)–(2.3) imply that the potential vorticity

$$P = \frac{f + v_x - u_y}{h} \tag{2.5}$$

is conserved by fluid columns. Hence, if the potential vorticity at any time is uniform throughout the flow, we may write

$$\frac{f + v_x - u_y}{h} = \frac{f}{H_0}, \tag{2.6}$$

where H_0 would be the uniform depth of the fluid when the relative vorticity is zero.

Let H be a typical depth of the undisturbed current (which, in examples, will often be the maximum depth and will occur at $y = 0$). The flow is then characterized by the radius of deformation $(g'H)^{\frac{1}{2}}f^{-1}$ and the time scale f^{-1}. Because we will be interested in downstream (x) variations with some – usually large – length scale λ, say, we define a dimensionless wavenumber

$$\epsilon = 2\pi(g'H)^{\frac{1}{2}}/f\lambda.$$

Convenient non-dimensional variables are then defined by

$$\left.\begin{array}{l} x = x^{*}\epsilon^{-1}(g'H)^{\frac{1}{2}}f^{-1}, \quad y = y^{*}(g'H)^{\frac{1}{2}}f^{-1}, \quad (u, U) = (u^{*}, U^{*})\,(g'H)^{\frac{1}{2}}, \\ v = v^{*}\epsilon(g'H)^{\frac{1}{2}}, \quad t = t^{*}\epsilon^{-1}f^{-1}, \quad h = h^{*}H, \end{array}\right\} \tag{2.7}$$

and, in the case of uniform potential vorticity, $H_0 = H\mathscr{H}$. Here the starred quantities are nondimensional. Dropping asterisks, (2.1) and (2.2) become

$$u_t + v(u_y - 1) = -(h + \tfrac{1}{2}u^2)_x, \tag{2.8}$$

$$\epsilon^2 v_t + u(\epsilon^2 v_x + 1) - U = -(h + \tfrac{1}{2}\epsilon^2 v^2)_y, \tag{2.9}$$

while the continuity equation (2.3) retains its original form. In the special case of flow with uniform potential vorticity, (2.6) becomes

$$u_y - \epsilon^2 v_x = 1 - \frac{h}{\mathscr{H}}. \tag{2.10}$$

The undisturbed flow

The undisturbed flow is taken as the steady solution of (2.8), (2.9), (2.3) with $v \equiv 0$. Then (2.9) reduces to the geostrophic relation

$$\bar{u} = U - \bar{h}_y, \tag{2.11}$$

where the bars denote the basic flow whose stability is to be investigated. If the flow has a uniform potential vorticity, (2.10) gives as an additional constraint the relative vorticity

$$\bar{u}_y = 1 - \frac{\bar{h}}{\mathscr{H}}. \tag{2.12}$$

As well as the case of general $\bar{u}$, we shall consider two special cases in this paper, both involving constant potential vorticity P. (The Rayleigh criterion for instability would need P_y to change sign, so these cases would be stable by this criterion.) One configuration is that of an infinitely long current (of dimensional width W) extending from $y = -L$ to $y = L$, where $L = fW(g'H)^{\frac{1}{2}}$. The boundary conditions on (2.11), (2.12) are then $\bar{h} = 0$ at $y = \pm L$, and the solution takes the form

$$\bar{h} = \mathscr{H}\left[1 - \frac{\cosh(y/\mathscr{H}^{\frac{1}{2}})}{\cosh(L/\mathscr{H}^{\frac{1}{2}})}\right], \quad \bar{u} = U + \mathscr{H}^{\frac{1}{2}}\frac{\sinh(y/\mathscr{H}^{\frac{1}{2}})}{\cosh(L/\mathscr{H}^{\frac{1}{2}})}. \tag{2.13}$$

Thus the flow involves two length scales, L and $\mathscr{H}$. In the limit of zero potential vorticity – the second special configuration – $\mathscr{H} \to \infty$, (2.12) yields $\bar{u}_y = 1$, and (2.13) reduces to

$$\bar{h} = 1 - \tfrac{1}{2}y^2, \quad \bar{u} = U + y. \tag{2.14}$$

In this case the current width is fixed at $L = \sqrt{2}$ and the flow is described, in dimensional terms, by the single length scale H.

The perturbation equations

We impose a small perturbation of the form $(u', v', h') = (\hat{u}, \hat{v}, \hat{h})\,e^{i(x-ct)}$ on the undisturbed flow $(\bar{u}, 0, \bar{h})$. Then the momentum and continuity equations (2.8), (2.9), (2.3) give the following linearized equations for the perturbation amplitudes.

$$(\bar{u} - c)\,\hat{u} + (1 - \bar{u}_y)\,i\hat{v} = -\hat{h}, \tag{2.15}$$

$$\hat{u} + i\epsilon^2(\bar{u}-c)\,\hat{v} = -\frac{d\hat{h}}{dy}, \tag{2.16}$$

$$\bar{h}\hat{u} - i\frac{d}{dy}(\hat{v}\bar{h}) + (\bar{u}-c)\,\hat{h} = 0. \tag{2.17}$$

From (2.16) it can be seen that the downstream velocity perturbation is ageostrophic at order ϵ^2. For currents with a uniform potential vorticity (2.10) gives the additional condition that

$$\frac{d\hat{u}}{dy} - i\epsilon^2\hat{v} = -\frac{\hat{h}}{\mathscr{H}}. \tag{2.18}$$

In § 3 we present a solution of (2.15), (2.17) and (2.18) for a very simple but illuminating problem – that with zero potential vorticity. In § 4 the system (2.15)–(2.17) is discussed for completely general vorticity profiles. This discussion reveals the influence, upon disturbances, of the cross-stream distribution of vorticity and of asymmetric profiles. An exact numerical solution of (2.15), (2.17) and (2.18) for uniform potential vorticity distributions is then presented in § 5, and compared with laboratory observations in § 6.

3. Flow with zero potential vorticity

Solution of the eigenvalue problem

When the potential vorticity vanishes, $\mathscr{H} \to \infty$ and $\bar{u}_y - 1 = 0$. The longitudinal momentum, continuity and potential-vorticity relations (2.15), (2.17) and (2.18) become

$$(\bar{u}-c)\,\hat{u} + \hat{h} = 0, \tag{3.1}$$

$$\bar{h}\hat{u} - i\frac{d}{dy}(\hat{v}\bar{h}) + (\bar{u}-c)\,\hat{h} = 0, \tag{3.2}$$

$$\frac{d\hat{u}}{dy} - i\epsilon^2\hat{v} = 0, \tag{3.3}$$

where $\bar{h}, \bar{u}$ are given by (2.14).

Elimination of $\hat{h}$ and $\hat{v}$ from the continuity equation (3.2) yields an eigenvalue problem for the complex phase velocity c:

$$\frac{d}{dy}\left(\bar{h}\frac{d\hat{u}}{dy}\right) - \epsilon^2[\bar{h} - (\bar{u}-c)^2]\,\hat{u} = 0. \tag{3.4}$$

Because $\bar{h}(\pm L) = 0$, this equation has singularities at the edges of the current, and we wish to find the solution for which the eigenfunction $\hat{u}$ is regular at $y = \pm L$.† From (3.3) we see that $d\hat{u}(L)/dy$ must be finite in order that $\hat{v}$ be finite on the free streamlines. Therefore, when (3.4) is integrated across the current, we require

$$\int_{-L}^{L} [\bar{h} - (\bar{u}-c)^2]\,\hat{u}\,dy = 0, \tag{3.5}$$

where $L = \sqrt{2}$.

---

† This condition may also be derived more formally by the requirement that the location of vanishing depth remain a streamline.

In order to solve (3.4), (3.5), with a finite wavenumber ϵ, c and $\hat{u}$ may be expanded in the power series

$$\left.\begin{aligned} c &= c_0+\epsilon c_1+\epsilon^2 c_2+\dots, \\ \hat{u}(y) &= u_0(y)+\epsilon u_1(y)+\epsilon^2 u_2(y)+\dots, \end{aligned}\right\} \tag{3.6}$$

where the amplitude is normalized by requiring

$$\hat{u}(0) = 1. \tag{3.7}$$

Substitution of the expansions (3.6) into (3.4), and requiring that du_0/dy be finite at $y = \pm L$, where $\bar{h} = 0$, shows that

$$\frac{du_0}{dy} = 0. \tag{3.8}$$

Hence the leading-order downstream velocity perturbation is independent of y. From (3.7) we set $u_0 = 1$ and require that $u_1(0) = u_2(0) = \dots = 0$. The eigenvalue c_0 is given by (3.5), in which the leading-order terms imply

$$u_0\int_{-L}^{L}[\bar{h}-(\bar{u}-c_0)^2]\,dy = 0.$$

This is a quadratic equation for c_0 which, with $\bar{h}$ and $\bar{u}$ given by (2.14) and $L = \surd 2$, can only be satisfied by

$$c_0 = U. \tag{3.9}$$

Thus normal modes are stable in the limit $\epsilon \to 0$, and are advected downstream at speed U.

The terms of order ϵ obtained from (3.4) imply that $du_1/dy = 0$, and, in order to satisfy (3.7), this requires $u_1 = 0$. Equating the terms of order ϵ^2 obtained from (3.4) yields an equation for the eigenfunction u_2:

$$\frac{d}{dy}\left(\bar{h}\frac{du_2}{dy}\right) = \bar{h}-\tilde{u}^2,$$

where

$$\tilde{u} = \bar{u}-U \tag{3.10}$$

is the current velocity relative to its mean velocity U. By again applying the conditions that du_2/dy be finite at $\bar{h} = 0$ and $u_2(0) = 0$, we find the ageostrophic perturbation $u_2 = \frac{1}{2}y^2$. The condition (3.5) gives

$$2Lc_1^2-\int_{-L}^{L}u_2(\bar{h}-\tilde{u}^2)\,dy = 0,$$

which yields the pure imaginary eigenvalues

$$c_1 = \pm 2i/\surd 15. \tag{3.11}$$

The positive root describes exponentially growing modes that are advected downstream at speed U. Disturbances with large but finite wavelengths are therefore unstable, even though the Rayleigh condition is not satisfied.

When the calculation is continued to higher orders in ϵ a pattern emerges, with even-numbered eigenvalues being zero (apart from c_0) and the rest imaginary. However, the power-series expansion reveals that the growth $\epsilon|c|$ reaches a maximum at a wavenumber only slightly less than unity, where the series converges slowly. In

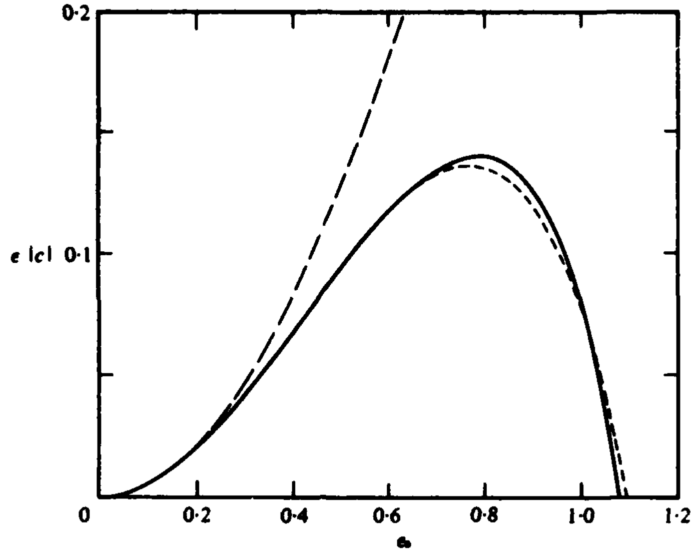

FIGURE 2. Growth rate of normal modes with wavenumber ε on a current with zero potential vorticity: ——, exact numerical results; – – –, first-order growth rate $\epsilon^2 c_1$ given by the wavenumber expansion; - - - - -, Padé approximation based on terms up to $O(\epsilon^{12})$ in the expansion.

order to investigate disturbances with $\epsilon \sim 1$, it was necessary to solve (3.1)–(3.3) numerically, using the Taylor system (Norman 1972). The solution was obtained by integrating from $y = L - \gamma$, where $\gamma = 10^{-4}$, with initial conditions obtained from an expansion of (3.1)–(3.3) near $\bar{h} = 0$. The solution at $y = 0$ was found. The equation was then solved again, beginning at $y = -L + \gamma$ and integrating to $y = 0$. The solutions for $\hat{u}$ were matched at $y = 0$ by scaling the solution from $y = L - \gamma$; c was then adjusted iteratively to match $\hat{u}_y$ (to an accuracy of 10^{-4}). Only imaginary eigenvalues c were found and, at $\epsilon \ll 1$, these are identical with those calculated using the expansion (3.6).

On figure 2 the computed dimensionless growth rate $\epsilon |c|$ is plotted as a function of the wavenumber (solid line). This numerical result is almost identical to the curve (dashed line) that is obtained from the power-series expansion (3.6), which is here extrapolated to $\epsilon > 1$ by taking the Padé approximation based on the first six non-zero terms. The growth rate achieves its maximum value at $\epsilon = 0{\cdot}80$, which corresponds to a wavelength that is 7·9 times the Rossby radius. Wavenumbers greater than $\epsilon = 1{\cdot}1$ yield only real eigenvalues and so are stable.

The eigenfunctions

Substitution of the individual functions $u_0, u_2, u_3, \ldots$ into the longitudinal momentum equation (3.1) and the vorticity equation (3.3) yields the depth and cross-stream velocity perturbations respectively, for successive orders in ϵ. Since the amplitude of each perturbation quantity (u', v', h') has the downstream dependence e^{ix} (neglecting the uniform advection velocity U), we write $(u_0', u_1', u_2', \ldots) = (u_0, u_1, u_2, \ldots)\, e^{ix}$, and similarly for v' and h'. Then the real parts of the eigenfunctions of lower order in ϵ are

$$u_0' = \cos x, \quad v_0' = y \sin x, \quad h_0' = -y \cos x, \tag{3.12}$$

$$v_1' = \frac{-4}{\sqrt{15}} \cos x, \quad h_1' = \frac{-2}{\sqrt{15}} \sin x.$$

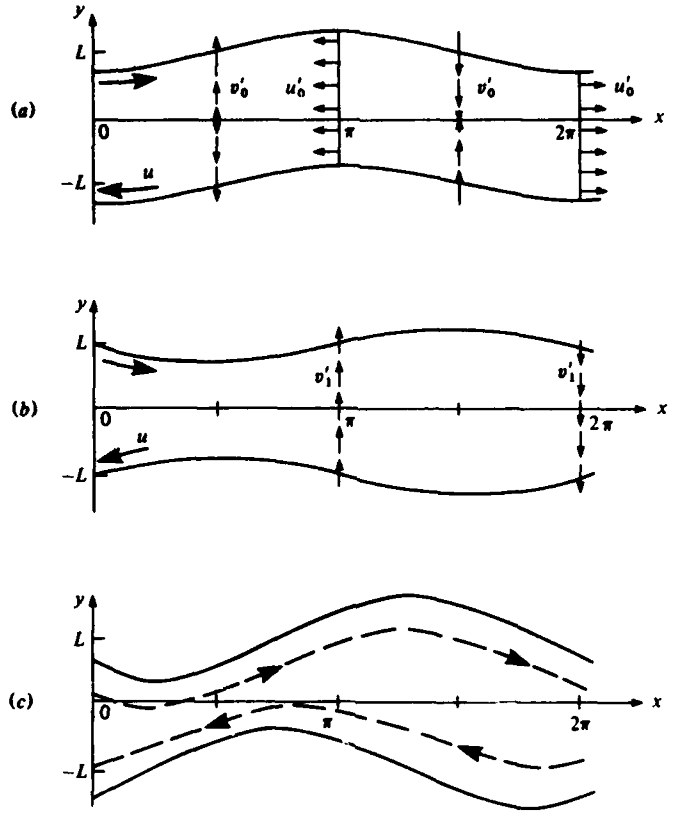

FIGURE 3. The structure of the zeroth-order eigenfunctions: (*a*) the first-order eigenfunctions; (*b*) (from (3.16)) and the combination of these two modes; (*c*) for ϵ of order one and a flow with zero potential vorticity. The undisturbed flow $\tilde{u}$ is linear with y.

The nature of the zeroth-order eigenfunctions is sketched in figure 3(*a*). Because both the cross-stream velocity v' and the undisturbed longitudinal flow $\tilde{u}$ are antisymmetric in y, the zeroth-order perturbation corresponds to a meandering of the stream. The corresponding depth perturbation is linear with y, so that the total depth profile $\bar{h}+h'_0$ remains symmetric and parabolic about the *local* midpoint of the current.

The first-order cross-stream velocity v'_1 is independent of position across the stream, but, because $\tilde{u} = y$, it corresponds to variations in the current width, as sketched in figure 3(*b*). This perturbation has an amplitude whose phase is $\frac{1}{2}\pi$ radians ahead of v'_0. The depth perturbation h'_1 is also independent of y, and therefore tends to maintain the symmetry about the midpoint $y = 0$. As a result of the form of h'_1, the depth increases uniformly at the widest section of the current and decreases at the narrowest section.

Higher-order eigenfunctions (such as v'_2 and v'_3) have structures similar to those already described, but tend to concentrate the amplitude of perturbations nearer the two free streamlines. When the perturbations sketched in figures 3(*a*, *b*) are superimposed, noting the comparable amplitudes in (3.12) and assuming $\epsilon \sim 1$, the structure of the flow becomes that sketched in figure 3(*c*). There is still a uniform reduction of the current depth at $x = \frac{1}{2}\pi$ and a uniform increase at $x = \frac{3}{2}\pi$. When such a disturbance

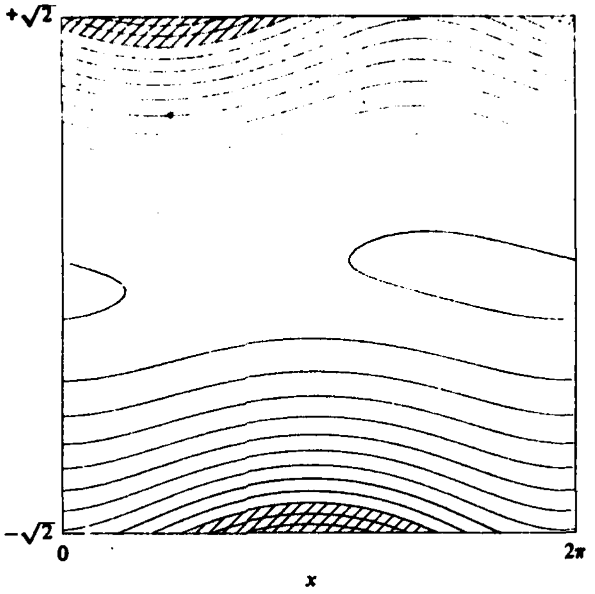

FIGURE 4. Equispaced contours of the total depth $\bar{h}+h'$ from the numerical solution for zero potential vorticity, for $\epsilon = 0{\cdot}8$ and a depth perturbation of maximum amplitude 0·28 (chosen for clarity). Regions of negative $\bar{h}+h'$ are hatched.

reaches sufficiently large amplitudes it is likely that regions of closed circulation will develop within the deeper, broader parts of the stream, and such regions will be centred about the midpoint of the flow. Figure 4 shows a plot of the contours of constant h (the total depth of the current) for the numerical solution at $\epsilon = 0{\cdot}8$. The meandering and variations of width are visible, along with a phase difference of $\frac{1}{2}\pi$ radians between the two edges of the flow. The widest sections of the current are also deepest, even deeper than the mid-point of the undisturbed flow.

Energetics

The source of energy for the growing disturbances may be determined from the structure of the depth and velocity perturbations. In order to calculate the energy changes we consider small perturbations (u', v', h') to (2.8), (2.9), (2.3), where we revert here to a general mean flow. Taking $\bar{h}u'$ times (2.8), $\bar{h}v'$ times (2.9), h' times (2.3), and adding yields the local energy equation

$$\frac{\partial E}{\partial t} + \bar{h}\bar{u}_y\langle u'v'\rangle + \{\bar{h}\langle h'v'\rangle\}_y = 0, \tag{3.13}$$

where the angle brackets denote an average in the x-direction and

$$E = \tfrac{1}{2}\langle \bar{h}(u'^2 + \epsilon^2 v'^2) + h'^2\rangle \tag{3.14}$$

is a convenient measure of the energy of the perturbations (kinetic plus potential). As is well-known, interpretation of the local terms in (3.13) as kinetic and potential energy transfers is dangerous. To avoid this, we integrate (3.13) to give

$$\frac{d}{dt}\int_{-L}^{L} E\,dy = -\int_{-L}^{L} \bar{h}\bar{u}_y\langle u'v'\rangle\,dy, \tag{3.15}$$

which shows that growing perturbations draw energy from the kinetic energy of the mean flow. However, at the end of §4 we shall show that potential energy is also released.

For the case of zero potential vorticity the Reynolds stress term $\langle u'v' \rangle$ is evaluated from (3.12) as

$$\langle u'v' \rangle = \frac{-2}{\sqrt{15}}\epsilon + O(\epsilon^2), \tag{3.16}$$

so that, as $\bar{h}\bar{u}_y$ is positive in (3.15), the perturbations induce a positive Reynolds stress which transports momentum across the stream. The superposition of meandering and varicose modes with a phase difference of $\frac{1}{2}\pi$ therefore removes kinetic energy from the mean flow. In general, though, it is not yet obvious that the right-hand side of (3.15) need be positive (and the flow unstable) for an arbitrary mean velocity profile. This is the subject of §4, where it is shown that indeed there must always be unstable perturbations to any mean flow with two free streamlines.

4. The case of arbitrary mean profile

Formulation of the problem

We again consider a current such as that discussed in §2. This time, however, no restrictions are placed on the depth profile save that $\bar{h} = 0$ at $y = \pm L$. The perturbation equations (2.15)–(2.17) are to be satisfied, while $\bar{u}$ and $\bar{h}$ are connected by the geostrophic constraint (2.11), and we shall show that an unstable mode exists for general depth profiles $\bar{h}$.

For convenience, an integrated depth perturbation $\phi(y)$ can be defined as

$$\phi(y) \equiv \int_{-L}^{y} \hat{h}\, dy \tag{4.1}$$

$$\equiv \phi_0 + \epsilon\phi_1 + \epsilon^2\phi_2 + \epsilon^3 \log \epsilon\, \phi_3 + \epsilon^3\phi_4 + \dots, \tag{4.1a}$$

where the wavenumber expansion (4.1*a*) also holds for c, $\hat{u}$ and $\hat{v}$, and

$$\hat{h}_n = \phi_{ny} \quad (n = 0, 1, 2, \dots). \tag{4.2}$$

The ϕ_n must satisfy some boundary conditions and, from (4.1), we have

$$\phi_n(-L) = 0, \tag{4.3}$$

where we may choose the magnitude of $\phi_y(-L)$ arbitrarily. Selecting for convenience the value $\phi_y(-L) = -\tilde{u}(-L)$, we have

$$\left.\begin{aligned} \phi_{0y}(-L) &= -\tilde{u}(-L), \\ \phi_{ny}(-L) &= 0 \quad (n > 0). \end{aligned}\right\} \tag{4.4}$$

In addition, application of the continuity equation (2.17) at $y = \pm L$ gives, since $\hat{v}$ is well behaved,

$$\bar{u} i \hat{v} + (\bar{u} - c)\phi_y = 0 \quad (y = \pm L). \tag{4.5}$$

In general the ϕ_n will have a boundary-layer structure of thickness ϵ at critical layers (where $\tilde{u} = 0$), and an inner expansion, followed by asymptotic matching across these layers, is necessary. The details of the inner expansion are not shown explicitly here, but are recorded in appendix B, which has been lodged with the editorial office of the *Journal of Fluid Mechanics*, and will be used in what follows. An alternative proof of the existence of an unstable mode, avoiding many of the boundary-layer problems, is given in appendix A. However, that approach assumes the existence of well-behaved eigenfunctions, while the expansion technique outlined in this section explicitly finds such well-behaved eigenfunctions.

The expansions of (2.15)–(2.17) may be written symbolically as

$$(\bar{u}-c_0)\,u_n+(1-\bar{u}_y)\,iv_n+\phi_{ny}+A_n=0, \tag{4.6}$$

$$u_n+B_n=-\phi_{nyy}, \tag{4.7}$$

$$\bar{h}u_n-(\bar{h}iv_n)_y+(\bar{u}-c_0)\,\phi_{ny}+C_n=0, \tag{4.8}$$

for $n=0,1,2,\ldots$, where A_n, B_n and C_n involve combinations of terms from previous values of n with eigenvalues up to c_n. Thus

$$iv_n=\frac{(\bar{u}-c_0)\,\phi_{nyy}-\phi_{ny}+B_n(\bar{u}-c_0)-A_n}{1-\bar{u}_y}. \tag{4.9}$$

Substitution of (4.9) into (4.8), integration from $-L$ to y, and multiplication by $(1-\bar{u}_y)/\bar{h}$ gives, remembering that $\bar{h}(-L)=0$,

$$(\bar{u}-c_0)\,\phi_{nyy}-\bar{u}_y\phi_{ny}+\frac{c_0(1-\bar{u}_y)}{\bar{h}}\,\phi_n=-\frac{(1-\bar{u}_y)}{\bar{h}}\int_{-L}^{y}(\bar{h}B_n-C_n)\,dy \\ -B_n(\bar{u}-c_0)+A_n. \tag{4.10}$$

Equations (4.9) and (4.10), with boundary conditions given by (4.4) and the expansion of (4.5), form an eigenvalue problem for each c_n. One particular solution, which couples the two free streamlines together, was isolated in § 3 for the special case of zero potential vorticity, and we now examine the corresponding solution for the general case. We show that, except under very special conditions, the mode is always unstable.

Solution up to order ϵ^2

To leading order, $A_0=B_0=C_0=0$, and, from (4.10), and (4.9), ϕ_0 and v_0 satisfy

$$(\bar{u}-c_0)\,\phi_{0yy}-\bar{u}_y\phi_{0y}+\frac{(c_0-U)(1-\bar{u}_y)}{\bar{h}}\,\phi_0=0, \tag{4.11}$$

$$iv_0=\frac{(\bar{u}-c_0)\,\phi_{0yy}-\phi_{0y}}{1-\bar{u}_y}. \tag{4.12}$$

The set (4.11), (4.4) and (4.5) pose an eigenvalue problem for c_0 which may have many solutions; no indication has been found of whether or not c_0 can be complex. However, we choose here to examine a *specific* solution to (4.11) in which c_0 is real, and show that to next order c is complex. We choose the solution

$$c_0=U,\quad \phi_0=\bar{h},\quad iv_0=\tilde{u},\quad u_0=\tilde{u}_y,\quad h_0=U-\bar{u}=-\tilde{u}, \tag{4.13}$$

so that, to leading order, the disturbance is simply propagated downstream at speed U. We see that, in general, u_0 and h_0 are real, while v_0 is imaginary, implying that u' and h' have phases which are $\frac{1}{2}\pi$ ahead of v'.

The $O(\epsilon)$ terms have $A_1 = -c_1 u_0$, $B_1 = 0$ (i.e. the along-stream flow remains geostrophic), and $C_1 = -c_1 \phi_{0y}$. Then (4.10) becomes

$$\tilde{u}\phi_{1yy} - \bar{u}_y \phi_{1y} + c_1 = 0, \tag{4.14}$$

and (4.4) gives the conditions $\phi_1 = \phi_{1y} = 0$ at $y = -L$, while the condition (4.5) gives no information to this order. Now (4.14) has two independent solutions, one with ϕ_{1y} proportional to $\tilde{u}$, and one with

$$\phi_{1y} = -c_1 \tilde{u} \int^y \frac{dy}{\tilde{u}^2}. \tag{4.15}$$

Consideration of (2.11) shows that $\tilde{u}$ must vanish at least once in the interval $(-L, L)$. The places where $\tilde{u}$ vanishes are the critical layers for this solution. We shall treat the case of one such layer (at $y = y_c$), but the extension to several layers is immediate. We shall also assume that $\bar{u}_{yc}$ (we denote values at the critical layer with a suffix c) is non-zero. (In the extreme case of $\tilde{u}$ vanishing quadratically, rather than linearly, at a critical layer, it can be shown that the solution is stable. Physically, there is stability if the vorticity $\bar{u}_y$ vanishes when $\tilde{u}$ vanishes.)

The solution (4.15) is well-behaved as $\tilde{u}$ approaches zero only if $\bar{u}_{yyc}$ is zero (as would be the case for all symmetric depth distributions, for example); otherwise the solution contains logarithmically growing terms. In either case, a matching across the critical layer is necessary. We therefore write

$$\phi_1^- = -c_1 \int_{-L}^{y} \tilde{u}(\eta)\, d\eta \int_{-L}^{\eta} \frac{d\xi}{[\tilde{u}(\xi)]^2} \quad (y < y_c), \tag{4.16}$$

$$\phi_1^+ = \beta - \alpha\bar{h} - c_1 \int_{+L}^{y} \tilde{u}(\eta)\, d\eta \int_{+L}^{\eta} \frac{d\xi}{[\tilde{u}(\xi)]^2} \quad (y > y_c), \tag{4.17}$$

where α, β are unknown constants, and the boundary conditions on (4.14) have been used to give (4.16). To match across the critical layer, we shall need the behaviour of $\phi_1^\pm$ near $y = y_c$. Writing $\eta = y - y_c$, we have

$$\phi_1^- \sim \phi_{1c}^- + \frac{c_1}{\bar{u}_{yc}}\eta + \frac{c_1 \bar{u}_{yyc}}{2\bar{u}_{yc}^2}\eta^2(\log\eta - \tfrac{1}{2}) - \tfrac{1}{2}c_1\bar{u}_{yc}\eta^2\left\{\int_{-L}^{y_c-\delta}\frac{dy}{\tilde{u}^2} - \frac{1}{\delta\bar{u}_{yc}^2} + \frac{\bar{u}_{yyc}}{\bar{u}_{yc}^2}\log(-\delta)\right\} + \frac{c_1\bar{u}_{yyc}\eta^2}{\bar{u}_{yc}^2} \quad (\eta < 0), \tag{4.18}$$

$$\phi_1^+ \sim \phi_{1c}^+ + \frac{c_1}{\bar{u}_{yc}}\eta + \tfrac{1}{2}\alpha\bar{u}_{yc}\eta^2 + \frac{c_1 \bar{u}_{yyc}}{2\bar{u}_{yc}^2}\eta^2(\log\eta - \tfrac{1}{2}) - \tfrac{1}{2}c_1\bar{u}_{yc}\eta^2\left\{\int_{L}^{y_c+\delta}\frac{dy}{\tilde{u}^2} + \frac{1}{\delta\bar{u}_{yc}^2} + \frac{\bar{u}_{yyc}}{\bar{u}_{yc}^2}\log\delta\right\} + \frac{c_1\bar{u}_{yyc}}{\bar{u}_{yc}^2}\eta^2 \quad (\eta > 0), \tag{4.19}$$

where $\delta > 0$ is a small positive number. The expression $\log(-\delta)$ is to be interpreted as $\log\delta \pm i\pi$, and from the inner expansion it is found that this must be

$$\log\delta - i\pi\,\mathrm{sgn}\,(\bar{u}_{yc}).$$

At $O(\epsilon^2)$ in (4.6)–(4.8), $A = -c_1 u_1 - c_2 u_0$, $B_2 = \tilde{u}^2$ and $C_2 = -c_1\phi_{1y} - c_2\phi_{0y}$. Hence the flow becomes ageostrophic at this order. Then from (4.10) ϕ_2 satisfies

$$\tilde{u}\phi_{2yy} - \bar{u}_y\phi_{2y} + \frac{1-\bar{u}_y}{\bar{h}}\int_{-L}^{y}\bar{h}\tilde{u}^2\,dy + \tilde{u}^3 - c_1\phi_{1yy} + c_2 + \frac{c_1(1-\bar{u}_y)}{\bar{h}}\phi_1 = 0, \tag{4.20}$$

together with $\phi_2 = \phi_{2y} = 0, y = -L$.

The condition (4.5) at $y = +L$ yields the same result as requiring ϕ_2 to be well-behaved in (4.20) when $\bar{h}$ vanishes, namely

$$c_1\phi_1(L) = -\int_{-L}^{L} \bar{h}\tilde{u}^2\,dy. \tag{4.21}$$

The results of the asymptotic matching are straightforward, with ϕ_1, ϕ_{1y} being continuous at $y = y_c$, the $\eta^2\log\eta$ behaviour being handled by the inner expansion, and the well-behaved part of ϕ_{1yy} being continuous at $y = y_c$. We now match the $O(\eta^2)$ terms in the expansions (4.18), (4.19) for ϕ_1 to find the coefficient α introduced in (4.17): for $\delta \rightarrow 0$

$$\alpha = \frac{i\pi\bar{u}_{yyc}}{|\bar{u}_{yc}|^3}c_1 - c_1\left\{\left(\int_{-L}^{y_c-\delta} + \int_{y_c+\delta}^{L}\right)\frac{dy}{\tilde{u}^2} - \frac{2}{\delta\bar{u}_{yc}^2}\right\}. \tag{4.22}$$

The term in brackets is well known to be the Hadamard 'finite part' of the (divergent) integral of $\tilde{u}^{-2}$, and is a well-defined negative quantity. Its value is that of a naive integration of $\tilde{u}^{-2}$ from $-L$ to $+L$, cavalierly ignoring the singularity at y_c, and simply substituting the end values $+L$ into the integration.

Having an expression for the constant α, we can now evaluate $\phi_1(L)$ and then make use of (4.21) to find the eigenvalue c_1. First note that ϕ_1 is continuous at y_c, so that

$$\begin{aligned}\phi_1(L) &= \left\{\int_{L}^{y_c-\delta} + \int_{y_c-\delta}^{y_c+\delta} + \int_{y_c+\delta}^{L}\right\}\phi_{1y}\,dy \\ &= -c_1\int_{-L}^{y_c-\delta} dy\,\tilde{u}\int_{-L}^{y}\frac{d\eta}{[\tilde{u}(\eta)]^2} + O(\delta) + \int_{y_c+\delta}^{L}\alpha\tilde{u}\,dy - c_1\int_{y_c+\delta}^{L} dy\,\tilde{u}\int_{y_c+\delta}^{L}\frac{d\eta}{[\tilde{u}(\eta)]^2}.\end{aligned} \tag{4.23}$$

Using the geostrophic relation (2.11), integrating (4.23) by parts, and substituting for α from (4.22) gives, for small δ,

$$\phi_1(L) = -c_1\left\{\left(\int_{-L}^{y_c-\delta} + \int_{y_c+\delta}^{L}\right)\frac{\bar{h}}{\tilde{u}^2}dy - \frac{2\bar{h}_c}{\delta\bar{u}_{yc}^2}\right\} + \frac{i\pi\bar{u}_{yyc}\bar{h}_c c_1}{|\bar{u}_{yc}|^3} \tag{4.24}$$

$$= -c_1\,\mathrm{Fp}\int_{-L}^{L}\frac{\bar{h}}{\tilde{u}^2}dy + \frac{i\pi\bar{u}_{yyc}\bar{h}_c}{|\bar{u}_{yc}|^3}\,c_1, \tag{4.25}$$

where we use the notation Fp to denote the finite part of the integral. Then (4.21) gives, finally,

$$c_1^2 = \frac{\displaystyle\int_{-L}^{L}\bar{h}\tilde{u}^2\,dy}{\mathrm{Fp}\displaystyle\int_{-L}^{L}\bar{h}\tilde{u}^{-2}\,dy - i\pi\bar{u}_{yyc}\bar{h}_c/|\bar{u}_{yc}|^3}. \tag{4.26}$$

(For several critical layers, the last term in the denominator becomes a sum over all critical layers.)†

If $\bar{u}_{yyc}$, the gradient of relative vorticity at the critical layer, does not vanish, then (4.26) gives c_1^2 as complex, and so there exists a mode with $\mathscr{I}(c_1) > 0$, and there is instability. If $\bar{u}_{yyc}$ does vanish, it is easy to see that the finite part of the integral is negative.† Hence c_1 is only imaginary and the positive root of (4.26) gives an unstable mode. We have therefore proved the existence of an unstable wave mode for all distributions of depth, except in the unusual case when $\bar{u}_{yc}$ vanishes at a critical layer. The above analysis even holds in the zero-potential-vorticity case (§ 3) despite the fact that $1-\bar{u}_y$ in (4.12) then vanishes identically. The expression (4.26) reduces to $c_1^2 = -\frac{4}{15}$ in that case, in agreement with the analysis in § 3.

---

† The formula (4.26) has been confirmed by numerical integration of (2.15)–(2.17) for specific asymmetric profiles.

Energy transfers

The energetics of currents with arbitrary velocity profiles are easily evaluated. We have (outside the critical layer, which has a negligible extra contribution) the Reynolds stress

$$\langle u'v'\rangle = \tfrac{1}{2}\mathscr{R}(u_0 v_0^*) + \tfrac{1}{2}\epsilon\mathscr{R}(u_0 v_1^* + u_1 v_0^*) + O(\epsilon^2), \tag{4.27}$$

where the asterisk denotes complex conjugate. Using (4.13), the zeroth-order terms cancel. The first-order perturbation eigenfunction can be found from (4.18) and gives, after simplification,

$$\mathscr{R}(u_0 v_1^*) = \bar{u}_y \mathscr{R}(ic_1 + i\phi_{1y}), \tag{4.28a}$$

$$\mathscr{R}(u_1 v_0^*) = \mathscr{R}(-i\bar{u}_y\phi_{1y} + ic_1), \tag{4.28b}$$

whence

$$\langle u'v'\rangle = -\tfrac{1}{2}\epsilon c_{11}(1+\bar{u}_y) + O(\epsilon^2), \tag{4.29}$$

where c_{11} is the imaginary part of c_1. Then (3.15) yields

$$\frac{d}{dt}\int_{-L}^{L} E\,dy = \tfrac{1}{2}\epsilon c_{11}\int_{-L}^{L} \bar{h}\bar{u}_y(1-\bar{u}_y)\,dy + O(\epsilon^2) \tag{4.30}$$

and, after use of (2.11),

$$\frac{d}{dt}\int_{-L}^{L} E\,dy = \tfrac{1}{2}\epsilon c_{11}\int_{-L}^{L} (\bar{h}\bar{u}_y^2 + \bar{h}_y^2)\,dy > 0.$$

Hence the perturbation energy is indeed growing with time (as it must for exponentially growing modes).

Finally, we note that the perturbation mass (i.e. heat) transfer across-stream is given by

$$\langle v'h'\rangle = \tfrac{1}{2}\epsilon c_{11}\tilde{u}. \tag{4.31}$$

In the problem of § 3 (and also in § 5), the sign of (4.31) is such that the mass flux is directed outwards from $y = 0$. The further significance of $\langle v'h'\rangle$ appears when we form an expression from the continuity equation (2.3) for the rate of change of mean potential energy $\frac{1}{2}\langle h\rangle^2$, where again $h = \bar{h} + h'$:

$$\frac{\partial}{\partial t}\tfrac{1}{2}\langle h\rangle^2 + \bar{h}\langle v'h'\rangle_y = 0. \tag{4.32}$$

---

† This is best seen by considering the sign of ϕ_{1y} in (4.16). (4.17). If $\tilde{u}$ vanishes only once, for simplicity, $\tilde{u}$ is negative for $y < y_c$ and positive for $y > y_c$. Hence (4.15) and (4.22) show that $\phi_{1y}c_1^{-1}$ is positive for $y < y_c$ and for $y > y_c$, so that $\phi_1(L)$ is a positive multiple of c_1 in this case. Then (4.21) implies that c_1 is purely imaginary.

Then

$$\frac{d}{dt}\int_{-L}^{L} \tfrac{1}{2}\langle h\rangle^2\,dy = -\int_{-L}^{L} \tilde{u}\langle v'h'\rangle\,dy$$

$$= -\tfrac{1}{2}\epsilon c_{11}\int_{-L}^{L} \tilde{u}^2\,dy < 0. \tag{4.33}$$

In other words, release of mean potential energy is also necessary during the growth of the unstable mode discussed here. However, after a little algebra it may also be shown that the *total* potential energy, given by the integral of $(\frac{1}{2}\langle h\rangle^2 + \frac{1}{2}\langle h'^2\rangle)$, is invariant. Conservation of total energy (kinetic plus potential) thus implies that *total* kinetic energy is also invariant.

5. An example: currents with uniform potential vorticity

The results in § 4 can be applied to any particular distribution of vorticity. They show that (almost) all currents of the form sketched in figure 1 are unstable to a wave mode whose growth relies upon a coupling of the two free streamlines, and the general analysis gives useful physical understanding of the flow. However, the expansion about small wavenumber is not suitable for describing the most rapidly growing mode, which is that likely to be observed in laboratory experiments. We therefore present exact numerical solutions of the eigenvalue problem (2.15)–(2.17) for one particular case: that of currents with a finite and uniform potential vorticity $\mathscr{H}^{-1}$, for which the undisturbed flow is given by (2.13). The current is now also assumed to be flowing over a horizontal plane, so that the advection velocity U is zero.

For both the numerical solutions and comparison of these with experimental results it is much more convenient, when there is a uniform potential vorticity, to modify the original non-dimensionalization (2.7). By using the 'potential vorticity depth' H_0, rather than the maximum current depth H, as a depth scale, one of the two length scales L and $\mathscr{H}$ can be eliminated from (2.13). Thus we define a new dimensionless wavenumber k and a current width L_0 by

$$k = \epsilon\mathscr{H}^{\frac{1}{2}} = 2\pi\frac{(g'H_0)^{\frac{1}{2}}}{f\lambda}, \quad L_0 = \frac{L}{\mathscr{H}^{\frac{1}{2}}} = \frac{fW}{(g'H_0)^{\frac{1}{2}}}, \tag{5.1}$$

and similarly rescale current depth and velocities using H_0 instead of H in (2.7). The potential vorticity $\mathscr{H}^{-1}$ can be expressed in terms of the current width L by using the definition $\bar{h}(0) = 1$ in (2.13), whence

$$\mathscr{H}^{-1} = 1 - \frac{1}{\cosh L_0}. \tag{5.2}$$

If $L_0 \to 0$, we approach the limit of zero potential vorticity $\mathscr{H}^{-1} = 0$, while a very wide current, $L_0 \to \infty$, implies that $\mathscr{H}^{-1} \to 1$. In these new variables the undisturbed flow becomes

$$\bar{h} = 1 - \frac{\cosh y}{\cosh L_0}, \quad \tilde{u} = \frac{\sinh y}{\cosh L_0}. \tag{5.3}$$

The momentum and continuity equations (2.8), (2.9) and (2.3), as well as the perturbation equations (2.15)–(2.17), are all unchanged except that ϵ is replaced by k.

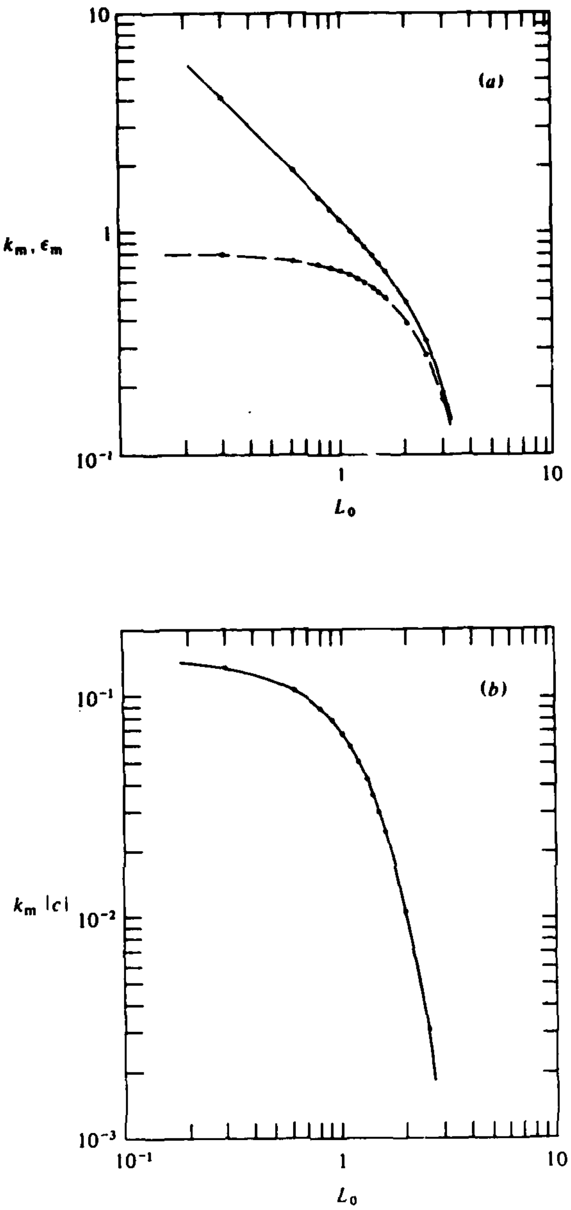

FIGURE 5. The computed wavenumber $k_m(a)$ and growth rate $k_m|c|\,(b)$ for the most rapidly growing mode on a current with uniform potential vorticity, as functions of the current width $L_0 = fW/(g'H_0)^{\frac{1}{2}}$. In (a) the wavenumber ϵ_m, which is non-dimensionalized by the Rossby radius based on the maximum depth H, is also plotted (broken line).

Numerical solutions

The perturbation equations (2.15)–(2.17), with k replacing ϵ and with the undisturbed flow defined by (5.3), have been solved using a numerical approach similar to that described in § 3. The solution was first computed for a range of values of the wavenumber k and a number of values of the width L_0. As for the case of flow with zero potential vorticity, the eigenvalues are all found to be pure imaginary. Hence the normal modes are unstable and are again advected downstream at speed U.

For each value of L_0, the dimensionless growth rate $k|c|$ increases with increasing wavenumber at $k \ll 1$, but reaches a maximum and decreases rapidly at sufficiently large wavenumbers. The wavenumber k_m at which the maximum growth rate is achieved was found by solving the equations at successively intermediate values of k near the maximum of the growth-rate curves. Resulting values of k_m are shown on figure 5(*a*). The most rapidly growing waves are relatively long ($k_m < 1$) when the current is 'wide' ($L_0 > 1$), and they are short (with $k_m > 1$) when the current is 'narrow'. More quantitatively, k_m satisfies the relation $k_m \simeq 1{\cdot}1 L_0^{-1}$ approximately for $L_0 < 2$, but decreases much more rapidly with increasing L_0 when $L_0 > 2$. On figure 5(*a*) we have also plotted ϵ_m (broken line), which is the dimensionless wavenumber (with maximum growth rate) based upon the length scale $(g'H)^{\frac{1}{2}} f^{-1}$. The two wavenumbers are related through L_0 by combining the definition $k = \epsilon \mathscr{H}^{\frac{1}{2}}$ with (5.2). (The two are significantly different at small values of L_0, where the current depth H differs more radically from the 'potential-vorticity depth' H_0.) As $L_0 \rightarrow 0, \epsilon_m$ approaches an upper limit of $\epsilon_m \simeq 0{\cdot}8$. This limit corresponds to flow with zero potential vorticity,† and the wavenumber is the same as that found in § 3. At $L_0 \gg 1$, on the other hand, $H \rightarrow H_0$, so that ϵ_m and k_m become identical. The most rapidly growing mode then has a wavelength that is very much larger than the Rossby radius $(g'H)^{\frac{1}{2}} f^{-1}$.

On figure 5(*b*) is plotted the growth rate $k_m|c|$ of the most rapidly growing mode as a function of the current width L_0. For small values of L_0 this growth rate approaches the maximum growth rate previously computed for normal modes on a current with zero potential vorticity (see figure 2). However, the growth rate decreases exponentially when the current width is increased beyond $L_0 = 1$. At $L_0 = 2$ the growth rate $k_m|c|$ is an order of magnitude smaller than it is at $L_0 = 0{\cdot}5$, giving an *e*-folding time $(k_m|c|f)^{-1}$ of eight rotation periods.

The rapid decrease of growth rate with increasing current width is predicted by the wavenumber expansion of § 4. For a current of the form (5.3), the general results (4.26) for the first-order eigenvalue reduces readily to

$$c_1^2 = -\tfrac{1}{2}(\cosh L_0)^{-2}\left[1 - \tfrac{2}{3}\tanh^2 L_0 - \frac{2L_0}{\sinh 2L_0}\right]. \tag{5.4}$$

Here, c_1 is imaginary for all values of L_0, but its magnitude decreases exponentially at large L_0: $c_1 \sim \pm i(\tfrac{2}{3})^{\frac{1}{2}} \exp(-L_0)$ $(L_0 \gg 1)$. It can also be shown that there are no other long-wave solutions for the case of constant potential vorticity.

The structure of growing disturbances

Examples of computed depth and velocity perturbations for a current with uniform potential vorticity are shown in figure 6. In this case the width was $L_0 = 1$ (giving a potential vorticity $\mathscr{H}^{-1} = 0{\cdot}35$) and the amplitude $\hat{h}$ of the depth perturbation was set at 10^{-1}. Figures 6(*a, b*) show contours of the total depth $h + h'$ and depth perturbation h', respectively, while figure 6(*c*) shows contours of the cross-stream velocity

---

† Note that use of the wavenumber-expansion technique discussed in §§ 3 and 4 will not allow us to approach the limit of zero potential vorticity ($\mathscr{H} \rightarrow \infty$) at any finite value of ϵ, since we would require $k = \epsilon \mathscr{H}^{\frac{1}{2}} \ll 1$ (but of course this is no deterrent to a numerical solution). Thus we cannot simply let $L_0 \rightarrow 0$ (analytically) to recover the zero-potential-vorticity case.

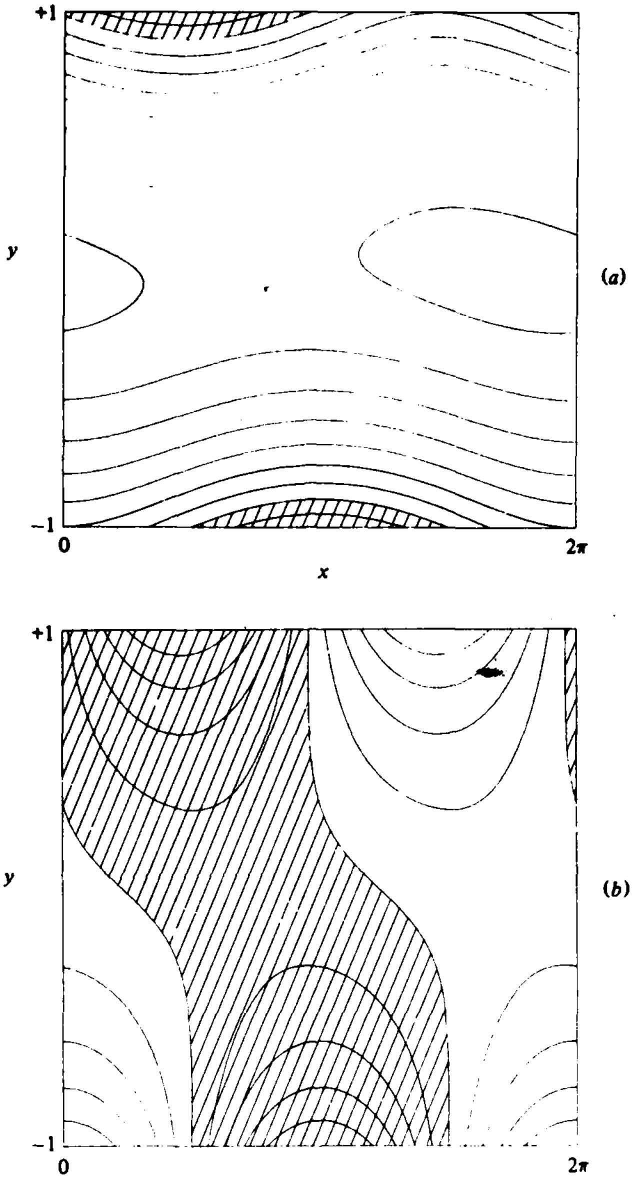

FIGURE 6 (*a*, *b*). Legend on p. 362.

perturbation v' for the same most-rapidly growing disturbance. As predicted by the wavenumber-expansion technique (§§3 and 4), the perturbation involves both a meandering and a longitudinal variation of current width. There is a phase difference of $\frac{1}{2}\pi$ radians between h' on the two free streamlines, and the greatest cross-stream excursions of the centre line occur at x-positions very close to where $|\partial L_0/\partial x|$ is greatest.

From figure 6 it can be seen that the depth perturbation and, similarly, the perturbation energy (as indicated by v') are confined more closely to the edges of the current

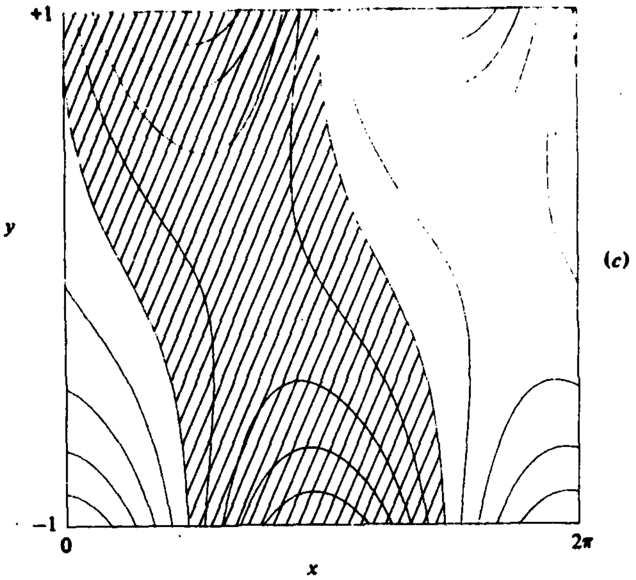

FIGURE 6. Contours of (a) the total depth $\bar{h}+h'$, (b) the depth perturbation h', and (c) the cross-stream velocity perturbation v' for the most rapidly growing mode on a current with uniform potential vorticity and $L_0 = 1$. The solution in (a) is for a depth perturbation of amplitude 0·1. Regions of negative values are hatched.

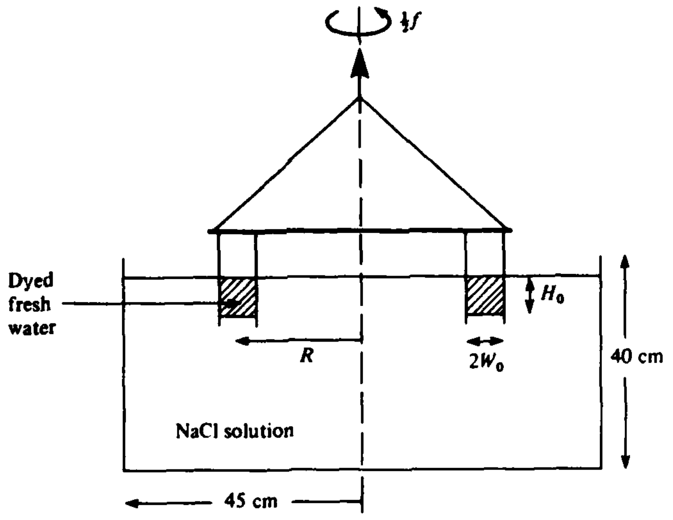

FIGURE 7. A sketch of the laboratory apparatus in vertical section. The cross-hatching indicates the upper layer of fresh, dyed water inside the annulus and the deep lower layer is a NaCl solution.

(even for $L_0 = 1$) than was the case for perturbations on currents with zero potential vorticity. From the power-series solution presented in §4 the leading-order eigenfunctions (4.13) reduce, for constant potential vorticity, to the simple forms

$$u_0 = \frac{\cosh y}{\cosh L_0}, \quad h_0 = -iv_0 = -\frac{\sinh y}{\cosh L_0}. \tag{5.5}$$

The hyperbolic functions at this and higher orders tend to concentrate the perturbation energy into regions closer to the two free streamlines. This is where the basic flow has the greatest depth variation and a concentration of relative vorticity:

$$-d\bar{u}/dy = -\cosh y/\cosh L_0.$$

The concentration of perturbations near the fronts is much stronger for wider currents, flows for which the vorticity $\bar{u}_y$ at the centre line is much smaller and for which we know that the disturbances grow much more slowly.

Hence our restriction that the flow has a uniform potential vorticity results in a coupling between the two free streamlines that becomes very much weaker as L_0 becomes larger. On the other hand, it must be remembered that currents with more-general vorticity distributions are able to be much wider than the Rossby radius based on the fluid depth H while still having a more uniform distribution of relative vorticity, thus making larger growth rates possible for wide currents.

6. Laboratory experiments

Apparatus

Currents with an approximately uniform potential vorticity and which were bounded on each side by a well-defined density front were produced in a rotating container. In order that the flow be initially uniform along the current, an axisymmetric configuration was used. The free surface of a relatively deep lower layer of dense fluid then served as a horizontal (geopotential) surface on which the current flowed. This also greatly reduced the influence of friction below that which would be induced by a solid boundary. The depth of the lower layer of sodium chloride solution was, in most experiments, either 28 cm or 40 cm. A large annulus with a relatively narrow gap between its walls was partially immersed in the lower layer, as sketched in figure 7. The annulus was suspended from above and held concentric with the vertical axis of rotation of the container and stationary in the rotating frame of reference. Three different annuli were used. One had an inner radius of 19·8 cm and an outer radius of 23·8 cm, leaving a gap of half-width $W_0 = 2{\cdot}0$ cm. The others had mean radii of 20·0 cm and 21·5 cm, with half-widths $W_0 = 3{\cdot}9$ cm and $W_0 = 3{\cdot}5$ cm, respectively. The outer wall of the rotating container was at a radius of 45 cm.

After the salt solution had come to the desired rotation rate $\Omega = \frac{1}{2}f$, dyed fresh water was carefully floated onto the free surface inside the annulus to form the shallow upper layer of depth H_0 shown in figure 7. The system was then left for at least 30 min to reach solid-body rotation everywhere. The depth H_0 could be determined both by observing a vertical scale horizontally through the Perspex walls and by measuring the volume of upper layer fluid placed in the annulus. At a time $t = 0$ the annulus was carefully drawn vertically upwards and removed. The subsequent flow was made visible by the dye in the upper layer and small pellets of paper floating on the free surface. Photographs were taken with a camera mounted in the rotating reference frame and time exposures of about one-half of a rotation period were used to obtain streaks. Such streaks, as well as direct observations, revealed no motion before the annulus was withdrawn. Values of the Coriolis parameter f ranged from 0·38 s^{-1} to 2·5 s^{-1}, while the reduced gravity g' lay in the range $0{\cdot}2 < g' < 12$ cm s^{-2}. The initial depth H_0 of the upper layer was always between 4 and 6 cm. This gave a ratio of layer

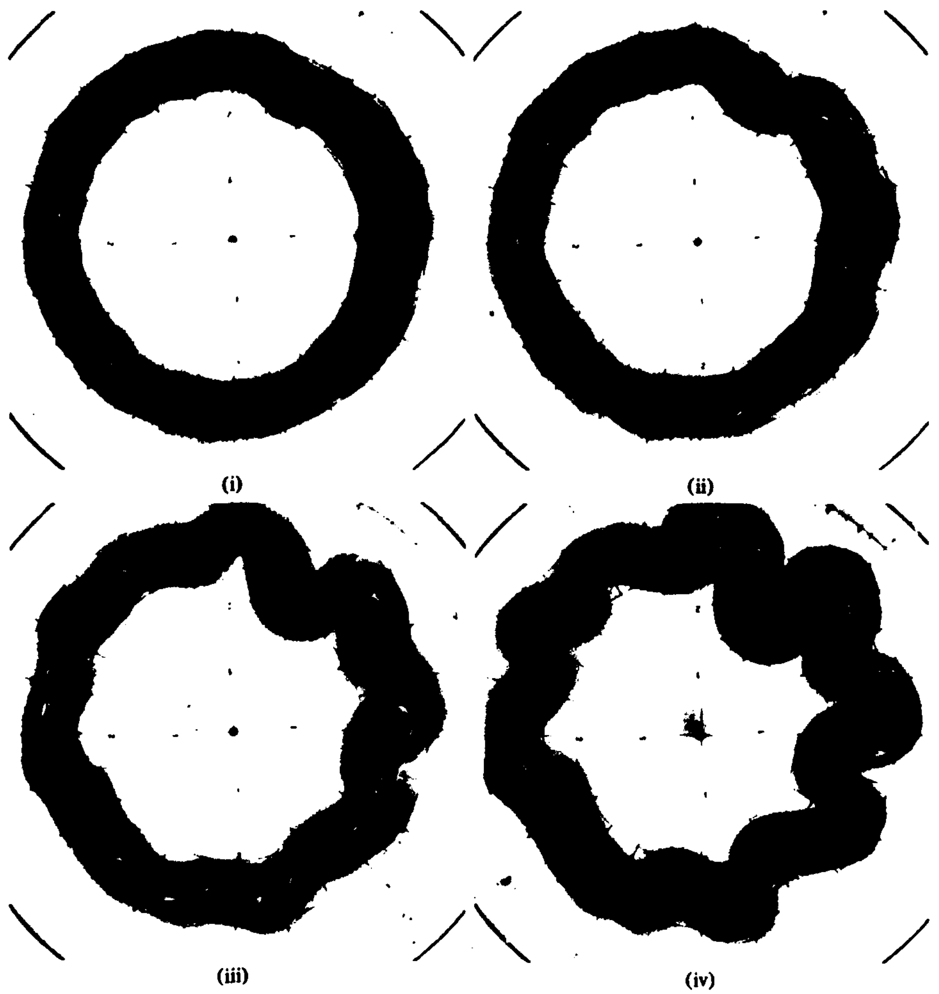
(i) (ii) (iii) (iv)

FIGURE 8. Streak photographs showing four stages in the evolution of a laboratory current with $W_0 = 2{\cdot}0$ cm, $f = 1{\cdot}77\ \mathrm{s}^{-1}$ and $\mathscr{L}_0 = 1{\cdot}18$ (4 s exposures). Times after withdrawal of the annulus are (in number of revolutions): (i) $t = 2$; (ii) 4; (iii) 6; (iv) 8. The ratio of layer depths is 0·17. Concentric circles on the bottom of the tank have a 5 cm spacing.

depths in the range 0·1–0·16 or in the range 0·16–0·2 when the lower layer was 40 cm deep or 28 cm deep, respectively. However, some experiments were also carried out with *shallow* lower layers in order to observe the influence upon the flow of the lower boundary. In these cases the initial ratio of layer depths was between 0·8 and 0·9.

Experimental observations

When the annulus was removed, the buoyant upper-layer fluid first spread radially toward and away from the axis of rotation by a distance that was measured to be close to the Rossby radius $(g'H_0)^{\frac{1}{2}} f^{-1}$. This collapse brought the flow into an approximately geostrophic balance (described by (2.11)) within a time scale of order f^{-1}. An anticyclonic (clockwise) flow is produced in the outer half of the upper layer and a cyclonic flow in the inner half, while any motion in the deep lower layer can be neglected. The axisymmetric geometry requires that both potential vorticity and angular momentum be conserved by the fluid in each layer during the collapse and that there is a balance between the buoyancy, Coriolis and centrifugal forces in the final state. The ratio of centrifugal and Coriolis accelerations is given by $\bar{u}/fr \sim (g'H_0)^{\frac{1}{2}}/fR$, where R is the radius of the annulus. For most experiments this parameter was less than 10^{-1}, but it reached 0·2 for experiments with large Rossby radii. Therefore the geostrophic basic flow assumed in the analysis in previous sections is only approximately realized.

Even before the geostrophic collapse was complete, rapidly growing billows (believed to be Kelvin–Helmholtz billows) with length scales of the order of 2 cm appeared on each edge of many of the currents. However, these disturbances also dissipated rapidly (often before the first photograph could be taken), presumably mixing some of the fluid near the fronts, and the current again became axisymmetric for a time. Later, but always within two or three revolution periods, disturbances with much larger downstream length scales appeared on the otherwise uniform flow. Subsequently, the current always broke up into a chain of eddies within five to ten revolutions.

If we assume that the deep bottom layer is stationary and that there is no mixing between the layers during the collapsing phase, then the laboratory current is described by the two dimensionless parameters $fW_0/(g'H_0)^{\frac{1}{2}}$ and W_0/H_0. In order to relate the parameters before and after the initial collapse, we write $W_0 = A/2H_0$, where A is the cross-sectional area of the current, and define

$$\mathscr{L}_0 \equiv \frac{fW_0}{(g'H_0)^{\frac{1}{2}}} = \frac{fA}{2H_0(g'H_0)^{\frac{1}{2}}}. \tag{6.1}$$

By integrating the hyperbolic depth profile (5.5), the area A can be found in terms of $L_0 = fW/(g'H_0)^{\frac{1}{2}}$ (where W is the half-width *after* collapse). Then (6.1) gives

$$\mathscr{L}_0 = L_0 - \tanh L_0. \tag{6.2}$$

Then the final width $L_0 \rightarrow 0$ when $\mathscr{L}_0 \rightarrow 0$, while $L_0 \simeq \mathscr{L}_0 + 1$ when $\mathscr{L}_0 \gg 1$.

In figure 8 are shown four stages during the evolution of a current that was formed when the initial Rossby radius was equal to the half-width W_0 of the annulus ($\mathscr{L}_0 = 1{\cdot}18$). In (i) the flow is largely axisymmetric and the relative vorticity is distributed throughout the width of the current. In (ii) the streaks reveal that regions of closed anticyclonic circulation have appeared near the centre line of the current. The fronts (edges of the dyed fluid) also reveal a wavelike structure. There appears to be some meandering away from the initial centre line as well as variations in current width. Both become more obvious in (iii), where the flow appears to be qualitatively very similar to that sketched in figure 4(*c*), except that at this large amplitude there are closed circulations within the deeper sections of the current. In this case there are nine or ten waves around the annulus. In (iv), individual eddies have broken off from their neighbours and the flow become a broad region of anticyclonic eddies. These subsequently decay very slowly due to friction.

In figure 9 is shown a similar sequence in the evolution of a current for which the initial Rossby radius was $1{\cdot}56W_0$ ($\mathscr{L}_0 = 0{\cdot}74$). Frame (i) again shows an almost axisymmetric flow. However, small 'cat's-eye'-shaped disturbances are already visible near the centre line ($y = 0$). Only one revolution later (ii) these disturbances influence

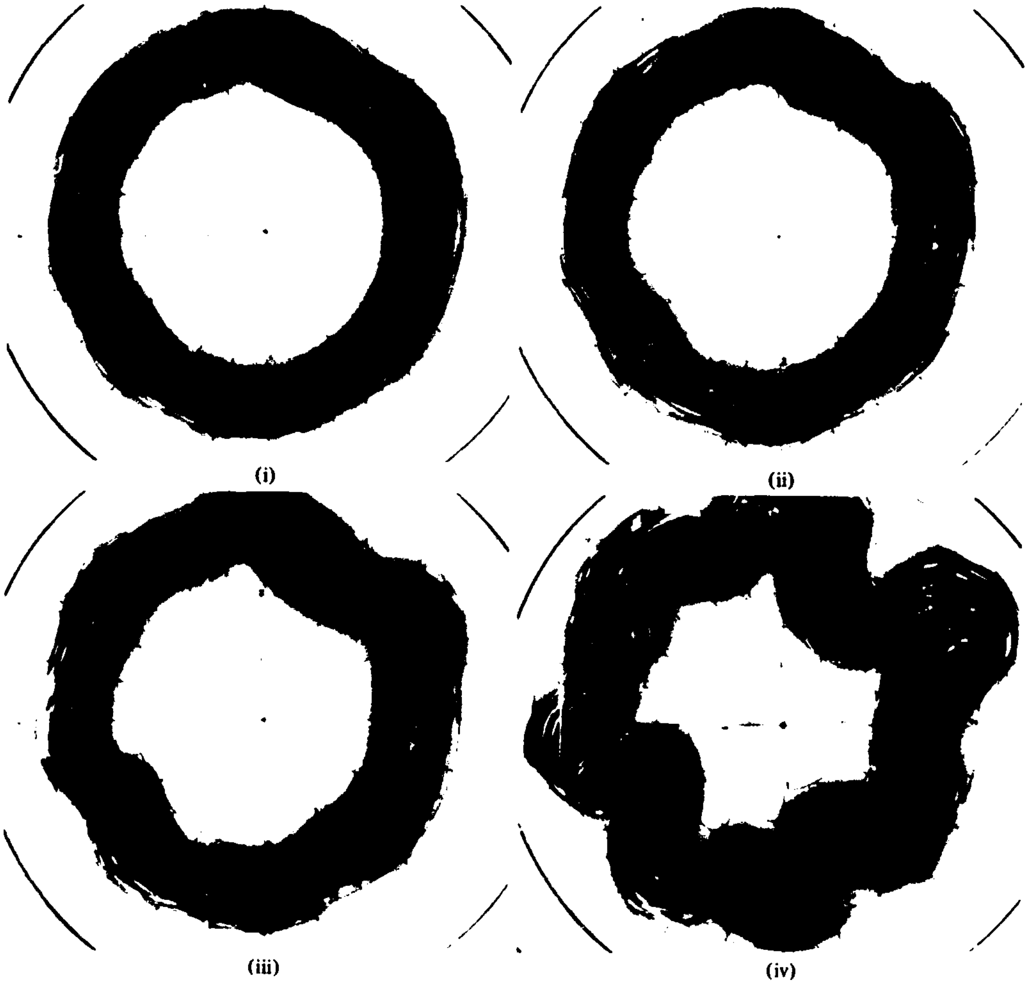

FIGURE 9. Streak photographs showing the evolution of a laboratory current with $W_0 = 2{\cdot}0$ cm, $f = 1{\cdot}11\ \mathrm{s}^{-1}$, and $\mathscr{L}_0 = 0{\cdot}74$ (4 s exposures). Times after withdrawal of the annulus are (in number of revolutions): (i) $t = 3$; (ii) 4; (iii) 6; (iv) 8. The ratio of layer depths is 0·17.

the whole flow. In this case there are seven waves around the annulus and both the varicose and meandering nature of the flow is visible. In (iii) and (iv) the anticyclonic eddies again develop and break up the current.

For contrast, figure 10 shows the evolution of a current that is much wider than the Rossby radius ($\mathscr{L}_0 = 4{\cdot}0$). As for the experiments shown in figures 8 and 9, the initial ratio of layer depths is 0·17. In this case disturbances could be seen first at the edges of the current (i) and rapidly grew in amplitude to take the form of waves that 'break' on their upstream side (ii). The two fronts then appear to behave independently. Vortices of opposite sign develop in the lower layer behind each 'breaking' crest (iii) and can lead to the formation of vortex pairs at each edge of the flow. The resulting turbulent current is shown in (iv). When the ratio of layer depths was less than 0·2 this apparently two-layer flow occurred for all currents with $\mathscr{L}_0 > 2$.

For large depth ratios, the transition between the two kinds of behaviour occurs

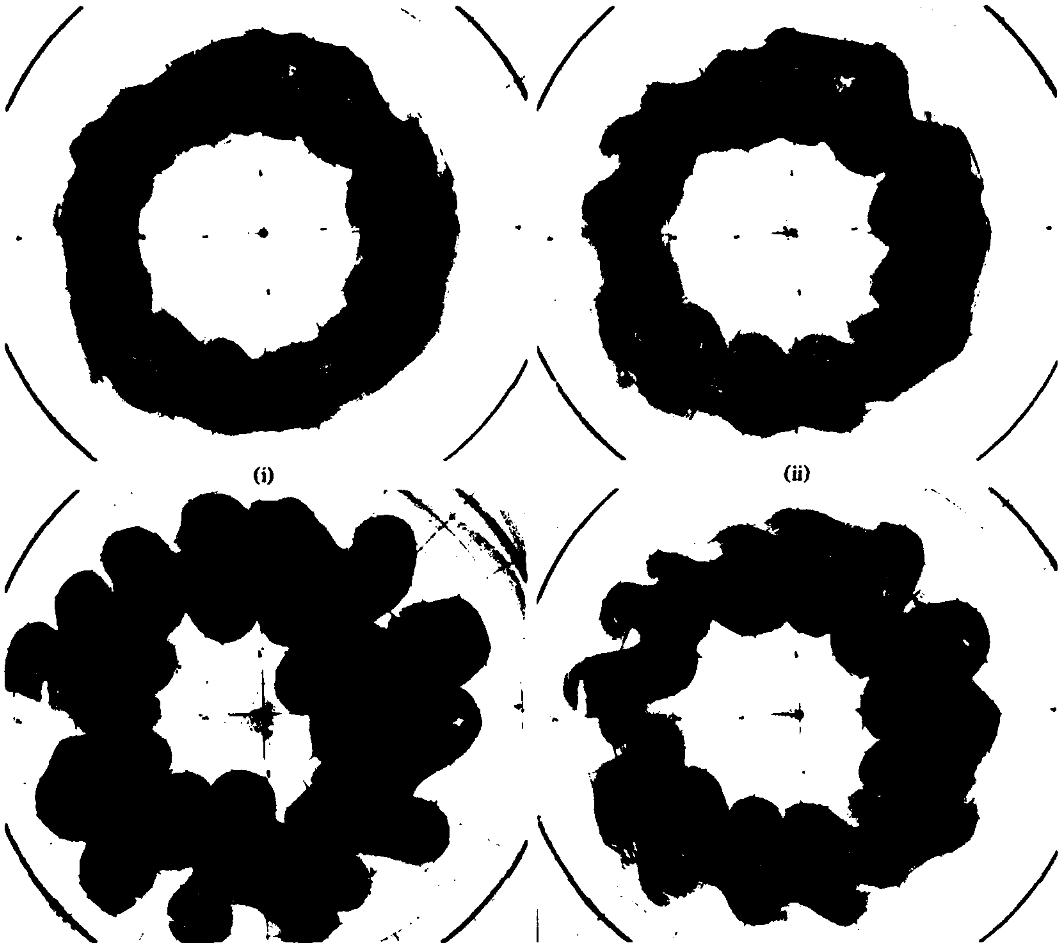
(i) (ii) (iii) (iv)

Figure 10. Streak photographs showing the evolution of a laboratory current with $W_0 = 3{\cdot}9$ cm, $f = 2{\cdot}87\ \mathrm{s}^{-1}$ and $\mathscr{L}_0 = 4{\cdot}0$ (4 s exposures). Times in number of revolutions after withdrawal of the annulus are (i) $t = 3$; (ii) 4; (iii) 6; (iv) 12. The ratio of layer depths is 0·17.

near $\mathscr{L}_0 = 1$. Figure 11 shows two stages in the evolution of a current with $\mathscr{L}_0 = 1{\cdot}07$ and a ratio of layer depths 0·84. The disturbances still appear to be dominated by a coupling between the two density fronts. The waves do not 'break' and no cyclonic eddies develop in the lower layer. On the other hand, when $\mathscr{L}_0 = 3{\cdot}7$ and the depth ratio is 0·9, each edge behaves independently. This case is shown in figure 12, where the initial axisymmetric current develops small-scale breaking waves on each edge.

In each experiment the number n of waves that appeared around the annular current were counted.† This wavenumber increased linearly with $\mathscr{L}_0$ for each annulus. The wavelength was then calculated from $\lambda = 2\pi R/n$, where R is usually the mean radius of the annulus used. For 'wider' currents ($\mathscr{L}_0 > 2$), though, there was a smaller number of waves on the inner edge of the current than on the outer edge. However,

---

† Measurements of wavelength were always taken after the disappearance of any small-scale Kelvin Helmholtz billows if the two length scales were distinctly separated.

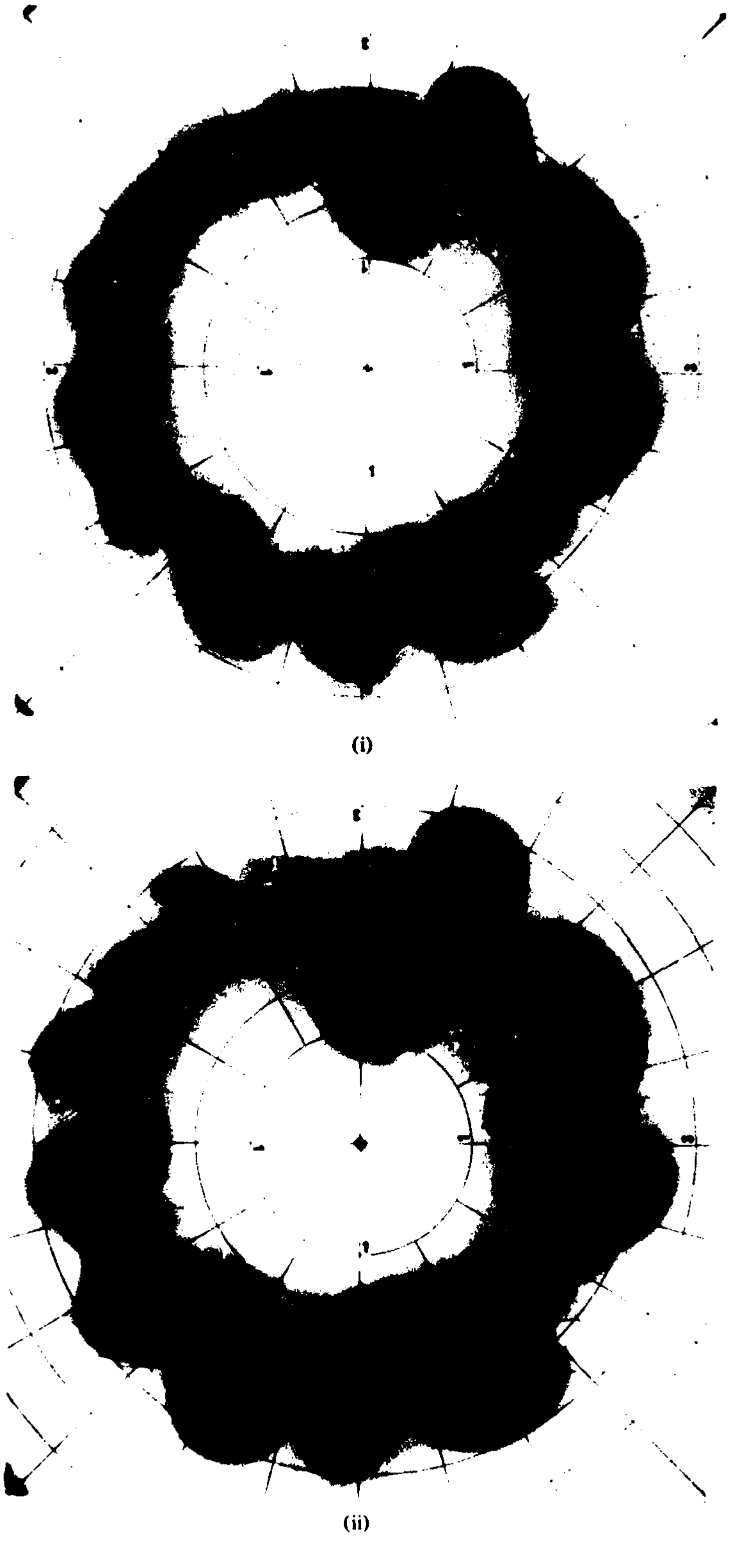

(i)

(ii)

FIGURE 11. The evolution of a laboratory current with a shallow lower layer. $W_0 = 2{\cdot}0$ cm, $f = 1{\cdot}44\ \mathrm{s}^{-1}$, $\mathscr{L}_0 = 1{\cdot}07$ and the ratio of layer depths is 0·84. Times in number of revolutions after withdrawal of the annulus are (i) $t = 2$; (ii) 4.

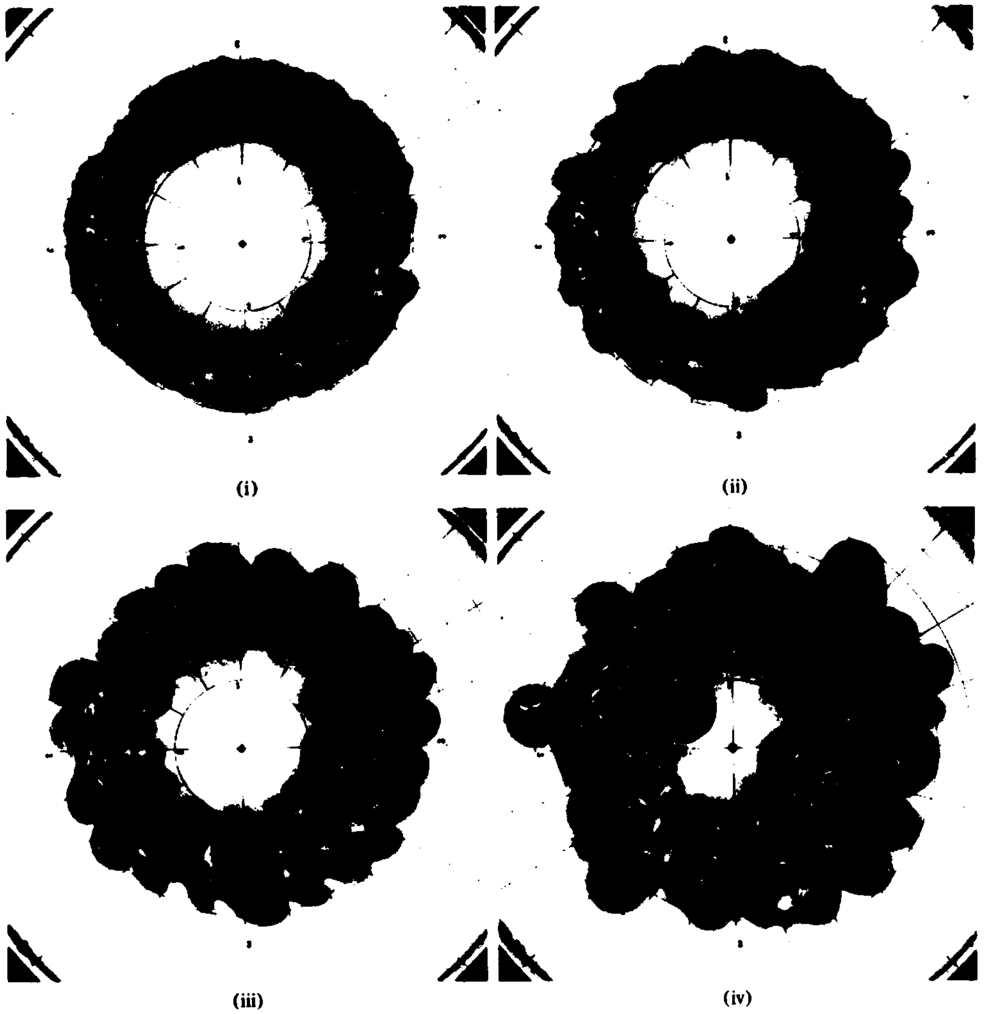
(i) (ii) (iii) (iv)

FIGURE 12. The evolution of a laboratory current with a shallow lower layer. $W_0 = 3{\cdot}9$ cm, $f = 1{\cdot}77\ \mathrm{s}^{-1}$, $\mathscr{L}_0 = 3{\cdot}7$ and the ratio of layer depths is 0·9. Times in number of revolutions after withdrawal of the annulus are (i) $t = 1$; (ii) 3; (iii) 5; (iv) 8.

using the appropriate radius of each edge after the initial collapse yielded two very similar wavelengths. A more serious problem at large $\mathscr{L}_0$ was that the wavelengths increased with time, and this may be due to a similarity of the scales of Kelvin–Helmholtz and rotationally dominated disturbances.

The dimensionless wavelength $f\lambda/(g'H_0)^{\frac{1}{2}}$ is plotted on figure 13, where the symbols indicate the annulus width and ratio of layer depths. Where the wavelength increased with time the two detectable extremes are plotted and connected by a vertical line. The computed wavelength $2\pi/k_m$ (from figure 5*b*) is also plotted and the upper scale of the figure shows the current width L_0 after collapse as given by (6.2). For $\mathscr{L}_0 < 1$ ($L_0 < 2$) the observed wavelength increases slowly with $\mathscr{L}_0$ in roughly the same way as does the computed wavelength, but is almost a factor of two smaller. At $\mathscr{L}_0 > 2$ the observed instability has a roughly constant length scale, while the computed wavelength for the one-layer instability then increases rapidly with current width.

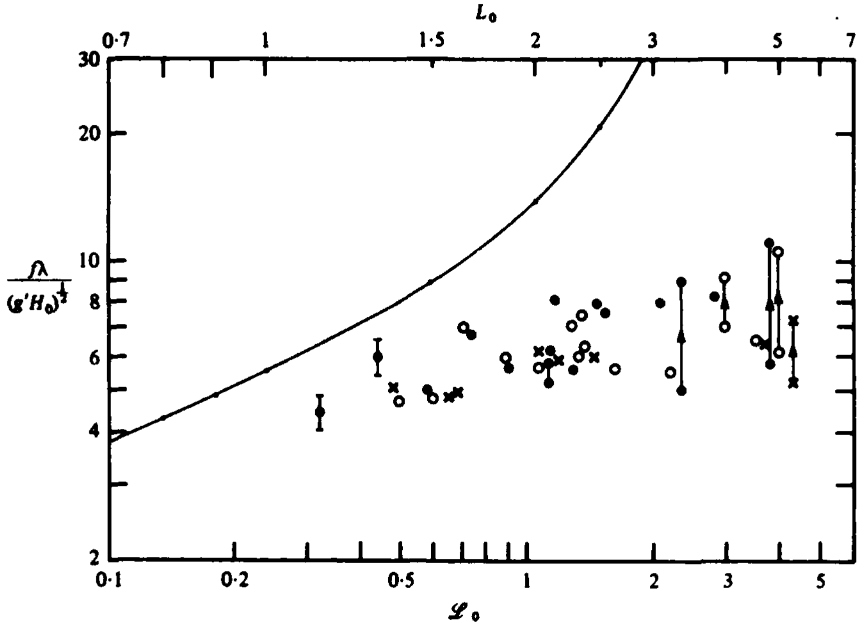

Figure 13. The observed dimensionless wavelength (based on the Rossby radius *before* geostrophic adjustment) as a function of the initial width of the current, $\mathscr{L}_0 = f W_0/(g'H_0)^{\frac{1}{2}}$. Data indicate the annulus used and the ratio of layer depths: ●, W_0 = 2·0 cm and depth ratio $\lesssim$ 0·2; ○, W_0 = 3·5 or 3·9 cm and depth ratio $\lesssim$ 0·2; ×, depth ratio 0·8–0·9. The upper scale is the width L_0 *after* geostrophic adjustment (calculated from $\mathscr{L}_0$ and (6.2)) and the computed wavelength $2\pi/k_m$ is plotted on this scale.

The growth rates of the observed disturbances are difficult to quantify because their appearance and growth at very small amplitude is poorly defined. However, their appearance within one to two revolutions after the annulus was withdrawn implies a growth rate $|kc| \sim O(4 \times 10^{-2})$. This lower limit is consistent with the computed growth rate on figure 5(*b*) for $\mathscr{L}_0 < 1$. A more clearly defined time scale, and one that is of importance in oceanographic observations, is the period required for the axisymmetric flow to break up into isolated eddies whose circulations have pinched off from their neighbours. For those experiments with layer-depth ratios less than 0·2 this time scale was always close to 5 or 6 rotation periods, but it was as small as three revolutions (at $\mathscr{L}_0 \simeq 1$) when the depth ratio was large.

Discussion of the experimental results

The data on figure 13 are presented again on figure 14, along with the computed wavelength $2\pi/\epsilon_m$ for the most rapidly growing mode described in § 5. However, this time the wavelengths are normalized by the Rossby radius based on the maximum depth H of the current *after* its collapse to geostrophic balance. This depth is calculated from (5.2) after finding the balanced width L_0 from (6.2), and assumes that the initially uniform potential vorticity remained after the collapse. To well within the scatter of the data, the measured wavelength λ is a constant multiple of the Rossby radius: $f\lambda/(g'H)^{\frac{1}{2}} = 7{\cdot}4 \pm 1{\cdot}2$.

For $\mathscr{L}_0 < 2$ we have already described the qualitative appearance of the growing

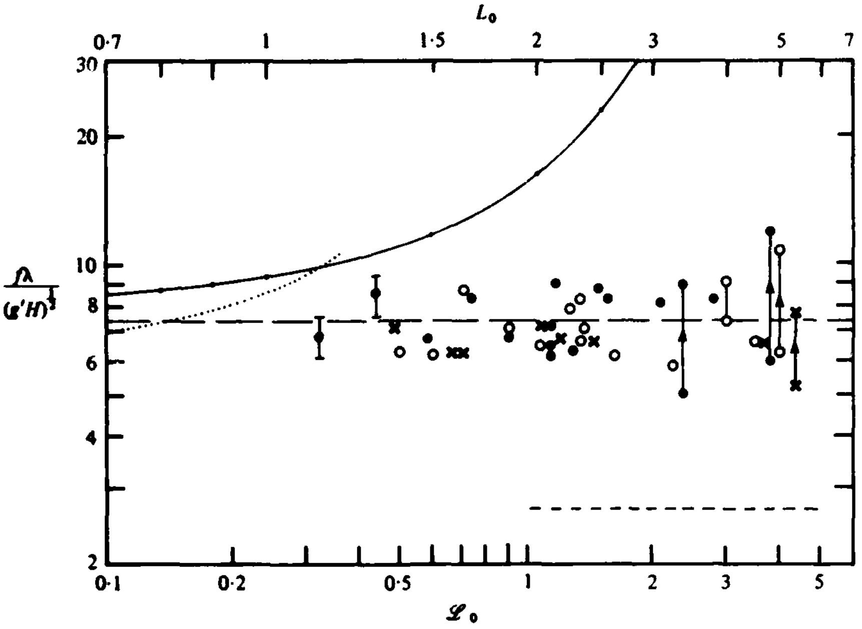

FIGURE 14. The data of figure 13 but with the wavelength renormalized using the calculated Rossby radius in the state of geostrophic balance (assuming conservation of potential vorticity). The data have a mean of $f\lambda/(g'H)^{\frac12} = 7\cdot4 \pm 1\cdot3$ (broken line), which corresponds to the wavenumber $\epsilon = 0\cdot85 \pm 0\cdot15$. The computed wavelength $2\pi/\epsilon_m$ for the coupled mode on a current with uniform potential vorticity is also plotted (solid line). The dotted line shows the computed wavelength (against the upper scale) of the coupled mode with maximum growth rate for the profile (6.3), which has a varying potential vorticity. The dashed line is the computed wavelength of the mode attached to a single front for the same profile (6.3).

disturbances, and, for a sufficiently deep lower layer, this appears to be identical to that predicted for the one-layer instability. The two edges of the current couple together and give rise to both meandering and varicose structures which are $\frac12\pi$ radians out of phase. The growing disturbances are stationary and large anticyclonic eddies develop from the wider and deeper sections of the wave. The computed and observed growth rates are also consistent with each other. On the other hand, no rapid change of growth rate with current width L_0 could be detected, and the measured wavelengths are smaller than those predicted. These discrepancies we attribute largely to the simultaneous instability of at least one other mode, a mode which becomes dominant only at larger current widths ($\mathscr{L}_0 > 2$), and which appears to have a length scale close to 2π deformation radii and growth rates of order 10^{-2}–10^{-1}. This mode is discussed below. There are also a number of other factors that may possibly influence the observed wavelength at $\mathscr{L}_0 < 1$. First, the formation of a 'narrow' current in our experiments requires that the upper layer have a large Rossby radius of deformation, which means that the collapse to geostrophic balance involves an extensive, rapid spreading of the buoyant fluid, leaving a rather shallow current. Both mixing by Kelvin–Helmholtz billows (which could be clearly seen in ciné films) and friction may then affect the vorticity and current depth throughout the width of the undisturbed flow. Alteration of the potential vorticity profile can in itself lead to only small changes in the most unstable wavelength at $L_0 < 1$, as the behaviour must then approach the same limit of zero potential vorticity. To illustrate this with a quantitative example we have chosen the convenient (but otherwise arbitrary) depth profile

$$\bar{h} = 1 - \frac{y^2}{L_0^2}\frac{\cosh y}{\cosh L_0}, \tag{6.3}$$

and computed the wavelength and growth rate of the most unstable mode that couples the two edges of the current. This wavelength is plotted on figure 14 (dotted line), while the dimensionless growth rate is somewhat greater than that found for the uniform potential vorticity profile ($kc_i = 0{\cdot}21$ at $L_0 = 1$).

Another result of the dissipation of vorticity during the collapsing phase is a small reduction of the current depth H. This would imply that we have underestimated the value of the observed dimensionless wavelength $f\lambda/(g'H)^{\frac{1}{2}}$ on figure 14 (and similarly overestimated the predicted wavelength on figure 13). Other factors that we have neglected are non-zero perturbation velocities in the finite lower layer and interfacial friction, both of which may have a direct influence upon the energy balance in the growing disturbances.

The two edges of the current are again strongly coupled when $\mathscr{L}_0 < 1$, and the ratio of layer depths is close to one. However, the structure of disturbances is different from that at small depth ratios, with the current showing less tendency to meander, and the growth rate is noticeably greater. In this case, the lower layer cannot be considered stationary, since its depth changes significantly during the collapse to geostrophic equilibrium. Conservation of potential vorticity implies that the fluid velocity in this layer is in the opposite direction to that in the upper layer, and this must be expected to influence the form of the coupling between the two density fronts.

At $\mathscr{L}_0 > 2$, with all the depth ratios used, the collapse to geostrophy has little influence upon the fluid near the centre line. Under these conditions we observe a clear qualitative difference in the instability. Each front is observed to behave independently and develop waves, which have a length scale determined by the Rossby radius. Furthermore, the growth rate of the coupled, one-layer instability at $\mathscr{L}_0 > 2$ is predicted to be more than an order of magnitude smaller than at $\mathscr{L}_0 = 1$,† while the length scale is predicted to increase exponentially with $\mathscr{L}_0$. Hence we conclude that another mode of instability is present for $\mathscr{L}_0 > 2$. However, we are uncertain of the nature of this second mode. There are two possibilities: it may be a mode in which the second layer and the lower boundary play an important role, or else it may be another unstable mode (other than the one discussed in this paper) that is described by the single-layer equations (2.15)–(2.17).

The particular solution to the perturbation equations (2.15)–(2.17) that is discussed in §§ 3, 4 and 5 has the leading-order phase velocity $c_0 = U$, and represents an unstable coupling of the two free streamlines. However, we find numerically that there can be other unstable solutions with larger wavenumbers than those for the coupled-front mode. Although these other modes are not yet fully understood, we do know that each is concentrated close to one of the free streamlines and, to be unstable, requires a non-zero gradient of potential vorticity. Since the laboratory currents do involve a variation of potential vorticity near their edges (due to mixing and friction), the one-layer model might therefore be able to describe the observed mode of instability for wide currents as well as the coupled mode observed for narrow currents. For the particular profile (6.3), which was chosen as a relatively simple variation on the profile (5.3) and which has a varying potential vorticity, numerical solutions show that the wavelength of the new frontal mode with maximum growth rate is a constant multiple of the Rossby radius. This result is plotted on figure 14 (broken line), where the predicted wavelength can be seen to be much smaller than those observed. However, it may be that the preferred length scale is determined by the width of the region of large shear at the current edge. This in turn is determined, in the experiments, by the Rossby radius $(g'H_0)^{\frac{1}{2}}/f$, and by mixing. Before useful conclusions can be drawn it will be necessary to investigate further profiles numerically, and to find a method by which the potential-vorticity profile of a laboratory current can be determined to a sufficient accuracy. At present we can only approximate this profile by assuming conservation of potential vorticity during the collapse to geostrophic balance.

---

† The expression (4.26) shows that a decrease of the growth rate should be expected for any profile that becomes steadily flatter near the critical layer; the argument is not limited purely to constant-potential-vorticity profiles.

The observed mode of instability for wide currents may also require the presence of a lower layer of finite depth. On the basis of previous quasi-geostrophic theories, conditions at $L_0 > 1$ are well-suited to the appearance of a two-layer baroclinic instability. Since L^2 (after the initial collapse) is a Froude number of the flow, all the laboratory currents should be baroclinically unstable, and larger values of L_0 will give rise to baroclinic waves with larger growth rates. In experiments similar to those reported in this article, Griffiths & Linden (1981) have investigated unstable waves on an isolated two-layer vortex that is bounded by a sharp density front. They found that each growing wave led to the formation of a cyclone–anticyclone pair when the ratio of layer depths was greater than 10^{-1}. This behaviour is similar to that seen in figures 10 and 12, where disturbances grow independently on each edge of the wide currents, the lower layer plays a visible role, and a number of vortex pairs appear. Griffiths & Linden also detected a variation of wavelength with the ratio of layer depths. While no such dependence has been established conclusively for the length scales in the experiments reported here, the depth ratio does appear to influence significantly the value of the current width $\mathscr{L}_0$ at which the two-layer instability becomes dominant over the one-layer, coupled instability. This transition occurs at $\mathscr{L}_0 \simeq 2$ for depth ratios near 0·2, but at $\mathscr{L}_0 \simeq 1{\cdot}2$ for depth ratios near one. Griffiths & Linden also observed that when the layer depths are comparable, velocities within the cyclonic eddies, which extended throughout the depth of the lower layer, were comparable to those in the upper layer anticyclones. Hence the dynamical role of the second layer may well be important for the wide currents and at the large depth ratios in the present experiments.

7. Conclusions

A single-layer model of a gravity current that is bounded by two free streamlines on a uniformly sloping surface predicts that such a flow is unstable. The influence of vanishing layer depth and large inertial effects near the fronts are included. Normal modes are stable in the limit of infinitely large downstream length scales, but finite wavelengths are unstable. For currents that are symmetric about their midpoint, perturbations are simply advected with the mean velocity of the fluid. A combination of meandering and 'varicose' modes with a phase difference of $\frac{1}{2}\pi$ radians releases kinetic and potential energy from the basic current. When the flow has zero potential vorticity, the mode with maximum growth rate is predicted to have the wavelength $7{\cdot}9(g'H_0)^{\frac{1}{2}}f^{-1}$, where H is the maximum depth of the current, and an e-folding time of $(0{\cdot}14f)^{-1}$, or 0·57 rotation periods. Flows with finite (uniform) potential vorticity are characterized by the variable length scale $L_0 = fW/(g'H_0)^{\frac{1}{2}}$, where W is the half-width of the current and H_0 is a depth scale that characterizes the potential vorticity. The most rapidly growing mode in this case has a wavelength that increases with L_0 and a growth rate that decreases rapidly when $L_0 \gg 1$. Thus, in contrast to the well-known Rayleigh inflection theorem for quasi-geostrophic flows, we have demonstrated an instability that does not require an extremum (or even a gradient) of potential vorticity. It seems likely that the presence of significant inertial forces might similarly destabilize other geophysical flows.

A second type of unstable solution to the single-layer equations has also been found, but has not been discussed here. In this second mode of instability, perturbations are linked to one edge of the current, and require a non-zero potential vorticity gradient if they are to grow. As this mode may also be of geophysical significance (perhaps even in the case of a single isolated density front), it will be described in another paper.

Our laboratory experiments with a current at the free surface of a rather deep lower layer confirm that a current with two fronts (and nearly uniform potential vorticity) is unstable. The observed structure of growing disturbances, when the current width $L_0 < 3$, corresponds closely to that predicted. The velocity perturbations first form 'cat's-eye' structures at the centre line of the current, and the two edges co-operate to form eventually a train of large anticyclonic eddies. The experiments also indicate that the single-layer instability due to the coupling of the two free streamlines is likely to continue to be important when the lower layer is relatively shallow, providing that $L_0 < 2$.

A different mode of instability appears to make the dominant contribution to the release of energy from the laboratory currents when $L_0 > 3$. Each edge of the upper layer then behaves independently and the lower layer plays a visible role. However, because the observed non-dimensional wavelength is independent of the theoretical parameter (current width) over the full range of parameters used, an unambiguous comparison of the experimental observations with theoretical predictions remains somewhat unsatisfactory.

The flow configuration that we have considered is somewhat similar to that of the Denmark Strait overflow, in which large, energetic oscillations are detected. Smith (1976) presents an intensive discussion of the data for this flow, and finds that the horizontal components of velocity are in quadrature, and there is a distinct cross-stream component of perturbation heat flux which has a uniform sign but varies in magnitude across the stream. The disturbances are attributed to a two-layer baroclinic instability and compared with the predictions of a quasi-geostrophic model. However, the presence of velocity components in quadrature and a cross-stream phase lag in the cross-stream velocity of up to 90°, may also be consistent with instability due to a coupling of the two edges of the dense current. The only mitigating factor in this hypothesis is that the cross-stream heat flux in the one-layer model, by (4.30), varies as $\tilde{u}$, and therefore takes both signs across the stream. However, an asymmetric depth profile could well lead to a very small region of reverse $\tilde{u}$ near one edge, so that detection of this area might be difficult. Further knowledge of the mean vorticity distribution and the influence of bottom curvature is necessary if the two instabilities are to be compared.

R. W. G. and M. E. S. wish to thank the staff and participants of the 1980 Geophysical Fluid Dynamics summer programme at the Woods Hole Oceanographic Institution for providing a stimulating environment during the summer. A first set of experiments was carried out at W.H.O.I. and we thank Mr B. Frazel for his expert assistance. The work was completed while R. W. G. and P. D. K. were supported by grants from the U.K. Natural Environment Research Council. M. E. S. also acknowledges partial support from the U.S. Office of Naval Research.

Appendix A. A Rayleigh integral argument

The following alternative derivation of the leading term in the growth rate may be found a helpful complement to the matching technique used in § 4 and appendix B, in so far as the assumptions on the structure of the eigenfunctions are apparently less severe.

From (2.15)–(2.17) and (4.1) it follows that, correct to $O(\epsilon^2)$, ϕ satisfies

$$(\tilde{c}+\bar{h}_y)\,\phi_{yy}-\bar{h}_{yy}\phi_y-\tilde{c}\left(\frac{1+\bar{h}_{yy}}{\bar{h}}\right)\phi = O(\epsilon^2), \tag{A 1}$$

where $\tilde{c} = c-U$. This is similar to (4.11). Division by $(\tilde{c}+\bar{h}_y)^2$ and integration yields

$$\frac{\phi_y}{\tilde{c}+\bar{h}_y}-\frac{\phi_y(-L)}{\tilde{c}+\bar{h}_y(-L)}-\tilde{c}\int_{-L}^{y}\frac{1+\bar{h}_{\eta\eta}}{(\tilde{c}+\bar{h}_\eta)^2}\frac{\phi}{\bar{h}}\,d\eta = O(\epsilon^2). \tag{A 2}$$

Equation (A 2) is to be solved subject to

$$\phi(-L) = 0, \tag{A 3}$$

and a condition at $y = +L$. To obtain this, note that integration of (2.17) gives

$$c\int_{-L}^{L}\hat{h}\,dy = \int_{-L}^{L}dy\,(\hat{u}\bar{h}+\bar{u}\hat{h}), \tag{A 4}$$

or, after use of (2.16),

$$\tilde{c}\int_{-L}^{L}\hat{h}\,dy = -i\epsilon^2\int_{-L}^{L}dy\,\bar{h}(\bar{u}-c)\,\hat{v}, \tag{A 5}$$

and so

$$\tilde{c}\phi(L) = -i\epsilon^2\int_{-L}^{L}dy\,\bar{h}(\bar{u}-c)\,\hat{v}, \tag{A 6}$$

which is equivalent to (4.21).

It is readily seen that, when $\epsilon = 0$, a solution to (A 1), (A 3) and (A 6) is

$$\phi = \phi_0 \equiv \alpha\bar{h}, \quad c = U \quad (\text{or} \quad \tilde{c} = 0), \tag{A 7}$$

where α is an arbitrary amplitude factor. We shall now obtain an integral expression for the next term in c, i.e. $\tilde{c}$. By integrating (A 2) for ϕ, and using (A 7) for $\phi\bar{h}^{-1}$ in the integral, we obtain

$$\phi(y)-\frac{\phi_y(-L)}{\tilde{c}+\bar{h}_y(-L)}\left\{\bar{h}+\tilde{c}(y+L)+\tilde{c}\int_{-L}^{y}(\tilde{c}+\bar{h}_\eta)\,d\eta\int_{-L}^{\eta}\frac{1+\bar{h}_{\zeta\zeta}}{(\tilde{c}+\bar{h}_\zeta)^2}\,d\zeta\right\} = O(\tilde{c}^2)+O(\epsilon^2), \tag{A 8}$$

where α is taken as $\phi_y(-L)\,(\tilde{c}+\bar{h}_y(-L))^{-1}$ for convenience. Substitution in condition (A 6) then gives

$$\tilde{c}^2\left\{2L+\lim_{\tilde{c}\to 0}\int_{-L}^{L}(\tilde{c}+\bar{h}_y)\,dy\int_{-L}^{y}\frac{1+\bar{h}_{\eta\eta}}{(\tilde{c}+\bar{h}_\eta)^2}\,d\eta\right\}=-\epsilon^2\int_{-L}^{L}dy\,\bar{h}\tilde{u}^2, \tag{A 9}$$

to leading order. Reversing the order of integration in (A 9) gives

$$\tilde{c}^2\left\{2L+\lim_{\tilde{c}\to 0}\int_{-L}^{L}\frac{1+\bar{h}_{yy}}{(\tilde{c}+\bar{h}_y)^2}\,[\tilde{c}(L-y)-\bar{h}]\,dy\right\}=-\epsilon^2\int_{-L}^{L}dy\,\bar{h}\tilde{u}^2. \tag{A 10}$$

The term in $\tilde{c}$ inside the integral is negligible, and by rearrangement we obtain

$$\tilde{c}^2\left\{2L-\lim_{\tilde{c}\to 0}\int_{-L}^{L}dy\,\frac{\bar{h}\bar{h}_{yy}}{(\tilde{c}+\bar{h}_y)^2}-\lim_{c\to 0}\int_{-L}^{L}\frac{\bar{h}\,dy}{(\tilde{c}+\bar{h}_y)^2}\right\}=-\epsilon^2\int_{-L}^{L}dy\,\bar{h}\tilde{u}^2. \tag{A 11}$$

It is readily shown that the first two terms inside the brackets combine to give a negligible term of order $\tilde{c}$. Thus

$$\tilde{c}^2=\frac{\epsilon^2\displaystyle\int_{-L}^{L}dy\,\bar{h}\tilde{u}^2}{\displaystyle\lim_{c\to 0}\int_{-L}^{L}\frac{\bar{h}\,dy}{(\tilde{c}+\bar{h}_y)^2}}. \tag{A 12}$$

The denominator in (A 12) can be written as

$$\int_{-L}^{L}\frac{\bar{h}\,dy}{(\tilde{c}+\bar{h}_y)^2}=\int_{-L}^{L}\frac{\bar{h}\,dy}{(\tilde{u}-\tilde{c})^2}=\left(\int_{-L}^{y_c-\delta}+\int_{y_c+\delta}^{L}\right)\frac{\bar{h}\,dy}{(\tilde{u}-\tilde{c})^2}+\int_{y_c-\delta}^{y_c+\delta}\frac{\bar{h}\,dy}{(\tilde{u}-\tilde{c})^2}, \tag{A 13}$$

where $\delta\to 0$, and y_c again represents (one of) the critical layer(s). For $\tilde{c}$ tending to zero, the right-hand side of (A 13) becomes

$$\begin{aligned}&\left(\int_{-L}^{y_c-\delta}+\int_{y_c+\delta}^{L}\right)\frac{\bar{h}\,dy}{\tilde{u}^2}+\int_{-\delta}^{\delta}\frac{[\bar{h}_c+O(\eta^2)]\,d\eta}{(\bar{u}_{yc}\eta+\tfrac{1}{2}\bar{u}_{yyc}\eta^2+\ldots-\tilde{c})^2}\\&=\left(\int_{-L}^{y_c-\delta}+\int_{y_c+\delta}^{L}\right)\frac{\bar{h}\,dy}{\tilde{u}^2}+\frac{\bar{h}_c}{\bar{u}_{y_c}^2}\int_{-\delta}^{\delta}\frac{d\eta}{\left(\eta-\dfrac{\tilde{c}}{\bar{u}_{yc}}\right)^2}\left\{1-\frac{\bar{u}_{yyc}\eta^2}{\bar{u}_{yc}\left(\eta-\dfrac{\tilde{c}}{\bar{u}_{yc}}\right)}+\frac{O(\eta^3)}{\left(\eta-\dfrac{\tilde{c}}{\bar{u}_{yc}}\right)}+\ldots\right\}.\end{aligned} \tag{A 14}$$

Now as $\delta\to 0$, integrals of $\eta^r(\eta-\tilde{c}\bar{u}_{yc}^{-1})^{-r}$ tend to $2\delta\to 0$, plus correction terms of order $\tilde{c}$ which also are negligible. Hence

$$\lim_{\tilde{c}\to 0}\int_{-L}^{L}\frac{\bar{h}\,dy}{(\tilde{c}+\bar{h}_y)^2}=\left(\int_{-L}^{y_c-\delta}+\int_{y_c+\delta}^{L}\right)\frac{\bar{h}\,dy}{\tilde{u}^2}+\frac{\bar{h}_c}{\bar{u}_{yc}^2}\left\{-\frac{2}{\delta}-\frac{\bar{u}_{yyc}}{\bar{u}_{yc}}[\log\delta-\log(-\delta)]\right\} \tag{A 15}$$

$$=\mathrm{Fp}\int_{-L}^{L}\frac{\bar{h}\,dy}{\tilde{u}^2}-\frac{i\bar{u}_{yyc}\pi\bar{h}_c}{|\bar{u}_{yc}|^3}, \tag{A 16}$$

taking $\log(-\delta)=\log\delta-i\pi\,\mathrm{sgn}\,(\bar{u}_{yc})$ as before. Hence the result (4.26) for $\tilde{c}^2$ is recovered.

REFERENCES

Griffiths, R. W. 1980 In *Report of* 1980 *Summer Program in Geophysical Fluid Dynamics, The Woods Hole Oceanographic Institution* (ed. G. Veronis & K. Mellor). *Woods Hole Tech. Rep.* WHOI-80-53.

GRIFFITHS, R. W. & LINDEN, P. F. 1981 The stability of vortices in a rotating stratified fluid. *J. Fluid Mech.* **105**, 283–316.

MANN, C. R. 1969 Temperature and salinity characteristics of the Denmark Strait overflow. *Deep-Sea Res.* **16**, 125–137.

NORMAN, A. C. 1972 A system for the solution of initial and two-point boundary value problems. In *Proc. Ass. Comp. Mech.* (*25th Anniv. Conf., Boston*), pp. 826–834.

ORLANSKI, I. 1968 Instability of frontal waves. *J. Atmos. Sci.* **25**, 178–200.

PEDLOSKY, J. 1964 The stability of currents in the atmosphere and ocean. Part I. *J. Atmos. Sci.* **21**, 201–219.

SMITH, P. C. 1976 Baroclinic instability in the Denmark Strait overflow. *J. Phys. Oceanog.* **6**, 355–371.

WORTHINGTON, L. V. 1969 An attempt to measure the volume transport of Norwegian Sea overflow water through the Denmark Strait. *Deep-Sea Res.* **16**, 421–432.

Geophys. Astrophys. Fluid Dynamics, 1982, Vol. 22, pp. 1-28
0309-1929/82/2202-0001 $06.50 0
© Gordon and Breach Science Publishers Inc., 1982
Printed in Great Britain

Instabilities on Density-Driven Boundary Currents and Fronts

PETER D. KILLWORTH
Department of Applied Mathematics and Theoretical Physics, University of Cambridge, England

and

MELVIN E. STERN
Graduate School of Oceanography, University of Rhode Island, Kingston, Rhode Island 02881, U.S.A.

(*Received February 16, 1982; in final form May 12, 1982*)

It is shown that a coastal density current in a rotating system is unstable to downstream wave disturbances when the mean potential vorticity increases towards the (vertically-walled) coast and when the mean current vanishes there. Other new instability modes are also found which do not require the potential vorticity extremum of quasi-geostrophic theory. All the instabilities in our equivalent one-layer model release mean kinetic energy and most of them release mean potential energy, but an increase of the latter can occur under certain circumstances.

Specifically, it is shown (a) that mean flows close to uniform potential vorticity can be unstable to disturbances of infinite wavelength (and hence also for finite wavelengths) even for monotonic potential vorticity distributions, and (b) that all mean flows which vanish at the wall and for which the potential vorticity has a maximum but not an extremum at the wall are unstable to waves of finite length. A logical extension shows that the second half of the latter criterion may be relaxed, in fact. The paper concludes with a discussion of the applications to recent laboratory experiments.

1. INTRODUCTION

Horizontal density differences near the coast of a rotating fluid tend to produce geostrophic flow parallel to the coast, and cross-stream spreading tends to be inhibited by the Coriolis force. There are many examples of such currents in the ocean, e.g. the East Greenland current, carrying water of Arctic origin southwards, and the West Spitzbergen current carrying Atlantic water northwards into the Arctic. Coastal currents, involving water denser than its surroundings, can also occur at the ocean floor: e.g., the overflow of dense Greenland-Iceland sea water at the bottom of the Denmark Strait into the Atlantic (Mann, 1969; Smith, 1976). All these coastal currents are bounded away from the coastline by a *front*, where an isopycnal intersects the ocean surface (or floor); such a front can be thought of as a boundary for the current.

Many observations of coastal currents also show them to be prone to large disturbances or instabilities, and this has prompted several laboratory investigations of the instabilities of simple fronts and coastal currents (Stern, 1980; Stern, Whitehead and Hua, 1982; Griffiths and Linden, 1981a, b). A variety of instabilities for these fronts has been found: breaking waves, wedges, bores and cyclone-anticyclone vortex pairs.

Both the experiments and the observations have frequently been interpreted in the framework of the classical quasi-geostrophic instability theory, despite the fact that the limits of validity of the latter are exceeded for a "strong" front. The latter consists of isopycnal layers with *large* variations in vertical thickness, and lateral shears comparable with the Coriolis parameter. Some support for this appeal to quasi-geostrophic theory can be found in the "strong" frontal model of Orlanski (1968), which consists of two active density layers separated by a uniformly sloping interface. A "generic" connection can be made between the unstable modes in this problem and those in the simpler quasi-geostrophic theories. But there is no lateral shear above and below the interfacial discontinuity in Orlanski's model, and consequently it may suppress new modes in which a distributed lateral shear is important, as well as the lateral density gradients. This is revealed by the following investigation of the instability of a single active layer with a continuous shear. In the context of the quasi-geostrophic theory, such a model should exhibit no instability unless the undisturbed potential vorticity has an extremum. All the modes discussed in this paper violate this condition, and the implication is that the quasi-geostrophic theory filters out these modes.

Although we shall concentrate on the dynamics of a single layer, this does not mean that the effect of the *second* layer is negligible in the applications mentioned above. But there may very well be a tendency, in the interpretation of the data, to exaggerate the dynamical significance of the "baroclinic mode" by extrapolating quasi-geostrophic theory too far. A better *starting* point for the interpretation of many (complex) frontal problems may be a one-layer ageostrophic model, which is to be subsequently modified by considering the coupling with the other layer(s).

Be this as it may, we have undertaken a series of analytical studies of an equivalent one-layer model. The first one: Griffiths, Killworth and Stern (1982), cited as GKS hereafter, considered a density current with two free fronts located on the same horizontal boundary. This problem is simpler than the one free front studied herein! GKS found that for any distribution of vorticity, the double front was unstable to a growing mode which coupled the fronts through a combination of varicose and meandering disturbances.† The disturbance grew by transferring mean potential energy to disturbance potential energy, and mean kinetic energy to disturbance kinetic energy.

In this paper we examine the general stability of a coastal current, bounded on one side by a rigid boundary, and on the other by a front. A reduced gravity model will again be used. Because the mechanisms of coupling the two fronts in GKS is now removed by the insertion of a wall, we can anticipate a stabilization of the flow. However, we shall show that at least two modes of instability can occur (with a third mode, relevant to an isolated front far from any wall, to be discussed in a later paper). The first of these is a longwave instability which can occur on flows of almost uniform potential vorticity, even if the vorticity varies monotonically across the current. We shall show that instabilities exist provided the width of the current exceeds a critical value, but a further necessary condition is that a mean-flow reversal occurs. This model is therefore artificial, but we note that it is possible for this instability to *increase* the mean potential energy of the flow.

Another mode of instability is found where there is no flow reversal, and in the realistic case when the mean flow is at rest at the wall. For this case, instability occurs where the potential vorticity increases towards the wall. Flows possessing reversals also have this mode, with growth rates typically greater than for flows of uniform direction. This instability possesses similar energetics to that in GKS, but rather weaker due to stabilization by the wall.

Section 2 of the paper describes the one-layer model used, and the mean flow. Section 3 proves the first main result, concerning infinitely long growing waves on a mean flow close to uniform potential vorticity, and discusses the energetics involved. Section 4 proves the second result, concerning long growing waves on a mean flow which vanishes at the wall; this necessitates some straightforward but tedious matched asymptotics. This section again discusses the energetics. Section 5 gives a qualitative discussion, based partially on computed results for non-long waves, of the dependence of the instabilities on current width. Section 6 discusses the applications of the theory to laboratory experiments.

---

†There are other disturbances possible; the thrust of GKS was to demonstrate that a general class of instability must exist on such a flow.

2. FORMULATION

We consider the configuration shown in Figure 1 in which a fluid of uniform density ρ_1 flows above an infinite fluid of density $\rho_2>\rho_1$. The undisturbed flow in the upper layer is parallel to the x-axis, and is bounded by a front at $y=0$ (where the depth of the upper fluid vanishes) and by a rigid vertical wall at $y=L$. The relative depth in the lower layer is assumed to be sufficiently great so that the velocities and pressure gradients produced in it are negligible compared with those in the upper layer. Consequently the momentum and continuity equations are (for shallow water)

$$u_t+uu_x+vu_y-fv=-g'h_x, \tag{2.1}$$

$$v_t+uv_x+vv_y+fu=-g'h_y, \tag{2.2}$$

$$h_t+(uh)_x+(vh)_y=0, \tag{2.3}$$

where (u,v) are the (x,y) components of velocity, t represents time, f is the Coriolis parameter, and $g'=g(\rho_2-\rho_1)/\rho_2$ is the reduced gravity. We choose non-dimensionalisation, following GKS, which will be convenient for motions with x-variations long compared with the radius of deformation $a=(g'H)^{1/2}f^{-1}$, where H is taken as the (upper layer) fluid depth at the wall. Nondimensional values are defined by

$$\begin{aligned} &x=x^*\varepsilon^{-1}a, \qquad && y=y^*a, \qquad && t=t^*\varepsilon^{-1}f^{-1}, \\ &u=u^*(g'H)^{1/2}, \qquad && v=v^*\varepsilon(g'H)^{1/2}, \qquad && h=h^*H, \end{aligned} \tag{2.4}$$

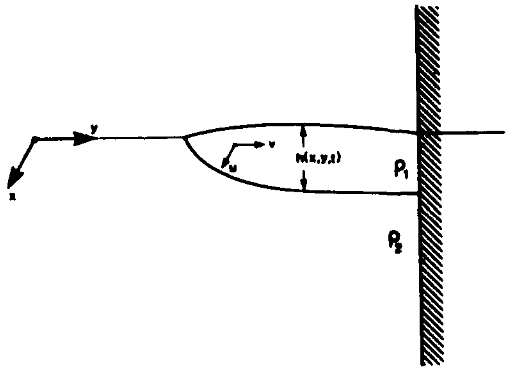

FIGURE 1 The configuration for the one-layer problem discussed in this paper.

where the starred quantities are nondimensional and the downstream lengthscale is $\varepsilon^{-1}a$. Analytically we shall be concerned with ε small (to demonstrate stability). However, no restriction is placed on ε in the scaling, or in numerical solutions. Upon dropping the asterisks, Eqs. (2.1)–(2.3) become

$$u_t + uu_x + v(u_y - 1) = -h_x, \tag{2.5}$$

$$\varepsilon^2(v_t + uv_x + vv_y) + u = -h_y, \tag{2.6}$$

$$h_t + (uh)_x + (vh)_y = 0, \tag{2.7}$$

and the mean flow, denoted by a bar, depends only on y and satisfies the geostrophic balance

$$\bar{v} = 0, \qquad \bar{u} = -\bar{h}_y, \qquad (2.8), (2.9)$$

$$\bar{h} = 0, \quad y = 0, \tag{2.10}$$

$$\bar{h} = 1, \quad y = L. \tag{2.11}$$

The potential vorticity of the mean flow is defined by

$$P = (1 - \bar{u}_y)/\bar{h} = (1 + \bar{h}_{yy})/\bar{h}. \tag{2.12}$$

We impose a small perturbation of the form

$$(u', v', h') = (\tilde{u}, \tilde{v}, \tilde{h}) \exp i(x - ct)$$

on the mean flow, where c is the phase velocity of the perturbations. Unstable modes will have $\mathrm{Im}(c) > 0$, with growth rate $\varepsilon\,\mathrm{Im}(c)$, since ε plays the role of a wavenumber. The linearised equations for these perturbations are then, dropping tildes,

$$(\bar{u} - c)u + (1 - \bar{u}_y)iv + h = 0, \tag{2.13}$$

$$u + \varepsilon^2(\bar{u} - c)iv + h_y = 0, \tag{2.14}$$

$$\bar{h}u - (\bar{h}iv)_y + (\bar{u} - c)h = 0. \tag{2.15}$$

By solving (2.13) and (2.14) for u and iv in terms of h and substituting in (2.15), we obtain a single equation for h, the simplification of which is

$$[\bar{h}Q^{-1}h_y]_y + h[1 - \varepsilon^2\bar{h}Q^{-1} - (\bar{h}Q^{-1})_y(\bar{u} - c)^{-1}] = 0, \tag{2.16}$$

where

$$Q=\varepsilon^2(\bar{u}-c)^2-1+\bar{u}_y. \tag{2.17}$$

The wall boundary condition $v(L)=0$ for (2.16) becomes

$$(\bar{u}-c)h_y-h=0, \qquad y=L, \tag{2.18}$$

when (2.13), (2.14) are used. The boundary condition at the front can be obtained by the requirement that (2.15) be well-behaved when $\bar{h}$ vanishes, or

$$iv=-(\bar{u}-c)h/\bar{u}, \qquad y=0. \tag{2.19}$$

Using (2.13) (2.14), this implies

$$h_y=h[Q\bar{u}^{-1}+(\bar{u}-c)^{-1}], \qquad y=0 \qquad [\text{if } Q(0)\neq 0]. \tag{2.20}$$

In the special but important case where $Q(0)=0$, we have

$$(\bar{u}-c)h_y-h=0, \quad y=0 \qquad [\text{if } Q(0)=0]. \tag{2.21}$$

This condition applies for all finite $P(y)$ when $\varepsilon=0$. For the case where the mean potential vorticity $P_0=-Q/\bar{h}$ also is constant, (2.16) reduces to $h_{yy}-P_0h=0$, and the solution satisfying (2.18)–(2.21) gives two *real* eigenvalues c. This does not mean, of course, that waves of finite length are stable.

3. LONGWAVE INSTABILITY OF PROFILES WITH NEARLY UNIFORM POTENTIAL VORTICITY

a) Demonstration of instability

In this section we shall prove that *there exist mean flows close to uniform potential vorticity which are unstable to disturbances of infinite wavelength, even if the vorticity distribution remains monotonic*. An immediate corollary, following an expansion for small ε, is that such flows are also unstable to waves of finite wavelength.

To obtain this result, we first set ε to zero in (2.16). Q then becomes equal to the negative absolute vorticity and (2.16) simplifies to

$$(h_yP^{-1})_y=h[1-P_yP^{-2}(\bar{u}-c)^{-1}], \tag{3.1}$$

where P is the mean potential vorticity defined by (2.12). Multiplication of (3.1) by h^*, where an asterisk now denotes a complex conjugate, and integrating from 0 to L gives

$$\left[\frac{h^*h_y}{P}\right]_0^L-\int_0^L\frac{|h_y|^2}{P}\,dy=\int_0^L|h|^2\,dy-\int_0^L\frac{|h|^2P_y}{P^2(u-c)}\,dy. \tag{3.2}$$

Regardless of whether P vanishes at $y=0$ or not, the imaginary part of (3.2) yields the same result after use of the boundary conditions (2.18), (2.21) for h_y, namely

$$\operatorname{Im}[|h|^2/P(\bar{u}-c)]_0^L=-\operatorname{Im}\int_0^L[|h|^2P_y/P^2(\bar{u}-c)]\,dy, \tag{3.3}$$

or

$$\operatorname{Im}(c)\cdot[|h|^2/P|\bar{u}-c)^2]_0^L=-\operatorname{Im}(c)\int_0^L(|h|^2P_y/P^2|\bar{u}-c|^2)\,dy. \tag{3.4}$$

When $P=P_0$ is constant [corresponding to mean flows $h=h_0(y)$, $u=u_0(y)$], the hyperbolic solutions of (3.1) yield real eigenvalues $c=c_0$, and (as proved later), $\bar{u}_0-c_0=0$ at some $y=y_c$ in $0<y_c<L$. We also assume† that for mean flows with potential vorticity

$$\bar{h}=\bar{h}_0+\mu\bar{h}_1,\quad P=P_0+\mu P_1(y),\quad \mu\ll 1, \tag{3.5}$$

(h,c) exists such that, for $\mu\to 0$,

$$h\sim h_0+\mu h_1;\qquad c\sim c_0+\mu c_1=c_0+\mu(c_{1r}+ic_{1i}). \tag{3.6}$$

(In fact both h and c may be expressed to $O(\mu)$ as a simple power series expansion; terms in $\log\mu$ enter at higher orders in the expansion.) Substituting (3.5), (3.6) into (3.4) and taking the limit as $\mu\to 0$, with $\mu c_{1i}>0$, yields

$$\begin{aligned}
&\mu c_{1i}[h_0^2/P_0|\bar{u}-c_0|^2]_0^L\\
&\quad=-\mu^2c_{1i}\lim_{\mu\to 0}\int_0^L(h_0^2P_{1y}/P_0^2|\bar{u}-c|^2)\,dy\\
&\quad=-\mu^2c_{1i}P_{1y}(y_c)h_0^2(y_c)P_0^{\;2}\lim_{\mu\to 0}\int_0^L[\bar{u}_y^2(y_c)(y-y_c)^2+\mu^2c_{1i}^2]^{\;1}\,dy\\
&\quad=-\mu P_{1y}(y_c)h_0^2(y_c)\pi/P_0^2|\bar{u}_y(y_c)|,
\end{aligned} \tag{3.7}$$

---

†This assumption has been verified by detailed matched asymptotic expansions similar in nature to those in GKS. The details are tedious and unenlightening, and are omitted here. However, such calculations are always necessary when some form of the argument in this paper is used, in order to show the existence of the assumed eigenfunctions.

or

$$c_{1i} = -h_0^2(y_c)\pi P_{1y}(y_c)/P_0|\bar{h}_{yy}(y_c)|[h_0^2|\bar{u}-c_0|^{-2}]_0^L. \tag{3.8}$$

This is an expression for Im(c) to first order in μ, where μ is a measure of the potential vorticity gradient. Now h_0 satisfies (3.1) with P_0 replacing P. i.e.

$$h_{0yy} = P_0 h_0, \quad (\bar{u}-c_0)h_{0y} = h_0, \quad y=0, L. \tag{3.9}$$

The first of these may be written as

$$d(h_{0y}^2 - P_0 h_0^2)/dy = 0,$$

so that the end point contribution in (3.8) becomes

$$[h_0^2(\bar{u}-c_0)^{-2}]_0^L = [h_{0y}^2]_0^L = P_0[h_0^2]_0^L, \tag{3.10}$$

giving

$$c_{1i} = -P_{1y}(y_c)h_0^2(y_c)\pi/P_0^2|\bar{h}_{yy}(y_c)|[h_0^2]_0^L. \tag{3.11}$$

Since $c_{1i} > 0$ was assumed, it follows that for long-wave instability $P_{1y}(y_c)$ must be positive (negative) according as $[h_0^2]_0^L$ is negative (positive).

Before evaluating (3.11), it may be helpful to give a qualitative demonstration of the crucial point: that $(\bar{u}-c_0)$ can vanish in $0<y<L$ for certain values of the parameters (P_0, L). The solution of (2.12) is

$$\bar{h}(y) = P_0^{-1}(1-\cosh P_0^{1/2}y) - \bar{u}(0)P_0^{-1/2}\sinh P_0^{1/2}y, \tag{3.12}$$

and $\bar{h}=1$ at $y=L$ implies that

$$\bar{u}(0) = -P_0^{1/2}\{1-P_0^{-1}(1-\cosh P_0^{1/2}L)\}/\sinh P_0^{1/2}L. \tag{3.13}$$

Hence

$$\bar{u}(L) = -\bar{h}_y(L) = P_0^{-1/2}\sinh P_0^{1/2}L + \bar{u}(0)\cosh P_0^{1/2}L. \tag{3.14}$$

It is clear that values of (P_0, L) can be found for which $\bar{u}(L)$ vanishes. In such cases, $c_0=0$ is an eigenvalue of (3.9), with eigenfunctions $h_0 = u$ (a fact which will be generalized and used again later). Thus for these (P_0, L) values, $\bar{u}(0)-c_0 < \bar{u}(L)-c_0 = 0$, assuming $\bar{u}$ to be monotonic. The critical layer is at $y=L$ for points on this (P_0, L) curve, and therefore points slightly on one side of this curve will yield values of $\bar{u}(L)-c_0$ which are positive. Since $\bar{u}(0)-c_0$ is still negative, the critical point y_c will now lie slightly inside $(0, L)$, and this completes the simple argument.

To evaluate (3.11) we need c_0 and y_c as functions of L and P_0, together with h_0. Now the solution of (3.9) is

$$h_0=\sinh P_0^{1/2}y+\beta\cosh P_0^{1/2}y, \tag{3.15}$$

where β is a constant of integration. Substitution into the boundary conditions and elimination of β yields a quadratic for c_0:

$$\begin{aligned}&[\bar{u}(L)-c_0]P_0^{1/2}\{\cosh P_0^{1/2}L+P_0^{1/2}\sinh P_0^{1/2}L\cdot[\bar{u}(0)-c_0]\}\\ &\qquad=\sinh P_0^{1/2}L+P_0^{1/2}[\bar{u}(0)-c_0]\cosh P_0^{1/2}L,\end{aligned} \tag{3.16}$$

which can be solved numerically using (3.13), (3.14); β is then found from a boundary condition. Of particular interest are the *critical values* L_c, i.e. the values of L for which either $\bar{u}(L)-c_0$ vanishes or $\bar{u}(0)-c_0$ vanishes. From (3.16), if $\bar{u}(L)=c_0$ then

$$c_0=\bar{u}(L)=\bar{u}(0)+(\sinh P_0^{1/2}L)/P_0^{1/2}\cosh P_0^{1/2}L, \tag{3.17}$$

while if $\bar{u}(0)=c_0$ then

$$c_0=\bar{u}(0)=\bar{u}(L)-(\sinh P_0^{1/2}L)/P_0^{1/2}\cosh P_0^{1/2}L. \tag{3.18}$$

Clearly (3.17), (3.18) give the same relationship between P_0 and L; after some algebra this reduces to

$$L=L_c=P_0^{-1/2}\cosh^{-1}[1/(1-P_0)]. \tag{3.19}$$

Instability can only occur, then, for values of L on one side of L_c; this is easily seen to involve $L>L_c$ for instability. The value (3.19) for L_c is also the maximum width for a parallel current upstream of a wedge solution, as discussed by Stern, Whitehead and Hua (1982).

The curve (3.19) is shown in Figure 2a. For small P_0, $L_c\sim 2^{1/2}+(5.2^{1/2}/12)P_0$, and $L_c\rightarrow\infty$ as $P_0\rightarrow 1$. So the condition for long-wave instability is that $L>L_c(P_0)\geqq 2^{1/2}$; in other words the width of the current must at least exceed $2^{1/2}$ radii of deformation for instability. A little algebra shows that $\bar{u}(L)$ vanishes when $L=L_c$, and is positive when $L>L_c$.

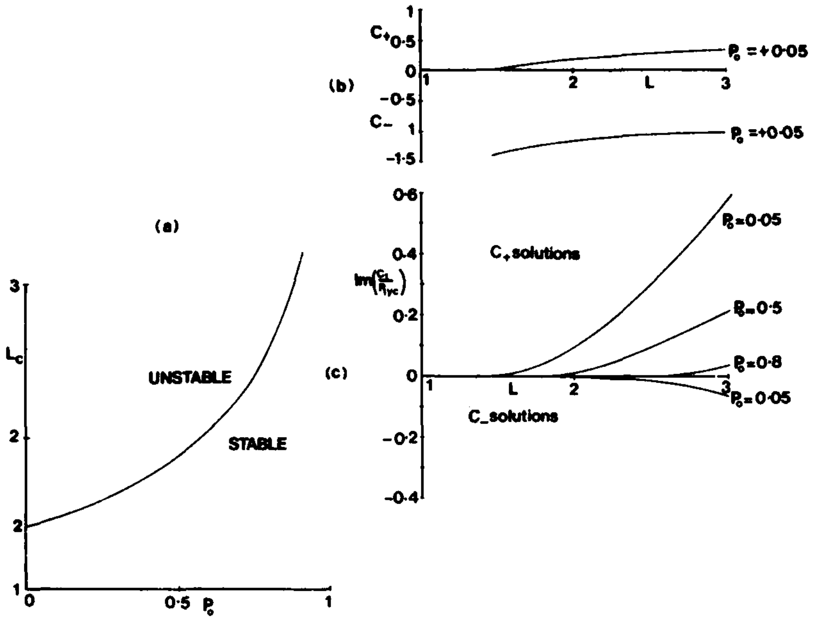

FIGURE 2 Details of the longwave instability of Section 3. (a) the critical width L_c of the current, as a function of basic potential vorticity P_0. (b) the phase speeds c_+, c_- as functions of L for $P_0=0.05$. (c) the growth rate $\mathrm{Im}(c_1)\,P_{1yc}^{-1}$ as functions of L for the c_+ solutions (upper quadrant) and c_- solutions (lower quadrant).

Since $\bar{u}(0)$ is always negative, it implies that long-wave instability is associated with mean flows which possess flow reversals.[†]

The growth rate of the solution (given by c_{1i}) depends crucially upon which solution of the quadratic (3.16) is selected. These solutions will be denoted c_+ and c_-, with suffixes denoting the direction of propagation; c_+ is associated with a critical layer near $y=L$, c_- with one near $y=0$. As Figure 2b shows, the c_+ solutions propagate slowly (at a fixed L, c_+ decreases with P_0, so that the 0.05 curve is one of the faster modes), while the c_- solutions propagate rapidly downstream. However, evaluation of (3.8), drawn in Figure 2c, shows that the growth rates are very tiny for the c_- solutions (indeed, for fixed L, $|c_{1i}|$ decreases with P_0, so that the 0.05 curve is one of the larger growth modes), but are quite sizeable for the c_+

[†] It might be assumed that the $O(\mu)$ modification to $\bar{h}$ could, for L near L_c, be sufficient to make $\bar{u}$ negative everywhere. However, such a modification must take $\bar{u}(L)$ through zero, at which value $c=0$ as noted already. Such a point is a bifurcation between two complex conjugate roots for c and two real roots, so that the statement in the text continues to hold.

solutions. The sign of the instability is such that the c instabilities need P_{1yc} negative, the c_{+} instabilities P_{1yc} positive, where P_{1yc} denotes $P_{1y}(y_c)$.

b) Energetics

GKS found that the two-front instability was associated with a release of mean potential energy, but that the perturbations drew their energy from the kinetic energy of the mean flow. The situation for the long-wave instability in this section is a little more complicated. The global energy source can be located from an energy integral. Following GKS, insert small perturbations (u', v', h') into (2.5, 2.6, 2.7); multiplying these equations by $\bar{h}u'$, $\bar{h}v'$, and h' respectively, setting ε to zero, adding, averaging in the x-direction (denoted by angle brackets) and integrating from $y=0$ to L gives

$$\frac{d}{dt}\int_0^L E\,dy = -\int_0^L \bar{h}\bar{u}_y\langle u'v'\rangle\,dy, \tag{3.20}$$

where

$$E=\tfrac{1}{2}\langle\bar{h}u'^2+h'^2\rangle \tag{3.21}$$

is a convenient measure of kinetic plus potential energy of the perturbations. Hence the perturbations draw their energy from the mean kinetic energy of the flow, through a transfer of momentum by the Reynold's stress

$$R=\langle u'v'\rangle. \tag{3.22}$$

Now

$$u'-h'_y, \tag{3.23}$$

$$v'=(h'_{yt}+\bar{u}h'_{xy}-h'_x)/(\bar{u}_y-1), \tag{3.24}$$

by perturbing (2.5), (2.6) successively, so that

$$R=\tfrac{1}{2}(1-\bar{u}_y)^{-1}\,\mathrm{Im}\,\{c|h_y|^2+hh_y^*\}, \tag{3.25}$$

where a star denotes a complex conjugate. To order μ, then, using (2.12), (3.6),

$$R=\mu c_{1i}(h_{0y}^2-\phi)/2P_0\bar{h}, \tag{3.26}$$

where

$$\mu c_{1i}\phi = \operatorname{Im}(h^* h_y). \tag{3.27}$$

Now ϕ can be found from an integration of h^* times (3.1), letting $\mu \to 0$, and takes the two discrete values

$$\phi = \begin{cases} h_{0y}^2(0) & y < y_c, \\ h_{0y}^2(L) & y > y_c, \end{cases} \tag{3.28}$$

and it is straightforward to show by integrating (3.9) that R is negative throughout (i.e. there is movement of negative u-momentum away from the front by the eddies). Hence (3.20) shows that the total perturbation energy increases for all time.

The contribution to the total energy from the potential energy is of interest. Straightforward algebra on the mean and fluctuating parts of (2.7) shows that

$$\frac{d}{dt}\int_0^L \langle \tfrac{1}{2}\bar{h}^2 \rangle\, dy = -\int_0^L \bar{u}\langle v'h' \rangle\, dy, \tag{3.29}$$

$$\frac{d}{dt}\int_0^L \langle \tfrac{1}{2}h'^2 \rangle\, dy = +\int_0^L \bar{h}\langle u'(h'_x - v') \rangle\, dy = \tfrac{1}{2}\mu c_{1i}\int_0^L |h_0|^2\, dy > 0. \tag{3.30}$$

The rate of change of mean potential energy depends on

$$S = \langle v'h' \rangle, \tag{3.31}$$

the eddy mass flux, given after use of (3.24) to (3.28), as

$$\frac{2P_0\bar{h}}{\mu c_{1i}}\langle v'h' \rangle = \begin{cases} (\bar{u} - c_0)h_{0y}^2(0) - h_0 h_{0y} & y < y_c, \\ (\bar{u} - c_0)h_{0y}^2(L) - h_0 h_{0y} & y > y_c. \end{cases} \tag{3.32}$$

We have been unable to simplify this expression further. However, numerical evaluation shows that the c_+ eigenfunctions (i.e. those with $c > 0$) have S negative for y approximately less than the value where $\bar{h}$ reaches a maximum, and positive thereafter. In other words, the mass flux acts roughly to *spread out* the mean depth profile. This is confirmed by evaluation of (3.29), which shows the mean potential energy to decrease with time. Conversely (3.30) shows that the perturbation potential energy increases with time, at a rate found numerically to be nearly equal and opposite so that total potential energy is approximately conserved.

However, the c_- eigenfunctions behave quite differently. S takes positive values nearly everywhere, so that there is a tendency to pile up fluid near its maximum depth. As a result, evaluation of (3.29) shows that mean and perturbation potential energies *both* increase with time, which means these weakly growing modes are driven only by the mean kinetic energy of the system.

c) Numerical confirmation

In order to confirm these results, (2.13) to (2.15), with ε set to zero, were solved numerically for the mean profile

$$\bar{h}=\alpha y-\tfrac{1}{2}y^2+\beta y^3;\quad \bar{h}(L)=1;\quad 0\leqq y\leqq L\equiv 2. \tag{3.33}$$

When $\beta=0$, this corresponds to the case of zero potential vorticity $(1+\bar{h}_{yy}=0)$ so that $|\beta|\ll 1$ represents a small perturbation to zero potential vorticity. Furthermore,

$$\frac{d}{dy}\left(\frac{1+\bar{h}_{yy}}{\bar{h}}\right)=\frac{6\beta}{\bar{h}}+\frac{6\beta y\bar{u}}{\bar{h}^2}; \tag{3.34}$$

for positive β, this is positive at the value of y_c corresponding to c_+ modes, while for negative β, this is negative at the value of y_c corresponding to c_- modes. So both values of β should yield unstable modes, those with positive β being more unstable.

The numerical results are shown in Figure 3 for $-0.06\leqq\beta\leqq 0.0625$. The latter value ($\beta=1/16$) represents a cut-off for longwave disturbances, since at this value $\bar{u}(L)$ vanishes and then $c=0$. Thus for $\beta>1/16$, there are only stable longwave disturbances, with $c>\max(\bar{u})$, as suggested by the upper curve. Evaluation of (3.11) for vanishingly small P_0 (i.e. zero potential vorticity) gives, in confirmation, a line tangential to the c_i curve for $\beta>0$, and a zero value (also tangential) for $\beta<0$. The values of the energy integrals were also found to be in agreement with the asymptotics, with mean and perturbation potential energy both increasing for negative β in the range shown (although the mean potential energy decreases for $\beta<-0.08$, but at a rate far less than the increase of perturbation potential energy).

In summary: although conventional instability theory for a one-layer fluid implies that an extremum of potential vorticity is necessary for instability, this turns out not to be the case. Infinitely long waves of infinitesimal amplitude can grow on a single front bounded by a coastline even for profiles with monotonic vorticity gradients.

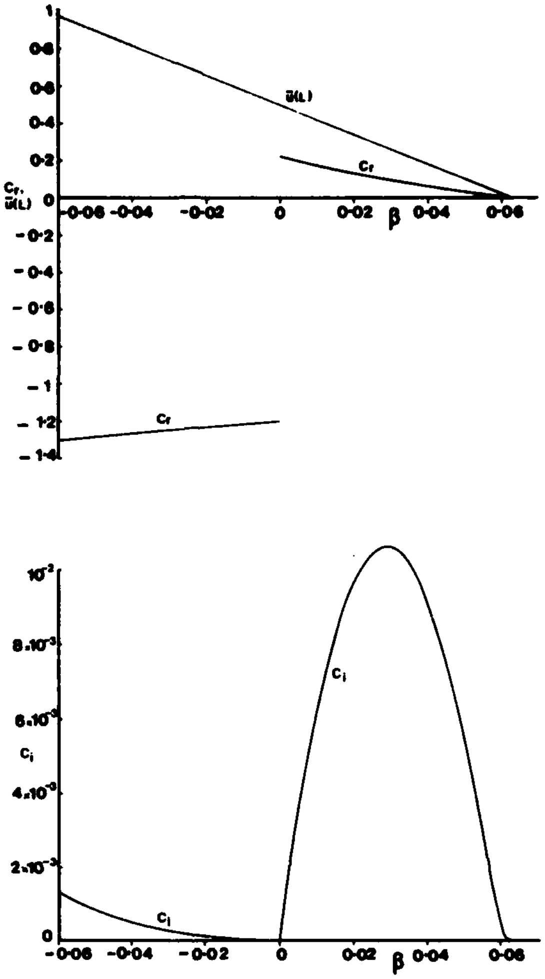

FIGURE 3 Numerical solutions for longwave disturbances to the profile $h=\alpha y-\frac{1}{2}y^2+\beta y^3$, $h(2)=1$. The lowest curve shows c_i as a function of β (there is stability for $\beta>1/16$). The upper curves show c_r for the c_+, c_- solutions, together with the mean velocity at the wall $\bar{u}(L)$.

The mean profiles so far have been restricted to those "near" uniform potential vorticity, because these are experimentally realizable. Due to friction, etc., however, most of these flows have $\bar{u}$ vanishing at a wall, without a flow reversal. Such flows are stable to longwave disturbances, with eigenvalue zero. The conditions under which they may be unstable to non-long waves will be examined in the next section.

4. INSTABILITY OF FLOWS TO DISTURBANCES OF FINITE WAVELENGTH

a) Demonstration of instability

We shall now remove the severely limiting restriction on the discussion in Section 3 by showing that all mean flows ($\bar{u} \leq 0$) are unstable for which

$$\bar{u}(L)=0, \quad \bar{u}_{yy}(L)<0.$$

The starting point for this investigation is the observation that the long wave ($\varepsilon=0$) Eq. (3.1) is satisfied by

$$h=\bar{u}, \quad c=0,$$

since the right-hand side of (3.1) reduces to $\bar{u}+\partial(P^{-1})/\partial y=\partial(-\bar{h}+P^{-1})/\partial y$ and the left-hand side reduces to $\partial[(-\bar{h}P+1)P^{-1}]/\partial y$. Moreover, the boundary condition (2.18) is obviously satisfied, as is (2.20), or (2.21), if ε and c both vanish. The foregoing means that $h=h_0=\bar{u}$ gives the leading term in an expansion in powers of ε of (2.16)–(2.20). We shall solve this to sufficiently high order to show that $c_i>0$ and the flow is unstable. Since the resulting matched asymptotics are algebraically lengthy, the following brief overview may be found useful.

Straightforward expansion of (2.16) in powers of ε fails for two reasons. First, the equation becomes *first-order* in y, the second-order term being multiplied by a small quantity. Thus a boundary layer structure must occur somewhere, within which the second-order term is important and the (outer) expansion fails. This layer turns out to be at the wall $y=L$. Second, the outer expansion is badly behaved at the wall, necessitating logarithmic terms in the ε expansion.

This forces the (outer) expansion

$$\begin{aligned} h &= h_0+\varepsilon^2 h_1+\varepsilon^4 \log\varepsilon h_2+\varepsilon^4 h_3+\dots, \\ c &= \varepsilon^2 c_1 \qquad\qquad\qquad +\varepsilon^4 c_2+\dots, \end{aligned} \tag{4.1}$$

since a little algebra shows that the $O(\varepsilon)$ term in the expansion for c must vanish. A simple matching at $O(\varepsilon^2)$ between outer and inner solution shows that c_1 and h_1 are both *real.* This yields a critical layer ($\bar{u}-c=0$) at a distance $O(\varepsilon^2)$ from the wall, where (2.16) becomes singular. (This singularity is present in both outer and inner solutions.) It is necessary to invoke a yet smaller layer (a "tiny" layer) of thickness $O(\varepsilon^4)$, situated a distance $O(\varepsilon^2)$ from the wall. This double layer structure is shown schematically in Figure 4, and has an "inner" layer of thickness ε^2, with co-ordinate Y defined by

$$y-L\equiv\hat{y}=\varepsilon^2 Y, \tag{4.2}$$

within which is the "tiny" layer of thickness ε^4, with coordinate z given by

$$z=[\hat{y}-\varepsilon^2 c_1\bar{u}_y^{-1}(L)]/\varepsilon^4=[Y-c_1\bar{u}_y^{-1}(L)]/\varepsilon^2. \tag{4.3}$$

(There will be little need to consider the formal details of the "tiny" layer, whose role is restricted to providing certain complex phase shifts of logarithms.) The matching at $O(\varepsilon^4)$ will then show that c_2 is complex, and $\bar{u}-c$ is $O(\varepsilon^4)$ in the "tiny" layer, which smooths the singularity in (2.16).

We now demonstrate the above assertions. The outer solution begins with

$$h_0=\bar{u}, \quad c_0=0, \tag{4.4}$$

and $iv_0=-h_0$ is the corresponding leading term in $v=v_0+\varepsilon^2 v_1+\ldots$. Higher orders may be obtained either from (2.16) or more easily, from expansion of (2.13) to (2.15). From these we obtain a first-order differential equation

$$\bar{u}h_{1y}-\bar{u}_y h_1-\bar{u}^3-c_1-(1-\bar{u}_y)\Gamma^{-1}\int_0^y \bar{h}\bar{u}^2\,dy=0. \tag{4.5}$$

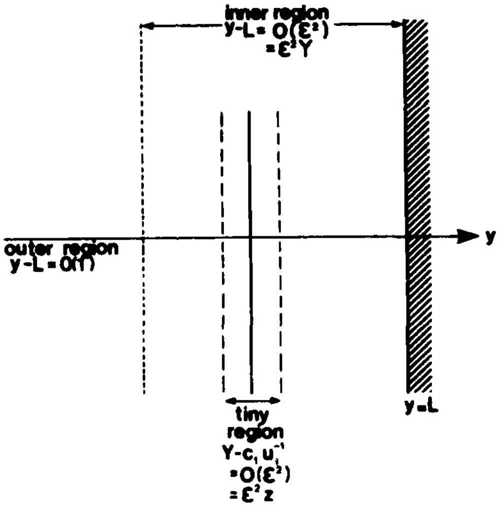

FIGURE 4 Schematic of the double layer structure for the problem of Section 4.

The succeeding terms in the h expansion are

$$h_2 = 0, \tag{4.6}$$

$$\bar{u}h_{3y} - \bar{u}_y h_3 - c_2 + \mathscr{L}(h_1) = 0, \tag{4.7}$$

where $\mathscr{L}(h_1)$ is a complicated second-order functional of h_1, and (4.6) has used the convenient scaling condition

$$h = \bar{u}, \quad y = 0. \tag{4.8}$$

Equations (4.5), (4.7) are singular when u vanishes, and the form of the solution is

$$h_1 \sim \alpha_1 + \beta_1 \hat{y} \log|\hat{y}| + \gamma_1 \hat{y} + \dots, \qquad \hat{y} \to 0, \tag{4.9}$$

$$h_3 \sim \omega \log|\hat{y}| + \alpha_3 + \dots, \qquad \hat{y} \to 0, \tag{4.10}$$

where most of the coefficients are determined by substitution in the equations.

The inner layer equations are much easier. Noting that h vanishes to leading order, we may write

$$h(y) = h(\varepsilon^2 Y) \equiv H(Y) = \varepsilon^2 H_1 + \varepsilon^4 \log\varepsilon\, H_2 + \varepsilon^4 H_3 + \dots \tag{4.11}$$

in the layer (H should not be confused with the dimensional depth of the fluid). Expansion of (2.16) yields

$$H_{1YY} = 0, \qquad H_{2YY} = 0, \tag*{(4.12), (4.13)}$$

$$H_{3YY} = -u_2 p H_{1Y} + u_2 p H_1 (Y u_1 - c_1)^{-1}, \tag{4.14}$$

where

$$u_n \equiv d^{(n)}\bar{u}(L)/dy^n, \quad p = [1 - \bar{u}_y(L)]^{-1} \equiv (1 - u_1)^{-1} \tag{4.15}$$

are conveniently defined. Because $\bar{u}$ is negative, $u_1 \geqq 0$. The boundary condition (2.18) gives (unless $u_1 = 1$, a singular case)

$$\left.\begin{aligned} &c_1 H_{1Y} + H_1 = 0, && \text{(4.16a)} \\ &c_1 H_{2Y} + H_2 = 0, && \text{(4.16b)} \\ &c_1 H_{3Y} + H_3 + c_2 H_{1Y} = 0, && \text{(4.16c)} \end{aligned}\right\} Y = 0.$$

The first step of the solution is to show c_1 to be real by matching at $O(\varepsilon^2)$. To this order, the outer solution is

$$h = \bar{u} + \varepsilon^2 h_1 = \varepsilon^2 (Yu_1 + \alpha_1), \tag{4.17}$$

after transformation to inner variables. The inner solution is merely

$$H_1 = A_1 Y + B_1, \tag{4.18}$$

with the tiny layer providing continuity of A_1, B_1 across the (as yet undefined) critical layer. Matching yields the inner solution as

$$H_1 = u_1 Y + \alpha_1, \tag{4.19}$$

and substitution into the first equation of (4.16) gives

$$c_1 u_1 + \alpha_1 = 0, \tag{4.20}$$

where α_1 is defined in (4.9). Now (4.5) gives

$$\alpha_1 = \left[-c_1 - (1 - u_1) \int_0^L \bar{h}\bar{u}^2 \, dy \right] \Big/ u_1, \tag{4.21}$$

which, after use of (4.20), gives

$$c_1 = -[1 + \bar{u}_y(L)]^{-1} \int_0^L \bar{h}\bar{u}^2 \, dy. \tag{4.22}$$

Hence c_1 is *negative* for all profiles under consideration, since $u_1 = \bar{u}_y(L)$ must be positive. Hence $\bar{u} - c$ vanishes at a value of $Y = c_1 u_1^{-1} < 0$ which is inside the fluid. Thus H_3, given by (4.14), is singular when $Yu_1 - c_1$ vanishes.

This singularity will force c_2 to be complex. As indicated in the preamble, the matching at $O(\varepsilon^4)$, now involving the tiny layer, will obtain c_2. To $O(\varepsilon^4)$, the outer solution is

$$\begin{aligned} h &= \bar{u} + \varepsilon^2 h_1 + \varepsilon^4 h_3 \\ &= \varepsilon^2 (u_1 Y + \alpha_1) + \varepsilon^4 \log \varepsilon (2\beta_1 Y + \omega) \\ &\quad + \varepsilon^4 (\tfrac{1}{2} u_2 Y^2 + \beta_1 Y \log|Y| + \gamma_1 Y + \omega \log|Y| + \alpha_3), \end{aligned} \tag{4.23}$$

after expression in inner variables and truncation to $O(\varepsilon^4)$. The inner solutions are

$$H_2 = A_2 Y + B_2, \tag{4.24}$$

$$H_3 = A_3^{\pm} Y + B_3^{\pm} + \tfrac{1}{2} u_2 Y^2 + u_2 c_1 u_1^{-1} (Y - c_1 u_1^{-1}) \{\log |Y - c_1 u_1^{-1}| - 1\}, \tag{4.25}$$

where the superscripts ± refer to $(Y - c_1 u_1^{-1}) \gtrless 0$ respectively. The jumps in A_3, B_3 are found by consideration of the tiny layer at $O(\varepsilon^6)$, where terms in $z \log(z - c_2 u_1^{-1})$ occur. As $\operatorname{Im}(c_2) > 0$ by supposition, this leads to $\log(-|Y|)$ being interpreted as $\log|Y| - i\pi$, so that

$$A_3^+ - A_3^- = i\pi u_2 c_1 / u_1, \tag{4.26}$$

$$B_3^+ - B_3^- = -i\pi u_2 c_1^2 / u_1^2, \tag{4.27}$$

which are the phase jumps in the evaluation of the logarithms in (4.25). Writing the inner solution to $O(\varepsilon^4)$, expressing it in outer variables and retruncating, leads to

$$\begin{aligned} h = {} & \varepsilon^2 u_1 (Y - c_1) + \varepsilon^4 \log \varepsilon (A_2 Y + B_2) \\ & + \varepsilon^4 (A_3^- Y + B_3^- + \tfrac{1}{2} u_2 Y^2 + u_2 c_1 u_1^{-1} Y \log |Y| \\ & + 2 u_2 c_1^2 u_1^{-2} - u_2 c_1 u_1^{-1} Y - u_2 c_1^2 u_1^{-2} \log |Y|). \end{aligned} \tag{4.28}$$

Matching the $O(\varepsilon^4)$ terms only (as these will yield c_2) between (4.23) and (4.28) gives

$$A_3^- = \gamma_1 + c_1 u_2 / u_1, \tag{4.29}$$

$$B_3^- = \alpha_3 - 2 c_1^2 u_2 / u_1^2. \tag{4.30}$$

The eigenvalue c_2 is now obtained by substitution into (4.16c). Using (4.26), (4.27) this gives

$$\begin{aligned} & c_1 \left[\gamma_1 + \frac{c_1 u_2}{u_1} (1 + i\pi) + \frac{c_1 u_2}{u_1} \log \left| -\frac{c_1}{u_1} \right| \right] \\ & \qquad + c_2 u_1 + \frac{u_2 c_1^2}{u_1^2} \left(-1 - i\pi - \log \left| \frac{-c_1}{u_1} \right| \right) + \alpha_3 = 0. \end{aligned} \tag{4.31}$$

Now c_1, u_1, u_2, γ_1 are all *real*. Furthermore the imaginary part of α_3 is, from (4.7), (4.10), only $-u_1^{-1}\,\mathrm{Im}(c_2)$. Hence the imaginary part of (4.31) gives

$$c_1^2 u_2 u_1^{-1}\pi + u_1\,\mathrm{Im}(c_2) - c_1^2 u_2 u_1^{-2}\pi - u_1^{-1}\,\mathrm{Im}(c_2) = 0, \tag{4.32}$$

from which

$$\mathrm{Im}(c_2) = -c_1^2 u_2 \pi / u_1(1+u_1). \tag{4.33}$$

So c_2 is complex, provided that $\mathrm{Im}(c_2) > 0$ as supposed when evaluating the phase shifts. Since u_1 is positive, this requires

$$u_2 = \bar{u}_{yy}(L) < 0 \qquad \text{for instability}, \tag{4.34}$$

as well as the assumption that the potential vorticity does not vanish at the wall. (Thus constant potential vorticity flows are stable because u_2 vanishes when $\bar{u}$ does.) Hence instability requires that the flow not be too "jet-like" near the wall (when $\bar{u}$ would have positive curvature). Equivalently, the potential vorticity P given by (2.12) must have a maximum (but not an extremum) at the wall $[P_y(L) > 0]$.

b) Energetics

The energetics of the instability demonstrated here are more straightforward than those considered earlier. The Reynolds stress

$$R = \langle u'v' \rangle = \tfrac{1}{2}\,\mathrm{Re}\,\{i[(\bar{u}-c)h_y - h](1-\bar{u}_y)^{-1}h_y^*\} + O(\varepsilon^6), \tag{4.35}$$

and, using (4.1),

$$R = \tfrac{1}{2}\varepsilon^4[1-\bar{u}_y(L)]^{-1}\{\mathrm{Im}(c_2)\bar{u}_y^2 + \mathrm{Im}(\bar{u}_y h_3 - \bar{u}h_{3y})\} \tag{4.36}$$

$$= -\tfrac{1}{2}\varepsilon^4\,\mathrm{Im}(c_2)\,[1+\bar{u}_y(L)] = -\tfrac{1}{2}c_i[1+\bar{u}_y(L)], \tag{4.37}$$

after use of (4.7), where $c_i = \mathrm{Im}(c)$.

This is the same expression (but two orders of magnitude smaller) found by GKS, showing that similar energetics to the two-front case are occurring, but heavily stabilized by the presence of a wall. Similarly, the mass flux is given by

$$S = \langle v'h' \rangle = \tfrac{1}{2}[1-\bar{u}_y(L)]^{-1}\,\mathrm{Re}\,\{-i(\bar{u}-c)h_y h^*\}$$

$$= \tfrac{1}{2}\varepsilon^4[1-\bar{u}_y(L)]^{-1}\{-\mathrm{Im}(c_2)\bar{u}_y\bar{u} + \bar{u}\,\mathrm{Im}(\bar{u}h_{3y} - \bar{u}_y h_3)\}$$

$$= \tfrac{1}{2}\varepsilon^4\bar{u}\,\mathrm{Im}(c_2) = \tfrac{1}{2}\bar{u}c_i < 0 \tag{4.38}$$

for all y. This is again formally the same expression as in the two-front case, and shows a redistribution of mass leading to a lowering of the mean centre of gravity.† Indeed,

$$\frac{d}{dt}\int_0^L \langle \tfrac{1}{2}\bar{h}^2\rangle dy = -\int_0^L \bar{u}\langle v'h'\rangle dy = -\tfrac{1}{2}c_i\int_0^L \bar{u}^2 dy < 0, \tag{4.39}$$

and

$$\frac{d}{dt}\int_0^L \langle \tfrac{1}{2}h'^2\rangle dy = \tfrac{1}{2}c_i\int_0^L |h_0|^2 dy = +\tfrac{1}{2}c_i\int_0^L \bar{u}^2 dy > 0, \tag{4.40}$$

so that

$$\frac{d}{dt}\int_0^L (PE + PE') = 0, \tag{4.41}$$

showing that total potential energy is conserved (and therefore so is total kinetic energy). However, (3.20) shows again that mean shear is necessary for the instability (i.e. a source of potential energy is insufficient), so that, for example, the two-layer configuration discussed by Jones (1977), with constant $\bar{u}$ in the top layer, is stable unless the deep lower layer is allowed to play a role.

c) Numerical confirmation and extensions

We again consider first the profile (3.33), with β chosen so that $\bar{u}(L)$ vanishes (i.e. $\beta = 1/16$). The stability curve is shown in Figure 5, together with the asymptotics (4.22) and (4.33) for the real and imaginary parts of c. The expression for Re(c) is quite accurate for $\varepsilon \lesssim 0.6$, whereas the higher terms in the expansion for c_i cause (4.33) to hold only for quite small values of ε. Nonetheless, the validity of the asymptotics is demonstrated. The growth rate εc_i reaches a maximum at $\varepsilon = 1.26$, $c_i = 9\times 10^{-3}$, $\varepsilon c_i = 0.012$. (This growth rate is an order of magnitude smaller than those found for the two-front instability by GKS, again demonstrating the strong stabilizing effect of the wall.) The structure of the fastest growing mode is very similar to that shown in GKS, in that the mode has horizontal velocities almost $\frac{1}{2}\pi$ radians out of phase, as the asymptotics above would suggest. It is quite surprising that small ε asymptotics should

---

†However, the mass transfer is now one-signed, because $\bar{u}$ is also. This means that the one-layer model now fits the observations of Smith (1976) in the Denmark Strait even better than the two-front model considered by GKS.

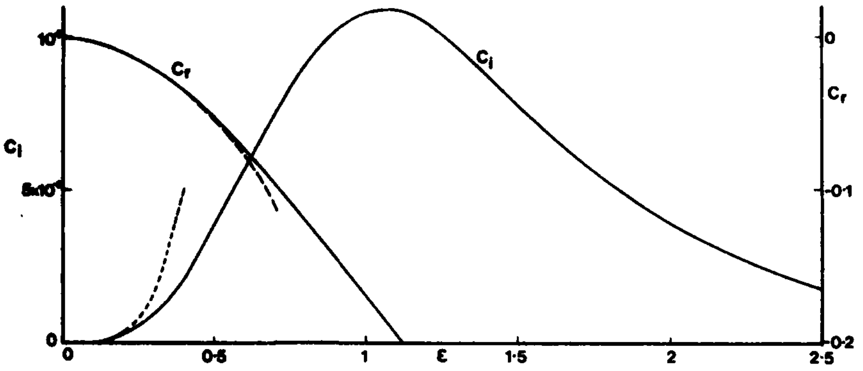

FIGURE 5 Numerical unstable solutions to the profile $h=(5/4)y-\frac{1}{2}y^2+(1/16)y^3$, $0\leqq y\leqq L=2$, for varying wavenumber ε. The dashed lines show the predicted asymptotics for small ε given by (4.22), (4.33).

continue to give a qualitatively correct picture at $\varepsilon=O(1)$. For large ε, c_i declines slowly with ε. The mode is concentrated within $O(\varepsilon^{-1})$ of the front, with $c_r\sim\bar{u}(0)+O(\varepsilon^{-1/2})$. This frontally-trapped instability mode can exist independently of other boundaries, and it is hoped to study this further in a later paper.

The effects of varying the conditions at the wall can be studied by means of the profile

$$\bar{h}=\alpha y+\beta y^2+\gamma y^3;\quad \bar{h}(L)=1;\quad \bar{u}(L)=0;\quad L=2, \tag{4.42}$$

for varying γ. The fastest growth rates, and corresponding wavenumbers, are shown in Figure 6, and it is interesting to compare this with the asymptotic theory above. We have, after some algebra, the following facts:

$$\bar{u}_{yy}(L)=0,\quad \gamma=0;\quad \bar{u}_{yy}(L)<0,\ \gamma>0; \tag{4.43}$$

$$\bar{u}_y(L)=0,\quad \gamma=\tfrac{1}{8},\quad \text{i.e.}\quad \bar{u}(y)\leqq 0,\ \gamma\leqq\tfrac{1}{8}; \tag{4.44}$$

$$\bar{u}_y(L)=-1,\quad \gamma=\tfrac{3}{8}. \tag{4.45}$$

Thus when γ is negative, $\bar{u}_{yy}(L)>0$ and there is stability. For $0<\gamma<\frac{1}{8}$, the flow does not have a reversal, and the theory of this section holds when ε is suitably small. As γ nears $\frac{1}{8}$, u_1 becomes small and the denominator of (4.33) begins to increase. When $|\gamma-\frac{1}{8}|$ becomes of order ε, there is a transition to a thicker boundary layer (of thickness ε). The asymptotic (4.22) for c_r continues to hold, but the c_i expression is

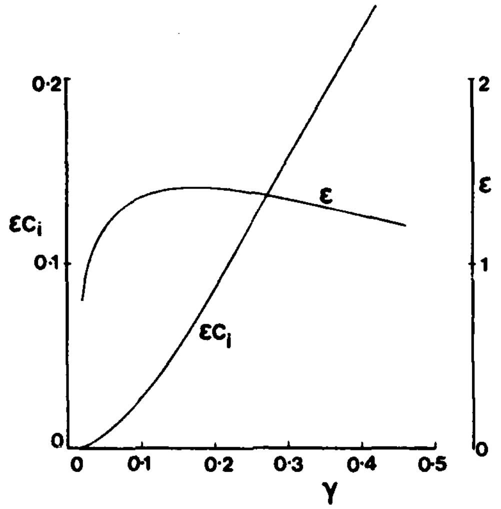

FIGURE 6 Fastest growing modes for the profile $h=\alpha y+\beta y^2+\gamma y^3$, $\bar{h}(L)=1$, $\bar{u}(L)=0$, $L=2$, as functions of γ, proportional to $\bar{u}_{yy}(L)$.

modified. For $\gamma>\frac{1}{8}$, there is a flow reversal. The expression (4.22) for c_r remains valid, and the critical layer leaves the wall and enters the fluid proper. It is straightforward, but tedious, to follow the phase jumps in the solutions and conclude that c remains complex. Only when γ nears $\frac{3}{8}$, when the $(1+u_1)$ term in the denominator of (4.22) nears zero, does (4.22) begin to break down. When $\gamma>\frac{3}{8}$, there is a strong flow reversal $[\bar{u}_y(L)<-1]$ and the unstable mode now possesses complex c even when $\varepsilon=0$, rather like the long-wave unstable flows of Section 3. However, it should be stressed that despite these subtle changes for small ε, the behaviour of the growth rate even at small ε, as well as the fastest growing mode, remains smooth, as Figure 6 shows. Values of ε for the fastest growing mode lie around 1.3 to 1.4, corresponding to wavelengths of 4–5 radii of deformation, with growth rates increasing almost linearly with γ. For small γ, ε decreases rapidly (indeed, it is a common feature that long waves are the most unstable near the stability boundary).

5. THE EFFECTS OF VARYING CURRENT WIDTH

The discussion of the previous sections has dealt with a current of fixed width L. It is of interest to see how the properties of the instabilities vary with the width of the current. In the case of longwave disturbances on profiles of nearly uniform potential vorticity (Section 3) the answer is straightforward. We have seen that L must exceed a critical value $L_c > 2^{1/2}$ for instability to occur, and that growth rates increase with L. The answer is not so simple for disturbances to a flow with zero velocity at the wall (Section 4). This is because the preferred mode of instability depends both on the *width* and the *shape* of the profile.

We can estimate this effect for a few simple cases. Suppose the shape of the profile is self-similar, so that

$$\bar{h} = \phi(\eta = yL^{-1}). \tag{5.1}$$

Then (4.22), (4.33) imply [making the plausible—from numerics—but unproven assumption that the small ε results give correct orders of magnitude when $\varepsilon \sim O(1)$]

$$c_r \simeq \varepsilon^2 c_1 \simeq -\varepsilon^2 L[L^2 - \phi''(1)]^{-1} \int_0^1 \phi(\phi')^2 \, d\eta, \tag{5.2}$$

$$c_i \simeq \varepsilon^4 c_{2i} \simeq \frac{-\varepsilon^4 L^3 \phi'''(1)\pi \left\{ \int_0^1 \phi(\phi')^2 \, d\eta \right\}^2}{\phi''(1)[L^2 - \phi''(1)]^3}. \tag{5.3}$$

For narrow currents, then ($L \ll 1$), the growth rate for small ε should vary as $L^3 \ll 1$, while for wide currents ($L \gg 1$), the growth rate should decay as $L^{-3} \ll 1$. The modes under discussion should have largest growth rate when $L \approx O(1)$, with much weaker values for wider or narrower currents. This conclusion may be different for the frontally-trapped modes to be discussed in a subsequent paper.

It is of course difficult to conceive of a flow in which the only length scale is the width L; the radius of deformation (here unity) must be a natural length scale also. If we now seek an almost total dependence on the radius of deformation, we have

$$\bar{h} = \phi(y). \tag{5.4}$$

The expressions for c_r and c_i yield, for narrow currents

$$c_r \simeq \varepsilon^2 \cdot O(1); \quad c_i \simeq \varepsilon^4 \cdot O(1), \tag{5.5}$$

so that growth rates should be order unity for $\varepsilon = O(1)$. For wide currents ($L \gg 1$), it is natural to assume that $\bar{u}$ decays exponentially away from the front on the scale of the deformation radius, so we pose $\bar{u} \sim e^{-y}, y \gtrsim 1$. Then

$$c_r \simeq \varepsilon^2 c_1 \simeq \frac{-\varepsilon^2 \int_0^L \bar{h}\bar{u}^2 dy}{1+u_1} \simeq \frac{-\varepsilon^2 \int_0^1 \bar{h}\bar{u}^2\, dy}{1} \simeq O(\varepsilon^2), \tag{5.6}$$

$$c_i \simeq \varepsilon^4 O(1) e^{-L}\pi / e^{-L}(1+e^{-L}) \simeq O(\varepsilon^4), \tag{5.7}$$

which would suggest that instabilities on wide currents can be vigorous and roughly independent of current width (again, the same will be true for frontally-trapped modes).

Typical mean flows will contain depth variations on scales of *both* the deformation radius and the current width. Similar calculations imply small growth rates for narrow currents and only slowly decaying growth rates for wide currents. However, it is clear that no general rule can be given, apart from the approximate rule of thumb that narrow currents are only weakly unstable.

Even this rule can fail, if the flow profile is chosen to give a large value of $\mathrm{Im}(c_2)$. Figure 7 shows the fastest growing mode for the profile

$$\bar{h} = 1 - [(L-y)^3 \cosh(L-y)]/L^3 \cosh L, \tag{5.8}$$

which has $\bar{u}$ and $\bar{u}_y$ both zero at $y=L$, implying strong growth rates by (4.33). The profile is chosen to be "near" the (stable) constant potential vorticity profile $[1-\cosh(L-y)/\cosh L]$. The main difference is the stronger fall-off in depth near the front (and correspondingly stronger mean flow) for the profile (5.8). For wide currents ($L \gtrsim 2$, say) the wavelength of the fastest growing mode is almost constant, at 2.5 radii of deformation. The growth rate decays slowly as L increases, and the phase velocity c_r (which always moves with the fluid) grows gradually as L increases. (The instability is one confined to the front for large L, hence the lack of dependence upon L.) However, the growth rate increases rapidly as L becomes small, with a corresponding increase in the preferred wavelength, because $\bar{u}$ becomes large at the front. The phase speed increases somewhat for small L. So this is an example of strong instability for narrow currents, although at longer wavelengths. Indeed, for $L<2$ the growth rates for profile (5.8) are stronger than for the two-front constant potential vorticity instability found by GKS, as suggested by u_1 vanishing in (4.33).

6. DISCUSSION

Conventional theory for a flow with one active layer (usually known as quasi-geostrophic theory) implies that an extremum in the potential

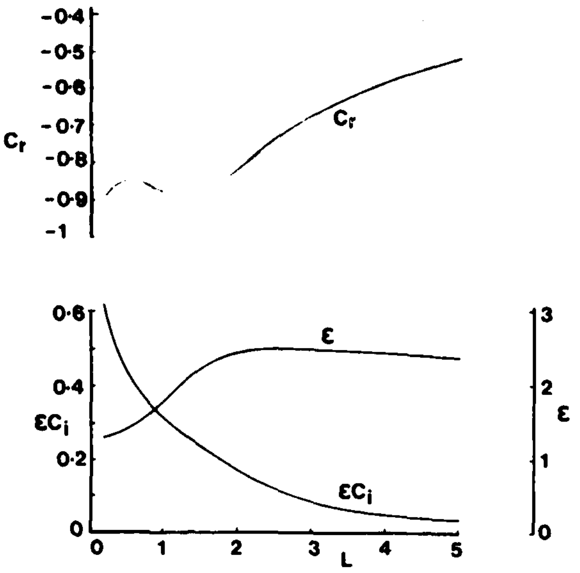

FIGURE 7 Fastest growing modes for the profile $h = 1 - (L-y)^3 \cosh(L-y)/(L^3 \cosh L)$ as functions of width L.

vorticity of a flow is necessary for that flow to be unstable to infinitesimal disturbances. Such theories are invalid, suppressing interesting instabilities, when the thickness of the active layer becomes small and when inertial terms become significant compared with Coriolis terms. In the previous paper in this series (GKS) we showed that flows with two fronts were almost always unstable, relative to a mode which couples the two fronts. This type of coupling cannot occur in the models considered herein, because of the rigid coastal boundary. However, we have shown here that the latter flows are also unstable under fairly general conditions, *even if the potential vorticity is monotonic.*

In detail, two classes of instability have been derived, both fairly general. In the first, mean flows close to uniform potential vorticity are shown to be unstable to infinitely long disturbances, and hence by extension to finite waves also. However, a flow reversal is needed for this instability. In the second, mean flows which vanish at the coastal boundary are also shown to be unstable to waves of long but finite wavelength.

It is interesting to compare the predictions in this paper with the observations of unstable buoyancy-driven coastal currents made by Griffiths and Linden (1981). They found that currents produced by leaking less dense fluid into a container of dense fluid from a source adjacent to a vertical wall became unstable when the width L of the current became wider than some critical width L_c, which varied greatly with source flow rates, friction and depth ratios (all of which affected the flow profile). L_c always exceeded three deformation radii, based on the layer depth at the wall. The observed wavelength was about $2L$, and the phase velocity was oriented downstream with a magnitude rather smaller than the maximum velocity of the fluid. Griffiths and Linden (1981a) interpret their observations within the framework of quasi-geostrophic baroclinic theory, i.e. the instability releases potential energy via an essential coupling between the upper and lower layers. The equivalent one-layer instabilities discussed in this paper can therefore be expected to explain only certain features of these observations.

The longwave theory of Section 3 predicts stability for narrow currents, and the theory of Sections 4 and 5 indicate that narrow currents are usually only weakly unstable. This is in qualitative agreement with observations, which do not show finite waves for $L \lesssim O(1)$. However, there are areas of disagreement. The observed value of $3 < L_c < 15$ is distinctly larger than is predicted by any of our calculations. Furthermore, one-layer disturbances on wide currents tend to be trapped at the front, and so also have wavelengths of order the deformation radius. As previously mentioned, a clearcut comparison is difficult to make, due to the unknown vorticity profiles, friction, and due to the modifications caused by the finite bottom layer in the experiments. The wide variation in growth rates and wavelengths between the theoretical profiles shows that accurate modelling of experiments needs a much more accurate knowledge of the mean flow, and a more detailed theory.

Later experiments (Griffiths and Linden, 1981b) concentrated upon density fronts produced by the collapse of an annulus of light fluid, so possessing approximately uniform potential vorticity. These later, more controlled, results were rather different. The observed disturbances were almost stationary, and the observed wavelength depended upon the width of the current. For (initial) widths L less than or of order the deformation radius, the wavelength scaled with the current width, with a value of about $2.2L$, but no critical width L_c was observed. For $L \geqq 1$, the wavelength scaled with the deformation radius, the nondimensional value being about 7. There is much better agreement with the theory in Section 4 for these later experiments. Theory predicts c_r to be weak [$O(\varepsilon^2)$ for small ε and fairly small numerically for $\varepsilon = O(1)$], so that the disturbances propagate only slowly. The wavelength is predicted to scale on the deformation radius for wide currents, as observed. The "short" waves observed for small L may be explained by the rise in growth rate in Figure 7 for small L, as the wavelength remains of order the deformation radius, which was small for narrow currents in the experiments. The only major discrepancy is that the profile in Figure 7 leads to wavelengths for large L of 2.5 times smaller than the 7 deformation radii observed. However, the sensitivity of growth rate and wavelength to the profiles in the theoretical model again point to the difficulty of making a comparison with experiment. We may conclude, however, that a large portion of the physics is captured by the simple one-layer model discussed in this paper.

Acknowledgements

PDK was supported by a grant from the Natural Environment Research Council of Great Britain; MES was partially supported by the U.S. Office of Naval Research.

Many fruitful discussions with R. Griffiths are gratefully acknowledged.

References

Griffiths, R. W., Killworth, P. D. and Stern, M. E., "Ageostrophic instability of ocean currents," *J. Fluid Mech.* **117**, 343–377 (1982).

Griffiths, R. W. and Linden, P. F., "The stability of buoyancy-driven coastal currents," *Dyn. Atmos. & Oceans* **5**, 281–306 (1981a).

Griffiths, R. W. and Linden, P. F., "Experiments on density-driven boundary currents and fronts," *Geophys. & Astrophys. Fluid Dyn.* (to appear) (1981b).

Jones, S., *Instabilities and Wave Interactions in a Rotating Two-Layer Fluid*, Ph.D. thesis, University of Cambridge (1977).

Mann, C. R., "Temperature and salinity characteristics of the Denmark Strait overflow," *Deep-Sea Research* **16**, 125–137 (1969).

Orlanski, I., "Instability of frontal waves," *J. Atmos. Sci.* **25**, 178–200 (1968).

Smith, P. C., "Baroclinic instability in the Denmark Straight overflow," *J. Physical Oceanography* **6**, 355–371 (1976).

Stern, M. E., "Geostrophic fronts, bores, breaking and blocking waves," *J. Fluid Mech.* **99**, 687–704 (1980).

Stern, M. E., Whitehead, J. and Hua, B.-L., submitted to *J. Fluid Mech.* (1982).

Linear Stability and Stable Modes of Geostrophic Fronts

by

Nathan Paldor

Department of Isotope Research
Weizmann Institute of Science
Rehovot 76100 Israel

ABSTRACT

A Rayleigh integral is used to prove that an unbounded geostrophic front of uniform potential vorticity is stable with respect to small perturbations of arbitrary wavelength. The ageostrophic theory developed in this study yields a stable, near-inertial, long trapped mode. Recent oceanic observations of the increase in the energy of the inertial peak in the vicinity of fronts support the existence of this inertial trapped mode. In addition the theory yields a geostrophic mode which is expected to become unstable when the potential vorticity is not uniform.

I. Introduction

The recently growing interest in the dynamics of surface fronts i.e. when the interface between layers of light and heavy fluids intersect the surface stems from their ubiquity in the atmosphere and the ocean (Mooen, 1975; Legeckis, 1978; McClimans, 1979). The Gulf Stream and the Kuroshio are two oceanic examples of an unbounded surface front while the Jet stream and the Southerly Buster are two atmospheric examples. Experiments (Stern, Whitehead and Hua, 1982; Griffiths, Killworth and Stern, 1982) as well as numerous observations demonstrate the highly unstable nature of surface fronts.

When trying to explain the origin of frontal instability it was natural to use as a starting point the classical instabilities which the quasi-geostrophic theory yielded, namely, the baroclinic and barotropic instabilities. The most renowned examples of instabilities on quasi-geostrophic systems were given by Charney (1947) and Eady (1949), and a complete investigation of the necessary conditions for these instabilities was carried out by Pedlosky (1964).

An essential element in the necessary conditions for instability on quasi-geostrophic systems is the gradient of the potential vorticity (Pedlosky, 1964). This gradient has to change sign in order for instabilities to develop in a two layer, quasi-geostrophic system (see also Killworth, 1980), and the same condition, holds when the lower layer is assumed passive and infinitely deep.

But the application of the quasi-geostrophic instability criteria to surface fronts is unjustified for two reasons. The lateral shear at the free streamline of such a front must equal the Coriolis parameter in order for the potential vorticity to remain finite. As a result the Rossby number is O(1) and the first assumption of the quasi-geostrophic approximation is violated. The second point is that the variations in depth of the interface are not small compared with the mean depth (actually they are singularly larger at the free streamline), and hence the second assumption of the quasi-geostrophic approximation is violated. An example of a frontal instability on a surface front which violates the necessary conditions for instability of the quasi-geostrophic theory is given by Killworth and Stern (1982) where a single layer, wall bounded, front with monotonic potential vorticity is shown to be unstable.

Since the extrapolation of quasi-geostrophic theory to the surface frontal problem fails in a qualitative way, a different theory has to be developed for surface fronts.

The first comprehensive study of frontal instability is given in Orlanski (1968) for a front consisting of two active layers of uniform speeds separated by a uniformly sloping interface. In this paper Orlanski found four intersecting families of instabilities differing in the region they occupy in the Rossby number - Richardson number phase space and in the generating mechanism. All the growth rates vanish when the wavelength becomes infintely long and a direct relationship between these frontal instabilities and the quasi-geostrophic barotropic and baroclinic instabilities could not be established. Although the potential vorticity in Orlanski's simple model is singular the study demonstrates that fronts have unstable modes which are generated by mechanisms other than those known from the classical instability theory.

Another approach used to develop a new theory is to infer from observations the essential components of such a theory. In this connection we note that the Gulf Stream has a very strong surface signiture (see for example the satellite observations of Cheney and Marsh, 1981) and can therefore be classified as a surface front. Observations on the Gulf Stream show that it has an abundance of instabilities in the form of eddies, rings and meanders (Lai and Richardson, 1979). Yet other observations indicate that the potential vorticity across the Stream is nearly uniform (Stommel, 1966; Luyten and Robinson, 1974). In view of the inapplicability of the quasi-geostrophic theory one might be inclined to look for unstable modes on an unbounded uniform potential vorticity, surface front. In chapter II we show, using a Rayleigh integral technique that such a front is stable with respect to small perturbations of arbitrary wavelength.

The implication of this stability theorem is that it is the slight departures from uniform potential vorticity, possibly through interaction with the lower layer, which produce the observed instabilities on a front like the Gulf Stream.

The instability found by Griffiths, Killworth and Stern (1982) on the coupled front with zero potential vorticity is another example of frontal instability which violates the quasi- geostrophic criteria for instability. This instability also demonstrates the highly unstable nature of surface fronts where even a dynamically simple front (no potential vorticity) is unstable.

But instabilities are not the only interesting dynamical features of fronts. Several recent observations reveal a conspicuous enhancement of near inertial oscillations in the vicinity of fronts. Fu (1981) compared current meter data from the Polymode arrays in the Western North Atlantic. He found an increase of 4dB in the energy of the near inertial peak under the Gulf Stream (4000m) compared with that of the mid-ocean. Fu himself, not being able to explain this increase pointed out the need for a theory of the coupling between inertial waves and currents.

Another relevant observation is that of Mayer et al. (1979) on the velocity spectrum at a midshelf location on the Middle Atlantic Shelf. They found that the inertial peak contains about 30% of the kinetic energy in the summer while in the winter the peak is totally eliminated. The wind pattern in the region is such that the wind stress is much larger in the winter than in the summer. Therefore the inertial peak in the velocity spectrum cannot be interpreted in terms of a wind induced inertial oscillation (Stern, 1977; Pollard and Millard, 1970). However, when the hydrography of the water column in the summer is compared to that of the winter it is found that in the summer there exists a strong front between the fresh water runoff and the shelf water. In the winter the winds erode away this sharp front and the water is nearly homogenous in the vertical.

Another relevant observation is that of Kunze and Sanford (1981) who studied the velocity profile in the vicinity of the North Pacific Subtropical Front. Their observations showed a sharp increase (a factor of 4) in the kinetic energy of the clockwise component of the horizontal velocity in the region of strongest horizontal temperature gradient.

All these observations (Fu, 1981; Mayer et al., 1979; Kunze and Sanford, 1981) suggest a strong correlation between the increase in the energy of the near inertial oscillation and the prevalance of fronts. A theoretical connection between the two is established in chapter III.

The observations of Kunze and Sanford (1981) show that the high correlation between the front and the near inertial oscillation exists only for the anti-cyclonic component of the rotary spectrum of the horizontal velocity. This is the only observation which makes this distinction, and the results of chapter III on the near inertial stable mode are in line with this differential increase in energy.

Another phenomenon which has been observed in numerous oceanic experiments is the slight shift (a few percent) in the frequency of the near inertial peak (Kundu, 1976; Gonella, 1971; Perkins, 1972; Webster, 1968; Day and Webster, 1965; Fu, 1981). Although many theories predict it (Munk and Phillips, 1968; Pollard, 1970; Stern, 1977) the results of chapter III provide another explanation for this shift in the vicinity of fronts.

II. LINEAR STABILITY OF SEMI-INFINITE SURFACE FRONTS

The front shown in figure 1 where a layer of fluid of density ρ_1 and depth h(y) overlays an infinitely deep layer of fluid density $\rho_2 > \rho_1$ is assumed to have a constant potential vorticity. The x and y momentum equations, for the u,v velocities respectively, the continuity equation and the conservation of (the constant) potential vorticity in the upper layer are:

fig 1

$$\frac{\partial u}{\partial t} + u\frac{\partial u}{\partial x} + v\frac{\partial u}{\partial y} - fv = -g'\frac{\partial h}{\partial x}$$

$$\frac{\partial v}{\partial t} + u\frac{\partial v}{\partial x} + v\frac{\partial v}{\partial y} + fu = -g'\frac{\partial h}{\partial y}$$

$$\frac{\partial h}{\partial t} + \frac{\partial}{\partial y}(hv) + \frac{\partial}{\partial x}(hu) = 0$$

$$f - \frac{\partial u}{\partial y} + \frac{\partial v}{\partial x} = h \cdot \frac{f}{H}$$

where $g' = g\frac{\rho_2 - \rho_1}{\rho}$ is the reduced gravity, f is the Coriolis parameter and H is the depth of the upper layer at $y = -\infty$.

The first three of these equations are familiar from shallow water theory and the fourth one expresses the major simplifying assumption of constant potential vorticity, this assumption is consistent with observations across the Gulf Stream (Stommel, 1966; Luyten and Robinson, 1974). The single layer model whereby the lower layer is considered totally passive and non-interacting is introduced for simplicity. Examination of quasi-geostrophic theories and other frontal instability problems shows that the interaction with the lower layer can introduce instabilities which are not present otherwise (see Orlanski, 1968; Pedlosky, 1964). We therefore anticipate that there exist instabilities which will not be recovered by our simple model. Nonetheless, an interesting stability theorem and a special inertial mode can be obtained from our simple, single layer model.

These equations are now nondimensionalized by scaling the u, v velocities by $(g'H)^{1/2}$, the time t by 1/f, the height h by H and the x, y coordinates by the radius of deformation $(g'H)^{1/2}/f$. In nondimensional form these equations become

$$\frac{\partial u}{\partial t} + u\frac{\partial u}{\partial x} + v\frac{\partial u}{\partial y} - v = -\frac{\partial h}{\partial x}$$

$$\frac{\partial v}{\partial t} + u\frac{\partial v}{\partial x} + v\frac{\partial v}{\partial y} + u = -\frac{\partial h}{\partial y}$$

$$\frac{\partial h}{\partial t} + \frac{\partial}{\partial y}(hv) + \frac{\partial}{\partial x}(hu) = 0$$

$$1 - \frac{\partial u}{\partial y} + \frac{\partial v}{\partial x} = h$$

The mean flow is assumed to consist of $\bar{u}$, $\bar{h}$ which are steady, independent of x, geostrophically balanced, and with constant potential vorticity; i.e.

$$\bar{u} = -\frac{\partial \bar{h}}{\partial y}$$

$$1 - \frac{\partial \bar{u}}{\partial y} = \bar{h}$$

The solutions of this which satisfy $\bar{h}(0)=0=\bar{u}(-\infty)$ are

$$\bar{u}(y) = e^{y} \tag{1}$$

$$\bar{h}(y) = 1 - e^{y} = 1 - \bar{u}(y) \tag{2}$$

We now let the total velocities and interface depth be of the form $u=\bar{u}+u'$; $v=v'$; $h=\bar{h}+h'$ where the primed variables are small perturbations to the mean. When we linearize the x momentum equation, the continuity equation and the conservation of potential vorticity and use (2) the result is :

$$\frac{\partial u'}{\partial t} - \bar{h}v' + \bar{u}\frac{\partial u'}{\partial x} + \frac{\partial h'}{\partial x} = 0 \tag{3}$$

$$\frac{\partial h'}{\partial t} + \frac{\partial}{\partial y}(\bar{h}v') + \frac{\partial}{\partial x}(\bar{h}u' + \bar{u}h') = 0 \tag{4}$$

$$\frac{\partial v'}{\partial x} = h' + \frac{\partial u'}{\partial y} \tag{5}$$

We assume that the perturbations represent a free wave traveling in the x direction, i.e. $(u',v',h') = (u(y), v(y), h(y))e^{ik(x-Ct)}$ where $C=\omega/k$ is the phase speed of the wave. The unstable modes are characterized by a non-vanishing imaginary part of $C=C_r+iC_i$ k is assumed, without loss of generality to be real positive.

Differentiating (3) with respect to y and eliminating $\frac{\partial}{\partial y}(\bar{h}v')$ between (3) and (4) we get with the aid of (1) and (2)

$$u + \frac{\partial h}{\partial y} - \left(h + \frac{\partial u}{\partial y}\right)(c - \bar{u}(y)) = 0 \tag{6}$$

When v from (5) is used in (3) we get

$$h = -\frac{\bar{h}\frac{\partial u}{\partial y} + k^2(\bar{u}(y) - c)u}{\bar{h} + k^2} \tag{7}$$

Before obtaining an ordinary equation for u we draw some qualitative conclusions on the behavior of the non-trivial solution in the longwave limit. We note that in the limit $K^2 \to 0$ equation (7) implies $h = -\frac{\partial u}{\partial y}$, while equation (6) yields $u = -\frac{\partial h}{\partial y}$ for bounded C. The resulting u, h which are regular at $y=-\infty$ are $u=Ae^y=-h$ and (5) implies that $v \sim k$. Therefore, in the longwave limit, when C is bounded, the motion is downstream $(v/u \sim K,\ K \to 0)$. For finite $\omega = kC$ (3) implies in the longwave limit $-i\omega u = \bar{h}v$ and near the free streamline u must vanish i.e. the motion is primarily across stream. For finite k, (7) implies $h(0)=-u(0).(1-C)$ and v in (3) is therefore regular at the free streamline.

Equation (7) is substituted in equation (6) to obtain a second order equation for u. The details of the algebraic manipulation can be found in Paldor (1982) and the result of the substitution is

$$\begin{aligned} 0 = {} & \frac{\partial^2 u}{\partial y^2}\left[\bar{h}(\bar{h}+K^2)\right] - \frac{\partial u}{\partial y}\left[\bar{u}K^2\right] \\ & - u\left[(\bar{h}+K^2)(\bar{h}+K^2-\bar{u}K^2) - \bar{u}K^2(\bar{u}-c) - K^2(\bar{h}+K^2)(\bar{u}-c)^2\right] \end{aligned} \qquad (8)$$

The problem is to compute C(k) and to find if $C_i > 0$ for any regular wave u(y) which solves (8).

In order to simplify the analysis we use the transformation

$$Z(Y) = \bar{h}(Y) = 1 - e^{Y} \qquad \text{i.e.} \qquad \bar{u} = 1 - Z$$

$$\text{and} \qquad \frac{\partial}{\partial Y} = -(1-Z)\frac{\partial}{\partial Z} \ ; \quad \frac{\partial^2}{\partial y^2} = (1-Z)^2\frac{\partial^2}{\partial Z^2} - (1-Z)\frac{\partial}{\partial Z}$$

When we define: $\Phi(Z(y)) = u(Y)$

we get from (8)

$$\begin{aligned} 0 = {} & \frac{\partial^2 \Phi}{\partial Z^2}\left[Z(1-Z)^2(Z+K^2)\right] + \frac{\partial \Phi}{\partial Z}\left[Z(Z-1)(Z+K^2) + K^2(1-Z)^2\right] \\ & + \Phi\left[K^2(1-Z)(1-Z-c) + K^2(Z+K^2)(1-Z-c)^2 - Z(1+K^2)(Z+K^2)\right] \end{aligned} \qquad (9)$$

which is simpler than (8) because the coefficients are algebraic.

For real k equation (9) has two regular singular points Z=0,1 (corresponding to the free streamline and infinity respectively). About each of these singular points we can find a regular solution in terms of a Frobenius series (see Bender and Orzag, 1978), the radius of convergence of which, is not greater than the distance between the singularities.

By multiplying (9) with some function F(Z) it may be converted to the Sturm-Liouville form

$$\frac{\partial}{\partial Z}\left(P\frac{\partial \phi}{\partial Z}\right)+\phi\left(Q+\gamma R_1+\gamma^2 R_2\right)=0 \qquad (10)$$

where

$$\gamma = 1-c = \gamma_r + i\gamma_i$$

Since the coefficients of $\frac{\partial^2\phi}{\partial Z^2}$ and $\frac{\partial \phi}{\partial Z}$ must be proportional in (10) and (9), the function P(Z) in (10) is determined by

$$\frac{\frac{\partial P(Z)}{\partial Z}}{P(Z)} = \frac{Z(Z-1)(Z+K^2)+K^2(1-Z)^2}{Z(1-Z)^2(Z+K^2)} = \frac{1}{Z}-\frac{1}{1-Z}-\frac{1}{Z+K^2}$$

or

$$\ln P(Z) = \ln\frac{Z(1-Z)}{Z+K^2}$$

i.e.

$$P(Z) = \frac{Z(1-Z)}{Z+K^2}$$

Therefore, the proper multiplier F(Z) of (9) is determined by the ratio of the coefficients of $\frac{\partial^2\phi}{\partial Z^2}$ in (10) and (9) i.e.

$$F(Z) = \frac{P(Z)}{Z(1-Z)^2(Z+K^2)} = \frac{1}{(1-Z)(Z+K^2)^2}$$

The other coefficients of (10) are

$$Q(Z) = -Z K^2\left[(Z+K^2)\left(1+\frac{1}{K^2}\right)+(1-Z)-Z(Z+K^2)\right]\cdot F(Z)$$

$$R_1(Z) = K^2\left[(1-Z)-2Z(Z+K^2)\right]\cdot F(Z)$$

$$R_2(Z) = K^2\left[Z+K^2\right]\cdot F(Z)$$

The transformed eigenfunction equation (10) is suitable for the application of the Rayleigh integral technique which has been used to obtain important qualitative properties of stability problems. We thus multiply (10) by ϕ^* (the complex conjugate of ϕ), and integrate the resulting equation from Z=0 to Z=1. The two equations for the real and imaginary parts are

$$\gamma_i\int_0^1|\phi(Z)|^2 R_1\,dZ + 2\gamma_i\gamma_r\int_0^1|\phi(Z)|^2 R_2\,dZ = 0 \qquad (11)$$

$$-\int_0^1 P\left|\frac{\partial\phi}{\partial Z}\right|^2 dZ + \int_0^1|\phi(Z)|^2\left[Q+\gamma_r R_1+(\gamma_r^2-\gamma_i^2)R_2\right]dZ = 0 \qquad (12)$$

The only boundary condition used here is the regularity of ϕ.

Equation (11) is obviously satisfied when $\gamma_i = 0$. Assuming the existence of unstable modes we let $\gamma_i \neq 0$ in which case (11) becomes

$$\int_0^1|\phi(Z)|^2 R_1\,dZ = -2\gamma_r\int_0^1|\phi(Z)|^2 R_2\,dZ \qquad (13)$$

When (13) is used in (12) we get

$$-\int_0^1 P\left|\frac{\partial\phi}{\partial z}\right|^2 dz + \int_0^1 |\phi(z)|^2 Q\,dz - (\gamma_r^2+\gamma_i^2)\int_0^1 |\phi(z)|^2 R_2\,dz = 0 \qquad (14)$$

The first and third terms in (14) are negative since P ~~is~~ and R_2 are positive for all $0 < Z \leq 1$. To show that the second (Q) term in (14) is negative we write Q as:

$$Q(Z) = -ZK^2\left[(1-Z) + (Z+K^2)(1-Z) + (Z+K^2)/K^2\right] \cdot F(Z)$$

Each of the terms in the square brackets is non-negative and therefore Q(Z) is not positive for $0 \leq Z \leq 1$. This proves that the second term in (14) is also negative for non trivial eigenfunctions $(\phi(z) \neq 0)$. The assumption $\gamma_i \neq 0$ therefore leads to a contradiction, and thus we have shown that the eigenvalues of (10) are all real. The single layer unbounded surface front of uniform potential vorticity shown in figure 1 is therefore stable.

III. STABLE TRAPPED MODES

As was mentioned in the preceding chapter, equation (9) has two regular singular points at Z=0 and Z=1. The regular solution $\phi_L(Z)$ about Z=0, and the regular solution $\phi_R(1-Z)$ about Z=1 can be expressed in terms of a Frobenius series in Z and 1-Z respectively. The radius of convergence of each of these series is not greater than the distance to the other singular point, and the series are asymptotic to the solution in the vicinity of the singularities. An eigenvalue equation which determines C(k) will be constructed by requiring $\phi_R(1-Z)$ to be asymptotic to $\phi_L(Z)$ as $Z \to 0$, and as a check we will invert the procedure by requiring $\phi_L(Z)$ to be asymptotic to $\phi_R(1-Z)$ as $Z \to 1$. As an additional check we will integrate equation (8) numerically from Y=-8 ("infinity") to $Y=-10^{-5}$ and compare the resulting eigenfunction to the one obtained by the series solution. We start by constructing the Frobenius series solutions $\phi_L(Z)$ and $\phi_R(1-Z)$ (see for example Bender and Orzag 1978).

A. The solution near the free stramline.

In the vicinity of the singular point Z=0 equation (9) can be written as

$$\phi_L'' + \phi_L' \frac{G(Z)}{Z} + \phi_L \frac{q(Z)}{Z^2} = 0 \tag{15}$$

where the prime denotes differentiation with respect to Z and where the functions G(Z), q(Z) are

$$G(Z) = -\frac{Z(Z+K^2)+K^2(Z-1)}{(1-Z)(Z+K^2)} = -\frac{Z}{1-Z} + \frac{1}{1+Z/K^2}$$

$$q(Z) = \frac{ZK^2(1-Z-C)}{(1-Z)(Z+K^2)} + \frac{ZK^2(1-Z-C)^2}{(1-Z)^2} - \frac{Z^2(1+K^2)}{(1-Z)^2}$$

$$= \frac{CK^2}{1+K^2}\left(-\frac{1}{1-Z} + \frac{1}{1+Z/K^2}\right) + \frac{ZK^2(1-Z-C)^2 - Z^2(1+K^2)}{(1-Z)^2}$$

In order to develop the Frobenius series (16) for the solution $\phi_\ell(z)$ we have to develop the power series $G(z)=\sum_{n=0}^{\infty} g_n z^n ; q(z)=\sum_{n=0}^{\infty} q_n z^n$. Since the power series expansion for $\frac{1}{1+z/K^2}$ converges only for $\frac{z}{K^2}<1$ it is clear that the power series expansion of G(Z) and q(Z) will converge at $0\leq z<1$ only for $K^2\geq 1$. The importance of the Frobenius series (16) is therefore that: first it yields the frontal boundary condition at Z=0, and second it can be used to check the eigenvalues (but not the eigenfunctions) we derive in the next section.

Substituting the Frobenius series

$$\phi_\ell(z)=z^{\gamma}\sum_{n=0}^{\infty} a_n z^n \qquad a_0 \neq 0 \qquad (16)$$

in (15) we first obtain the indicial equation $\gamma^2=0$. Therefore one solution has the form (16) (with $\gamma=0$) while the second solution has a logarithmic singularity at Z=0.

Furthermore the coefficients $\{a_n\}$ in (16) can be derived recursively by assuming, without any loss of generality, $a_0=1$. The algebraic expression for the general recursion relation of $\{a_n\}$ is

$$a_n=\frac{-1}{n^2}\sum_{\ell=0}^{n-1} a_\ell\left(\ell g_{n-\ell}+q_{n-\ell}\right) \qquad n\geq 1$$

where g_n, q_n are the power series coefficients of G(Z), and q(Z) respectively. We note that $\phi_\ell(0)=0=a_0$ implies, according to the recursion relation, $a_n=0$, $n\geq 1$ and we therefore conclude that all the eigenfunctions have a finite diplacement of the free streamline. Moreover, identifying $a_0=\phi(0)$; $a_1=\frac{\partial\phi(0)}{\partial z}$ the recursion relation $a_1=-q_1 a_0$ yields the frontal boundary condition at Z=0 in terms of q_1 (the coefficient of Z in the power series expansion of q(Z)) namely:

$$\frac{\partial \phi(0)}{\partial Z} = -\left[1 - C + K^2(1-C)^2\right]\phi(0) \tag{17}$$

We shall see shortly that the regular solution at Z=1 is zero there. Hence the proper boundary condition for these trapped modes is $\phi(1)=0$. When (16) was summed at Z=1 it was found to diverge there. Nevertheless we were able to determine the eigenvalues C(k) by fixing k, and finding the value(s) of C at which $\phi_L(1)=\sum_{n=0}^{N} a_n$ changes sign. The eigenvalues determined in this way were independent of the number of terms (N) taken in (16) when N was large (N>15). Direct summation of (16) does not provide any information on the eigenfunction away from Z=0 and we turn now to the solution near Z=1.

B. The Solution at Infinity.

In order to construct the solution near Z=1 we repeat the same procedure used to construct ϕ_L, thus we define $1-Z=\delta$ and we rewrite (9) in the form

$$\phi_R'' + \phi_R' \frac{R(\delta)}{\delta} + \phi_R \frac{S(\delta)}{\delta^2} = 0 \tag{18}$$

where the prime denotes differentiation with respect to δ $\left(\frac{\partial}{\partial \delta} = -\frac{\partial}{\partial Z}\right)$ and where the functions $R(\delta)$, $S(\delta)$ are

$$R(\delta) = 1 - \frac{\delta K^2}{(1-\delta)(1+K^2-\delta)} = 1 - \frac{1}{1-\delta} + \frac{1}{1-\delta/(1+K^2)}$$

$$S(\delta) = -(1+K^2) + \frac{\delta K^2(\delta - C)}{(1-\delta)(1+K^2-\delta)} + \frac{K^2(\delta-C)^2}{1-\delta}$$

$$= -(1+K^2) + \delta\left[\frac{1-C}{1-\delta} - \frac{1+K^2-C}{1+K^2}\cdot\frac{1}{1-\delta/(1+K^2)}\right] + \frac{K^2(\delta-C)^2}{1-\delta}$$

We now use the power series expansions

$$\frac{1}{1-\delta} = \sum_{n=0}^{\infty} \delta^n, \quad \delta < 1 \quad ; \quad \frac{1}{1-\delta/(1+K^2)} = \sum_{n=0}^{\infty}\left(\frac{\delta}{1+K^2}\right)^n, \quad \frac{\delta}{1+K^2} < 1$$

in order to develop the power series expansions

$$R(\delta)=\sum_{n=0}^{\infty} R_n \delta^n \quad ; \qquad S(\delta)=\sum_{n=0}^{\infty} S_n \delta^n$$

The result is:

$$R_n=\begin{cases} 1 & n=0 \\ -1+\left(\frac{1}{1+K^2}\right)^n & n\geqslant 1 \end{cases}$$

$$S_n=\begin{cases} 1-K^2(1-c^2) & n=0 \\ K^2 c\left(c-2-\frac{1}{1+K^2}\right) & n=1 \\ (1-c)(1+K^2(1-c))-\frac{1+K^2-c}{(1+K^2)^n} & n\geqslant 2 \end{cases}$$

The series $\sum_{n=0}^{\infty} R_n \delta^n$ and $\sum_{n=0}^{\infty} S_n \delta^n$ converge for $0\leq\delta<1$, and therefore (19) will converge at all $0\leq\delta<1$ regardless of k. Numerical summation of (19) at $\delta=1$ shows that it converges there too. The solution of (18), ϕ_R, can be written as

$$\phi_R(\delta)=\delta^\beta \sum_{n=0}^{\infty} b_n \delta^n=(1-Z)^\beta \sum_{n=0}^{\infty} b_n (1-Z)^n \;, \quad b_0\neq 0 \quad (19)$$

By direct substitution of (19) in (18) we first obtain the indicial equation for the index β

$$\beta^2=1+K^2(1-c^2)$$

and the recursion relation for the coefficients $\{b_\circ\}$ is

$$b_n=\frac{-1}{n(n+2\beta)}\sum_{\ell=0}^{n-1} b_\ell\left[(\beta+\ell)R_{n-\ell}+S_{n-\ell}\right] \qquad n\geqslant 1$$

For real $\omega^2=K^2c^2<1+K^2$ only the solution with the index $\beta=+(1+K^2-\omega^2)^{1/2}$ is regular at Z=1 hence the boundary condition there is $\phi(Z=1)=0$. When $\omega^2>1+K^2$, β is imaginary and there are two oscillatory solutions at infinity (Z=1). We defer a discussion of the latter case to chapter IV and turn to the trapped modes characterized by real β. When (19) is used in (17) the latter becomes

$$\sum_{n=0}^{\infty} b_n(\beta+n-q_1)=0 \tag{20}$$

Equation (20) constitutes the eigenvalue equation which determines C(k). It converges rapidly on account of the convergence of (19).

C. Eigenvalues and Eigenfunctions

The dispersion relation ω(k) (Figure 2) was determined numerically by sweeping for fixed k, over $-(1+k^2)^{1/2}<\omega<(1+k^2)^{1/2}$ to find the ω(k) which satisfy the eigenvalue equation (20). In the regions $\omega^2>1+k^2$ there is a continuous spectrum which is discussed in the next chapter. Since (20) converges rapidly only 20 terms were sufficient and subsequent summation of 80 and 200 terms yielded indistinguishable results. The eigenfunctions of the different modes for k=3 shown in figure 3 were computed with 20 terms from (19). The curve shown in figure 3a was reproduced with 80 and 200 terms without any discernible difference.

fig

fig

The behavior of the eigenfunctions of figure 3 (found by summing (19) numerically) near the boundaries Z=0, Z=1 can be derived analytically. In the vicinity of Z=0, (17) implies that $\frac{\partial\phi(z)}{\partial z}$ and $\phi(z)$ have opposite signs provided $q_1 > 0$. From figure 2 (we could also derive this result analytically from eq. (12)) it is clear that all eigenvalues satisfy $C(k)=\frac{\omega(k)}{k}<1$ and this assures that $q_1 > 0$ for all the eigenvalues. Thus if $\phi(0)$ is positive the derivative is negative and vice versa. There is no solution with $\phi(0)=0$ since if $\phi(0)=0=a_0$ then $a_n=0,\ n\geq 1$ and hence $\phi(z)\equiv 0$. Near Z=1 on the other hand

$$\phi(z)\sim(1-z)^{\beta} \qquad ,z\to 1$$

and the derivative satisfies there

$$\frac{\partial\phi}{\partial z}\sim-\beta(1-z)^{\beta-1} \qquad ,z\to 1$$

Hence all the eigenfunctions have a negative slope as $z \to 1$. All the eigenfunctions shown in figure 3 satisfy these asymptotic behaviors near the boundaries.

D. The Longwave Limit.

Our objective in this section is to show that there are no more modes than given by the numerical summation of the series solution (20) (Fig. 2) and to compute explicit asymptotic expressions for the eigenfunctions in the long-wave limit. We thus let $c = c_0 k^\alpha$ and expand ϕ_R in a matching power series in k using the asymptotic form of the recursion relation for $\{b_n\}$. The resulting highest order term in (20) is then used to solve for C_0 for the various α. We first note that on physical grounds we have to require $\alpha \geq -1$ since otherwise $\omega = kc = c_0 k^{1+\alpha}$ is infinite in the limit $k \to 0$. When $\alpha > -1$ we let $k \to 0$ and get the following asymptotic expressions for R_n, S_n (which comprise the leading terms in b_n)

$$R_n \sim -n k^2 \qquad n \geq 1$$

$$S_n \sim \begin{cases} c k^2 (c-3) & n = 1 \\ k^2 (c^2 - c(n+2) + n), & n \geq 2 \end{cases}$$

For $\alpha > 0$, $kc = c_0 k^{1+\alpha}$ is of higher order than k and $(\beta - q_1)$ is $O(k^2, k^\alpha)$. The problem becomes tractable since $b_1 \sim R_1 + S_1 \sim k^2$ is of lower order (in k) than $b_n \sim R_n + S_n \sim c_0 k^{2+\alpha}$, $n > 1$ and therefore only the n=0, 1 terms in (20) have to summed in the equation of the leading order term.

The first three line of table 1 summarize the results of this range of α. Only when $\alpha = 2$ there exists a non-trivial solution for C_0 in $c = c_0 k^\alpha$ namely $c = \frac{k^2}{6}$. For any $\alpha > 0$, $\alpha \neq 2$ no such solution exists.

When $-1<\alpha\leq 0$, $k\zeta = c_0 k^{1+\alpha}$ is of lower order than k. Thus $b_n, n>0$ are all of order $k^{2(1+\alpha)}$ while b_0 is O(1). $(\beta - q_1)$, on the other hand, is $O(k^{\alpha}) \gg 1$ and therefore the leading order term on the left-hand side of (20) is just $b_0(\beta - q_1)$. The fourth line in table 1 summarizes this case [illegible]ows that in this range of α too there is no non-trivial solu[illegible]n [illegible] C_0.

The last case to consider is the most interesting and the most intri[illegible]ate one, namely $\alpha = -1$. This case corresponds to $\omega \simeq k\zeta = c_0$ and is expect[illegible] to yield the high frequency, longwave mode. Since $\alpha=-1$ we let [illegible]$= \frac{c_0}{k}$ and this implies $q_1 = -\frac{c_0}{k} + O(k)$ $k \to 0$. The recursion relation [illegible]or $\{b_n\}$ is:

$$b_n = \frac{-1}{n(n+2\beta)} \sum_{\ell=0}^{n-1} b_\ell \left[c_0^2 - k c_0 (n-\ell+2)\right] + O(k^2)$$

Therefore $b_n, n \geq 1$ is O(1) and the infinite series of (20) has to be summed. The value of β depends on C_0. For $c_0^2 > 1$, β is imaginary and there are no trapped modes (this corresponds to the shaded area in figure 2). When $C_0^2=1$ we get $\beta=k$ and

$$b_1 = b_0\left(-1 + k(2+3c_0)\right)$$

thus

$$b_0 + b_1 = b_0 k (2+3c_0)$$

Using mathematical induction it is easy to show that

$$b_n = -b_0 \frac{1+c_0}{n(n-1)} \cdot k + O(k^2) \qquad n \geq 2$$

Therefore

$$q_1 b_n = \frac{c_0(1+c_0)}{n(n-1)} b_0 + O(k) \qquad n \geq 2$$

while

$$q_1(b_0+b_1) = b_0 c_0 (2+3c_0) = b_0 (3c_0^2 + 2c_0)$$

The implication of this last estimate is that although q_1 is $O(1/k)$ the highest order term on the left- hand side of (20) is $O(1)$.

This $O(1)$ term in (20) satisfies

$$0 = q_1(b_0 + b_1) - b_0 + q_1 \sum_{n=2}^{\infty} b_n \quad + O(K)$$

and when the explicit expression for b_n, $n \geq 2$ is used we get for $b_0 = 1$

$$0 = -1 + (3c_0^2 + 2c_0) + c_0(1 + c_0) \sum_{n=2}^{\infty} \frac{1}{n(n-1)}$$

The infinite ("telescopic") series is easily summed by writing

$$\sum_{n=2}^{\infty} \frac{1}{n(n-1)} = -\sum_{n=2}^{\infty} \left(\frac{1}{n} - \frac{1}{n-1} \right) = -1$$

Therefore the equation for C_0 from the $O(1)$ term in (20) is

$$0 = 2c_0^2 + c_0 - 1 = (c_0 + 1)(2c_0 - 1)$$

The solution of this equation which also satisfies $c_0^2 = 1$ is $c_0 = -1$. It turns out that the "solubility" of the problem in this $c = \frac{-1}{K}$ case is due to the fact that b_n, $n \geq 2$ is $O(k^2)$ while $b_1 = -b_0(1+K)$ so that $b_0 + b_1 = -K b_0$.

Thus we have verified the two eigenvalues which were found numerically in the longwave limit of figure 2, namely: $\omega = \frac{K^3}{6}$ and $\omega = -1$. We are now in a position to get an explicit expression for the eigenfunctions using the highest order terms in (19). In the eigenfunction of the $\omega = \frac{K^3}{6}$ mode the only $O(1)$ terms is b_0 and therefore in this case

$$\phi_R \sim b_0(1 - z) \quad + O(K^2)$$

so that

$$u(y) = b_0 e^y \quad + O(K^2)$$

This is precisely the result we got from qualitative arguments following eq. (7). The $O(1)$ terms of the eigenfunction of the $\omega = -1$ mode involve only b_0 and b_1, since $b_n \sim K^2$, $n \geq 2$. Thus we get

$$\phi_R \sim (1-z)^{\kappa} b_o \left(z - \kappa(1-z)\right) + o(\kappa^2)$$

and therefore

$$u(y) = b_o e^{\kappa y}\left(1 - e^{y} - \kappa e^{y}\right) + o(\kappa^2)$$

$$= b_o e^{\kappa y}\left(1 - e^{y}\right) + o(\kappa)$$

From equations (7) and (3) we can calculate v(y) and the hodograph v(u) for the two modes. For the $\omega = \frac{\kappa^3}{6}$ mode, $u(y) = b_o e^{y} + o(\kappa^2)$ and equation (7) implies $h(y) = -b_o e^{y} + o(\kappa^2)$. Since $\frac{\partial}{\partial t} \equiv -i\kappa c \sim \kappa^3$ equation (3) implies

$$(1-e^{y})v = b_o(-i\kappa)(1-e^{y})u + o(\kappa^3)$$

so that $v = -iku + o(k^3)$.

Therefore the hodograph is the same ellipse at all y with motion being essentially longitudinal and the sense of rotation is counter clockwise in the northern hemisphere (where f which is the scaling of t is positive).

For the $\omega = -1$ mode $\frac{\partial}{\partial t} \equiv -i\kappa c = i$ and equation (3) implies

$$(1-e^{y})v = iu + o(\kappa)$$

Therefore although u diminishes at the free streamline $v = ib_o e^{\kappa y}$, is O(1) everywhere. Thus we see that the motion is transverse near the free streamline while far away from it $v = iu$ and the motion is circular. These results are shown in figure 4.

The $\omega = -1$ mode does not exist for infinitely long waves since when $k=0$, $v = ib_o$ and requiring $v(-\infty) = 0$ we get $b_o = 0$ which implies $\phi_R \equiv 0$. This result is generalized in Appendix A where we show that oscillations

AD-A126 396 FINAL TECHNICAL REPORT ON CONTRACT N00014-81-C-0010 1 OCTOBER 1980-30 SEPTEMBER 1982(U) WOODS HOLE OCEANOGRAPHIC INSTITUTION MA J A WHITEHEAD MAR 83 2/3

UNCLASSIFIED WHOI-83-11 N00014-81-C-0010 F/G 8/3 NL

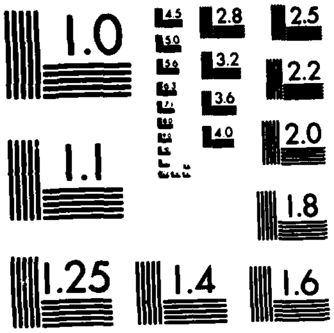
1.0
4.5
2.8
2.5
5.0
3.2
2.2
5.6
3.6
6.3
7.1
4.0
2.0
8.0
1.1
1.8
1.25
1.4
1.6

MICROCOPY RESOLUTION TEST CHART
NATIONAL BUREAU OF STANDARDS-1963-A

at the inertial frequency are impossible when k=0 regardless of the potential vorticity of the basic state.

E. Additional Checks.

Although the analytical considerations in the previous section and in the end of section C agreed with the numerical results of section C we carried out additional numerical checks.

The eigenvalues $\omega(k)$ (Fig. 2) were checked by summing

$$\phi_L(Z=1)=\sum_{n=0}^{N} a_n(K,\omega)$$

with $\omega \approx \omega(k)$. The result was that $\phi_L(Z=1)$ changed sign at $\omega=\omega(k)$ and in spite of the divergence of (16) at Z=1 similar results were encountered when the number of terms summed (N) was 20, 50, or 80.

As a check on the eigenfunctions (Fig. 3) we integrated eq. (8) numerically from y=-8 ("infinity") to $Y=-10^{-5}$ with $C(k)=\omega(k)/k$ using a fourth order Runge-Kutta procedure. The resulting eigenfunctions were indistinguishable from those of Fig. 3 and the boundary conditions were satisfied.

IV FREE WAVES AND THEIR REFLECTION

When $\omega^2 > 1+K^2$ we have already noted that there is a continuum of free modes since β becomes imaginary. Away from the front (i.e. at $Z \sim 1$) there are, in this case, two oscillatory, linearly independent solutions and the general solution can be written as

$$\phi_R = \phi_R^+ + \gamma \phi_R^-$$

where

$$\phi_R^\pm = (1-Z)^{\pm i\bar{\beta}} \cdot \sum_{n=0}^{\infty} b_n^\pm (1-Z)^n = e^{\pm i\bar{\beta} y} \sum_{n=0}^{\infty} b_n^\pm e^{ny} \qquad (21)$$

$$b_0^\pm = 1$$

and where $\bar{\beta} = (\omega^2 - (1+K^2))^{1/2}$ is real.

The function ϕ_R^+ represents a wave propagating toward the front from $y = -\infty$ whereas ϕ_R^- is the reflected wave which propagates away from the front. γ is the reflection coefficient and if $|\gamma| = 1$ then $|\phi_R^+| = |\phi_R^-|$ and the wave is reflected by the front without any change in the amplitude.

If $|\gamma| \neq 1$ the amplitude of the reflected wave is different from that of the incident wave. This indicates that energy was transferred between the free waves and the mean flow and in this case the kinetic energy of the front will increase (decrease) provided $\gamma < 1$ $(\gamma > 1)$

We notice that the case $|\gamma| = 0$ $(|\gamma| = \infty)$ is impossible since then $\phi_R = \phi_R^+$ $(\phi_R = \phi_R^-)$ is complex but ϕ_L, which represents the solution at $0 \le Z \le Z_0 < \min(1, K^2)$, is real and (the complex) ϕ_R cannot be matched with (the real) ϕ_L in that region. Only when ϕ_R is the sum of two complex functions can it yield a real function in the sub-interval where ϕ_L is the solution.

The boundary condition (20) implies

$$\sum_{n=0}^{\infty}\left[b_n^+(n+i\bar{\beta}-q_1)+\gamma b_n^-(n-i\bar{\beta}-q_1)\right]=0$$

or

$$\gamma=-\frac{\sum_{n=0}^{\infty} b_n^+(n+i\bar{\beta}-q_1)}{\sum_{n=0}^{\infty} b_n^-(n-i\bar{\beta}-q_1)} \qquad (22)$$

The coefficients $b_n^\pm$ satisfy the recursion relation:

$$b_n^\pm=\frac{-1}{n(n\pm 2i\bar{\beta})}\sum_{l=0}^{n-1} b_l^\pm\left[(l\pm i\bar{\beta})R_{n-l}+S_{n-l}\right] \qquad n\geq 1$$

Since R_n, S_n are all real it is easy to show (by mathematical induction, for example) that b_n^+ is the complex conjugate of b_n^-. Therefore in (22) the nth term in the numerator is the complex conjugate of the nth term in the denominator and the implication is that $|\gamma|=1$ so that the front does not exchange energy with the free waves and no overreflection occurs.

Moreover since $|\gamma|=1$ we can let $\gamma=e^{i\theta}$ and then (21) implies

$$\phi_R=e^{i\frac{\theta}{2}}\left[e^{-i\frac{\theta}{2}}\phi_R^+ + e^{i\frac{\theta}{2}}\phi_R^-\right]=2e^{i\frac{\theta}{2}}Re\left[e^{-i\frac{\theta}{2}}\phi_R^+\right]$$

Therefore up to a trivial multiplicative factor, ϕ_R is real and this is consistent with ϕ_L being real except perhaps for the multiplicative factor a_0.

V. DISCUSSION

The unbounded front of figure 1 bears a strong similarity to (say) the 15°C isotherm of the Gulf Stream (Watts and Johns, 1982), but numerous observations on the occurrence of eddies and meanders indicate the highly unstable nature of the Gulf Stream (Lai and Richardson, 1979). Since the uniform potential vorticity front of figure 1 has been shown to be stable (chapter II) the model cannot explain the observations and we are led to the conclusion that even a small (but finite) gradient of potential vorticity is of utmost dynamical significance. The effect of a gradient of the potential vorticity can be studied by either adding it to the upper layer or coupling the two layers. However, the present study shows that without it, a geostrophic front like the Gulf Stream will be linearly stable. This conclusion cannot be inferred from the existing quasi- geostrophic theory due to the strong surface signature of the Gulf Stream (Cheney and Marsh, 1981) and the inapplicability of this theory to surface fronts.

The near inertial longwave stable mode of the unbounded front provides an explanation for several recent observations of the enhancement and the establishment of the near inertial peak in oceanic spectra. The first of these observations is that of Fu (1981) who found an increase of 4dB in the energy of the near inertial peak under the Gulf Stream over that of the Mid Ocean peak. Although this measurement pertains to the lower layer which was neglected in our model we expect that the oscillations of the interface will induce the same oscillations in the lower layer. The coupling between the oscillations in the two layers is beyond the scope of this work. The second observation is that of Mayer et al.

(1979) on the seasonal establishment and disappearance of that peak on the Middle Atlantic Shelf. Both observations cannot be explained in terms of a wind generated phenomenon (Stern, 1977; Pollard and Willard, 1979), the first (Fu, 1981) because of its depth (4000m) and the second because the peak disappears in the winter when the winds are strong and is quite pronounced in the summer when the winds are calm. The hydrography of the water column, however, suggests a strong correlation with a sharp front. In the case of Fu (1981) the front is the Gulf Stream and in Mayer et al. (1979) the front is associated with the freshwater runoff into the shelf water.

An observation even more supportive of this mode is that of Kunze and Sanford (1981) on the North Pacific Subtropical Front. Not only does the energy of the near-inertial peak increase by a factor of 4 in their observation but the increase is observed only in the clockwise (anti-cyclonic) component of the horizontal velocity profile. This is in perfect agreement with the inertial mode of section III and figure 4.

This longwave mode might also be relevant to the slight shift (a few percent) in the frequency of the near inertial peak observed in numerous oceanic experiments (for example Fu, 1981; Kundu, 1976; Gonella, 1971; Perkins, 1972; Webster, 1968; Day and Webster, 1965). For small but finite k the frequency of this longwave mode is slightly above the inertial frequency with a maximum shift of 2.2% ($\omega = \overset{1.022f}{\cancel{1.022f}}$) at k=1. Other theories provide an explanation for this shift in the presence of wind (Stern, 1977; Pollard, 1970) or randomly distributed sources (Munk and Phillips, 1968). Our model indicates that a sharp horizontal temperature gradient can also cause the inertial peak to be shifted.[9] The proximity of this long inertial trapped wave to the shaded region of Fig. 2 provides a possible mechanism for its excitation by the free waves. The suggestion is that the front acts like a one-way mirror whereby long free waves with frequency slightly above the inertial which travel across the front excite the inertial trapped mode. The details of this excitation involve a wave-wave interaction theory which is beyond the scope of the present study.

The low frequency long trapped $(\omega \sim \frac{K^3}{6}, K \to 0)$ indicates that an increase in the low frequency energy should be observed in the vicinity of fronts. We are not aware of any such observation. One possible explanation for this, is that this mode is far from the boundary $\omega^2 \approx 1 + K^2$ and thus cannot be easily excited by free waves having only slightly different frequencies.

Another explanation is that the neglected gradient of potential vorticity, as well as, a finite depth of the lower layer, will overwhelm the slow, low frequency mode but will have little effect on the fast inertial mode. This slow mode $C \sim K^2$ is expected to become unstable when the potential vorticity is not uniform and the waves are finite but long (k is small but finite). The inertial mode propagates too fast and a small gradient of potential vorticity is expected merely to alter the (real) phase speed.

VI CONCLUSIONS

A. An unbounded single layer geostrophic front of uniform potential vorticity is stable at all wavelengths.

B. An inertial long trapped mode exists on such a front and can easily be excited by the free inertial waves.

C. For small but finite k the frequency of this trapped mode is slightly above the inertial frequency.

D. Trapped waves of finite frequency cannot exist on the unbounded front when the wavenumber is zero regardless of the mean potential vorticity.

APPENDIX A

The result of chapter III that the inertial mode of the unbounded surface front ceases to exist for infinitely long waves is shown in this appendix to be of a more general applicability. We will show that infinitely long trapped inertial waves cannot exist on a geostrophic front regardless of the mean potential vorticity.

Setting $\frac{\partial}{\partial x} = ik = 0$ and following the geometry and scaling of chapter II the x and y momentum equations and the continuity equation of the upper layer are:

$$\frac{\partial u}{\partial t} + v\frac{\partial u}{\partial y} - v = 0 \tag{A1}$$

$$\frac{\partial v}{\partial t} + v\frac{\partial v}{\partial y} + u = -\frac{\partial h}{\partial y} \tag{A2}$$

$$\frac{\partial h}{\partial t} + \frac{\partial}{\partial y}(hv) = 0 \tag{A3}$$

The basic (mean) state is assumed to be in geostrophic balance

$$\bar{u} = -\frac{\partial \bar{h}}{\partial y} \tag{A4}$$

When the mean and perturbations are separated $u = \bar{u} + u'$; $h = \bar{h} + h'$ and when we set $\frac{\partial}{\partial t} = i\omega$ the linearization of equations (A1)-(A2) yields

$$i\omega u' = v\left(1 - \frac{\partial \bar{u}}{\partial y}\right) = v'\left(1 + \frac{\partial^2 \bar{h}}{\partial y^2}\right) \tag{A5}$$

$$i\omega v' + u' + \frac{\partial h'}{\partial Y} = 0 \qquad \text{(A6)}$$

$$i\omega h' + \frac{\partial}{\partial Y}(\bar{h}\, v) = 0 \qquad \text{(A7)}$$

where (A4) has been used in the second eq. of (A5).

When (A5) and (A7) are used to replace u' and $\frac{\partial h'}{\partial Y}$ in (A6), respectively, the result is

$$-\omega^2 v' + v'\left(1 + \frac{\partial^2 \bar{h}}{\partial Y^2}\right) - \frac{\partial^2}{\partial Y^2}(\bar{h}\, v') = 0 \qquad \text{(A8)}$$

Carrying out the differentiation in (A8) and multiplying it by $\bar{h}$ we get

$$\bar{h}\frac{\partial^2 v'}{\partial Y^2} + 2\bar{h}\frac{\partial \bar{h}}{\partial Y}\cdot\frac{\partial v'}{\partial Y} + (\omega^2 - 1)v' = 0$$

or

$$\frac{\partial}{\partial Y}\left(\bar{h}^2 \frac{\partial v'}{\partial Y}\right) + (\omega^2 - 1)v' = 0 \qquad \text{(A9)}$$

We assume now that the front is either bounded by a second free streamline (where $\bar{h}$=o) or a wall (where v' vanishes) or that it extends to infinity (where v' vanishes for a trapped mode). Multiplying (A9) by v'^* and integrating the result between the boundaries of the front where the boundary term $\bar{h}^2 \frac{\partial v'}{\partial Y} v'^*$ vanishes we get

$$-\int \bar{h}^2 \left|\frac{\partial v'}{\partial Y}\right|^2 dY + \int \bar{h}\, |v'|^2 (\omega^2 - 1)\, dY = 0 \qquad \text{(A10)}$$

One trivial solution of (A10) is v'=o. This corresponds to solutions of (A5)-(A7) with either $\omega = 0$ in which case $u' = -\frac{\partial h'}{\partial Y}$ or u'=o=h'. Both represent trivial solutions: the former is merely a change in the undetermined amplitude of $\bar{u}$, $\bar{h}$ and the second is the zero solution.

Since the integrand in the first integral on the left- hand side of (A10) is positive, eq. (A10) can be satisfied only if $\omega^2 > 1$ while if $\omega^2 \leq 1$ there is no non-trivial solution.

For an unbounded front far away from the front $\bar{h}=1$ and in this region (A9) becomes

$$\frac{\partial^2 v'}{\partial y^2} + (\omega^2 - 1)\, v' = 0 \qquad \text{(A11)}$$

In order for the solution of (A11) to represent a trapped wave which decays at infinity $\omega^2 < 1$ has to be satisfied. but in this case (A10) cannot be satisfied. Therefore, on the unbounded front there is no trapped mode except for the trivial solution .

If the front is bounded by a wall or by a second free streamline, then there are non-trivial solutions with $\omega^2 > 1$.

ACKNOWLEDGEMENT

This work was done while the author was a student at the University of Rhode Island. The continuous interest and excellent guidance of Prof. Melvin E. Stern are gratefully acknowledged as is the financial support of the Office of Naval Research under contract No. N00014-81-C-0010 to U.R.I.

Legend to Tables and Figures

TABLE 1. The highest order term in (20) in the limit $K \to \infty$ and the resulting solution for C_o in $C = C_o k^{\alpha}$ for various α.

Figure 1. Unbounded surface front with uniform potential vorticity. The lower layer is assumed inifinitely deep and non interacting with the upper layer.

Figure 2. The dispersion relation for the unbounded front. The shaded region $\omega^2 > 1 + K^2$ represents a continuum of free waves whereas the various curves with $\omega^2 < 1 + K^2$ represent trapped waves. The $\omega = -1$ mode exists for $K > 0$ only.

Figure 3. The eigen-functions $\phi(z)$ representing the perturbation downstream velocity as a function of the depth of the upper layer, for k=3. The eigen-functions were produced by using the eigen-value indicated near each eigen-function and summing 20 terms in eq. 19.

Figure 4. The ellipse of rotation of the two longwave modes. Note that the inertial mode is rotating clockwise.

REFERENCES

Bender, M.L. and Orzag, S.A. Advanced Mathematical Methods for Scientists and Engineers. McGraw Hill, Inc. (1978).

Charney, J.G. "The Dynamics of Long Waves in a Baroclinic Westerly Current." J. Meteorol. 4, 135-163. (1947).

Cheney, R.E. and Marsh, J.G. "Seasat Altimeter Observations of Dynamic Topography in the Gulf Stream." J. Geophys. Res. 86, 473-486. (1981).

Day, C.G. and Webster, F. "Some Current Measurements in the Saragasso Sea." Deep-Sea Res. 12, 805-814. (1965).

Eady, E.T. "Long Waves and Cyclone Waves." Tellus 1, 33-52. (1949).

Fu, L.L. "Observations and Models of Inertial Waves in the Deep Ocean." Rev. Geophys. Space Phys. 19, 141-170. (1981).

Gonella, J. "A Local Study of Inertial Oscillation in the Upper Layer of the Ocean." Deep-Sea Res. 18, 775-788. (1971).

Griffiths, R.W., Killworth, P.D. and Stern, M.E. "A geostrophic Instability of Ocean Current." J. Fluid Mech. 343-377. (1982).

Legeckis, R. "A Survey of Worldwide Sea Surface Temperature Fronts Detected by Environmental Satellites." J. Geophys. Res. 83, 4501-4522. (1978).

Killworth, P.D. "Barotropic and Baroclinic Instability in Rotating Stratified Fluids." Dyn. Atmos. Oceans 4, 143-184. (1980).

Killworth, P.D. and Stern, M.E. "Instabilities on Density-Driven Boundary Currents and Fronts." Submitted to Phys. Fluids. (1982).

Kundu, P.K. "An Analysis of Inertial Oscillations Observed Near Oregon Coast." J. Phys. Ocenaogr. 6, 879-893. (1976).

Kunze, E. and Sanford, T.B. "Observations of Near-Inertial Waves in the North Pacific Subtropical Front." *Trans. Am. Geophys. Union* 62 (45), 914. (1981).

Lai, D.Y. and Richardson, P.L. "Distribution and Movement of Gulf Stram Rings." *J. Phys Oceanogr.* 7 (5), 670-683. (1979).

Luyten, J.R. and Robinson, A.R. "Transient Gulf Stream Meandering. Part II: Analysis via a Quasi-Geostrophic Time-Dependent Model." *J. Phys. Ocenaogr.* 4, 256-269. (1974).

Mayer, D.A., Hansen, D.V. and Ortman, D.A. "Long-Term Current and Temperature Observations on the Middle Atlantic Shelf." *J. Geophys. Res.* 84, 1776-1792. (1979).

McClimans, T.A. "Fronts in the Atmosphere and Oceans." Unpublished manuscript. (1979).

Mooers, C.N.K. "Several Effects of a Baroclinic Current on the Cross-Stream Propagation of Inertial Waves." *Geophys. Fluid Dyn.* 6, 245-275. (1975).

Munk, W. and Phillips, N. "Coherence and Band Structure of Inertial Motion in the Sea." *Rev. Geophys.* 6 (4), 447-472. (1968).

Orlanski, I. "Instability of Frontal Waves." *J. Atmos. Sci.* 25, 178-200. (1968).

Paldor, N. "Stable and unstable modes of Surface Fronts." Ph.D. dissertation - University of Rhode Island. (1982).

Pedlosky, J. "The Stability of Currents in the Atmosphere and the Ocean: Part I." *J. Atmos. Sci.* 21, 201-219. (1964).

Pedlosky, J. *Geophysical Fluid Dynamics.* Springer-Verlag, 624 pp. (1979).

Perkins, H. "Inertial Oscillation in the Mediterranean." Deep-Sea Res. 19, 289-296. (1972).

Pollard, R.T. "On the Generation by Wind of Inertial Waves in the Ocean." Deep-Sea Res. 17, 795-812. (1970).

Pollard, R.T. and Millard, R.C. "Comparison Between Observed and Simulated Wind-Generated Inertial Oscillations." Deep-Sea Res. 17, 813-821. (1970).

Stern, M.E. "Interaction of Inertia-Gravity Waves with the Wind." J. Mar. Res. 35 (3), 479-498. (1977).

Stern, M.E. "Geostrophic Fronts, Bores, Breaking and Blocking Waves." J. Fluid Mech. 99 (4), 687-703. (1980).

Stern, M.E., Whitehead, J., And Hua, B.L. "The Intrusion of a Density Current Along the Coast of a Rotating Fluid." Accepted for publication by J. Fluid Mech. (1982).

Stommel, H. The Gulf Stream. Second Edition. Cambridge University Press, 248 pp. (1966).

Watts, R.D. and Jones, W.E. "Gulf Stream meanders: Observations on Propagation and Growth." Accepted for publication by J. Geophys. Res. (1982).

Webster, F. "Observations of Inertial-Period Motions in the Deep Sea." Rev. Geophys. 6 (4), 473-490. (1968).

α	q_1	β	b_1	$b_n, n \geq 2$	Order of Leading term in (20)	Equation of Leading term in (20)	Solution for $C_o \neq 0$
$\alpha > 2$	$1 + k^2$	$1 + \frac{1}{2}k^2$	$\frac{k^2}{3}$	$k^2 + \alpha$	k^2	$0 = \frac{1}{2}k^2 + \frac{k^2}{3}$	-
$\alpha = 2$	$1+(1-C_o)k^2$	"	"	"	$k^2(=k^\alpha)$	$0=(-\frac{1}{2}+C_o)K^2+\frac{k^3}{3}$	$C_o=\frac{1}{6}$
$0 < \alpha < 2$	$1-C_o k^\alpha$	"	"	"	k^α	$0=C_o k^\alpha$	-
$-1 < \alpha \leq 0$	$1-C_o k^\alpha$	1	$k^{2(1+\alpha)}$	$k^{2(1+\alpha)}$	"	$0=-C_o k^\alpha$	-
$\left.\begin{array}{l}\alpha = -1 \\ C_o^2 = 1\end{array}\right\}$	$\frac{C_o}{k}$	k	$-1+k(2+3C_o)$	$-k\frac{1+C_o}{n(n-1)}$	1	$0=2C_o^2+C_o-1$	$C_o=-1$

Table 1

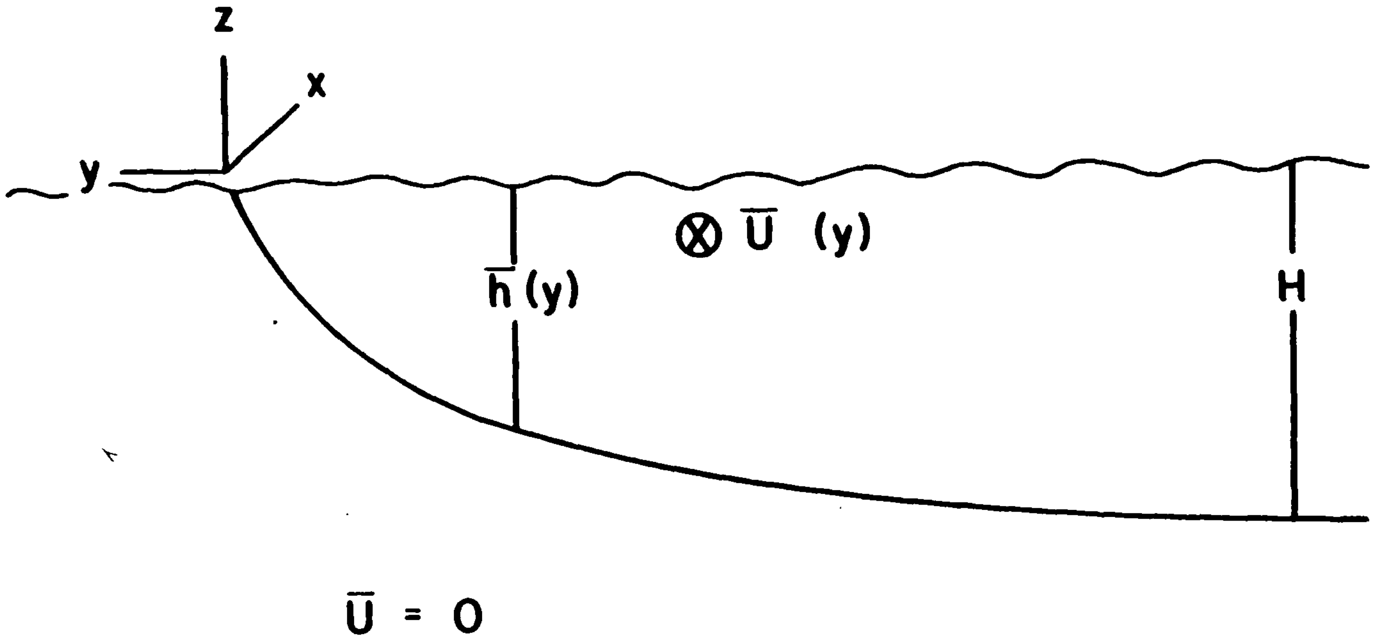
z
x
y
⊗ $\overline{U}$ (y)
$\overline{h}$ (y)
H
$\overline{U}$ = 0

21

2

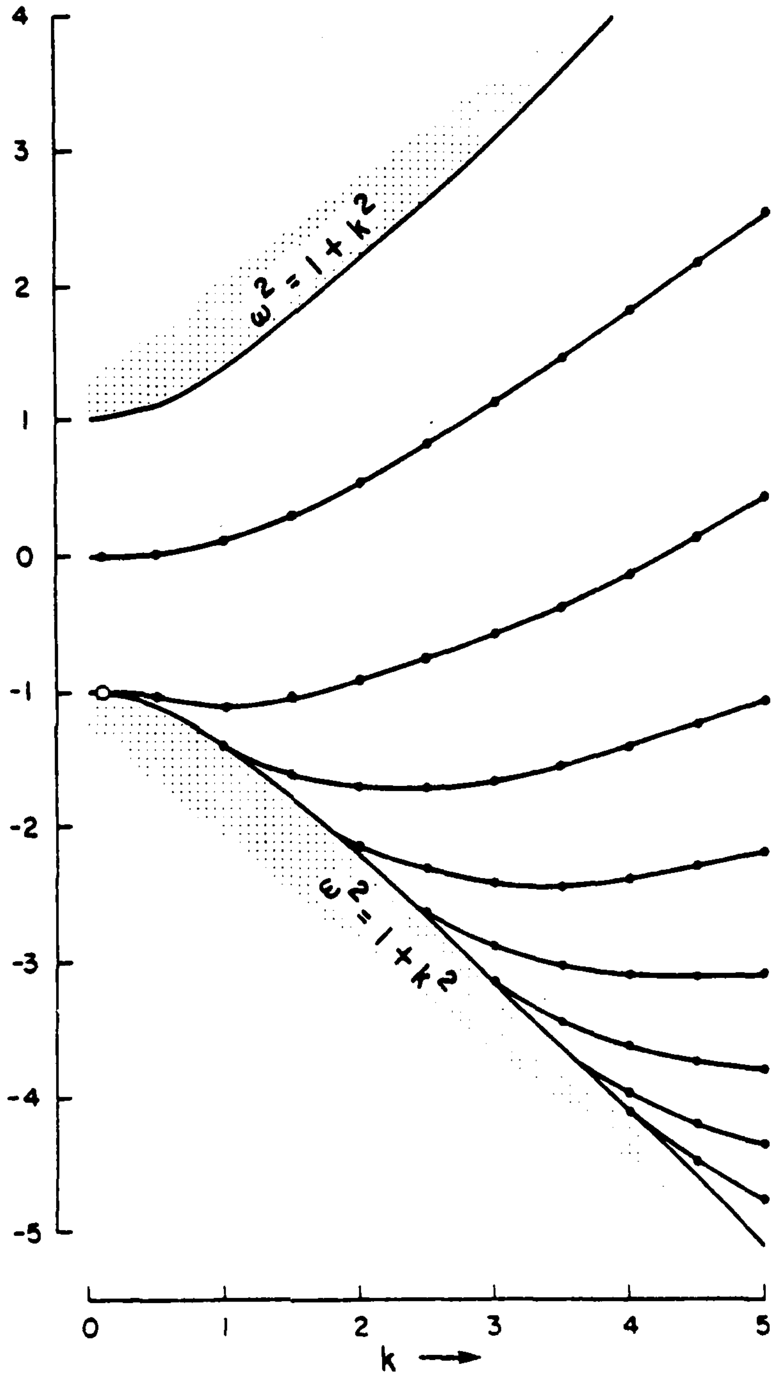

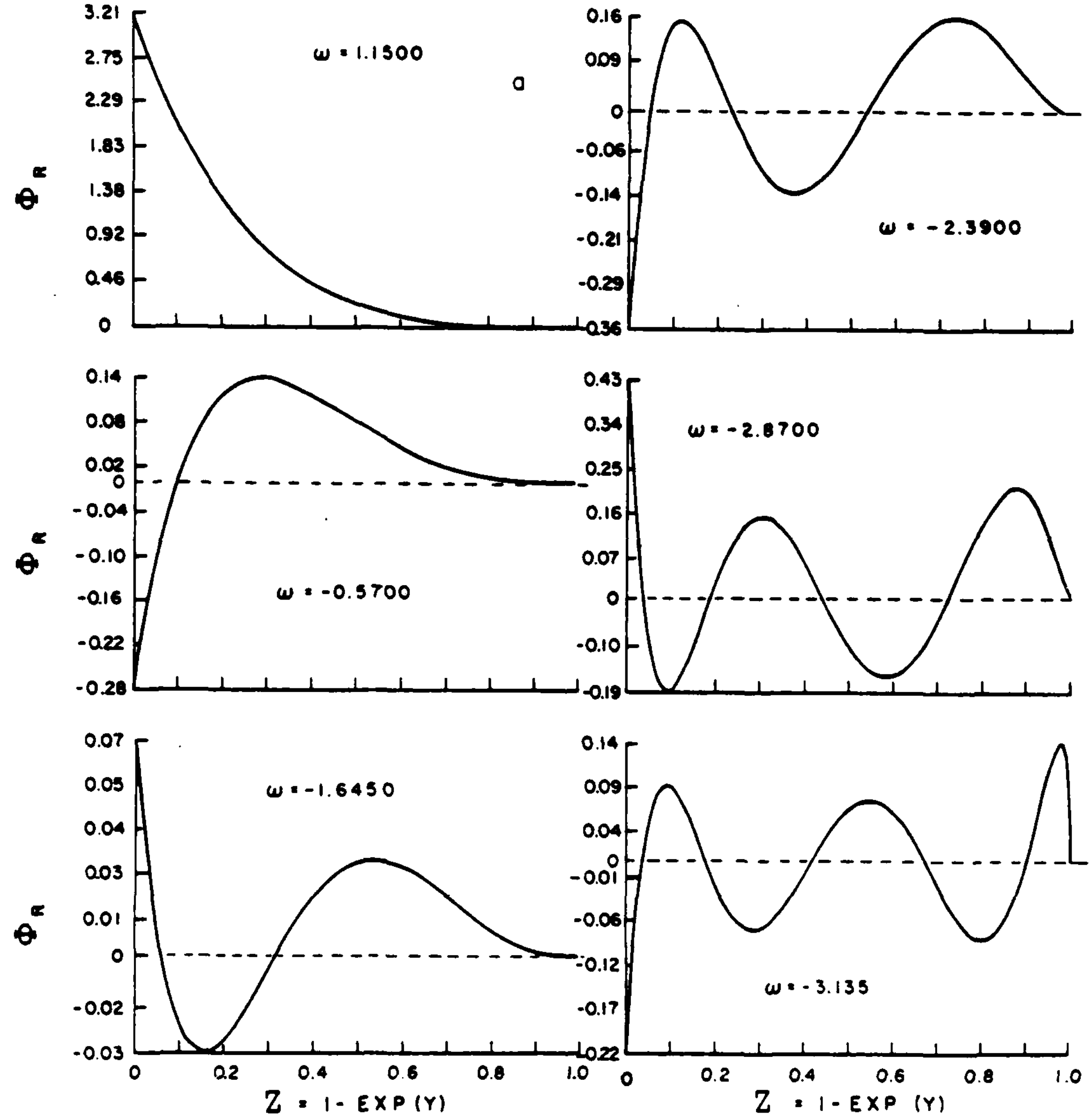
ω = 1.1500
3.21
2.75
2.29
1.83
1.38
0.92
0.46
0
Φ_R
0.16
0.09
0
-0.06
-0.14
-0.21
-0.29
-0.36
ω = -2.3900
0.14
0.08
0.02
0
-0.04
-0.10
-0.16
-0.22
-0.28
ω = -0.5700
0.43
0.34
0.25
0.16
0.07
0
-0.10
-0.19
ω = -2.8700
0.07
0.05
0.04
0.03
0.01
0
-0.02
-0.03
ω = -1.6450
0.14
0.09
0.04
0
-0.01
-0.06
-0.12
-0.17
-0.22
ω = -3.135
0
0.2
0.4
0.6
0.8
1.0
Z = 1- EXP (Y)

4

4

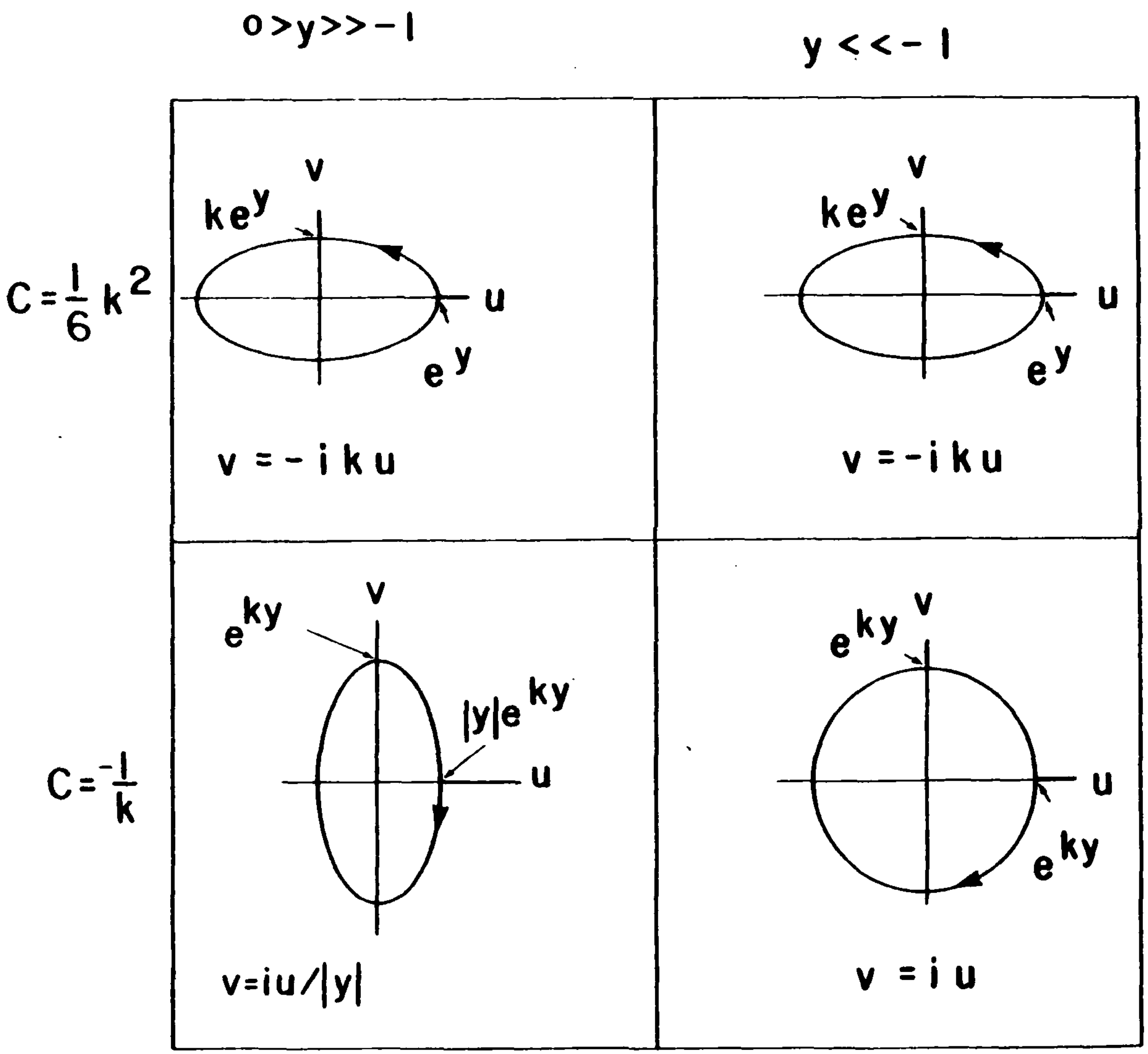
o>y>>-1
y<<-1
C=$\frac{1}{6}$k^2
C=$\frac{-1}{k}$
v
u
ke^y
e^y
v = - i k u
v
u
ke^y
e^y
v =-i k u
v
u
e^{ky}
|y|e^{ky}
v=iu/|y|
v
u
e^{ky}
e^{ky}
v = i u

J. Fluid Mech. (1982), vol. 123, pp. 237-265
Printed in Great Britain

The intrusion of a density current along the coast of a rotating fluid

By **MELVIN E. STERN,**
Graduate School of Oceanography, University of Rhode Island
JOHN A. WHITEHEAD
Woods Hole Oceanographic Institution
AND **BACH-LIEN HUA**
Museum National d'Histoire Naturelle, Paris

(Received 19 June 1981 and in revised form 25 February 1982)

When light rotating fluid spreads over heavier fluid in the vicinity of a vertical wall (coast) a boundary jet of width $\hat{L}$ forms, the leading edge or nose of which propagates with speed $\hat{c}$ along the coast. A certain fraction δ of the boundary transport is not carried by the nose but is deflected backwards (detrained) and left behind the propagating nose. Theoretical and experimental results for $\hat{L}$, $\hat{c}$, and δ are given for a quasi-equilibrium (constant-$\hat{c}$) regime. Over longer time intervals the laboratory observations suggest that the nose slows down and stagnates, whereupon the trailing flow separates from the coast and an intermittent boundary current forms. These processes may be relevant to the mixing of oceanic coastal currents and the maintenance of the mean current.

---

1. Introduction and statement of the problem

The way in which rotation inhibits the lateral spreading and mixing of a density current is illustrated by the Rossby adjustment problem (Saunders 1973; Stern 1975, chap. III). In the initial state a circular cylinder of radius R, height H and density ρ is resting in a frame rotating with angular velocity $\frac{1}{2}f$, and is surrounded by a deep resting fluid of density $\rho+\Delta\rho$. Gravity then causes the cylinder of uniform potential vorticity f/H to collapse vertically and spread horizontally, with individual columns tending to conserve potential vorticity. A balanced geostrophic (cyclostrophic) vortex may then result, in which the surface front advances only a distance $\Delta R \sim (g^*H)^{\frac{1}{2}}f^{-1}$ of the order of the Rossby radius of deformation, where $g^* = g\Delta\rho/\rho$. The vortex may be unstable, and more than one vortex may form if the initial radius is large compared with ΔR (Griffiths & Linden 1981).

The adjustment and the overall mixing process is drastically altered, however, when there is a vertical wall (figure 1). Although the adjustment of the semi-infinite light fluid is essentially unaltered at *large* distances $\hat{y}$ from the wall, a boundary current near $\hat{y} = 0$ must develop to accommodate the geostrophic flow into the wall. This coastal current transports the light fluid away from its source region, and thereby allows mixing to occur over much greater distances than would occur without the boundary (Wadhams, Gill & Linden 1979). What is the width of the boundary current: what is the nature of the leading edge (nose) of the coastal intrusion; is the

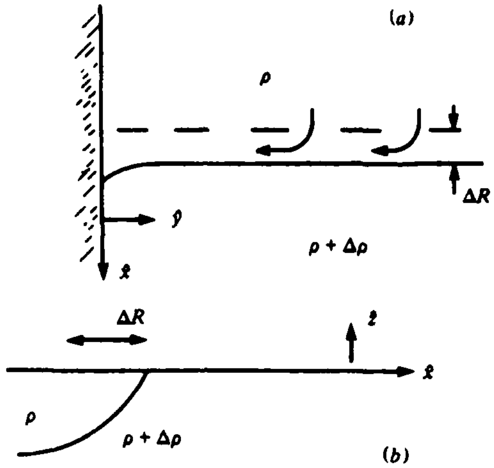

FIGURE 1. The initial stage in the rotating dam-break problem when a vertical wall ($\hat{y}=0$) is present. The semi-infinite upper fluid has density ρ and the very deep lower layer has density $\rho+\Delta\rho$. The top view (*a*) shows the surface front advancing a distance ΔR at position far from the wall. But the geostrophic flow that develops runs into a wall stagnation point and a coastal intrusion must form. The vertical section (*b*) shows the equilibrium front far from the wall.

boundary current laminar, and if not, how does it mix into the adjacent water? These questions are addressed here by a combined theoretical and experimental study. The experiments (see §2) consist of lifting a vertical gate ('dam-break' experiment) which was initially in the position of the dashed line in figure 1. The thin layer of light water (ρ) in this figure then spread laterally and was deflected to the coast, where a boundary current finally emerged. The dimensional width $\hat{y}$ of the latter was measured, as well as the nose speed of the density current. Considerable *lateral* detrainment from the seaward portion of the nose was also observed, this effect being somewhat similar to the vertical detrainment through the interface of a non-rotating intrusion in a two-layer fluid (Britter & Simpson 1978; Simpson & Britter 1979). Benjamin (1968) has given a theory for the latter case, the experimental agreement being good in a limiting regime where the detrainment is relatively weak. Our theory of the rotating intrusion therefore begins (§3) with the generalization of Benjamin's theory. We do not, however, neglect the (experimentally) important detrainment effect. Another notable novelty of our problem is the additional horizontal dimension and structure of the fluid behind the bore. We identify those regions where the flow is approximately steady, and also those unsteady regions in which the important detrainment occurs. With these additional considerations Benjamin's theory for the nose speed will obviously not close, and additional constraints on the trailing current are necessary. For this purpose we advance (§4) a model and a similarity solution, which predicts an upstream width (cf. equations (4.31), (C 23)) for a so-called 'limiting bore' (Stern 1980) which agrees closely with experiment (equations (2.1), (2.2)). By combining the model with Benjamin's formula, a nose speed and detrainment coefficient are predicted which are also in acceptable agreement with experiments.

The reader should be warned, however, that the simple theory corresponds to a different *initial*-value problem than does the complex experiment, and it will be argued that a connection between the two exists at *later* times. In view of the admitted weakness of this argument, an alternative derivation of one main theoretical result, involving much weaker assumptions, is given in appendix A. This leads to an upper bound on the width of semi-permanent intrusions, and any wider initial state could not propagate along a coast before it suffered great alterations (e.g. bifurcation into a thin current which leaves the wide current behind).

2. The laboratory experiment

2.1 *Set-up and procedure*

Although the problem in which a heavy density current intrudes on the bottom of the rotating tank will have similar properties, it is experimentally more convenient to work with a surface intrusion so as to minimize Ekman friction and to eliminate topographic effects due to the slope of the bottom relative to the level parabolic surfaces.

The experiments were conducted in a rectangular tank which was made from Plexiglas one-half inch wide. The tank, sketched in figure 2, was 183 cm long, 29·2 cm deep, and 20 cm wide (inside dimensions). Grooves were cut into the sides and bottom of the tank at various places in order to allow a sliding gate, of 22-gauge stainless steel, to divide the tank into two chambers. The grooves were approximately 2 mm wide and 3 mm deep. Since only one set of grooves was used at a time, the unused grooves were covered with cellophane tape to make the walls smoother. A mirror was placed next to the tank at an angle of approximately 45° so that an observer who was looking down from above could see both a top and side view of the tank. The tank and apparatus were mounted on the two-metre turntable at the Woods Hole Oceanographic Institution. The shaft of the table had been levelled to better than five seconds of arc. A 16 mm motor-driven ciné camera was rotated in synchronization with the turntable so that films could be taken of the flows in the tank with the use of small paper floats that were sprinkled on the surface of water in the tank.

For each experimental run the tank was first filled with tap water to a depth of 18·7 cm. The temperature of the water matched the temperature of the room to within 0·1 °C, to minimize convectively driven flows. A measured amount of salt was then added to the water, and mixed thoroughly in order to eliminate the slightest detectible stratification. The gate was then slid into the set of slots that were 49 cm from one end of the tank. The bottom of the gate was 10 cm above the bottom of the tank so that pressure equilibration existed. Two pieces of one-quarter inch plywood were then floated in the 49 cm long chamber, the tank was covered by a Plexiglas lid, the turntable was brought to the desired rate of rotation, and the salt water was allowed to spin up for 15 min to a state close to solid-body rotation. The preparation for the experiment was completed by slowly and carefully siphoning some coloured fresh water onto the plywood floats in the small chamber until a desired depth (2, 4 or 8 cm) of fresh water floated above the salty water. The density of the two waters was not measured directly but was estimated by means of a linear curve of density as a function of weight of salt added to the bottom water. Fractional density differences $\Delta\rho/\rho$ in the experiments were estimated to be 2·1, 3·2, 4·3, 8·7, 13·1 or $17{\cdot}5\times10^{-3}$. All these values are below the densities which were in the table in Hodgman (1961). The curve we used was a linear extrapolation from the one and two per cent values in the handbook. Errors are less than ten per cent, and to this accuracy, temperature and potassium permanganate have negligible effect on density.

Just before the experiment was started, the Plexiglas cover was removed from the

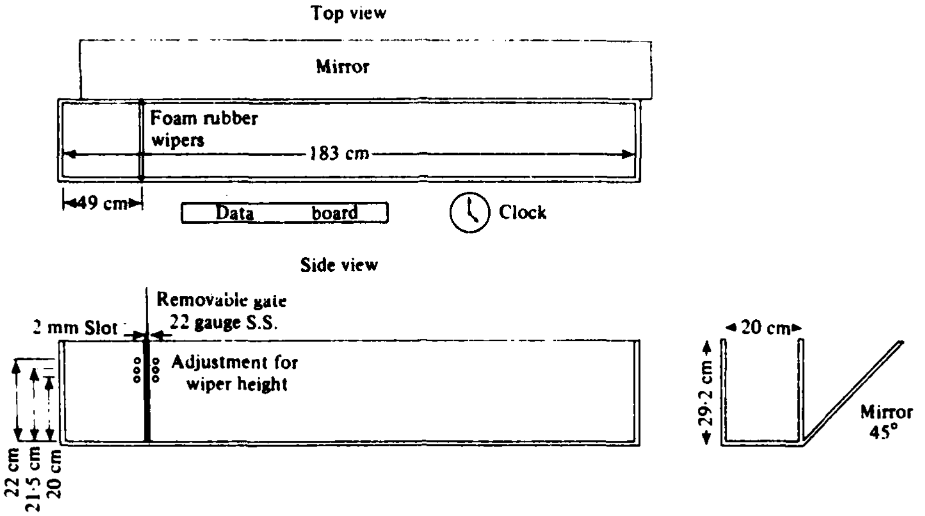

FIGURE 2. Sketch of the experimental apparatus.

tank, the ciné camera was started, and the sliding gate was carefully removed. In order to reduce the dripping effect from the emerging gate, a foam wiper was placed on each side of the guiding frame through which the gate was slid. The foam wipers were positioned so as to just contact the surface of the water after the coloured water had been put in. Use of the wipers and the guide frame in removing the gate resulted in a less-disturbed starting interface between the light and heavy fluids.

2.2. *Measurements and analysis of data*

After the gate was lifted, small paper floats were 'sprinkled' on the radially collapsing dye front in the channel, and ciné pictures were taken of the side-view mirror as well as the plan view.

The method of analysis was strongly tailored after the features of the flowing bore that were observed. The principal features of the bore (sketched in figure 3) are somewhat visible in figure 4. The nose of the bore (figure 4*a*) was not steady, but eddies peeled off the outer region and were left behind with a much slower translational velocity than the nose of the bore. On the wall immediately behind the nose was a 'neck', which was often the thinnest and shallowest portion of the laminar jet behind the nose. Although the neck was visible a sizable percentage of the viewing time, it was sometimes obscured by the edge of an eddy that had been detrained from the nose. Behind the neck were two regions. Near the wall an approximately laminar current supplied fresh fluid to the nose of the bore. This current was bordered on the outside by a region of strong cyclonic vorticity ('vortex sheet'), which separated the current from a region of eddies. These 'large-scale' eddies were complicated and turbulent in appearance. Some had been generated from the detraining process at the nose of the bore and some seem to have been detrained further upstream as illustrated more clearly in figure 4(*b*). Particles in the laminar current near the wall appeared to speed up and slow down as the eddies deformed the outer edge of the jet, but the particles in this current did not reverse direction relative to the nose, while the particles in the eddy region clearly did. There are many instances in the

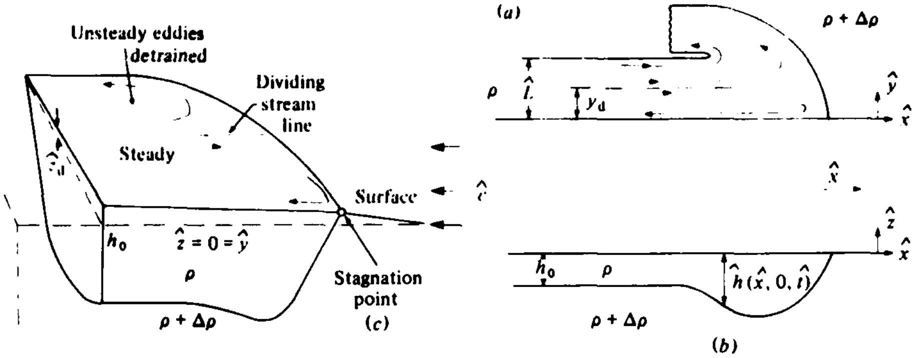

FIGURE 3. Schematic diagram of a quasi-equilibrium rotating bore far from the source region. The streamlines show the motion relative to an observer moving with the nose speed $\hat{c}$. The relative mass transport (*a*) at $\hat{x} = -\infty$ is non-zero. The detrained fraction δ of the flow reappears on the other side of the laminar vortex sheet ($\hat{y} = \hat{L}$), and is left behind as the nose propagates along the coast.

ciné films when it was difficult or even impossible to distinguish the laminar current from the eddies, but there are other instances when it was easy to distinguish between the two. In those cases the eddy activity was small outside of the laminar current, and the region separating the boundary current from the eddies had a strong shear. The continuity of this vortex sheet is visible in the ciné films, and more so to the eye while the experiment is running. We have therefore attempted to quantify the width of the boundary current by measuring the distance from the vortex sheet, when visible, to the wall.

The measuring procedure was to set up a ciné projector at a set distance from a piece of white cardboard screen. An investigator (J.W.) would sit next to the screen and look for clear instances of the vortex sheet. When one was sighted, dividers would be placed on the screen, with one point on the vortex sheet and one on the tank wall. The projector was then stopped as promptly as possible, and the distance from the span of the dividers measured. With the projector still stopped, the corresponding wall depth of the dyed fluid (in the 45° mirror) was also measured with a ruler and dividers. The time and downstream location of this measurement were recorded, as well as the nose location. This procedure was repeated in each run until measurements were taken at all positions of a clear vortex sheet. The number of samples in each run ranged from two to sixteen according to the quality and the subjective identification of a vortex sheet. We intentionally ran as many extreme values of g^* and f as possible (see table 1) in order to sample a wide variety of parameter space, so some runs are close to marginal in quality. We emphasize, however, that an unmistakable difference exists between this 'vortex sheet' and the density or dye front, aside from the fact that a precise measurement of the latter is also ambiguous and difficult.

The reason for the qualitative difference is quite clear from the observations. Dyed fluid that entered the nose (figure 3) exited in the rear and was left behind as an eddy or wave as the nose marched on. Although this was a major event for the long-time mixing of density (and also vorticity) in the boundary current, it was clearly a 'secondary' effect, and, in order to determine the primary width of the boundary current, it is quite reasonable to bias the observations towards a measurement of the shear lines. The number of 'independent' and usable measurements of $\hat{L}$ in each run

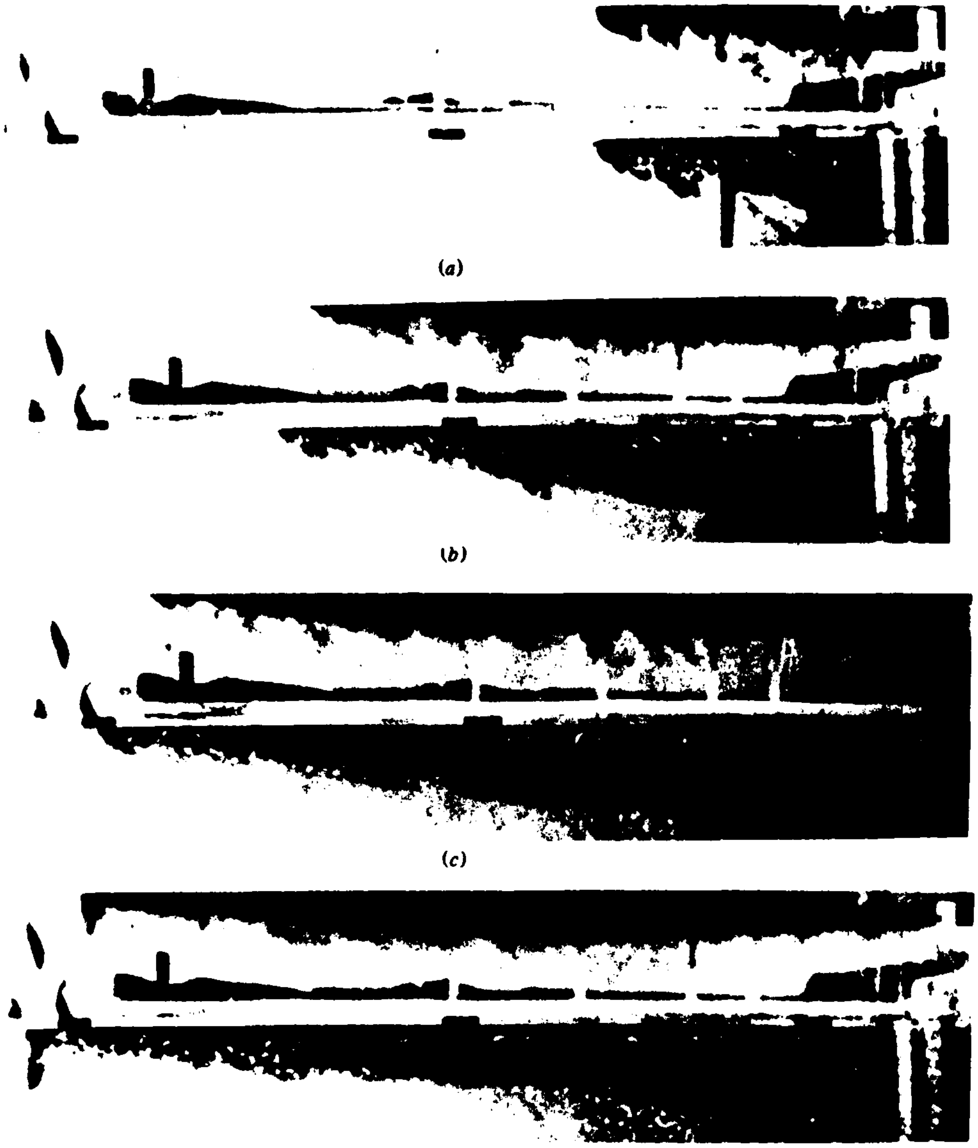

(*a*)

(*b*)

(*c*)

(*d*)

FIGURE 4 (*a–d*). For caption see facing page.

is shown by the numbers inside the circled data points (figure 5). The plotted $\hat{L}$ is the average distance from the wall of the points of maximum lateral shear in each run, and $\hat{h}$ is the average value of the corresponding wall height. The measurements of $\hat{L}$ and $\hat{h}$ were confined to a certain space–time interval that is determined by theoretical and practical considerations. Thus no measurements were taken until some time after the gate was lifted, and no measurements were taken after the nose reached the end of the tank and started to wind around the tank. No $(\hat{L}, \hat{h})$-measurements were taken in the nose of the bore, or at very large distances upstream

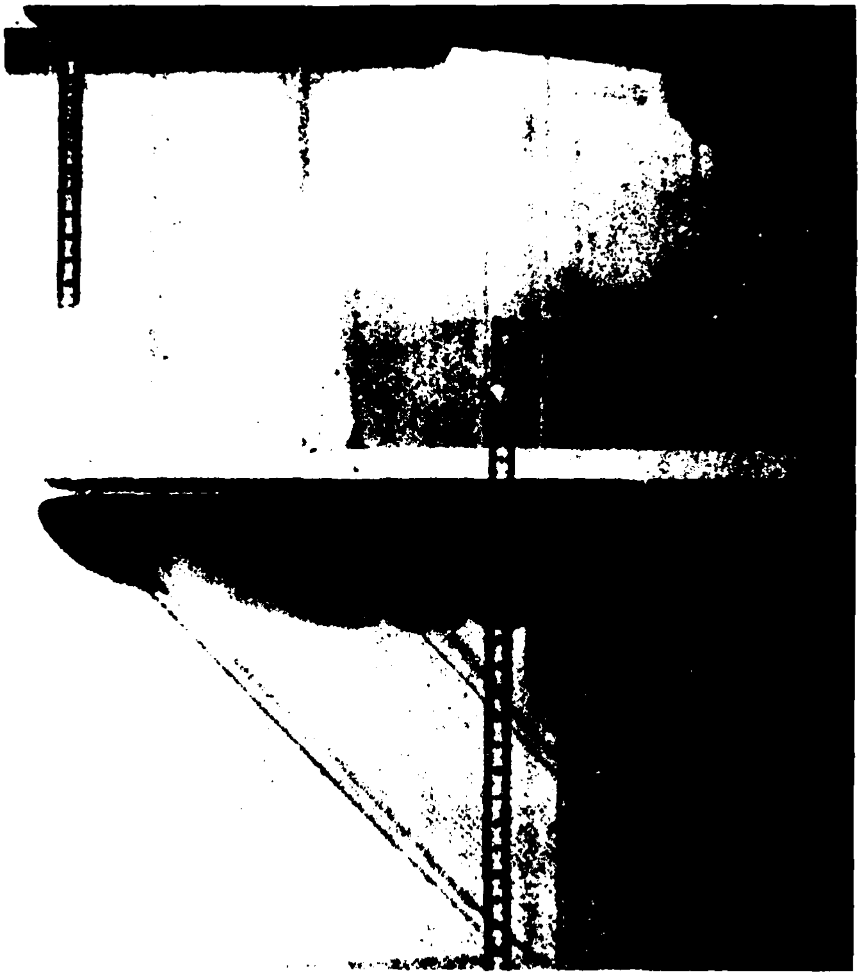

(e)

FIGURE 4. (a) A rotating density current in its early stage propagating along the right-hand wall of the tank. The image on the top is viewed through a 45° mirror and is a side view of the current with gravity downward in this figure. The image on the bottom is a plan view. The parameters are $g^* = 8{\cdot}5$, $T = 15{\cdot}4$ and $H = 8{\cdot}7$. (b) The same current 18 s later. The properties of the nose, such as speed, upstream width, and height, have changed little, although the eddies being shed are a little smaller. (c) The same current 31 s after (a). The current exhibits a great deal of similarity to (b). (d) After the current has hit the end of the tank, it turns the corner. The side view shows the depth of penetration of the fluid at the corner stagnation point, and illustrates that the fluid still possesses a significant amount of its original potential energy. (e) This intrusion (plan view) was at a relatively low Reynolds number, and the eddy that is being shed at the nose is almost laminar.

from the nose, and only a relatively small number of measurements were taken in the 'neck' behind the nose.

Conversion of the ciné film measurements to real centimetres was determined from the image of 5 cm fiduciary marks in the side and top images. In both cases, no correction was made for parallax as the bore moved along the tank, since we estimate that the geometric corrections are smaller than the uncertainty due to the

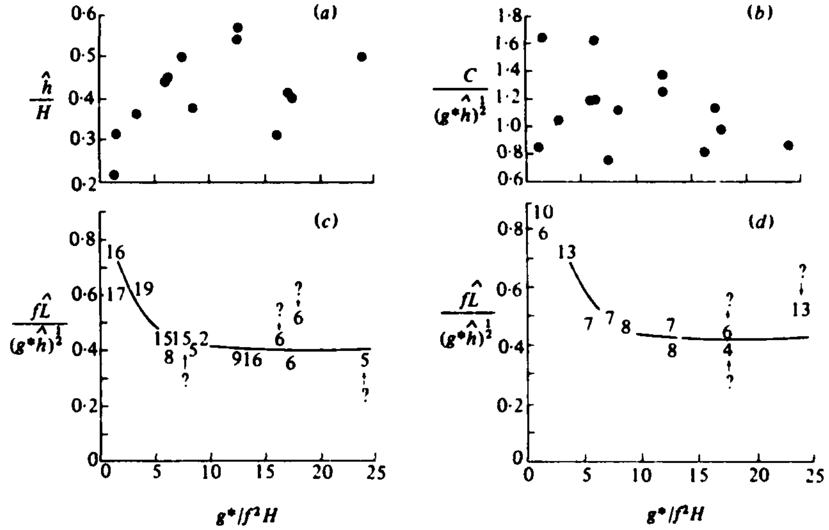

FIGURE 5. Suitable normalized values of height (*a*), bore nose velocity (*b*), and bore width for 90° gate (*c*) and 45° gate (*d*) as a function of the hydrostatic number. The numbers in (*c*) and (*d*) denote the number of observations of regions of distinct shear that went into the average.

g^* (cm/s)	$T(=4\pi/f)$ (s)	H (cm)	g^*/f^2H	$(g^*H^3)^{\frac{1}{2}}/\nu$	$f\hat{L}(g^*\hat{h})^{-\frac{1}{2}}$	$c(g^*\hat{h})^{-\frac{1}{2}}$	h_{nose}/H
17·15	14·5	4	5·84	3313	0·495	1·19	0·438
17·15	15·0	4	6·27	3313	0·494	1·19	—
12·8	20·25	4	8·5	2862	0·435	1·12	0·375
3·1	59·6	4	17·8	1408	0·52	0·98	0·400
3·1	40·6	4·2	7·68	1515	0·42	0·74	0·500
8·5	30·1	4	12·5	2332	0·37	1·25	0·571
8·5	15·4	8·7	1·57	7481	0·605	1·65	0·314
8·5	29·4	8	6·20	6597	0·382	1·64	0·450
4·2	15·3	4·6	1·24	2022	0·763	0·85	0·215
12·8	30·5	6·0	12·6	5258	0·387	1·37	0·542
2·1	60·7	3·0	16·3	753	0·435	0·82	0·318
3·1	59·3	4·0	17·25	1409	0·343	1·14	0·414
3·1	60·6	3·0	24·03	915	0·369	0·87	0·500
4·2	21·9	4·0	3·18	1640	0·632	1·04	0·357

TABLE 1. 90° Experimental parameters and results.

subjective factor entering the measurement. Data for the experiments are shown in tables 1 and 2.

The measurements of depth and width were used in the non-dimensionalized number $f\hat{L}(g^*\hat{h})^{-\frac{1}{2}}$ in the above tables, and the results were plotted as a function of g^*/f^2H in figure 5. This latter number we call a 'hydrostatic number' as it is the inverse-square ratio of the thickness H of the less-dense fluid layer in the reservoir and the Rossby radius of deformation. The reciprocal hydrostatic number is also a measure of the slope of the undisturbed front in the vertical plane sketched in figure 1. In shallow-water dynamics, and in most other large-scale geophysical problems the

g^* (cm/s^2)	$T(=4\pi/f)$ (s)	H (cm)	g^*/f^2H	$f\mathcal{L}(g^*\hat{h})^{-\frac{1}{2}}$
17·5	14·5	4·4	5·18	0·48
12·8	20·4	4·0	8·43	0·47
3·1	59·6	4·0	17·4	0·45
4·2	21·9	4·0	3·18	0·73
8·5	15·5	8·7	1·49	0·80
8·5	29·3	8·0	5·78	0·49
3·1	60·5	3·0	24·03	0·53
8·5	30·3	4·0	12·35	0·46
12·8	30·4	6·0	12·48	0·37
4·2	15·3	4·6	1·11	0·86
3·1	59·3	4·0	17·26	0·38

TABLE 2. 45° Experimental parameters and results.

hydrostatic number is large and irrelevant, since it disappears with the introduction of the hydrostatic assumption. This might not be true for engineering or some estuarine problems, however.

Figure 5 shows that when the hydrostatic number is above five, $f\mathcal{L}(g^*\hat{h})^{-\frac{1}{2}}$ is relatively constant; for the data in figure 5 and table 1 with hydrostatic number greater than five, the average value is 0·423 with a standard deviation of 0·056.

In view of the subjective and arbitrary factors in the measured width, three reproducibility tests were conducted. Experiments were performed for two initial conditions: a gate at right angles to the wall of the tank, and another at 45°. The quality of the latter experiments was somewhat lower, but it was attempted to duplicate the external parameters (g^*, H and f) as closely as possible and to compare results. Both results are shown in figure 5. For the 45° gate the average value of the width for $g^*/f^2H > 5$ is 0·453 with a standard deviation of 0·051. The most severe reproducibility test involved the use of a student to re-analyse the movies! Approximately 50 % of the data agreed with the measurements by J.W. to within 10 %. This occurred for those runs where the vortex sheets were clearly the most visible and least ambiguous. There was one period at the beginning of the test where the student was consistently lower by approximately 50 %. This occurred during one afternoon and may be due to a conservative streak during that day. The remaining 20 % were also somewhat smaller than the measurements by J.W., but appeared to be better in quality. Therefore J.W. repeated his measurements very carefully, and those data are reported here. These occurred in the experiments which were most difficult to measure denoted by question marks in figure 5.

Another check on the quality of the data was to look at the ciné films at one sitting and rate them good or marginal, based upon the clarity of the vortex sheets seen in the films. (As is often the case, the vortex sheet is easier to see in the laboratory than it is in the film because the movement of head and eyes aids the perception.) The marginal ones are labelled with a question mark in figure 5, and they only occurred when g^* was small (2·1 or 3·2 cm s^{-2}). Under the latter conditions surface tension may generate a surface 'stiffness' by creating a surface traction against convergence and divergence. It is evident that some of the marginal cases were furthest from the line.

The curves for $\mathcal{L}$ in figure 5 have been drawn by eye, and are slightly biased by the preceding consideration, but the asymptote at large hydrostatic number seems

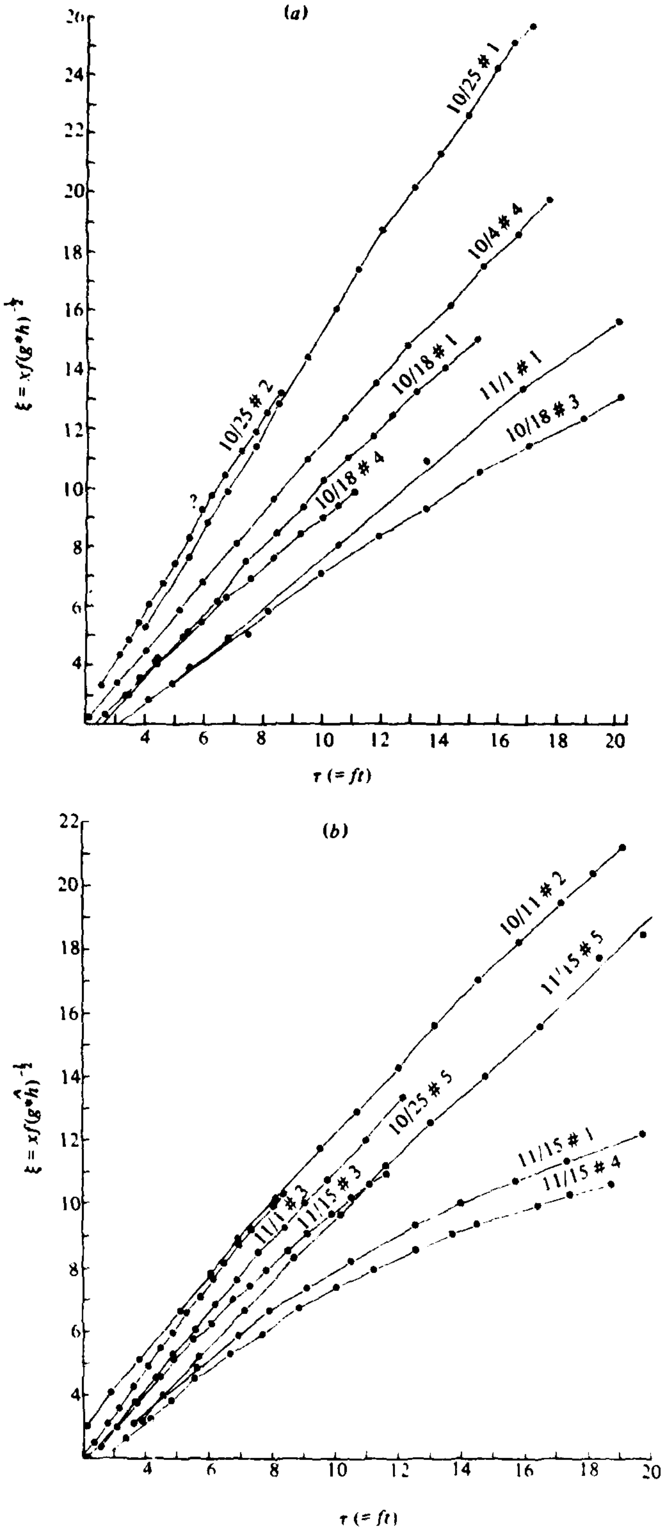

FIGURE 6. Position of the nose of the bore as a function of scaled time for the fourteen experimental runs with the 90° gate.

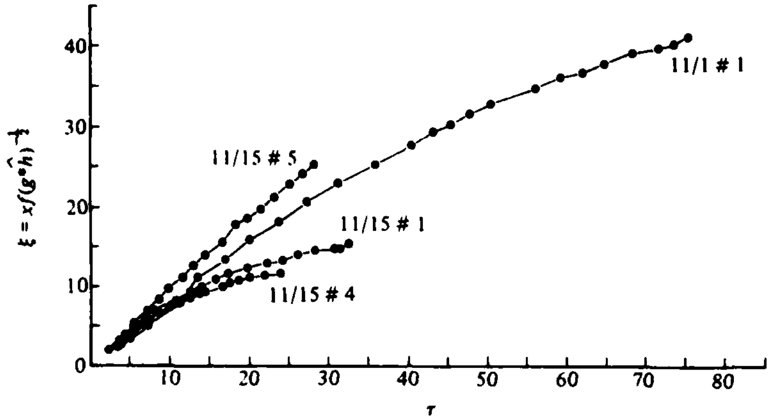

FIGURE 7. Position of the nose of the bore as a function of time for runs that lasted a large number of rotation time scales.

to be highly significant and relevant to the theory in the following sections. Thus we tentatively conclude that there is a unique width for the shear zone for the large hydrostatic number, with

$$\frac{f\hat{L}}{(g^*\hat{h})^{\frac{1}{2}}} = 0{\cdot}423 \pm 0{\cdot}056 \tag{2.1}$$

for the 90° barrier, and

$$\frac{f\hat{L}}{(g^*\hat{h})^{\frac{1}{2}}} = 0{\cdot}453 \pm 0{\cdot}051 \tag{2.2}$$

for the 45° barrier.

It is conceivable, however, that there may be not *one* curve, but a whole band of curves, i.e. the jet width may not be unique but may depend on other factors which are not within our control – such as the instability waves that form on the front in the reservoir when the barrier is removed.

This point of view is also suggested by the measurements of bore speed (figures 6*a*, *b*), which were only taken for the runs with a gate at 90°. The ordinate is the non-dimensional displacement of the nose bore from the dam, the abscissa is the non-dimensional time, and the points are the observations for each run. The identifying date and run numbers are also indicated. The curves drawn through these points have smoothed out some small variations in bore speed that may be real. A decrease of slope with increasing time can be clearly seen in some of the runs, and after very large times (figure 7) some of the noses stagnate and curve away from the wall forming a large gyre! The lack of 'similarity' of the curves is apparent. For each curve the extrapolated (small time) tangent has been drawn, and the corresponding non-dimensional speed $\hat{c}(g^*\hat{h})^{-\frac{1}{2}}$ computed. For figure 6(*a*) the mean speed is $c = 1{\cdot}09$, and for figure 6(*b*) it is $c = 1{\cdot}16$. In both figures the variation of $\hat{c}$ is real, but no correlation with g^*/f^2H has been found. Figure 8, however, indicates some systematic variation of $\hat{c}$ with the product of the velocity scale $(g^*H)^{\frac{1}{2}}$ and the depth scale H; and therefore the results (figure 8) have been plotted as a function of the overall Reynolds number $H(g^*H)^{\frac{1}{2}}\nu^{-1}$, even though the viscosity was not varied in the experiment. The implicit assumption here is not unreasonable, because Simpson & Britter (1979) observe that the nose speed in a non-rotating density current depends on Reynolds number when the latter is less than 10^3. The *dynamically* significant

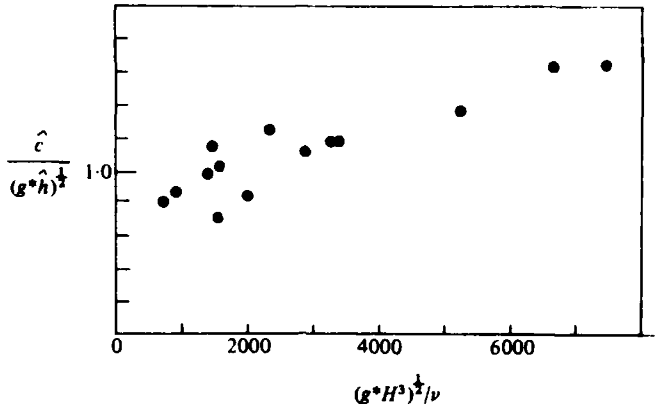

FIGURE 8. Scaled velocity as a function of the overall Reynolds number.

Reynolds number may be a proportionally smaller value for three reasons: (i) the depth of the jet is less than upstream height H (figure 5); (ii) the depth of the jet varies across the stream and goes to zero; and (iii) the depth of the nose is small and goes to zero at the leading edge. At large Reynolds number (> 4000) the envelope of the data tends to $c = 1{\cdot}56$ with a standard deviation of 0·05. At smaller Reynolds number the phase speed is approximately 20 % less. It is plausible that the systematic effect of the nose viscosity on the upstream width (figure 5*c*, *d*) is less than or equal to this 20 %.

3. A quasi-steady theory for a rotating density current

Figure 3 is a schematic diagram of the nose of the boundary intrusion as it is flowing along in a statistically steady state. The streamlines are drawn relative to an observer who moves with speed $\hat{c}$ of the nose of the intrusion (and in this frame of reference the nose is thus a stagnation point).

Under ideal conditions one would like to consider the light fluid to be separated from the heavy fluid by an interfacial surface that intersects the free surface ($\hat{z} = 0$) at the 'front'; the latter being a free streamline and a vortex sheet. This idealization differs somewhat from a more realistic sketch (figure 3) of our experimental observations, which shows part of the boundary flow entering the nose region and being left behind (*detrained*) as it folds the front backwards. The sketch in figure 3 illustrates the continuous nature of the fields and replaces the vortex discontinuity of the free streamline by a strong maximum-shear line (at $\hat{L}$) lying outside the dividing streamline. The width $\hat{L}$ that was actually measured in the experiments corresponds to this strong maximum-shear line. Another dynamically significant width is the dividing streamline (figures 3*a*, *c*), located at distance $\hat{y}_d$ from the wall. The distance $\hat{y}_d$ is defined such that the mass transport relative to the nose vanishes in the interval $\hat{y} = 0$ to $\hat{y} = \hat{y}_d$, i.e.

$$\int_0^{\hat{y}_d} (\hat{u}-\hat{c})\,\hat{h}\,d\hat{y} = 0, \tag{3.1}$$

where $\hat{u}$ is the longshore ($\hat{x}$) component of the vector velocity $\hat{\mathbf{V}}$ in the non-translating (f-frame) system, and $\hat{h}$ is the local layer thickness of a two-layer model. All the quantities in (3.1) are evaluated far upstream from the nose ($\hat{x} = -\infty$), in a region

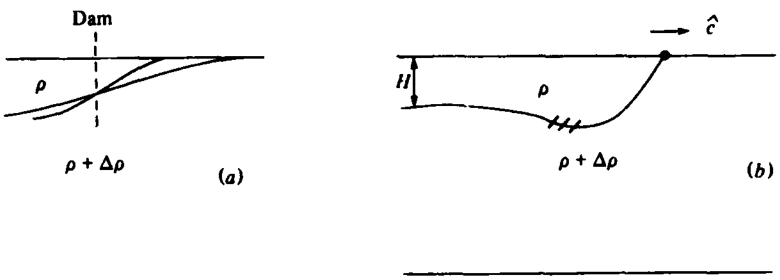

FIGURE 9. (*a*) For a non-rotating dam-break problem, the initial-value solution gives a thinning 'wedge' for the shape of the intruding light water of density ρ. (*b*) The non-rotating bore in the quasi-equilibrium Kármán–Benjamin theory.

$\hat{y} < \hat{y}_d$ where our observations indicate the flow to be approximately steady and laminar. On the other side of the dividing streamline, however, our observations indicate a much more unsteady and non-laminar flow. Thus a conservative Bernoulli function exists for the region inside the dividing streamline, and this function is found by transforming the equations of motion from the f-frame to a frame that translates with relative speed $\hat{c}$.

If $\hat{p}$ is the pressure, and if $\hat{z}$ is the height of a point above a level surface in the f-frame, then the $\hat{c}$-frame velocity $\hat{\mathbf{V}}_c$ satisfies

$$d\hat{\mathbf{V}}_c/d\hat{t}+f\mathbf{k}\times\hat{\mathbf{V}}_c+f\mathbf{k}\times\hat{\mathbf{c}} = -\rho^{-1}\nabla\hat{p}-g\nabla\hat{z}.$$

A Bernouli equation may be formed from this by taking the scalar product with the solinoidal $\hat{\mathbf{V}}_c$ and writing the result in the form

$$\frac{1}{2}\frac{d\hat{\mathbf{V}}_c^2}{d\hat{t}}+f\hat{c}\frac{d\hat{y}}{d\hat{t}} = -\rho^{-1}\frac{d\hat{p}}{d\hat{t}}+\rho^{-1}\frac{\partial\hat{p}}{\partial\hat{t}}-\frac{gd\hat{z}}{d\hat{t}}.$$

If the motion on any free-surface (p = constant) streamline is steady in the translating frame, then the Bernoulli function

$$B = \tfrac{1}{2}\hat{\mathbf{V}}_c^2+f\hat{c}\hat{y}+g\hat{z} \tag{3.2}$$

is invariant, and this assumption will be made for certain regions in the flow.

Reference is first made to Benjamin's (1968) selective use of the Bernoulli invariant for the problem (figure 9) of a non-rotating density intrusion. Von Kármán (1940) proposed a completely steady solution, but this does not exist. The main region of unsteadiness is located in the hatched region of figure 9, which region is somewhat analogous to the unsteady lateral front in our problem. We shall, therefore, follow Benjamin by assuming invariance of (3.2) in regions removed from the mixing sites.

Steady relative motion is now assumed on the free-surface streamlines located at $\hat{y} = 0$, i.e. along the two streamlines passing through the stagnation point. At $\hat{x} = \infty$ in the heavy-fluid region, the velocity $\hat{\mathbf{V}}_c$ relative to the nose is given by $\hat{u}_c = -\hat{c}$, and the Bernoulli invariant then gives:

$$\tfrac{1}{2}\hat{c}^2 = g\hat{z}_s, \tag{3.3}$$

where $\hat{z}_s$ is the geopotential height of the stagnation point. The other streamline lying in the light-fluid region yields:

$$\tfrac{1}{2}(\hat{u}_{-\infty}-\hat{c})^2+g\hat{z}_{-\infty} = g\hat{z}_s, \tag{3.4}$$

where $\hat{u}_{-\infty}$ is the velocity ($\hat{\mathbf{V}}$) and $\hat{z}_{-\infty}$ is the geopotential far upstream from the nose.

The elimination of $\hat{z}_s$ gives

$$\tfrac{1}{2}(\hat{u}_{-\infty}-\hat{c})^2+g\hat{z}_{-\infty} = \tfrac{1}{2}\hat{c}^2. \tag{3.5}$$

Since the geopotential height of the upstream free surface on the wall is related to the layer thickness $\hat{h}_0$ by the hydrostatic consideration, i.e. $(\rho+\Delta\rho)\,\hat{z}_{-\infty} = \Delta\rho\hat{h}_0$, one can rewrite (3.5) as

$$\hat{c} = \tfrac{1}{2}\hat{u}_{-\infty}+\frac{g^*\hat{h}_0}{\hat{u}_{-\infty}}, \tag{3.6}$$

where $g^* = g\Delta\rho/\rho$.

In the non-rotating theory with no detrainment $\hat{u}_{-\infty}$ is a constant equal to $\hat{c}$, and the use of this gives $\hat{c} = (2g^*\hat{h}_0)^{\frac{1}{2}}$. Although a mass flux relative to the nose is always observed (Britter & Simpson 1978), the quantitative effect on $\hat{c}$ of this detrainment is small (in a limiting case), presumably because of the strong opposition of gravitational stability.

But in our problem (figure 3) *lateral* detrainment can occur without great gravitational opposition, and the effect is indeed most striking in our experiments. We will therefore reject the assumption that the upstream volume transport of the intrusion (relative to the nose) is zero, and the finite ratio of this transport to the absolute transport, i.e.

$$\delta \equiv \frac{\int_0^{\hat{L}} (\hat{u}-\hat{c})\,\hat{h}(\hat{y})\,d\hat{y}}{\int_0^{\hat{L}} \hat{u}\hat{h}\,d\hat{y}} \quad (\text{at}\,\hat{x} = -\infty), \tag{3.7}$$

will be called the detrainment coefficient. Furthermore, $\hat{u}(-\infty, \hat{y})$ is not independent of $\hat{y}$, and therefore additional information is required to determine the wall velocity $\hat{u}_{-\infty} = \hat{u}(-\infty, 0)$.

The reader may want to turn to appendix A at this point, where Bernoulli invariance is also applied to the dividing streamline, and where a simple argument leads to an upper bound on $\hat{y}_d$. The following argument, on the other hand, claims to give a sharper prediction of the width of the current to use in connection with (3.6).

4. Intrusion of finite potential vorticity

What are the dynamical factors that determine $\hat{L}, \hat{c}, \delta$? As a start, we are obliged to introduce rather drastic assumptions, one of which, (see §4.3), involves a recognition that the experiment involves a 'self-limiting' process in which certain factors $(\hat{L}, \hat{c}, \delta)$ are largely independent of the initial conditions. Another assumption is the use of the shallow-water equations

$$d\hat{\mathbf{V}}/d\hat{t}+f\mathbf{k}\times\hat{\mathbf{V}} = -g^*\nabla\hat{h}, \tag{4.1}$$

$$\partial\hat{h}/\partial\hat{t}+\nabla\cdot\hat{\mathbf{V}}\hat{h} = 0 \tag{4.2}$$

as the starting point. These apply to two layers (figure 1) of slightly different $(\Delta\rho)$ density, the lower layer being relatively thick and passive. The upper layer has thickness $\hat{h}(\hat{x}, \hat{y}, \hat{t})$ and velocity $\hat{\mathbf{V}} = (\hat{u}, \hat{v})$. There is a vertical coast at $\hat{y} = 0$ so that the transverse velocity is $\hat{v}(\hat{x}, 0, \hat{t}) = 0$, and there is a free streamline at $\hat{y} = \hat{L}(\hat{x}, \hat{t})$ so that $\hat{h}(\hat{x}, \hat{L}(\hat{x}, \hat{t}), \hat{t}) = 0$. The neglect of the friction forces in (4.1) must be kept in mind, especially when one considers explicitly the nose region.

Relevant initial-value solutions of (4.1)–(4.2) are still difficult to obtain, and we shall therefore retreat still further to a generalization of Stern's theory for the evolution of long waves on a uniform potential vorticity current. Plausible similarity assumptions (cf. (4.29) and the last paragraph in §4) will be made which relate the evolution of the long-wave solution to a corresponding state of the experiment.

4.1. *Long-wave equations for uniform potential vorticity*

Let us first write (4.1) in the alternative form

$$\partial\hat{\mathbf{V}}/\partial\hat{t}+(f+\hat{\zeta})\,\mathbf{k}\times\hat{\mathbf{V}} = -\nabla(g^*\hat{h}+\tfrac{1}{2}\hat{\mathbf{V}}^2), \tag{4.3}$$

$$\hat{\zeta} = k\cdot\nabla\times\hat{\mathbf{V}}, \tag{4.4}$$

and the conservation of potential vorticity $(f+\hat{\zeta})/\hat{h}$ is also implied. Therefore, if the initial state has uniform potential vorticity $f/\hat{H}$, where $\hat{H}$ is the uniform initial vertical thickness, then

$$\frac{f+\hat{\zeta}}{\hat{h}} = \frac{f}{\hat{H}} \tag{4.5}$$

at all subsequent times. The component of $\hat{\mathbf{V}}$ parallel to the coast is denoted by $\hat{u}$, the $\hat{y}$-component is denoted by $\hat{v}$, and the foregoing equations are made non-dimensional by the transformations

$$\left.\begin{array}{c}\hat{h} = h_0h(x,y,t), \quad \hat{y} = (g^*h_0)^{\frac{1}{2}}f^{-1}y, \quad \hat{x} = \epsilon^{-1}(g^*h_0)^{\frac{1}{2}}f^{-1}x, \\ \hat{u} = (g^*h_0)^{\frac{1}{2}}u, \quad \hat{v} = \epsilon(g^*h_0)^{\frac{1}{2}}v, \quad \hat{t} = \epsilon^{-1}f^{-1}t, (4.6) \\ \hat{H} = h_0H, \quad \hat{L} = (g^*h_0)^{\frac{1}{2}}f^{-1}L(x,t), \quad \hat{h}(\hat{x},\hat{L},\hat{t}) = 0; \end{array}\right\} \tag{4.6}$$

where h_0 is a given vertical depth scale, and ϵ is the scale value of cross-stream/downstream velocities. In figure 3(*b*), and in that which follows, h_0 is conveniently taken as the wall height of the intrusion far upstream in the laminar portion of the coastal current, and from geostrophy it follows that $g^*h_0^2/2f$ equals the volume flux.

When the non-dimensional equations are written in Cartesian form, and when the long-wave ($\epsilon\to 0$) limit is taken, the result is

$$\frac{\partial u}{\partial t}-\left(1-\frac{\partial u}{\partial y}\right)v+\frac{\partial}{\partial x}(h+\tfrac{1}{2}u^2) = 0, \tag{4.7}$$

$$u = -\frac{\partial h}{\partial y}, \tag{4.8}$$

$$\frac{\partial h}{\partial t}+\frac{\partial hu}{\partial x}+\frac{\partial hv}{\partial y} = 0, \tag{4.9}$$

$$1-\frac{\partial u}{\partial y} = \frac{h}{H}. \tag{4.10}$$

It is easy to show (by taking the y-derivative of (4.7)) that (4.7) is satisfied at all y if it is satisfied at any one particular y, and if (4.8)–(4.10) are satisfied at all y.

Equations (4.8) and (4.10) give an ordinary differential equation for h, and if $U(x,t)$ denotes the value of u on $y = L$ (where $h = 0$) then the solution is

$$h(x,y,t) = H\left[1-\cosh\frac{L-y}{H^{\frac{1}{2}}}\right]+H^{\frac{1}{2}}U\sinh\frac{L-y}{H^{\frac{1}{2}}}, \tag{4.11}$$

$$u(x,y,t) = -H^{\frac{1}{2}}\sinh\frac{L-y}{H^{\frac{1}{2}}}+U\cosh\frac{L-y}{H^{\frac{1}{2}}}. \tag{4.12}$$

The zero-potential-vorticity limit $H^{-1}\to 0$ yields Stern's (1980) results with $h = U(L-y)-\frac{1}{2}(L-y)^2$ and $u = U-L+y$.

4.2. *Time-dependent equations*

When profiles of u and h are substituted in (4.7), and the result evaluated at the particular $y = L$ (where $1-\partial u/\partial y = 0$), we get

$$\frac{\partial U}{\partial t}+U\frac{\partial U}{\partial x}-\frac{\partial L}{\partial t} = 0. \tag{4.13}$$

Note that v appears only in (4.7), and its coupling with (U, L) only appears via the boundary conditions, or via the integrated version of (4.9), viz

$$\frac{\partial}{\partial t}\int_0^{L(x,t)} h\,dy+\frac{\partial}{\partial x}\int_0^{L(x,t)} uh\,dy = 0. \tag{4.14}$$

The substitution of (4.11) and (4.12) in this, and the simplification of the result using (4.13), yields

$$\begin{aligned} 0 = &\left(UH^{-1}\sinh\frac{L}{H^{\frac{1}{2}}}\right)\frac{\partial L}{\partial t}\\ &+\left[UH^{-\frac{1}{2}}\sinh\frac{L}{H^{\frac{1}{2}}}-\cosh\frac{L}{H^{\frac{1}{2}}}+1\right]\left[UH^{-\frac{1}{2}}\cosh\frac{L}{H^{\frac{1}{2}}}-\sinh\frac{L}{H^{\frac{1}{2}}}\right]\frac{\partial L}{\partial x}\\ &+\left[UH^{-\frac{1}{2}}\cosh\frac{L}{H^{\frac{1}{2}}}-\sinh\frac{L}{H^{\frac{1}{2}}}\right]\left[\cosh\frac{L}{H^{\frac{1}{2}}}-1\right]\frac{\partial U}{\partial x}, \end{aligned} \tag{4.15}$$

which together with (4.13) form a complete set of quasi-linear hyperbolic equations for the position of the front $L(x, t)$ and the velocity $U(x, t)$ along that free streamline.

The thickness of the fluid on the wall as obtained from (4.11) is

$$h(x,o,t) = H\left[1-\cosh\frac{L}{H^{\frac{1}{2}}}\right]+H^{\frac{1}{2}}U\sinh\frac{L}{H^{\frac{1}{2}}}, \tag{4.16}$$

and by using our normalizing condition $h(-\infty, 0, t) = 1$ we get the boundary condition for the upstream state section (curve *PWQ* in figure 10):

$$1 = H\left[1-\cosh\frac{L}{H^{\frac{1}{2}}}\right]+H^{\frac{1}{2}}U\sinh\frac{L}{H^{\frac{1}{2}}} \quad \text{at} \quad x = -\infty. \tag{4.17}$$

The non-dimensional H is inversely proportional to the potential vorticity, and the simple case of zero potential vorticity may be obtained from (4.15) and (4.17) by expanding the hyperbolic functions in an $L/H^{\frac{1}{2}}$ power series. By neglecting small terms of order $L/H^{\frac{1}{2}}$ we then get

$$U\frac{\partial L}{\partial t}+(U-\tfrac{1}{2}L)(U-L)\frac{\partial L}{\partial x}+\tfrac{1}{2}L(U-L)\frac{\partial U}{\partial x} = 0, \tag{4.18}$$

$$1 = L(U-\tfrac{1}{2}L) \quad \text{at} \quad x = -\infty. \tag{4.19}$$

4.3. *Similarity solutions*

There are no solutions of (4.13) that preserve their form, and the 'simplest' solutions are those in which the functional relations between $L(x, t)$, $U(x, t)$, $h(x, 0, t)$ are *independent of time* and position x. (We also note that the experimental relation between $\hat{L}$ and $\hat{h}$ is 'universal'.) Therefore, we now look for solutions such that U is some (unknown) function of $L(x, t)$ *alone*, i.e.

$$U = U(L), \tag{4.20}$$

$$\frac{\partial U}{\partial t} = U'(L)\frac{\partial L}{\partial t}, \tag{4.21}$$

$$\frac{\partial U}{\partial x} = U'(L)\frac{\partial L}{\partial x}. \tag{4.22}$$

Upon substituting this in (4.13) and (4.15) we obtain two simultaneous quasilinear equations for $(\partial L/\partial t, \partial L/\partial x)$, the first of which is

$$\frac{\partial L}{\partial t}+\frac{UU'(L)}{U'(L)-1}\frac{\partial L}{\partial x} = 0. \tag{4.23}$$

This implies that L (and U and $h(x, 0, t,)$) is constant relative to an observer moving with the local propagation speed

$$\frac{dx}{dt} = \frac{U}{1-1/U'(L)}. \tag{4.24}$$

When (4.20) is used in (4.15) we obtain a second quasi-linear equation for $\partial L/\partial t$ and $\partial L/\partial x$. Elimination of these two derivatives from the two simultaneous equations gives a quadratic equation for U'. After using some hyperbolic trigonometry to solve for $1/(U'-1)$, the roots of this quadratic can be expressed as

$$\frac{dU}{dL} = 1-\frac{(2U/H^{\frac{1}{2}})\cosh\left(L/2H^{\frac{1}{2}}\right)}{a\pm(a^2+b)^{\frac{1}{2}}}, \tag{4.25}$$

$$a = \sinh\left(L/H^{\frac{1}{2}}\right)\left[\cosh\frac{L}{2H^{\frac{1}{2}}}-\frac{U}{H^{\frac{1}{2}}}\sinh\frac{L}{2H^{\frac{1}{2}}}\right], \tag{4.26}$$

$$b = 2\sinh\left(L/H^{\frac{1}{2}}\right)\left[\frac{U}{H^{\frac{1}{2}}}\cosh\frac{L}{H^{\frac{1}{2}}}-\sinh\frac{L}{H^{\frac{1}{2}}}\right]. \tag{4.27}$$

Equation (4.25) gives two (±) intersecting families of curves in the (U, L)-plane, and the intrusive solutions of interest pass through the nose point $L = 0$. The two families are given in figure 10 for uniform potential vorticity $H = 2$, and comparison with the zero-potential-vorticity curves (figure 11) shows that there is not much difference in the vicinity of $L = 0$.

Corresponding values of L, U far upstream must correspond to one of the points (say P) lying on the dashed auxiliary curve in figures 10 and 11. Through this point P, pass two (±) solution (4.25) curves, one of which represents a 'wedge' and the other a 'bore' intrusion (Stern 1980). A wedge solution ⊕ passing through P has a local propagation speed that increases towards the nose, so that an observer moving with the nose sees the wedge get thinner with time until frictional forces eventually become dominant in the nose region and slow the nose down. Thus all the 'wedges' have a divergent energy flux in the nose region, and these solutions are apparently irrelevant for the model we seek. The ⊖ solution (curve PS), on the other hand, can be shown (see Stern 1980) to have a local propagation speed that decreases with L, and the nose of this *bore*-like intrusion advances slower than the rear. Thus an observer sees the front steepen with time, whereupon the short-wave terms neglected in this

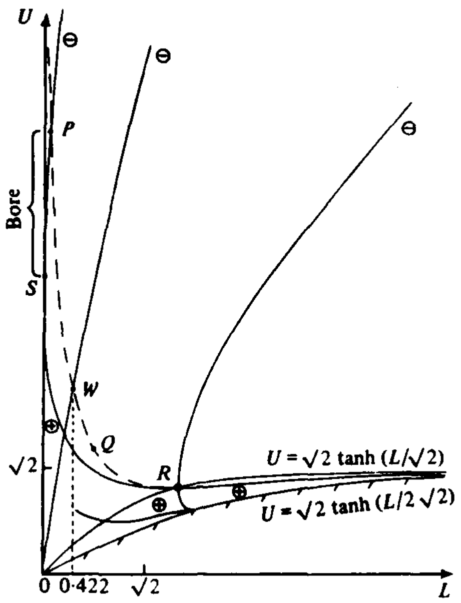

FIGURE 10. The trajectories of solutions in (U, L)-space for non-dimensional potential vorticity = 2. The limiting bore solution corresponds to the line OW and the long-dashed line corresponds to the upstream condition (4.17), which any solution must lie on.

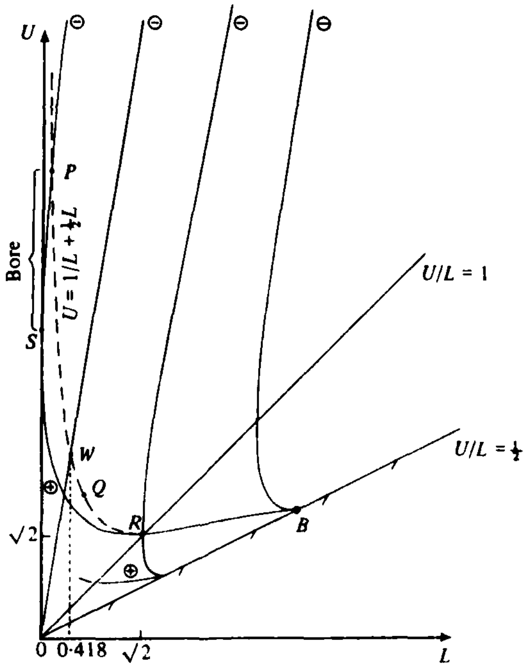

FIGURE 11. The trajectories of the solutions in (U, L)-space for zero potential vorticity.

theory become important and the 'shock' modifies the nose. Although these solutions might be relevant, we note that there is an entire family of bore solutions, corresponding to all the P-type points, and further specification is necessary.

Consider the nose region ($L = 0$) of the current, and replace the hyperbolic functions in (4.25)–(4.27) by the leading terms in a small-L expansion. The result

$$\frac{dU}{dL} = 1 - \frac{2U}{L \pm [L^2 + 2L(U-L)]^{\frac{1}{2}}}, \tag{4.28}$$

is valid for small L and all H. This relation also holds for all L when $H^{-1} \rightarrow 0$. The bore solutions are obtained by using the $-$ sign.

Equation (4.28) is infinite at $L = 0$ if $U(0)$ is finite, so that the frontal slope

$$\left.\frac{\partial L}{\partial x}\right|_{L=0} = (U'(L))^{-1} \left.\frac{\partial U}{\partial x}\right|_{L=0},$$

will vanish if $U(0) > 0$. Under these 'unrealistic' conditions, a thin nose ($\partial L/\partial x = 0$) exists at all times at $L = 0$ and, furthermore, the shock which will occur for this solution will be located *behind* the nose. The only exception occurs for the bore solution satisfying the end condition

$$U(0) = 0, \tag{4.29}$$

for then (4.28) is finite at $L = 0$. $\partial L/\partial x$ can then be finite, and $\partial L/\partial x = \infty$ can occur first at the nose. This (4.29) 'limiting bore' also has the property that its upstream width is maximal among all the intrusions that propagate as a bore. Initial states with a greater width have to adjust so that a thinner portion propagates down the coast, leaving the thicker portions behind. Further discussion of (4.29) appears in §6.

The maximum width of this limiting bore is found by integrating (4.25) with the $-$ sign:

$$\frac{dU}{dL} = 1 - \frac{(2U/H^{\frac{1}{2}})\cosh(L/2H^{\frac{1}{2}})}{a - (a^2 + b)^{\frac{1}{2}}}, \tag{4.30}$$

and by using the boundary condition $U(0) = 0$. The resulting curve OW is extended until it intersects the upstream state curve at point W (figure 10).

For zero potential vorticity, Stern (1980) found that the abscissa of the latter point W is (figure 11)

$$L = 0{\cdot}418 \quad \text{for} \quad x = -\infty \tag{4.31a}$$

For finite H (4.30) was integrated by a Runge–Kutta scheme, and the result for $H = 2$ is the curve OW in figure 10. The upstream state curve (4.17) is RQW, and the point of intersection W corresponds to $L = 0{\cdot}422$. A number of values of H were taken in the range $1 < H < \infty$ and the computed L lies in the range

$$0{\cdot}418 < L(-\infty) < 0{\cdot}426. \tag{4.31b}$$

Thus we conclude that the *limiting bore* width $L \simeq 0{\cdot}42$ is essentially independent of potential vorticity.

The foregoing long-wave theory is obviously not uniformly valid, and it will fail when the first shock forms (at the nose). At that time it is reasonable to suppose that the short-wave theory ((4.1) and (4.2)) will modify the entire nose region and accelerate the nose. But it is reasonable to assume that there will be no modification upstream. This means that the value of L in the latter regions will equal the long-wave-theory result even though the nose is more drastically modified. This assumption is testable in principle by integrating (4.1) and (4.2) numerically. The non-limiting bores ($U'(0) = \infty$), on the other hand, will break first behind the nose and will probably evolve into a more complicated structure (e.g. separated flow).

5. Quasi-steady nose speed and detrainment coefficients

The limiting value of the nose speed (in the post-steepening phase mentioned above) must be consistent with the upstream mass flow, and with the Bernoulli condition, i.e. (3.6) and (3.7). The $\hat{u}(y)$, $\hat{h}(y)$ appearing in the latter are to be evaluated far upstream, and, according to the main assumption at the end of §4.3 are given by the long-wave theory.

The calculations are given first for zero potential vorticity, ($H^{-1} \rightarrow 0$), in which case (4.11), (4.12) and (4.17) reduce to

$$u = U-L+y, \quad h = U(L-y)-\tfrac{1}{2}(L-y)^2, \quad 1 = UL-\tfrac{1}{2}L^2 \quad \text{at} \quad x=-\infty,$$

and from these we get

$$\int_0^L hu\,dy = \tfrac{1}{2}h^2(0) = \tfrac{1}{2} \quad \text{at} \quad x=-\infty,$$

$$\int_0^L h\,dy = \tfrac{1}{2}UL^2-\tfrac{1}{6}L^3 = \tfrac{1}{2}L+\tfrac{1}{12}L^3 \quad \text{at} \quad x=-\infty.$$

The wall velocity is then $u(-\infty, 0) = 1/L-\frac{1}{2}L$. Since $L = 0{\cdot}418$ (4.31*a*), (3.6) and (3.7) yield

$$c = 1{\cdot}546, \tag{5.1}$$

$$\delta = 0{\cdot}332. \tag{5.2}$$

For finite potential vorticity, one has

$$u = \frac{(1-H)\cosh L/H^{\frac{1}{2}}+H}{H^{\frac{1}{2}}\sinh L/H^{\frac{1}{2}}} \quad \text{at} \quad x=-\infty, \quad y=0, \tag{5.3}$$

$$\int_0^L hu\,dy = \tfrac{1}{2}h^2(0) = \tfrac{1}{2} \quad \text{at} \quad x=-\infty, \tag{5.4}$$

$$\int_0^L h\,dy = H\left[L+\frac{1-2H}{H^{\frac{1}{2}}\sinh L/H^{\frac{1}{2}}}\left(\cosh\frac{L}{H^{\frac{1}{2}}}-1\right)\right] \quad \text{at} \quad x=-\infty. \tag{5.5}$$

When $H = 2$, we have found that $L = 0{\cdot}42$ (figure 10), and the values of (3.6) and (3.7) are then computed to be $c = 1{\cdot}57$ and $\delta = 0{\cdot}32$. For the whole range $1 < H < \infty$, the values of (c, δ) do not differ by more than 3% from the above values. Thus we conclude that the nose speed, detrainment coefficient and boundary-current width are essentially independent of the potential vorticity for a given volume transport (i.e. h_0).

We have also investigated (appendix C) the effect of a finite bottom layer, and found that this increases the range of widths of the boundary current to

$$0{\cdot}413 \leqslant L(-\infty) \leqslant 0{\cdot}516,$$

and $L(-\infty) = 0{\cdot}43$ when the total depth is twice the upper layer depth (h_0) and when $H = 2$. Under these conditions $C = 1{\cdot}56$ and $\delta = 0{\cdot}34$. Thus we conclude that the boundary current width, speed c, and detrainment coefficient are insensitive to the lower-layer depth as well as to the upper-layer potential vorticity.

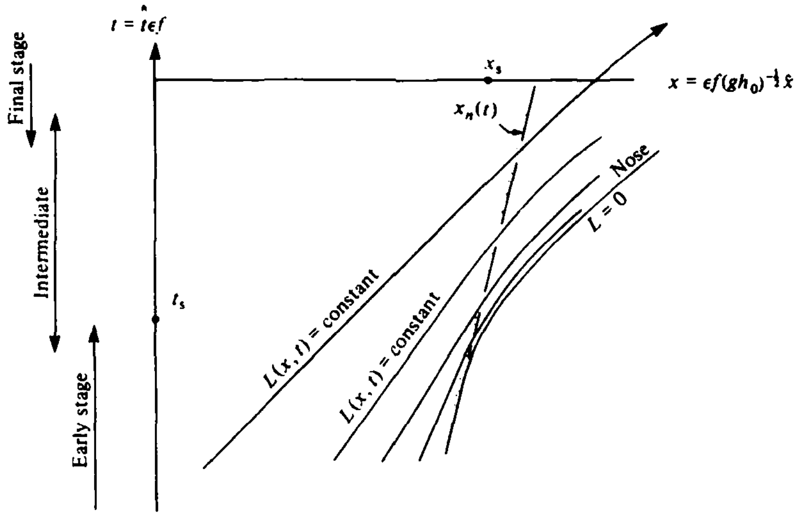

$t = \hat{t}\epsilon f$
x_s
$x = \epsilon f(gh_0)^{-\frac{1}{2}}\hat{x}$
$x_n(t)$
Nose
$L = 0$
$L(x, t) = \text{constant}$
$L(x, t) = \text{constant}$
t_s
Final stage
Intermediate
Early stage

FIGURE 12. Sketch of the evolution of a bore, as modelled by the present theory. At early non-dimensional times ($t < t_2$) no shock has formed and all characteristics flow toward the right. The dotted trajectory is the position of the nose. At slightly before t_s, a shock forms at the nose if the solution is that of the limiting bore. However, for the 'bore' class of solutions, information from the shock does not flow to the left, so trajectories of characteristics to the left of the bore are unaltered.

6. Critical remarks and conclusions

A dynamically consistent model of the evolution of a coastal intrusion has been developed, starting from an initial configuration in which the distance of the front from the vertical wall varies slowly in the downstream direction. The uniqueness of (L, c) depends on an assumption, the physical significance of which may be argued in a slightly different way from that used in the text.

Suppose that at some initial time we have a front that varies slowly in $\hat{x}$ from $\hat{x} = -\infty$ to the nose point $\hat{x}_n$. We seek self-similar solutions $(\hat{u}(\hat{x}, \hat{L}(\hat{x}, \hat{t}), \hat{t}) = \hat{C}(\hat{L}))$ of the long-wave equations, subject to certain side conditions, whch will evolve into the limiting observable state. The local propagation velocities are required to decrease towards the nose, for otherwise the initial state will develop into a thinning wedge and the solution will be greatly modified by friction. The proper solution must therefore tend to develop a shock, which, according to the long-wave theory, forms first at some point (t_s, x_s) in the phase plane (figure 12). The 'early-stage' (long-wave) equations obviously cease to be uniformly valid at this point, and the more exact equations (4.1) and (4.2) must be used to continue the solution into the intermediate stage. The next stipulation for our particular solution is that there be no 'upstream influence', in the following sense. Let $x_n(t)$ be that straight line which extrapolates the nose position as computed from the early-stage equations. We then require that the solution at all (x, t)-points to the left $(x - x_n(t) < 0)$ of this line remain at the values given by the early-stage equation. Implicit here is the (theoretically) testable assumption that the early and intermediate stage can be joined in the vicinity of the line $x_n(t)$, such that the shock forms first at the nose. Otherwise, the early-stage solution will *not* be uniformly valid for all $x < x_n(t)$, and such an 'interior' shock $(x_s(t_s) < x_n(t_s))$ will not evolve as simply as the solution being proposed. As mentioned following (4.28), a shock at the nose implies that dU/dL must be finite at $L = 0$, and this boundary condition closes the early stage problem. Although the corresponding nose speed is zero, this will be greatly modified by the later stage. The upstream width L, on the other hand, will not be altered, and we have shown how the later-stage nose velocity can be computed by an adaptation of Benjamin's theory. The mathematical existence of such a simple solution has, of course, not been proven.

The question of whether this 'limiting bore' can be realized does not depend critically upon geometrical similitude between the *initial* state of the experiment and the theory. The initial-value problem posed by the experimental set-up is theoretically intractable (in our opinion), and only the later stages of the evolution requires rationalization. We have shown that the width L of the bore that finally emerges in the dam-break experiment ($0{\cdot}42 \pm 0{\cdot}06$) is in acceptable agreement with the theoretical model. The same is true for the nose speed (5.1), and the detrainment coefficient (5.2) is also accounted for qualitatively. (The numbers are insensitive to the potential vorticity, and rather insensitive to a second layer of finite depth (see appendix C).) We therefore conclude that the limiting bore is approximately realized in the complex adjustment process that occurs at the coastal stagnation point after the dam is broken, and when a constant-velocity boundary current is found. We have no explanation as to why this should occur.

Other types of coastal intrusions (i.e. solutions) can perhaps be realized by different experimental set-ups. Experiments in basins larger than ours would be desirable to test the Reynolds-number dependence suggested by figure 8. Such experiments may show that the downstream distance $\hat{x}$ is an important dimension, as is the case in the downstream spread of a *non*-rotating turbulent jet. A statistically steady source–sink experiment in a rotating frame would be desirable to resolve the 'large' scale eddies that we see, and the averaged profiles should eliminate the subjective element that enters into our determination of the width of the boundary current.

The general aspects of density currents discussed herein may be oceanically relevant, even though coasts are not vertical (the topographical effects must be taken into account (Stern 1980, p. 701)). We have in mind the formation of surface bores during spring runoff, and the formation of abyssal bores during the intermittent flow over the sills (e.g. Denmark Straits, Anagada–Jungfern Passage, Gibraltar Straits) that separate basins with different water masses. It would be unnecessarily restrictive to regard the bore as merely a starting (transient) phenomenon. It may occur at any boundary where there are strong longshore density gradients, even when these are intermittent features of a stationary process. The longshore fronts may form and dissipate (rather quickly), with the whole process being an important part of the mean boundary current. Such is the impression we get from the experiments, wherein the fluid detrained at the nose as well as the frontal instabilities give rise to a larger-scale mean baroclinic boundary current.

A substantial portion of the work was completed while the authors were in attendance at the Summer Study Program in Geophysical Fluid Dynamics at the Woods Hole Oceanographic Institution. The program is supported by the Office of Naval Research under contract N00014-79-C0671. Some of the latest experiments were conducted with support of the Office of Naval Research contract N0001481-C-0010. The authors are grateful for the skilled laboratory assistance of Robert Frazel and want to thank Nathan Paldor for his analysis of the data. This paper is Woods Hole Oceanographic Institution Contribution no. 4824.

Appendix A. A general constraint on the width

Following the remark made at the end of §3, we now examine the consequences of assuming invariance of $\frac{1}{2}\hat{\mathbf{V}}_c^2+f\hat{c}\hat{y}+g\hat{z}$ (3.2) on the free-surface dividing streamline. At one end $\hat{x}=-\infty$, we have $\hat{\mathbf{V}}_c^2=(\hat{u}_\mathrm{d}-\hat{c})^2$ where $\hat{u}_\mathrm{d}$ is the f-frame velocity on the dividing streamline far upstream from the nose, and $\hat{z}_\mathrm{d}$ is the corresponding free-surface height. The datum surface for measuring the latter quantity is the parabolic level surface that passes through the undisturbed free surface at $\hat{x}=+\infty$. The dividing streamline under consideration must also pass through the nose stagnation point at which $\hat{\mathbf{V}}_c=0$, $\hat{y}=0$, and the height is $\hat{z}=\hat{z}_\mathrm{s}$. By equating the Bernoulli functions at the two ends of the dividing streamline we get

$$\tfrac{1}{2}(\hat{u}_\mathrm{d}-\hat{c})^2+g\hat{z}_\mathrm{d}+f\hat{c}\hat{y}_\mathrm{d}=g\hat{z}_\mathrm{s}.$$

Using (3.3) to eliminate $\hat{z}_\mathrm{s}$ yields

$$\tfrac{1}{2}(\hat{u}_\mathrm{d}-\hat{c})^2+g\hat{z}_\mathrm{d}+f\hat{c}\hat{y}_\mathrm{d}=\tfrac{1}{2}\hat{c}^2.$$

Now $\hat{z}_\mathrm{d}$ is a positive number (proportional to $\hat{h}$ if the lower layer is relatively deep), and therefore the above equation gives the important inequality $f\hat{c}\,\hat{y}_\mathrm{d}<\frac{1}{2}\hat{c}^2$, which becomes

$$f\hat{y}_\mathrm{d}<\tfrac{1}{2}\hat{c}=\frac{1}{2}\frac{\displaystyle\int_0^{\hat{y}_\mathrm{d}}\hat{u}\hat{h}\,d\hat{y}}{\displaystyle\int_0^{\hat{y}_\mathrm{d}}\hat{h}\,d\hat{y}}$$

when (3.1) is used; it being understood that the integrals are evaluated at $\hat{x}=-\infty$.

The terms that have been consistently discarded in the formation of this inequality from the preceding equations are believed to be larger than the terms (unsteadiness and friction) neglected in the primitive equations, and therefore we have high confidence in the upper bound for $\hat{y}_d$. This involves no far-reaching assumptions, such as have been made in the text to obtain an explicit equation for the width of the intrusion.

Since the right-hand side of the inequality is certainly less than half the maximum $\hat{u}(y)$, we conclude that the upstream Rossby number based on maximum $\hat{u}$ and $\hat{y}_\mathrm{d}$ must be *greater* than two, for a quasi-laminar bore to propagate along a coast. Initial distributions of density having widths larger than that permitted by the above inequality must therefore suffer a profound readjustment (such as bifurcation) before the density current can propagate.

If the lower layer is very deep, so that the corresponding current in the rotating frame is zero then $\hat{u}=-(\Delta\rho/\rho)\,(g/f)\,\partial\hat{h}/\partial\hat{y}$. Upon substituting this and noting the geometrical inequality

$$\int_0^{\hat{y}_\mathrm{d}}\hat{h}\,d\hat{y}>\int_0^{\hat{y}_\mathrm{d}}\hat{h}_0(1-\hat{y}/\hat{y}_\mathrm{d})\,d\hat{y},$$

where $\hat{h}_0$ is the upstream wall height, we get

$$\hat{y}_\mathrm{d}<\frac{(g^*\hat{h}_0)^{\frac{1}{2}}}{f\sqrt{2}},\quad g^*\equiv g\Delta\rho/\rho.$$

This states that the laminar bore width $\hat{y}_\mathrm{d}$ (which we interpret to be the $\hat{L}$ measured in our experiments) must be less than 0·717 times the Rossby radius of deformation.

Appendix B. Some additional features of the evolution of the solutions

Although this paper is primarily concerned with the leading edge of the intrusion, the nature of the waves that can propagate on the trailing front are also of interest. This subject has been studied by Stern (1980), for the case of zero potential vorticity, and the modifications required by a finite potential vorticity are given below.

The discussion is based on the properties of the similarity solutions (4.25)–(4.27), which will be summarized here. Typical solutions of the two Riemann-invariant families ($\pm$) of (4.25)–(4.27) are given in figure 10 for a non-dimensional potential vorticity $H = 2$, along with other auxiliary curves. A comparison with the zero-potential-vorticity case in figure 11 yields no qualitative differences.

A curve such as *PS* in both figures corresponds to propagating bores as defined by Stern in which the upstream velocities are larger than the nose speed and in which the energy flux converges towards the nose. The wedge solutions such as curve *SR* have the opposite behaviour, that is the thickness of the nose decreases with time.

The functional relation between $L(x, t)$, $U(x, t)$ and $h(x, o, t)$ is independent of time relative to an observer moving with the local propagation speed given by (4.24), and which for finite potential vorticity is given by

$$\frac{dx}{dt} = \frac{2H^{\frac{1}{2}}\left[\frac{U}{H^{\frac{1}{2}}}\cosh\frac{L}{H^{\frac{1}{2}}} - \sinh\frac{L}{H^{\frac{1}{2}}}\right]}{c \pm d^{\frac{1}{2}}}, \tag{B 1a}$$

$$c = 1 + \cosh\frac{L}{H^{\frac{1}{2}}},$$

$$d = \frac{2\sinh\frac{L}{H^{\frac{1}{2}}}\left[\left(\sinh^3\frac{L}{2H^{\frac{1}{2}}}\right)\frac{U}{H^{\frac{1}{2}}} - \cosh^3\frac{L}{2H^{\frac{1}{2}}} + 2\cosh\frac{L}{2H^{\frac{1}{2}}}\right]}{\frac{U}{H^{\frac{1}{2}}}\cosh\frac{L}{2H^{\frac{1}{2}}} - \sinh\frac{L}{2H^{\frac{1}{2}}}}.$$

For $H \rightarrow \infty$, one regains the zero-potential-vorticity case

$$\frac{dx}{dt} = \frac{U - L}{1 \pm (L/2U - L)^{\frac{1}{2}}}. \tag{B 1b}$$

Other curves in figures 10 and 11 that limit the regions of physical meaning are also drawn in the phase space (U, L) and are listed below.

The possible values of the upstream state of the current are given by the curve *PQR*, which is obtained by setting $h(-\infty, o, t) = 1$ in (4.11), and thus we have

$$U = \frac{1 + H\left(\cosh\frac{L}{H^{\frac{1}{2}}} - 1\right)}{H^{\frac{1}{2}}\sinh\frac{L}{H^{\frac{1}{2}}}}. \tag{B 2}$$

when $H \rightarrow \infty$ this reduces to Stern's results

$$U = \frac{1}{L} + \tfrac{1}{2}L.$$

Solutions of physical meaning must lie above the curve *OB*, which corresponds to the sections of the boundary current where the depth at the wall goes to zero, and which is obtained by setting $h(x, o, t) = 0$ in (4.11):

$$U = H^{\frac{1}{2}}\left(\tanh\frac{L}{2H^{\frac{1}{2}}}\right). \tag{B 3}$$

The limit for zero potential vorticity yields

$$U = \tfrac{1}{2}L.$$

Curve OR is the locus of sections where the flow at the wall reverses, and is found by setting $u(x, o, t) = 0$ in (4.12):

$$U = H^{\frac{1}{2}}\left(\tanh\frac{L}{H^{\frac{1}{2}}}\right). \tag{B 4}$$

The limit for $H \rightarrow \infty$ yields $U = L$.

Many of the conclusions for the zero potential vorticity are not changed for non-zero constant potential vorticity, as the illustration below for the quasi-geostrophic wave shows.

Let us consider a boundary geostrophic current with a front that lies parallel to the coast in the interval $-\infty < x < +\infty$. If the current is unidirectional, then the largest possible width will correspond to the point R in figure 10, i.e. to the value

$$L_R = H^{\frac{1}{2}} \operatorname{arg\,cosh} \frac{H}{H-1}, \tag{B 5}$$

which is found by intersecting the upstream-state curve (B 2) with the locus of sections where the flow reverses at the wall (B 4). If this basic state is perturbed by a wavelike motion corresponding to a similarity solution such as the (+) Riemann invariant passing through R, then the local propagation speed (B 1*a*) will have opposite signs for sections of the boundary current lying on each side of curve OR, i.e. for a width $L >$ or $< L_R$. If $L > L_R$, then the local propagation speed (B 1*a*) will be negative since $U_{(+)}$ (L) lies below the curve OR and will increase in magnitude as $L - L_R$ increases. Therefore, the front will steepen on the upstream side of the wave and the amplitude dispersion depending on the boundary-current width will lead to a backwards-breaking wave. Moreover, one can verify from the expression of the transverse velocity dL/dt along the streamline,

$$v = \frac{\partial L}{\partial t} + U\frac{\partial L}{\partial x} = \frac{U}{1-U'}\frac{\partial L}{\partial x},$$

and by evaluating $\partial h/\partial x$ from (4.11),

$$\frac{\partial h}{\partial x} = \left[-H^{\frac{1}{2}}\sinh\frac{L-y}{H^{\frac{1}{2}}} + U\cosh\frac{L-y}{H^{\frac{1}{2}}}\right]\frac{\partial L}{\partial x},$$

that $v \simeq |\partial h/\partial x|_{y=L}$ at point R (since $U' \simeq 0$) and the wavelike motion is quasi-geostrophic for both longitudinal and transverse velocities. Thus the discussion above is independent of the finite value of constant potential vorticity, and the generalization of 'the other waves and blocking waves' as discussed by Stern (1980) is also straightforward.

Appendix C. The effect of the finite bottom-layer depth

Although the thickness of the heavy fluid in our experiments was an order of magnitude larger than the thickness of the intrusion, there will be some vertical compression of the heavy fluid columns as the bore passes over them, and it is of interest to investigate the feedback. For this purpose the rigid bottom of the tank is assumed to be a level surface so that the fluid in advance of the nose has uniform thickness and a uniform potential vorticity. The non-dimensional value of the latter is denoted by $1/H_2$, whereas $1/H_1$ now denotes the potential vorticity of the upper layer: both of these being based on h_0 as the unit of height. If $P_1(x, y, t)$ denotes the pressure on the upper $z = 0$ surface, and $P_2(x, y, t)$ the pressure on the bottom surface, then the generalization of (4.7) and (4.8) to the two-layer case is

$$\left.\begin{aligned} u_{1t}-(1-u_{1y})\,v_1 &= -(p_1+\tfrac{1}{2}u_1^2)_x, \\ u_{2t}-(1-u_{2y})\,v_2 &= -(p_2+\tfrac{1}{2}u_2^2)_y. \end{aligned}\right\} \tag{C 1}$$

$$u_1 = -(p_1)_y, \quad u_2 = -(p_2)_y. \tag{C 2}$$

The hydrostatic relation connects the upper-layer thickness h with the pressure gradients:

$$\nabla p_1 - \nabla p_2 = \nabla h, \tag{C 3}$$

and thus the elimination of p_1 and p_2 in (C 1) and (C 2) gives

$$(u_1-u_2)_t - [(1-u_{1y})\,v_1-(1-u_{2y})\,v_2] = -(h+\tfrac{1}{2}u_1^2-\tfrac{1}{2}u_2^2)_x, \tag{C 4}$$

$$(u_1-u_2) = -h_y. \tag{C 5}$$

The continuity relations for the two layers are

$$h_t+(hu_1)_x+(hv_1)_y = 0, \tag{C 6}$$

$$-h_t+[(H_2-h)u_2]_x+[(H_2-h)v_2]_y = 0, \tag{C 7}$$

and the potential-vorticity equations are

$$\frac{1-u_{1y}}{h} = \frac{1}{H_1}, \tag{C 8}$$

$$\frac{1-u_{2y}}{H_2-h} = \frac{1}{H_2}. \tag{C 9}$$

The top layer extends from $y = 0$ to $y = L(x, t)$, where $h = 0$, whereas the bottom layer extends from $y = 0$ to $y = \infty$ with a non-analytic behaviour at $y = L(x, t)$. The circulation theorem precludes a vortex sheet in the heavy fluid, and thus u_2 must be continuous on either side of the front. Moreover (C 9) implies $u_{2_y} = 0$ for all $y \geqslant L$, and therefore

$$\frac{\partial u_2}{\partial y} = 0 = u_2 \quad \text{at} \quad y = L(x, t), \tag{C 10}$$

for otherwise u_2 would be infinite at $y = \infty$.

The solutions of (C 5), (C 8) and (C 9) that satisfy the $y = L$ boundary conditions (C 10) are

$$h(x, y, t) = H\left(1-\cosh\frac{L-y}{H^{\frac{1}{2}}}\right)+H^{\frac{1}{2}}U\sinh\frac{L-y}{H^{\frac{1}{2}}}. \tag{C 11}$$

$$u_1(x, y, t) = \frac{H}{H_2}(y-L+U)+\frac{H}{H_1}\left(-H^{\frac{1}{2}}\sinh\frac{L-y}{H^{\frac{1}{2}}}+U\cosh\frac{L-y}{H^{\frac{1}{2}}}\right). \tag{C 12}$$

$$u_2(x, y, t) = \frac{H}{H_2}(y-L+U)-\frac{H}{H_2}\left(-H^{\frac{1}{2}}\sinh\frac{L-y}{H^{\frac{1}{2}}}+U\cosh\frac{L-y}{H^{\frac{1}{2}}}\right). \tag{C 13}$$

where

$$H \equiv \frac{H_1 H_2}{H_1+H_2}$$

now denotes an 'equivalent depth', and $U = u_1(x, L, t)$ as previously.

To obtain the long-wave equations for (U, L) we will evaluate (C 4) on $y = L$ where $\partial u_1/\partial y = 1$, $\partial u_2/\partial y = u_2 = 0$, and therefore

$$[(u_1-u_2)_t]_{y=L}+[(h+\tfrac{1}{2}u_1^2)_x]_{y=L}+[v_2]_{y=L} = 0. \tag{C 14}$$

We will also use the integrated version of (C 6) and (C 7), or

$$\left.\begin{aligned}\int_0^{L(x,t)} h_t\,dy+\int_0^{L(x,t)}(hu_1)_x\,dy &= 0,\\ -\int_0^{L(x,t)} h_t\,dy+\int_0^{L(x,t)}((H_2-h)u_2)_x\,dy+[H_2v_2]_{y=L} &= 0.\end{aligned}\right\} \tag{C 15}$$

Eliminating between (C 14) and (C 15) gives the following system:

$$\begin{aligned}[(u_1-u_2)_t]_{y=L}+[(h+\tfrac{1}{2}u_1^2)_x]_{y=L}+\frac{1}{H_2}\int_0^{L(x,t)} h_t\,dy&\\ -\int_0^{L(x,t)} u_{2x}\,dy+\frac{1}{H_2}\int_0^{L(x,t)}(hu_2)_x\,dy &= 0,\end{aligned} \tag{C 16}$$

$$\frac{\partial}{\partial t}\int_0^{L(x,t)} h\,dy+\frac{\partial}{\partial x}\int_0^{L(x,t)} hu_1\,dy = 0. \tag{C 17}$$

When the profiles of $u_1(x, y, t)$, $h(x, y, t)$ and $u_2(x, y, t)$ given by (C 11)–(C 13) are used to evaluate the above terms, and when the result is simplified, we get

$$\begin{aligned}&\left(\frac{U}{H}\sinh\frac{L}{H^{\frac{1}{2}}}\right)\frac{\partial L}{\partial t}\\ &+\left\{\left(\cosh\frac{L}{H^{\frac{1}{2}}}-1\right)\left(\frac{U}{H^{\frac{1}{2}}}\cosh\frac{L}{H^{\frac{1}{2}}}-\sinh\frac{L}{H^{\frac{1}{2}}}\right)\left[1+\frac{H}{H_2}\left(\cosh\frac{L}{H^{\frac{1}{2}}}-1\right)\right]\right\}\frac{\partial U}{\partial x}\\ &+\left\{\left(\frac{U}{H^{\frac{1}{2}}}\sinh\frac{L}{H^{\frac{1}{2}}}-\cosh\frac{L}{H^{\frac{1}{2}}}+1\right)\left(\frac{U}{H^{\frac{1}{2}}}\cosh\frac{L}{H^{\frac{1}{2}}}-\sinh\frac{L}{H^{\frac{1}{2}}}\right)\left(1+\frac{H}{H_2}\left(\cosh\frac{L}{H^{\frac{1}{2}}}-1\right)\right)\right.\\ &\left.+\frac{H}{H_2}\frac{U}{H^{\frac{1}{2}}}\sinh\frac{L}{H^{\frac{1}{2}}}\left(\frac{U}{H^{\frac{1}{2}}}-\frac{L}{H^{\frac{1}{2}}}-\left(\frac{U}{H^{\frac{1}{2}}}\cosh\frac{L}{H^{\frac{1}{2}}}-\sinh\frac{L}{H^{\frac{1}{2}}}\right)\right)\right\}\frac{\partial L}{\partial x} = 0,\end{aligned} \tag{C 18}$$

$$\begin{aligned}&\frac{\partial U}{\partial t}-\frac{\partial L}{\partial t}+\frac{\partial U}{\partial x}\left\{U-\frac{H}{H_2}H^{\frac{1}{2}}\left[\frac{L}{H^{\frac{1}{2}}}+\sinh\frac{L}{H^{\frac{1}{2}}}\left(\frac{U}{H^{\frac{1}{2}}}\sinh\frac{L}{H^{\frac{1}{2}}}-\cosh\frac{L}{H^{\frac{1}{2}}}\right)\right]\right\}\\ &+\frac{\partial L}{\partial x}\frac{H}{H_2}H^{\frac{1}{2}}\left[\frac{L}{H^{\frac{1}{2}}}-\tfrac{1}{2}\sinh\frac{2L}{H^{\frac{1}{2}}}-\frac{U}{H^{\frac{1}{2}}}\sinh\frac{L}{H^{\frac{1}{2}}}\left(\frac{U}{H^{\frac{1}{2}}}\cosh\frac{L}{H^{\frac{1}{2}}}-2\sinh\frac{L}{H^{\frac{1}{2}}}\right)\right] = 0.\end{aligned} \tag{C 19}$$

One can verify that for $H/H_2 \rightarrow 0$, i.e. in the case of a boundary current overlying an infinitely deep second layer, (C 18) and (C 19) are identical with the system found in §4, (4.15) and (4.13) respectively. Terms multiplying H/H_2, i.e. due to the coupling of the bore with a second layer of *finite depth*, give an extra contribution of order L^2/H_2 for small $L/H^{\frac{1}{2}}$.

The similarity solutions satisfying the functional relation (4.20) obey the ordinary differential equation

$$\frac{dU}{dL} = 1 - \frac{2\dfrac{U}{H^{\frac{1}{2}}}\cosh\dfrac{L}{2H^{\frac{1}{2}}}\left[1-\dfrac{H}{H_2}\sinh\dfrac{L}{H^{\frac{1}{2}}}\left(\dfrac{U}{H^{\frac{1}{2}}}\cosh\dfrac{L}{H^{\frac{1}{2}}}-\sinh\dfrac{L}{H^{\frac{1}{2}}}\right)\right]}{a \pm (a^2+b)^{\frac{1}{2}}}. \tag{C 20}$$

$$a = \sinh\frac{L}{H^{\frac{1}{2}}}\left[\cosh\frac{L}{2H^{\frac{1}{2}}}-\frac{U}{H^{\frac{1}{2}}}\sinh\frac{L}{2H^{\frac{1}{2}}}-2\frac{H}{H_2}\sinh\frac{L}{2H^{\frac{1}{2}}}\left(\frac{U}{H^{\frac{1}{2}}}\cosh\frac{L}{H^{\frac{1}{2}}}-\sinh\frac{L}{H^{\frac{1}{2}}}\right)\right]. \tag{C 21a}$$

$$\begin{aligned} b = {} & 2\sinh\frac{L}{H^{\frac{1}{2}}}\left(\frac{U}{H^{\frac{1}{2}}}\cosh\frac{L}{H^{\frac{1}{2}}}-\sinh\frac{L}{H^{\frac{1}{2}}}\right) \\ & \times\left\{1+\frac{H}{H_2}\left[\cosh\frac{L}{H^{\frac{1}{2}}}-1+\sinh\frac{L}{H^{\frac{1}{2}}}\left(\frac{U}{H^{\frac{1}{2}}}\cosh\frac{L}{H^{\frac{1}{2}}}-\sinh\frac{L}{H^{\frac{1}{2}}}\right)\right]\right. \\ & \left.-\left(\frac{H}{H_2}\right)^2\sinh\frac{L}{H^{\frac{1}{2}}}\left(\cosh\frac{L}{H^{\frac{1}{2}}}-1\right)\left(\frac{U}{H^{\frac{1}{2}}}\cosh\frac{L}{H^{\frac{1}{2}}}-\sinh\frac{L}{H^{\frac{1}{2}}}\right)\right\} \end{aligned} \tag{C 21b}$$

When putting $H/H_2 = 0$ in (C 20) and (C 21), we recover the system found for an infinitely deep second layer, (4.25) and (4.26). Again the leading terms in an expansion in $L/H^{\frac{1}{2}}$ in (C 20) near $L = 0$ are identical with those previously found for the zero-potential-vorticity case. Therefore the discussion concerning the nose boundary condition still applies, i.e. we need $U(0) = 0$.

The upstream width of this simple bore will be found by integrating (C 20) using (4.29), and by finding the intersection with the upstream-state curve

$$U = \frac{1+H\left(\cosh\dfrac{L}{H^{\frac{1}{2}}}-1\right)}{H^{\frac{1}{2}}\sinh\dfrac{L}{H^{\frac{1}{2}}}} \tag{C 22}$$

obtained by setting $h(-\infty, 0, t) = 1$ in (C 11).

Table 3 gives $L(-\infty)$ as a function of the initial equivalent depth H and the ratio H/H_2. However, for a given H, not all values of H/H_2 are allowed, since $H_2 \geqslant 1$ and $H_1 \geqslant 1$. The entire range of $L(-\infty)$ in table 3 is

$$0{\cdot}418 \leqslant L(-\infty) \leqslant 0{\cdot}516, \tag{C 23}$$

and thus the coupling with a second layer may increase the width of the boundary current up to 25 %. The largest values of $L(-\infty)$ are found for small H $(0{\cdot}5 < H < 1)$, i.e. for values of both H_1 and H_2 close to 1. The maximum of $L(-\infty)$ is reached for $H = 0{\cdot}5$ $(H_1 = 1$ and $H_2 = 1)$.

However, interesting values of H_1 and H_2 would be closer to 2 (remember that the upstream height has been chosen for normalizing the heights) and in this range the width of the boundary current remains within 10 % of the value found for the very simplest case of one layer with zero potential vorticity. The new profiles of current

$H \backslash H/H_2$	0·1	0·3	0·5	0·7	0·9
0·5	—	—	0·516	—	—
0·75	—	0·450	0·470	0·496	—
1	0·431	0·442	0·454	0·469	0·488
2	0·425	0·429	0·435	0·440	0·446
10	0·420	0·421	0·422	0·422	0·423

TABLE 3. Values of upstream width $L(-\infty)$ as a function of initial equivalent depth H and of ratio H/H_2

given by (C 11)–(C 13) have also been used to evaluate the nose speed c and the detrainment coefficient δ. For the upstream wall velocity we have

$$u_1 = \frac{H}{H_2}(U-L) + \frac{H}{H_1}\frac{(1-H)\cosh\dfrac{L}{H^{\frac{1}{2}}}+H}{H^{\frac{1}{2}}\sinh\dfrac{L}{H^{\frac{1}{2}}}} \quad \text{at} \quad x=-\infty, \quad y=0, \tag{C 24}$$

where U is defined by the upstream condition (C 22). The other quantities $\int h\, dy$ and $\int hu\, dy$ needed for (δ, c) have the same formal expression as (5.5) and (5.4) respectively, but in this case H is the initial equivalent depth. Choosing $H_1 = H_2 = 2$ and $L(-\infty) = 0{\cdot}43$ yields for c and δ

$$c = 1{\cdot}56, \tag{C 25}$$

$$\delta = 0{\cdot}34. \tag{C 26}$$

Again we conclude that the bore speed seems to be independent of the structure of the current.

REFERENCES

BRITTER, R. E. & SIMPSON, J. E. 1978 Experiments on the dynamics of a gravity current head. *J. Fluid Mech.* **88**, 223–240.

BENJAMIN, T. B. 1968 Gravity currents and related phenomena. *J. Fluid Mech.* **31**, 209–248.

GRIFFITHS, R. W. & LINDEN, P. F. 1981 The stability of vortices in a rotating, stratified fluid. *J. Fluid Mech.* **105**, 283–316.

HODGMAN, C. D. (ed.) 1961 *Handbook of Chemistry and Physics*, 43rd edn. Chemical Rubber.

KÁRMÁN, T. v. 1940 The engineer grapples with nonlinear problems. *Bull. Am. Math. Soc.* **46**, 615.

SAUNDERS, P. M. 1973 The instability of a baroclinic vortex. *J. Phys. Oceanogr.* **3**, 61–65.

SIMPSON, J. E. & BRITTER, R. E. 1979 The dynamics of the head of a gravity current advancing over a horizontal surface. *J. Fluid Mech.* **94**, 477–495.

STERN, M. E. 1975 *Ocean Circulation Physics*. Academic.

STERN, M. E. 1980 Geostrophic fronts, bores, breaking and blocking waves. *J. Fluid Mech.* **99**, 687–703.

WADHAMS, P., GILL, A. E. & LINDEN, P. F. 1979 Transects by submarine of the east Greenland polar front. *Deep-Sea Res.* **26A**, 1311–1327.

LARGE AMPLITUDE LONG WAVES IN A SHEAR FLOW

MELVIN E. STERN

NATHAN PALDOR

Graduate School of Oceanography, University of Rhode Island,
Kingston, Rhode Island 02881

ABSTRACT

Large amplitude disturbances in a boundary layer shear flow are considered in an inviscid and longwave theory. Initially weak horizontal convergences are concentrated and amplified in time, thereby increasing the maximum normal velocity (V) until it becomes comparable with the horizontal velocity. The effect is first demonstrated in a two dimensional model having piecewise uniform vorticity. The leading edge of the compact disturbance propagates downstream more rapidly than the trailing edge, but no "quiet" zone appears in the center. Instead $V \to \infty$ and a tendency for wavebreaking occurs. The evolving large V pattern is consistent with observations [1] of the laminar spike just prior to its breakdown. The longwave theory is generalized to three dimensional motions, and the effect of an initial spanwise divergence is such as to rationalize the initial vorticity assumed in the two dimensional model.

I. INTRODUCTION

Because of its laminar-like initial behavior the "spike" in the experiment of Kovasznay, Komoda, and Vasudeva [1] is perhaps the simplest member of the "spot" family which have been the subject of many recent investigations of the transition to turbulence. [2,3,4] When a small amplitude and spanwise modulated Tollmien-Schlichung wave is generated [1] by means of an oscillating ribbon in the boundary layer, the wave amplifies downstream and the spanwise vortex stretching produces the anomalously high vorticity region shown in Fig. 1a. The spanwise variation of this vorticity at a later stage of development of the disturbance is shown in Fig. 1b. Notice that the normal velocity field is weak and broad in Fig. 1c, which corresponds to the same stage as Fig. 1a. But this field concentrates and greatly increases in magnitude in Fig. 1d, which corresponds to a later stage of development than either Fig. 1a or Fig. 1b. The vorticity isopleths (not shown) corresponding to Fig. 1d show that the maximum value increases only by a factor of two, whereas the normal velocity increases sevenfold from Fig. 1c to Fig. 1d. Moreover, the lateral scale of the vortex stretching effect is much larger than the scale of the intense updraft (Fig. 1d), and therefore it is hard to see how the latter effect can be explained solely on the basis of the former effect. We shall therefore investigate first the ability of a two dimensional (vorticity conserving) model, based on an initial state resembling Fig. 1a, to explain the large normal velocities at the later time (Fig. 1d). The two dimensional approximation has also been used [5,6,7] in a restricted sense to analyze the motion on the axis of symmetry of a spot. Some of our restrictions will be removed by the generalization to three dimensions in Sec. VI.

The simplest idealization of Fig. 1 is a model (Fig. 2) which contains three piecewise uniform layers. The lower region corresponds to the disturbed boundary layer, the middle region is a compact "inclusion" representing the vorticity anomaly, and the upper layer is the disturbed free stream. The question of the origin of this anomaly is, as previously mentioned, beyond the scope of a two dimensional theory, and we first address the question of how the anomaly evolves in time. Since the cross-stream velocities in Fig. 1c are relatively weak and broad (compared to the boundary layer thickness and the horizontal velocities therein), it is reasonable to start with a long wave approximation, and to see if solutions evolving from the initial state resemble Fig. 1d. If so, then the theory will have to be modified at this stage, because the normal velocities in Fig. 1d are no longer "small" and slowly varying.

Fig. 2 shows the model with the undisturbed horizontal velocity profile appearing on the left. In non-dimensional units the undisturbed vorticity of the lower layer is unity, the undisturbed velocity of the upper layer is unity, the undisturbed lower layer thickness is $L=1$, and the upper boundary is at $y=H$. Between the two uniform vorticity layers of the undisturbed state a compact "inclusion" having a uniform vorticity δ^{-1} is introduced in the initial state. The inclusion is bounded below by the vorticity discontinuity surface $L(x,t)$, and bounded above by another discontinuity surface at $y=L_2(x,t)$.

The piecewise uniform vorticity of the initial state of the two dimensional flow must, according to the conservation of vorticity, be piecewise uniform and constant at all time. The initial variations in $L-1$ are large $O(1)$ in amplitude but slowly varying in the downstream direction, i.e. the characteristic downstream scale is larger than the cross-stream scales by a factor $\epsilon^{-1}\rightarrow\infty$. Therefore the dominant contribution to the vorticity is $\partial u/\partial y$, where $u(x,y,t)$ is the x

component of velocity, and it follows that $\partial u/\partial y$ is piecewise uniform. Therefore u is piecewise linear in y, $\partial u/\partial x$ is independent of y, and the normal (or vertical) velocity $v(x,y,t)$ must be a piecewise linear function of y which vanishes at the lower boundary $y=0$. These qualitative features hold for all nondimensional times t for which the computed magnitude of V is compatible with the long wave assumption, and these features allow us (Sec. II) to separate the y coordinate from the equations of motion. The derivation of the long wave equations for $L(x,t)$ is straightforward when $H-1=O(1)$ whereas the experimentally[1,2,3,4] relevant case of infinite H (treated in Sec. III) requires more intricate treatment. Moreover, an exact similarity solution can be found for the finite H case, the results of which will support some general inferences drawn from numerical solutions and qualitative considerations of the equations.

We will show that the leading edge of a large amplitude vorticity inclusion propagates with the free stream velocity, and although the trailing edge propagates with a lesser velocity no "quiet" zone appears in the middle of the compact disturbance. Instead, the normal component of velocity increases and a "shock" discontinuity forms in the middle of the disturbance - according to the solution of the hyperbolic equations. This behavior $(|v|\to\infty)$ contrasts with (or perhaps complements) Landahls[8] solution for an infinitesimal three dimensional perturbation, in which $|v|$ decreases with t although the total perturbation energy of the spreading wave packet increases. Our result (Fig. 3) provides a qualitative explanation for the large normal velocities in Fig. 1d.

Our long wave approximation seems to be justified for the early stage (cf. Fig. 1a) but it obviously must be modified when the solution nears the "shock" stage (defined as the discontinuity point of the hyperbolic long wave equations). The neglected short wave terms will probably tend to disperse the shock, but it is plausible that nonlinear "wave steepening" (large lateral gradients of vorticity and large normal velocities) will predominate for sufficiently large amplitudes (i.e. $L-1 = O(1)$). "Wave breaking" (folding of the vorticity isopleths) may also occur, and the investigation of these strong nonlinear effects within the framework of a piecewise uniform vorticity model seems feasible. We shall return to these motivating remarks in Sec. VI.

II. LONG WAVE EQUATIONS

As previously mentioned, the free stream velocity is the scale for the horizontal velocity u ; the scale for the y coordinate is the undisturbed boundary layer thickness; δ^{-1} is the relative vorticity of the inclusion. The scale for the nondimensional downstream coordinate is the initial width of the inclusion, which is larger than the boundary layer thickness by a factor $\epsilon^{-1} \gg 1$, and the scale for nondimensional time t is the downstream width divided by the downstream velocity. The scale for the nondimensional vertical velocity $v(x,y,t)$ is taken to be ϵ times the u-scale, so that neither the nondimensional continuity equation

$$\frac{\partial u}{\partial x} + \frac{\partial v}{\partial y} = 0 \qquad (1)$$

nor the nondimensional kinematic boundary condition

$$v(x, L(x,t), t) = \frac{dL}{dt} = \frac{\partial L}{\partial t} + u(x, L, t)\frac{\partial L}{\partial x} \tag{2}$$

contains the ϵ parameter.

The vorticity in each of the three layers is then given (respectively) by

$$\frac{\partial u}{\partial y} - \frac{\partial v}{\partial x}\epsilon^2 = (0, \delta^{-1}, 1) \tag{3a}$$

$$0 \neq \delta^{-1} \neq 1 \tag{3b}$$

We now let $\epsilon \to 0$ with all other quantities (most notably H) kept constant at $O(1)$, and a separate derivation will be given (Sec. III) for the interesting case $H = \infty$. Therefore the long wave limit of 3a is

$$\frac{\partial u}{\partial y} = \{0, \delta^{-1}, 1\} \tag{4}$$

and u must be a piecewise linear function of y. From (1) And (4) it then follows that

$$\frac{\partial}{\partial y}\frac{du}{dt} = \left(\frac{\partial}{\partial t} + u\frac{\partial}{\partial x} + V\frac{\partial}{\partial y}\right)\frac{\partial u}{\partial y} + \frac{\partial u}{\partial y}\left(\frac{\partial u}{\partial x} + \frac{\partial v}{\partial y}\right) = \frac{d}{dt}\frac{\partial u}{\partial y} = 0 \tag{5}$$

or du/dt (and the horizontal pressure gradient) is independent of y. ~~(Conversely, if $d(\partial u/\partial y)/dt = 0$ and (4) are satisfied in the shear layers, then the continuity equation (1) must be satisfied~~). We shall therefore set the value of du/dt at the top of each layer equal to the value at the bottom.

If the initial values of the velocity are continuous across each discontinuity surface, then the circulation theorem requires u to be continuous at all t. Let $U_L(x,t)$ denote the horizontal velocity at $y = L(x,t)$, and let $U(x,t)$ denote the horizontal velocity at the upper discontinuity surface of the inclusion; then the local thickness of the middle layer is

$$\delta(U - U_L) \tag{6}$$

It is readily proved* that the value of $du/dt = \partial u/\partial t + u\,\partial u/\partial x + v\,\partial u/\partial y$ at $y = L(x,t)$. is the same as the acceleration

$$\frac{\partial U_L}{\partial t} + U_L \frac{\partial U_L}{\partial x} \tag{7a}$$

of a material parcel on the lower discontinuity surface; and also

---

*Let a layer of vorticity δ_*^{-1} be bounded by a discontinuity surface at $y = \eta(x,t)$. The linear velocity in this layer may be written as $u(x,y,t) = u(x,\eta,t) - (\eta - y)\,\delta_*^{-1}$, and since $v(x,\eta,t) = d\eta/dt$ we have

$$\left(\frac{du}{dt}\right)_{y=\eta} = \frac{\partial}{\partial t}\left[u(x,\eta,t) - \eta\delta_*^{-1}\right] + u(x,\eta,t)\frac{\partial}{\partial x}\left[u(x,\eta,t) - \delta_*^{-1}\eta\right] + \delta_*^{-1}\frac{d\eta}{dt}$$

The terms containing δ_*^{-1} are seen to cancel, and the result proves (7a).

$$\frac{\partial U}{\partial t} + U\frac{\partial U}{\partial x} \tag{7b}$$

equals du/dt at the upper discontinuity surface. Eq. (5) then implies that (7a) equals the value of the acceleration at $y = 0$, where the horizontal velocity is $U_L - L$, and thus we have

$$\frac{\partial}{\partial t}(U_L - L) + (U_L - L)\frac{\partial}{\partial x}(U_L - L) = \frac{\partial U_L}{\partial t} + U_L\frac{\partial U_L}{\partial x} \tag{8a}$$

or

$$\frac{\partial L}{\partial t} + \frac{\partial}{\partial x}\left(L U_L - L^2/2\right) = 0 \tag{8b}$$

Likewise the acceleration (7b) at the top of the middle layer must equal the acceleration (7a) at the bottom of that layer, or

$$\frac{\partial U}{\partial t} + U\frac{\partial U}{\partial x} = \frac{\partial U_L}{\partial t} + U_L\frac{\partial U_L}{\partial x} \tag{9}$$

Instead of writing a differential equation for the third layer, it is much simpler to use the vertically integrated continuity equation. Thus, a third equation connecting U_L, U, L is obtained by equating the transport $\int_0^H u\,dy$ at $x = -\infty$, or $H - 1 + 1/2 = H - 1/2$, to the transport at any x viz.

$$\int_0^H u\,dy = \frac{L}{2}\left[\bar{U}_L + (\bar{U}_L - L)\right] + \frac{\delta}{2}(\bar{U} - \bar{U}_L)(\bar{U} + U_L) + \left[H - L - \delta(\bar{U} - \bar{U}_L)\right]U$$

When this is set equal to $H - 1/2$ the result simplifies to

$$L(\bar{U}_L - L/2) + \bar{U}(H - L) + \frac{\delta}{2}(\bar{U} - \bar{U}_L)(\bar{U}_L - \bar{U}) = H - 1/2$$

or

$$\bar{U} = H^{-1}\left[H - \tfrac{1}{2} + L^2/2 - LD + \delta D^2/2\right] \tag{10}$$

where

$$D \equiv \bar{U}_L - \bar{U} \tag{11}$$

is the velocity difference across the inclusion. When these are used to eliminate $\bar{U}_L, \bar{U}$ in (8)-(9) we get the longwave equations of motion

$$\frac{\partial D}{\partial t} + \frac{1}{2}\frac{\partial}{\partial x} D\left[D + H^{-1}(2H - 1 + L^2 - 2LD + \delta D^2)\right] = 0 \tag{12}$$

$$\frac{\partial L}{\partial t} + \frac{1}{2}\frac{\partial}{\partial x} L\left[2D - L + H^{-1}(2H - 1 + L^2 - 2LD + \delta D^2)\right] = 0 \tag{13}$$

Since $L(\pm\infty, t) = 1$ and $D(\pm\infty, t) = 0$, the horizontal integrals of (12)-(13) yield

$$\frac{\partial}{\partial t}\int_{-\infty}^{+\infty} D\,dx = 0 = \frac{\partial}{\partial t}\int_{-\infty}^{+\infty} L\,dx \tag{14}$$

which merely express the conservation of volume for the inclusion (local thickness of $-D\delta$) and for the lower layer. A more interesting momentum integral

$$\frac{\partial}{\partial t}\int_{-\infty}^{+\infty} dx \int_{0}^{L} u\,dy = \int_{-\infty}^{+\infty} L\dot{U}\,dx$$
$$\dot{U} = \frac{\partial U}{\partial t} + U\frac{\partial U}{\partial x} \tag{15}$$

for the lower layer can be derived by using $u = U_L - (L-y)$ (8a), (8b), and (9). Eq. (15) states that the total momentum of the lower layer can only change if there is a horizontal pressure gradient ($\dot{U}$) in the upper layer.

We confine attention to disturbances with positive vorticity $\delta^{-1} > 0$ (changing the sign yields profiles with jet-like structures), and since the layer thickness (6) must be positive, it follows that (11) must be negative, or

$$D(x,t) \leq 0$$

III. DEEP UPPER LAYER

The foregoing asymptotic expansion is still valid when $1 \gg H^{-1} \gg \epsilon^2$ in which case (12), (13), (10) and (11) simplify to

$$\frac{\partial (D+1)}{\partial t} + \frac{\partial}{\partial x}\frac{(D+1)^2}{2} = 0 \tag{16a}$$

$$\frac{\partial L}{\partial t} + \frac{\partial}{\partial x}\left[L(D+1) - L^2/2\right] = 0 \tag{16b}$$

$$U(x,t) = 1 \quad , \quad U_L = D+1$$

or, equivalently

$$\frac{\partial U_L}{\partial t} + U_L \frac{\partial U_L}{\partial x} = 0 \tag{17a}$$

$$\frac{\partial U_B}{\partial t} + U_B \frac{\partial U_B}{\partial x} = 0 \tag{17b}$$

$$U_B \equiv u(x, 0, t) = U_L - L \tag{17c}$$

Although the foregoing derivation is not valid for the most interesting case $H^{-1} \ll \epsilon^2$, because the vertical scale of the irrotational motion in the upper layer becomes the same as the horizontal scale, we shall give a new derivation at the end of this section which shows that (17a,b,c) are still valid, but to $O(\epsilon)$ rather than $O(\epsilon^2)$ when $H \to \infty$

The well known solution of (17a)

$$x(U_L, t) = x(U_L, 0) + tU_L \tag{17d}$$

states that each value of U_L (and also U_B) in the initial state is propagated with constant speed. Two different shock waves will therefore form at the two points where U_L and U_B first become double valued.

The behavior of the two interfaces can be computed from

$$L = U_L - U_B \tag{18a}$$

$$L_1 \doteq L + \delta(U - U_L) \to L + \delta(1 - U_L) \tag{18b}$$

and the vertical velocities can be computed from

$$\frac{\partial v}{\partial y} = -\frac{\partial U_B}{\partial x}, \qquad 0 < y < L \tag{19a}$$

$$\frac{\partial v}{\partial y} = \left(\frac{1}{\delta} - 1\right)\frac{\partial U_L}{\partial x} - \frac{\partial U_B}{\partial x} \quad , \qquad L < y < L_2 \tag{19b}$$

Suppose that the initial values of U_L , U_B consist of either an elevation or a depression wave, i.e. they each have a single maximum or minimum in $-\infty < x < \infty$. The only other feature of the initial distribution which will be assumed is that $\delta < 1$, i.e. the inclusion is a positive vorticity anomaly. Now if $U_B(x,0)$ contains a maximum, then the solution of (17b) yields a shock $\partial U_B/\partial x \to -\infty$ located downstream of the maximum U_B , and if $U_B(x,0)$ contains a minimum, the shock will occur upstream of minimum U_B , so that we again have $\partial U_B/\partial x \to -\infty$. Likewise for the sense of the U_L shock. Since $U_L = U_B + L > U_B$ the "fast" U_L shock will occur ~~prior to an~~d further downstream than the "slow" U_B shock, unless the amplitude of the former is small compared to the latter.

When the fast shock develops at a point (x, t) , eq. (19a) is finite, but eq. (19b) is $-\infty$, since $\delta < 1$. Therefore strong downdrafts $v = -\infty$ develop in the intrusion, and also above (in the lower part of the irrotational region). Behind this ~~and at a later time~~ the slow shock develops at a point x, t where $\partial U_L/\partial x$ is finite and $\partial U_B/\partial x = -\infty$. Therefore (19a) and (19b) are $+\infty$, and large updrafts occur in the lower $(y < L)$ layer as well as in the two other layers. ~~After both shocks have evolved~~ The field of strong vertical velocities, indicated schematically in Fig. 3, (see Sec. V for a more detailed calculation), is in qualitative agreement with Fig. 13 of Kovasznay et al[1].

We now reconsider, for previously mentioned reasons, the validity of the long wave equations when $H = \infty$, and this derivation will also indicate the first order effect of the short waves when the shock stage is entered. Eqs. (8)-(9) are valid prior to this time because the lower and middle layers are thin, whereas the upper layer is not, and it is therefore required to derive the equation of motion for this region whose lower boundary is

$$y = L_2(x,t) = L + \delta(U - \bar{U}_L)$$

Since the vertical/horizontal scales herein will be comparable, and since the vertical/horizontal perturbation velocities will also be comparable, we first transform (u, y) by

$$u = 1 + \epsilon u_1 \qquad\qquad y = y_1/\epsilon$$

to the new parameters (u_1, y_1), while leaving the other variables x, t, v unaltered. This returns us to the familiar (zero) vorticity equation $\partial u_1/\partial y_1 - \partial v/\partial x = 0$, and the continuity equation $\partial u_1/\partial x + \partial v/\partial y_1 = 0$, or $\nabla^2 v = 0$ in the upper layer. The small ϵ simplification enters in the lower $(y_1 = \epsilon L_2)$ boundary condition, where the vertical velocity is

$$v = \frac{\partial L_2}{\partial t} + \frac{\partial L_2}{\partial x} + O(\epsilon), \qquad \text{AT } y_1 = 0 + O(\epsilon)$$

With this and $v(x, \infty, t) = 0$ Laplace's equation for v can be solved, and from this u_1 at $y_1 = \epsilon L_2$ can be computed. The result expressed in terms of the Cauchy Principle Part of an integral is

$$u_1 = -\frac{1}{\pi}\left(\frac{\partial}{\partial t}+\frac{\partial}{\partial x}\right)\fint_{-\infty}^{\infty}\frac{d\xi}{\xi}\cdot L_a(x-\xi,t)$$

Since $\bar{U} = 1+\epsilon u_1$, it follows from (9) that

$$\frac{\partial \bar{U}_L}{\partial t} + \bar{U}_L\frac{\partial \bar{U}_L}{\partial x} = -\frac{\epsilon}{\pi}\left(\frac{\partial}{\partial t}+\frac{\partial}{\partial x}\right)^2\fint_{-\infty}^{\infty}\frac{d\xi}{\xi}\left[L(x-\xi,t)-\delta\,\bar{U}_L(x-\xi,t)\right] \quad (20)$$

correct to $O(\epsilon^2)$. To the same order of accuracy, we may replace the $\partial\bar{U}_L/\partial t$ term on the right hand side of (20) by $-\bar{U}_L\,\partial\bar{U}_L/\partial x$, and the $\partial L/\partial t$ term by (8b). Two simultaneous equations for $\bar{U}_L, L$, first order in time, are thereby obtained in which the new $O(\epsilon)$ term in (20) contains the highest x-derivates. These will give the leading dispersive effects, whereas the corresponding terms from the lower layers are $O(\epsilon^2)$, and will only become significant at later times than do the $O(\epsilon)$ terms. A discussion of these interesting dispersive effects is beyond the scope of this paper, and it suffices to note that (17a,b) are still asymptotically valid when $\varepsilon \to 0$, $H^{-1} \ll \varepsilon^2$.

The reader may prefer, at this point, to pass directly to Sec. VI, which can be read independently of Secs. IV & V.

IV. A SIMILARITY SOLUTION

We shall see that Eqs. (12) - (13) are hyperbolic over most of the regime of interest. But the propagation characteristics are notably different from that which occurs in passive wave systems, e.g. in the nonlinear evolution of a "bump" of water on the free surface of a shallow layer of resting water. In the latter case the surface elevation separates into the two modes of propagation associated with the two characteristics. A single isolated disturbance thereby separates into two oppositely propagating modes leaving a "quiet" intervening zone in between. But the disturbances in a shear flow are not passive, and we shall show that the variation in propagation speed of large amplitude long waves is such that there is a tendency for the two "modes" (Riemann invariants) to "lock" (rather than to separate) in the center of an isolated disturbance. The width of this coherent feature tends to increase linearly with time, at least until a "shock" (rather than a quiet zone) forms in the center. This interesting property will be exhibited by an exact similarity solution of Eqs. (12) - (13), and a similar behavior seems to occur in numerical solutions [Sec. V] under conditions less severe than those that will be required for the similarity solution.

Before turning to this problem, it is instructive to note some formal properties of Eqs. (12) - (13). When $L-1$ and D are sufficiently small, the linearization of those equations gives

$$\frac{\partial D}{\partial t} + \frac{\partial D}{\partial x} = 0 \tag{21a}$$

$$\left(\frac{\partial}{\partial t} + \frac{1}{H}\frac{\partial}{\partial x}\right)L + \left(1 - \frac{1}{H}\right)\frac{\partial D}{\partial x} = 0 \tag{21b}$$

These have the general solution

$$D(x,t) = D_0(x-t) \tag{22a}$$

$$L(x,t) - D(x,t) = L_0(x - t/H) - D_0(x - t/H) \tag{22b}$$

where $D_0(x)$, $L_0(x)$ are the initial conditions. Therefore when the perturbations are infinitesimal, D propagates with unit speed, whereas $L - D$ propagates with the slower speed $H^{-1} < 1$, so that L is a combination of the two normal modes.

Consider next the simplest nonlinear solution which occurs when $L - 1$ is finite but $D = 0$, so that (13) reduces to

$$\frac{\partial L}{\partial t} + c_-(L)\frac{\partial L}{\partial x} = 0 \tag{23}$$

where

$$c_-(L) = H^{-1}(H - 1/2 + 3L^2/2) - L \tag{24a}$$

is the local propagation speed, having the properties

$$C_-(1) = H^{-1} < 1 \tag{24b}$$

$$\frac{dc_-}{\partial L} = \frac{3L}{H} - 1 \tag{25}$$

Eq. (24b) indicates that this finite amplitude disturbance corresponds to the "slow" infinitesimal wave solution of (21a,b). But for finite $L-1$, the local propagation speed (24a) will increase downstream if

$$\frac{\partial c_-}{\partial x} = \frac{\partial L}{\partial x}\frac{dc_1}{\partial L} = \frac{\partial L}{\partial x}\left(\frac{3L}{H}-1\right) > 0 \tag{26}$$

If the other mode is also present $(D \neq 0)$, one may anticipate that when (26) is sufficiently large, the local propagation speed of the "slow wave" may actually exceed the speed of the fast wave (equal to unity according to the foregoing linear theory), so that the latter may not be able to "separate".

To verify this remark, we look for similarity solutions of (12)-(13) such that $D(x,\tau)$ is a function of $L(x,\tau)$ independent of $\cancel{x}t$, i.e.

$$D = D[L(x,t)]$$

$$\frac{\partial D}{\partial x} = D'(L)\frac{\partial L}{\partial x}, \qquad \frac{\partial D}{\partial t} = D'(L)\frac{\partial L}{\partial \tau} \tag{27}$$

These functions $D(L)$ will be shown to consist of two families of curves, branches of which will be properly pieced together to construct a well behaved solution. The more general significance of these functions (Riemann invariants) in the theory of characteristics appears in Sec. V, when we address the general initial value problem, and show that the locking tendency occurs under far less severe conditions than will be required for the following similarity solution.

Substitution of (27) in (12)-(13) gives two simultaneous linear equations for $\partial L/\partial t, \partial L/\partial x$:

$$D'(L)\frac{\partial L}{\partial t} + \frac{\partial L}{\partial x}\left\{H^{-1}(LD-D^2)+D'\left[D+H^{-1}\left(H-\frac{1}{2}+\frac{L^2}{2}-2LD+\frac{3}{2}\delta D^2\right)\right]\right\}=0 \tag{28}$$

$$\frac{\partial L}{\partial t}+\frac{\partial L}{\partial x}\left\{D-L+\left[L-H^{-1}(L^2-DL\delta)\right]D'+H^{-1}\left(H-\frac{1}{2}+\frac{3L^2}{2}-2LD+\frac{D^2\delta}{2}\right)\right\}=0 \tag{29}$$

whose determinant must vanish, and therefore

$$\left[L\left(1-\frac{L}{H}\right)+\frac{LD\delta}{H}\right](D')^2-\left[L\left(1-\frac{L}{H}\right)+\frac{\delta D^2}{H}\right]D'-H^{-1}D(L-D)=0 \tag{30a}$$

The two roots of this quadratic equation, or

$$2D'_{\pm}=\frac{L(H-L)+\delta D^2\pm\left\{\left[L(H-L)+\delta D^2\right]^2+4LD(L-D)(H-L+\delta D)\right\}^{1/2}}{L(H-L)+\delta DL} \tag{30b}$$

are differential equations for two curves $D_{\pm}(L)$ passing through each point in the hodograph plane. For each such curve the corresponding L, D values in physical space will be conserved for a point which moves with the local propagation speed $dx/dt = c_{\pm}$ equal to the coefficient in (29), i.e.

$$C_{\pm} = D - L + H^{-1}\left(H - \frac{L}{2} + \frac{3L^2}{2} - 2LD + \frac{\delta D^2}{2}\right) + L\left(1 - \frac{L}{H} + \frac{\delta D}{H}\right)D_{\pm}' \tag{31}$$

The term inside the radical of (30b) must be positive, of course, and the more general significance [Sec. V] of this is that it defines the hyperbolic domain of (12), (13), whereas negative values are in the elliptic domain. The boundary of the two domains in the hodograph plane is therefore given by

$$\left[L\left(1 - \frac{L}{H}\right) + \frac{D^2\delta}{H}\right]^2 = -\frac{4LD}{H}(L - D)\left(1 - \frac{L}{H} + \frac{D\delta}{H}\right) \tag{32}$$

and the elliptic side is beyond the scope of the theory [because there will be perturbations which increase exponentially with time, and the smallest waves will grow the fastest].

Consider first the case $\delta = 0$ in which the intrusion degenerates into a vortex sheet* at $y = L(x, t)$ and the solution of (32) then simplifies to

$$D = \frac{1}{2}\left(L - \sqrt{HL}\right) < 0 \tag{33}$$

$$D = \frac{1}{2}\left(L + \sqrt{HL}\right) > 0 \tag{34}$$

As previously mentioned, attention will be restricted to velocity profiles which increase monotonically with y , i.e. $D \leq 0$ so that (33) defines the lower boundary of the hyperbolic domain of interest. This boundary has a minimum value of $D = -H/8$ and satisfies $D = 0$ at $L = 0, H$ (Fig. 4).

---

*We have verified the validity of (12)-(13) when $\delta = 0$ by means of a separate long wave expansion $\epsilon^2 \ll 1$ for this special case.

In the hyperbolic region above this curve (but below $D = 0$) we look for solutions of (30b) with $\hat{c} = 0$, or

$$2D'_{\pm} = 1 \pm \left\{ 1 + \frac{4D(L-D)}{L(H-L)} \right\}^{1/2} \tag{35}$$

and such that the local propagation speed

$$c_{\pm} = D_{\pm} - L + H^{-1}\left(H - \frac{1}{2} + \frac{3L^2}{2} - 2LD_{\pm}\right) + L\left(1 - \frac{L}{H}\right)D'_{\pm} \tag{36}$$

is a continous function of L , i.e.

$$D'(L) \quad \text{is continuous.} \tag{37}$$

The solution $D(L)$ in the hodograph plane has the following correspondence with the solution $L(x,t)$, $D(x,t)$ in physical space (Fig. 2). The trailing edge a_1 of the compact similarity solution corresponds to $L = 1$, $D = 0$ and the leading edge a_2 corresponds to the same point in the hodograph plane. Therefore the solutions of (35) must form a closed curve (as in Fig. 4). But (37) must be satisfied as the points $a_1 \to b_1 \to b_2 \to a_2$ are traversed, and this very strong constraint can only be satisfied by having the (maximum L, minimum L) points b_1, b_2 lie on the elliptic boundary curve (33). The reason is that the two solutions $D_{\pm}$ have the same slope $D'(L)$ at such points. We shall now patch branches of (35) together to satisfy the foregoing conditions.

One of the two solutions of (35) passing through $D=0, L=1$ (the edge point) is

$$D_-(L) = 0 \tag{38}$$

and this branch will correspond to the curve $a_1 b_1$ in Fig. 4 The other solution of (35),

$$2D_+'(L) = 1 + \left\{1 + \frac{4D(L-D)}{L(H-L)}\right\}^{1/2} \tag{39}$$

has a finite slope $D_+'(1) = 1$ at $D=0, L=1$. For each L value on (38) the local propagation speed (36) is

$$\begin{aligned} C_-(L) &= -L + H^{-1}\left(H - \frac{1}{2} + \frac{3L^2}{2}\right) \\ C_-(1) &= \frac{1}{H} < 1 \end{aligned} \tag{40}$$

whereas for (39) the $C_+(L)$ branch of (36) gives the propagation speed, and in particular

$$C_+(1) = 1 \tag{41}$$

at $D=0, L=1$. Since (41) exceeds (40), it is obvious that we want to take the C_+ branch for the leading edge and C_- for the trailing edge of our similarity solution.

These two branches passing through $D=0, L=1$ need to be joined by another solution of (35), such that (37) is satisfied at the two joining points, and this is clearly impossible unless the latter lie on the boundary (33). Through each point of (33) there pass two solutions $D(L)$ with the same $D'(L)$

and with the same propagation speed. Therefore the solution (39) is extended [corresponding to $a_2 b_2$] until it intersects the elliptic boundary, and at the point of intersection the other solution:

$$2D_-'(L) = 1 - \left\{1 + \frac{4D_-(L-D_-)}{L(H-L)}\right\}^{1/2} \tag{42}$$

is constructed, and will correspond to the curve $b_2 b_1$ (Fig. 3).

The slope of this curve is $D_-' = 1/2$ at point b_2 and the slope decreases as one goes along the solution curve. This cannot intersect the elliptic boundary again, because $D' = 1/2$ at all points on this boundary (except the singular point $L = H$, see below). Neither can the curve $b_2 b_1$ intersect the $D = 0$ axis, for otherwise $D = 0$ would be implied. The exception in both previous statements is the singular point $L = H,\ D = 0$ of the differential equation (30a). It only remains to show that through this point there pass a whole family of solutions of (42), each of which satisfies the cusp condition $D'(H) = 0$, and one of which corresponds to $b_2 b_1$

In the vicinity of the singular point $L = H,\ D = 0$ we look for a class of solutions of (42) having the form $D = -(1-L/H)\alpha(L)$, where α is a differentiable function satisfying the cusp condition $\alpha(H) = 0$ Substitution of this D in (42) yields

$$\frac{2\alpha}{H} - 2\left(1 - \frac{L}{H}\right)\frac{d\alpha}{dL} = 1 - \left\{1 - \frac{4\alpha}{HL}\left[\left(1-\frac{L}{H}\right)\alpha + L\right]\right\}^{1/2}$$

$$= \frac{2\alpha}{HL}\left[L + \alpha\left(1 - \frac{L}{H}\right)\right] + \frac{2\alpha^2}{H^2L^2}\left[L + \alpha\left(1 - \frac{L}{H}\right)^2\right]^2 + O(\alpha^3)$$

$$-\left(1-\frac{L}{H}\right)\frac{d\alpha}{dL} = \frac{\alpha^2}{H^2} + O\left[\alpha^2\left(1-\frac{L}{H}\right)\right] + O(\alpha^3)$$

The asymptotic $(L \to H)$ solution obtained by neglecting the last two terms is $1/\alpha = -H^{-1}\ln(1-L/H)$ plus a constant, or

$$D \to \frac{(1-L/H)\,H}{\ln\left(1-\frac{L}{H}\right)} \times \text{(constant)}$$

where the different values of the "constant" generate the family of curves passing through the singular point. One and only one such curve passes through b_2, and this completes the demonstration of the existence of the similarity solution. More specifically, the solutions were obtained as follows.

The first order ordinary differential equations (30b) for the hodograph were integrated numerically using a grid interval of $\Delta L = 0.001$, and the results for $(H=2, \delta=0)$ and $(H=2, \delta=1/2)$ are shown in Fig.5. The results for $\delta=0$ and $\delta=1/2$ do not differ materially. The variation of local propagation speed (c) and upper layer velocity U is shown in Fig.6 for $\delta=0$. Starting at the downstream edge $(1,1)$ [Point a_2 in Fig.2.], the values of both C and U decrease until the minimum L is reached in Fig.5 at the left hand cusp (Point b_2 in Fig.2), whereupon (c, U) increase to their maximum value at the maximum L (Point b_1 in Fig.2.). Both quantities then decrease to their values at $(1,1)$ along a branch which has been omitted from Fig.6 for the sake of clarity. Fig.7 contains a plot of the velocity U_L at the top of the lower layer, and the superscripts $U_L^{\pm}$ indicate the branch of the hodograph (see inset Fig.7). The area under the lowest curve is proportional to the rate of increase of mean square L, because multiplication of (8) by L yields

$$\frac{1}{2}\int_{-\infty}^{+\infty}\frac{\partial L^2}{\partial t}\,dx = \int_{-\infty}^{+\infty} U_L \frac{\partial L}{\partial x}\,dx = \oint L\,U_L\,dL$$

In physical space the similarity solution looks like the sketch (Fig. 1), except that point b_1 is required to lie on the upper boundary, and this is very unrealistic. But we shall show that the following features of the similarity solution are generalizable and appear in more realistic calculations. The Lagrangian trajectories of particles entering the leading edge must first be displayed downwards, relative to their undisturbed level, whereas upwards displacement occurs later in the center of the region. The leading edge of the disturbance moves with the free stream velocity, and the trailing edge moves slower. But the maximum propagation speed occurs at the crest (max. L), which therefore tends to overtake the trough (min. L). Large vertical velocities tend to occur as the wave steepens in the center, and the neglected short wave dispersive effects which become important prior to this time may extend the period of laminar locking by delaying the "shock" stage.

V. THE INITIAL VALUE PROBLEM

We will now show that the apparent locking occurs under much more general conditions than is indicated by the similarity solution. Of equal importance is the wave breaking and other strong nonlinear effects suggested by the following general theory.

The theory of quasi-linear hyperbolic equations[9] assures us that if at some time $t = t_0$ the two independent variables [e.g. $D(x,t)$, $L(x,t)$ in (12)-(13)] are single valued in the vicinity of x_1, then certain (Riemann) functions

$R_\pm(D, L)$ are invariant on certain (characteristic) paths whose slopes

$$\frac{dx_+}{dt} = \lambda_+(D,L) \qquad \frac{dx_-}{dt} = \lambda_-(D,L) \qquad (43$$

are only functions of the local D, L, and do not depend explicitly on x, t. The same property is also true for the slope of the Riemann [$R_\pm$] invariants in the hodograph plane, and so through any given point $D=D_1, L=L_1$ there pass two curves $R_\pm(D, L) = R_\pm(D_1, L_1)$ which are determined by the form of the partial differential equation and not by the initial data. This consideration allows us to obtain the functional forms of $R_\pm, \lambda_\pm$ from some of the properties already computed for the particular solutions (Sec. IV). After obtaining the functional forms of $R_\pm, \lambda_\pm$ we shall apply them to the general initial value problem.

What happens if the initial distribution of $D(x,t_0), L(x,t_0)$ is taken to be such that (the as yet unknown Riemann invariant) $R_+(D, L)$ is independent of X at $t=t_0$, so that two neighboring points("1", "3")or $(x_1, x_3 = x_1 - dx)$ (Fig. 7a) satisfy

$$R_+(D_3, L_3) = R_+(D_1, L_1)$$

The corresponding (but as yet unknown) "fast" characteristic is drawn through both x_1, and x_3; and a "slow" characteristic $\lambda_- < \lambda_+$ is also drawn through x_1. The latter must therefore intersect the λ_+ characteristic passing through x_3 at some point "2" whose ordinate is $t_0 + dt > t_0$

Point "4" is then constructed by drawing a horizontal line through point "2", and by finding the intersection with the λ_+ characteristic passing through x_1. By definition R_+ must be constant on each of the two λ_+ lines or

$$R_+(D_4, L_4) = R_+(D_1, L_1)$$
$$R_+(D_2, L_2) = R_+(D_3, L_3)$$

and it then follows from our assumption on the functional form of R_+ at $t = 0$ that

$$R_+(D_4, L_4) = R_+(D_2, L_2)$$

This means that the value of $R_+(D, L)$ is independent of λ at $t_0 + dt$ and therefore at all subsequent times, if it is initially independent of x. The explicit relation $D = D(L)$, obtained from the implicit $R_+ =$ constant relation is therefore independent of x, t, and the class of functions (27) having this property is already given by the family of solutions of (30b). Thus the class of similarity solutions obtained in Sec. IV, gives the family of the constant Riemann invariants. The only remaining question is: which of the two similarity solutions $D_\pm$ (passing through a given point D_1, L_1) corresponds to that function $R_+(D, L) = R_+(D_1, L_1)$ which is invariant along the fast $\lambda_+ = c_+ > c_-$ characteristic.

We have already shown that points "1" and "2" have the same R_+ value or

$$0 = R_+(D_2, L_2) - R_+(D_1, L_1) = \frac{\partial R_+}{\partial D}(D_2 - D_1) + \frac{\partial R_+}{\partial L}(L_2 - L_1)$$

and since these points are also on a λ_- characteristic, we have $R_-(D_2, L_2) = R_-(D_1, L_1)$ or

$$0 = \frac{\partial R_-}{\partial D}(D_2 - D_1) + \frac{\partial R_-}{\partial L}(L_2 - L_1)$$

The only solution of these two equations is

$$D_2 - D_1 = 0 = L_2 - L_1$$

because the $D_\pm$ curves form an intersecting family (linear independence). This shows that the individual values of D and L are independent of time on the slow characteristic if $R_+(D, L)$ is independent of x. Therefore the slowly propagating similarity solution D_- must be the one that corresponds to the fast invariant, in the sense that the relation $R_+(D, L) = R_+(D_1, L_1)$ may be obtained from dD_-/dL (30b) with $D = D_1$, $L = L_1$. Likewise, the slowly propagating invariant passing through this point is obtained by solving dD_+/dL.

The use of this theory may be illustrated by considering an initial $t = 0$ distribution (Fig. 8b) for which $D(x, 0) < 0$, $L - 1 = 0$. The entire region to the left of the trailing edge $x < a_1$ in Fig. 1, and to the right of the leading edge, is called the "constant state" and corresponds to $D = 0$, $L = 1$. Through this point $(0, 1)$ in Fig. 8b there pass two Riemann invariants

$R_\pm = D_\mp$, with the abscissa axis $D(L)=0$ being the R_+ invariant. The dashed curves through $\min D(x,0)$ are sketches of the two Riemann invariants passing through that point, and at the subsequent times these curves must be tangent to the hodograph of $D(x,t), L(x,t)$. Moreover, the $t=0$ hodograph must evolve onto the two constant state Riemann invariants for the following reason. From the region downstream of the trailing edge $x>a_2$ there emerge slow characteristics, each of which will eventually be intersected by a fast characteristic emerging from the constant state $x<a_1$. At the intersection the values of D, L must satisfy $R_+(D, L) = R_+(0,1)$ i.e. $D=0$ is the state to which the trailing edge tends to evolve. The leading edge tends to evolve on the R_- invariant passing through $(0,1)$ because the slowly propagating characteristics from $x>a_2$ are intersected by the fast characteristics originating from $x<a_2$, whereupon $R_-(D, L) = R_-(0,1)$. The temporal evolution of the hodograph is illustrated in Fig. 7b, and thus we see how the extreme amplitudes in the fully evolved (constant) states can be computed from the initial hodograph by drawing the (dashed) $R_\pm$ invariants and finding their intersections with the constant state invariants.

The local propagation speeds can also be computed from the results of Sec. IV. A necessary condition for mode separation is that the propagation speeds so computed do not overlap, i.e. the minimum propagation speed of the fast mode (Riemann invariant) must exceed the maximum speed in the slow mode. If this is not the case, the modes cannot separate with a "quiet" intervening zone.

These important qualitative and semi-quantitative conclusions have been verified by numerical solutions of (12)-(13), using a standard finite difference scheme which satisfies the Courant-Friedrichs-Lewy criterion for computational stability. In all of the following examples the results at selected t are given relative to a coordinate system which moves with the mean speed of the two infinitesimal amplitude waves, and cyclic boundary conditions are used for the (essentially compact) perturbation. The numerical program was first tested against the known solutions of 21a,b).

In Fig. 9 the initial amplitude: $\min D(x,0) = -0.125$ was chosen large enough to prevent the modes from separating. Since the fast wave propagation speed decreases upstream from the leading edge, the slope of the leading half of the D wave decreases (Fig. 9a). The L wave steepens on its rear side as the wave (Fig. 9b) evolves (from zero) into a crest and trough configuration, and a shock tends to form in the downward sloping interfacial region at $t = 2.5$ (Fig. 9b). Some of the points lying in the shock region have been deleted (from Fig. 9a, 9b, but not Fig. 9c) for clarity of presentation. The deleted points are obviously numerical artifacts since they do not preserve the $D \leq 0$ inequality, as required by the solution of the differential equation. Fig. 9c shows the expected evolution of the initial hodograph $(L = 1)$ onto the Riemann invariants, together with the numerical artifacts of the shock.

For the infinite H case we have shown (Sec. III) that the evolutionary equations (17a,b) are independent of δ. Fig. 10 gives the results of an explicit numerical integration of (12)-(13) with $H = 10^5, \delta = 0$, and the numerics have been checked against the exact solution (17d). The initial state $t = 0$ consisted of Gaussian curves for D and L, as shown in

Figs. 10a,b. Also shown is the evolution of $D(x,t)$, $L(x,t)$, and the hodographs are given in Fig. 10c. Of special interest is the "bursting bubble" effect (Fig. 10b), which is shown in 2.5 times as great resolution in Fig. 11. There is a rather spectacular eruption of the boundary layer at $t \simeq$ .75 just prior to the time $t \simeq$ 1.1 of shock formation, and there is the suggestion of an event which transfers low momentum fluid out of the boundary layer. There is certainly no tendency for the modes to separate, and the computer printout at $t >$ 1.1 (not shown here) indicates that the mid region is not quiet but (numerically) chaotic.

VI. LONGWAVE THEORY FOR THREE DIMENSIONAL DISTURBANCES

We now generalize the foregoing work by introducing a spanwise velocity $w(x,y,z,t)$ scaled in the same way as u relative to the longwave expansion parameter $\epsilon \ll 1$, where the spanwise coordinate z is scaled in the same way as x , so that the nondimensional continuity equation is

$$u_x + v_y + w_z = 0 \tag{44}$$

For the pressure gradient we have $\partial p/\partial y = -\epsilon^2 dv/dt$ in a subsequently defined boundary layer $y < L_2(x,z,t)$, above which is an infinitely deep $(H=\infty)$ free stream whose velocity u equals $1+O(\epsilon)$ at all x, y, z, t . It follows that $\partial p/\partial x = O(\epsilon) = \partial p/\partial z$ for $y < L_2$, and the longwave momentum equations are

$$0 = du/dt = u_t + u u_x + v u_y + w u_z \tag{45}$$

$$0 = dw/dt = w_t + u w_x + v w_y + w w_z \tag{46}$$

From eqs. 44-45 we obtain the vorticity equation

$$\frac{d}{dt} u_y = w_z u_y - w_y u_z \tag{48}$$

A compatibility requirement on the given initial values of (u, w) is that $u = 1, w = 0$ on and above some surface $y = L_2(x, z, 0)$, and we shall also require $u_y(x, L_2^-(x, z, 0), z, 0] =$ constant, on this top surface of the boundary layer. Since the Jacobian of (u, w) in (48) vanishes on this surface, a material point on it will have the same value of u_y (and the same $u = 1, w = 0$) at time dt as it had at $t = 0$. Let us therefore define the upper boundary $y = L_2(x, z, t)$ as the solution for y of any two of the equations: $u(x, y, z, t) = 1$ $w(x, y, z, t) = 0$, $u_y(x, y, z, t) =$ constant. Since particles on this surface must remain there, the y component of velocity is

$$v(x, L_2(x, z, t), t) = \frac{\partial L_2}{\partial t} + \frac{\partial L_2}{\partial x} \tag{49}$$

This variable free streamline boundary (i.e L_2) is necessary, of course, for the compatibility of eqs. (44) - (46) and the lower boundary condition $v(x, 0, z, t) = 0$.

If we allow the initial (u, w) to be non-zero on $y = 0$, then two parcels moving towards each other on the line which connects them, and having equal velocities perpendicular to that line must "collide" in a finite time according to eqs. (45) - (46). This is the simplest indication that horizontal converge~~s~~nces are amplified. But it is desireable to remove this special case from consideration by imposing the initial condition $u(x, 0, z, 0) = 0 = w(x, 0, z, 0)$, in which case $u(x, 0, z, t) = 0 = w$ at all times, and the solutions of our inviscid model will satisfy the important viscous boundary condition.

The next simplest case has a phane of symmetry ($z = 0$) for (u, v), and w is an antisymmetric function of z vanishing at large $|z|, |x|$. When the z derivative of (46) is evaluated on $z=0$ where $w(x,y,0,t)=0$ we get the important result

$$\frac{d}{dt} w_z(x,y,0,t) = -w_z^2(x,y,0,t)$$
$$w_z(x,y,0,t) = \frac{1}{t+\mathcal{D}^{-1}(\bar{x},\bar{y})} \tag{50}$$
$$\mathcal{D} \equiv w_z(\bar{x},\bar{y},0,0)$$

where $x = x(\bar{x},\bar{y},t)$, $y = y(\bar{x},\bar{y},t)$ are the Lagrangian coordinates of a parcel located at $x=\bar{x}$, $y=\bar{y}$ AT $t=0$.

Eq. (48) with (50) may also be integrated for parcels on the axis and we get

$$u_y = \bar{u}_y(\bar{x},\bar{y})(1+t\mathcal{D}(\bar{x},\bar{y}))$$
$$\bar{u}_y \equiv \frac{\partial u}{\partial y}(\bar{x},\bar{y},0,0) \tag{51}$$

Eqs. (50) - (51) show that if a parcel has initial spanwise convergence Then its spanwise convergence increases, and its vorticity decreases up to the time

$$t_s = -\left[\text{minimum}\, \mathcal{D}(\bar{x},\bar{y})\right]^{-1} \tag{52}$$

whereupon a discontinuity forms in the vicinity of the parcel and $u_y \to 0$. On the other hand, parcels with spanwise divergence $(\mathcal{D} > 0)$ at $t=0$ increase their vorticity linearly with time, and this behavior suggests a rationalization for the vorticity anomaly (δ^{-1}) assumed previously.

Confining attention to the motion of parcels on the $z=0$ axis, eqs. (45) gives $x = \bar{x} + \bar{u}t$. By using this and (51) in the transformation equation

$$\frac{\partial \bar{u}}{\partial \bar{x}} = \frac{\partial}{\partial \bar{x}} u(x,y), \quad \frac{\partial \bar{u}}{\partial \bar{y}} = \frac{\partial u}{\partial \bar{y}}$$

we get

$$\frac{\partial \bar{u}}{\partial \bar{x}} = (1+t\,\bar{u}_{\bar{x}})\frac{\partial u}{\partial x} + \bar{u}_{\bar{y}}\,(1+t\mathcal{D})\frac{\partial y}{\partial \bar{x}}$$

$$\frac{\partial \bar{u}}{\partial \bar{y}} = t\,\bar{u}_{\bar{y}}\,\frac{\partial u}{\partial x} + \bar{u}_{\bar{y}}\,(1+t\mathcal{D})\frac{\partial y}{\partial \bar{y}}$$

Eliminating $\partial u/\partial x$ and simplifying the result yields

$$\frac{\partial y}{\partial \bar{y}} - \frac{t\bar{u}_{\bar{y}}}{1+t\bar{u}_{\bar{x}}}\,\frac{\partial y}{\partial \bar{x}} = \frac{1}{1+t\mathcal{D}} - \frac{t\bar{u}_{\bar{x}}}{(1+t\mathcal{D})(1+t\bar{u}_x)} \qquad (53)$$

which, at any t, is a readily integrable first order linear equation for y. The slope of the characteristics in the $(\bar{x},\bar{y})$ plane is

$$\left(\frac{d\bar{x}}{d\bar{y}}\right)_t = \frac{-t\,\bar{u}_y(\bar{x},\bar{y})}{1+t\bar{u}_{\bar{x}}} \qquad (54)$$

and the derivative $dy/d\bar{y}$ along these curves equals the right hand side of (53). Integration of the ordinary differential equation along the characteristics gives $y(\bar{x},\bar{y},t)$.

A simple and interesting example occurs if we take $\bar{u}=\bar{y}$, corresponding to an initially linear downstream velocity profile, which is perturbed by a $\mathcal{D}(\bar{x},\bar{y})$ corresponding to a spanwise circulation cell. In this case (54) simplifies to $\bar{x}$ = constant $-t\bar{y}$, and the integration of $dy/d\bar{y}$ along the characteristic lines yields the solution

$$y = \int_0^{\bar{y}} \frac{d\eta}{1+t\mathcal{D}(\bar{x}+t\bar{y}-t\eta,\eta)} \qquad (55)$$

$$y(x,u,t) = \int_0^{u} \frac{d\eta}{1+t\mathcal{D}(x-t\eta,\eta)} \qquad (56)$$

and from $v = (\partial y/\partial t)_{\bar{x},\bar{y}}$ we have

$$V(x,u,t) = -\int_0^u d\eta \, \frac{\vartheta(x-t\eta,\eta)+t(u-\eta)\vartheta_x(x-t\eta,\eta)}{[1+t\vartheta(x-t\eta,\eta)]^2} \tag{57}$$

$$\left[\vartheta(x,y) \equiv -\frac{\partial V(x,y,0,0)}{\partial y}\right]$$

The main result (eq. 57) gives [with the help of (56)] the normal velocity at any desired point in terms of the initial values of V on $z = 0$.

For further discussion suppose that $\vartheta \leq 0$ in the lower half of the interval $0 \leq \bar{y} \leq 1$, and $\vartheta \geq 0$ in the upper half; a distribution corresponding to an initial updraft $(V \geq 0)$ on the axis of an isolated initial disturbance, and such as might be realized by squirting some fluid out of an opening in the $y = 0$ boundary. From (55) we see that all the parcels in the lower region are displaced upwards in time, with $V \rightarrow +\infty$ at time t_s (eq. 52) at the parcel having the maximum initial value of $\partial V/\partial y$. The velocity profile (56) in the vicinity of the shock has relatively low shear at small y, and large shear $\left(\partial u/\partial y = 1 + t\vartheta > 1\right)$ in the uppermost region. Since $u = 0$ at $y = 0$, the lower half of the velocity profile will have much smaller downstream velocities than occurs at the same elevation in the undisturbed flow $(u = y)$. The region of anomalously low u might be identified with the spike, and the positive vorticity anomaly in the upper region is also explained.

If the initial V is reversed, so that downdrafts $(V<0)$ occur (on $z=0$) with $\mathcal{D}\geq 0$ in the lower part of the boundary layer, then (55) is finite in this region for finite t, and no discontinuity occurs here. But the vorticity in the lower region increases with t as the descending fluid brings large u close to the boundary. The large V singularity occurs in the upper region and further downstream from the strong shear region which forms at small y. The limiting factor in the latter region may therefore be the short wave instabilities on the generated shear layer, rather than the wavebreaking at larger y.

In general eq. (53) will have two singular domains, one of which $[1+t\mathcal{D}(\bar{x},\bar{y})=0$ appears in the illustrative example of this section, and the other $[1+t\bar{u}_{\bar{x}}(\bar{x},\bar{y})=0]$ appears in the two dimensional theory of the preceeding sections. The unifying thread is that "shocks" or large V Tend To appear if the horizontal divergence $\partial u/\partial x+\partial w/\partial z$ has negative values in the initial conditions.

It remains to indicate how the motion off the axis of symmetry can be computed. For the most general longwave problem we have $x=\bar{x}+\bar{u}(\bar{x},\bar{y},\bar{z})t$, $z=\bar{z}+\bar{w}(\bar{x},\bar{y},\bar{z})t$ from the momentum equations. When these are substituted into the Lagrangian form of the continuity equation, which states that the Jacobian $\partial(x,y,z)/\partial(\bar{x},\bar{y},\bar{z})=1$, we obtain

$$\begin{vmatrix} 1+t\bar{u}_{\bar{x}} & \partial y/\partial\bar{x} & t\bar{w}_{\bar{x}} \\ t\bar{u}_{\bar{y}} & \partial y/\partial\bar{y} & t\bar{w}_{\bar{y}} \\ t\bar{u}_{\bar{z}} & \partial y/\partial\bar{z} & 1+t\bar{w}_{\bar{z}} \end{vmatrix} = 1$$

At any time t this gives a first order linear equation for $y(\bar{x},\bar{y},\bar{z})$ with the boundary condition $y(\bar{x},0,\bar{z})=0$, and the equation can be integrated by the method of characteristics.

VII. CONCLUSION

Longwave disturbances having small finite normal velocities evolve such that the maximum V becomes comparable to the horizontal velocities of the basic shear flow, and there is a tendency for wavebreaking at later times (where the theory must be modified to include the neglected short waves).

The two dimensional model (Secs. II- V) illustrate this effect in the simplest way, and the detailed calculations provides useful information for constructing a more general theory of the breakdown of a laminar disturbance. We refer to the tendency for wavebreaking to appear at the center of a compact initial disturbance whose endpoints separate linearly with time (Fig. 11). The important discontinuities ("shocks") Tend To form not only when the upper layer is infinitely deep $(H = \infty)$, but also in the ~~(somewhat academic)~~ case of finite H for which the horizontal pressure gradients in the boundary layer are important.

The three dimensional longwave theory outlined in Sec. VI shows that the large v effect is generalizeable, and removes or weakens the assumptions made for the two dimensional theory. In particular the vorticity anomaly in the latter, is rationalized in terms of an initial spanwise divergence, and the spanwise convergences here are responsible for the evolution of large v. In general (eq. 57), any weak horizontal convergence on the axis of symmetry will lead to large normal velocities, such as is observed in the laminar spike [1] just prior to its breakdown.

The time t_s (52) when the first shock tends to form equals the reciprocal of the minimum horizontal divergence (ϑ) in the initial state, and at the shock point the shear (51) vanishes independent of $|\vartheta|$. If max $\vartheta = |\min \vartheta|$ then the maximum shear ($u_y = 2$) at t_s is also independent of the initial amplitude. These features, as well as $V \to \infty$ in the shock region, strongly suggest that

$$\lim_{|\vartheta| \to 0} \lim_{t \to \infty} u(x, y, z, t)$$

does not tend to the undisturbed ($\vartheta \equiv 0$) flow, in which case the latter is said to be unstable to small finite amplitude perturbations (ϑ). Although the post shock stage ($t \geq t_s$) is beyond the scope of a long wave theory, we believe that the wavebreaking effects will lead to an even greater degree of irreversibility than is indicated for the pre-shock stage.

The longwave theory is also applicable to cylindrically symmetric perturbations in a round jet bounded by free streamlines (flow out of a nozzle). Nonlinear amplication of the outward radial velocities is implied, suggesting eventual entrainment of the irrotational fluid outside the free streamlines ($u = 0$).

ACKNOWLEDGEMENT

We thank Professors J. Keller and C. Van Atta for valuable discussions. Part of this work was done at the G.F.D. Summer Program at the Woods Hole Oceanographic Institution, under the auspices of ONR. Additional support by that Agency to the University of Rhode Island under contract P025111 is also acknowledged.

[1] L.S.G. Kovasznay, H. Komoda and B.R. Vasudiva, in Proceedings of the 1962 Heat Transfer and Fluid Mechanics Institute, Ellers, F.E., Kauzlarich J., Sleicher, C.A., Jr. and Street, R. (Eds.), Stanford University, Stanford, California (1962).

[2] I. Wygnanski, M. Sokolov and D. Friedman, J. Fluid Mech., 78, 785 (1976).

[3] A.F. Perry, T.T. Lim and E.W. Teh, J. Fluid Mech., 104, 387 (1981).

[4] B.J. Cantwell, Ann. Rev. Fluid Mech., 13, 457 (1981).

[8] M.T. Landahl, J. Fluid Mech., 98, 243 (1980).

[5] M. Sokolov, R.A. Antonia and A.J. Chambers, Physics of Fluids, 23(12), 2561 (1980).

[6] B. Cantwell, D. Coles and P. Dimotakis, J. Fluid Mech., 87(4), 641 (1978).

[7] C.W. Van Atta, M. Sokolov, R.A. Antonia and A.J. Chambers, Phys. Fluids 25, 424 (1982).

[9] R. Courant and K.O. Friedrichs, Supersonic flow and shock waves, Interscience, N.Y. (1948).

LEGENDS

Fig. 1 (After Kovasznay et al.[1] (a) Normalized vorticity isopleths on the axis of symmetry of a developing laminar spike. y is normalized by the boundary layer thickness δ, and time is normalized by the oscillation period T. Stretching the diagram horizontally by a factor of five gives a non-exaggerated picture of the disturbance in the $x-y$ plane. (b) Pictorial view of the distribution of the streamwise vorticity in a plane parallel to the boundary at a later stage of spike development than in (a). (c) Isopleths of velocity normal to the boundary at stage (a). (d) Isopleths of normal velocity at a stage later than (a) and also later than (b). The maximum streamwise vorticity at stage (d) is[1] only 1.0/0.6 times the corresponding value in (a).

Fig. 2. An undisturbed shear flow of non-dimensional height L=1 lies below a free stream of non-dimensional speed $U = 1$ in a channel of height H. The finite amplitude long wave perturbation $a_1-b_1-b_2-a_2$ contains another layer of uniform vorticity, and L (x,t) is its lower boundary.

Fig. 3. Schematic distribution of the regions of strong vertical velocity generated by a positive vorticity anomaly (stippled) in a boundary layer flow with $H=\infty$. The strong updrafts occur in all three layers, whereas the strong downdrafts do not occur in the lower boundary layer. The relative positions are such as to generate a clockwise eddy.

Fig. 4. Sketch of the hodograph plane in which corresponding values of L (x,t) and D (x,t) are plotted. The governing equation is hyperbolic above the curve $D=(L-\sqrt{HL})/2$, and the cusped curve a_1-b_1-b_2-a_2 is a similarity solution for a locked mode.

Fig. 5. Numerical solution for the locked mode similarity solution when $\delta=0$ (vortex sheet) and when $\delta=1/2$, with H=2.0 in both cases.

Fig. 6. Partial hodograph plots of local propagation speed c and upper layer velocity U for $\delta=0$. The two cusps on the left correspond to point b_2 (Fig. 2). The cusp on the right corresponds to the point b_1 and the central cusp corresponds to a_2. The curves connecting the central and right cusps are not drawn.

Fig. 7. Partial plot of lower layer velocity $U_L^{\pm}$ on different branches of hodograph (see inset). The areas under the lower curves give the rate of increase of mean square L. The symbol (•) is for $\delta=0$ and (x) is for $\delta=1/2$.

Fig. 8. (a) The fast characteristics λ_+ and the slow characteristics λ_- emerging from the $t=t_0$ axis, along which the Riemann invariant $R_+(D,L)$ is assumed constant. (b) The temporal evolution of an initial hodograph L=1 onto the "constant state" Riemann invariants.

Fig. 9. Large amplitude numerical calculation,

(a) The initial D (x,o) is Gaussian. $t=0$ (◇), $t=1.5$ (×), $t=2.0$ (+), $t=2.5$ (△) (b) The initial L (x,o)-1=0, and L(x,t). (c) The initial (+) and last computed (△) hodograph. The points above D=0 are numerical artifacts of the shock region The solid line is a Riemann invariant drawn through min D (x.t), and it should pass through min D (x.o) according to the analytic theory. H=2, δ = 0. Grid interval Δx = .0125, Δt = .01.

Fig. 10. "Wave breaking" when $H = \infty$. (a) $D(x)$, (b) $L(x)$ (c) $D(L)$ for $t = 0$ (△), .5 (×) and 1.0 (◇)

Fig. 11. The "bursting bubble" of Fig. 10b in greater resolution (Δx = .005) for the times indicated near the graphs. For t = 0.6, 0.7, 0.8 only the central regions are drawn. Note that these results are independent of δ (16a,b).

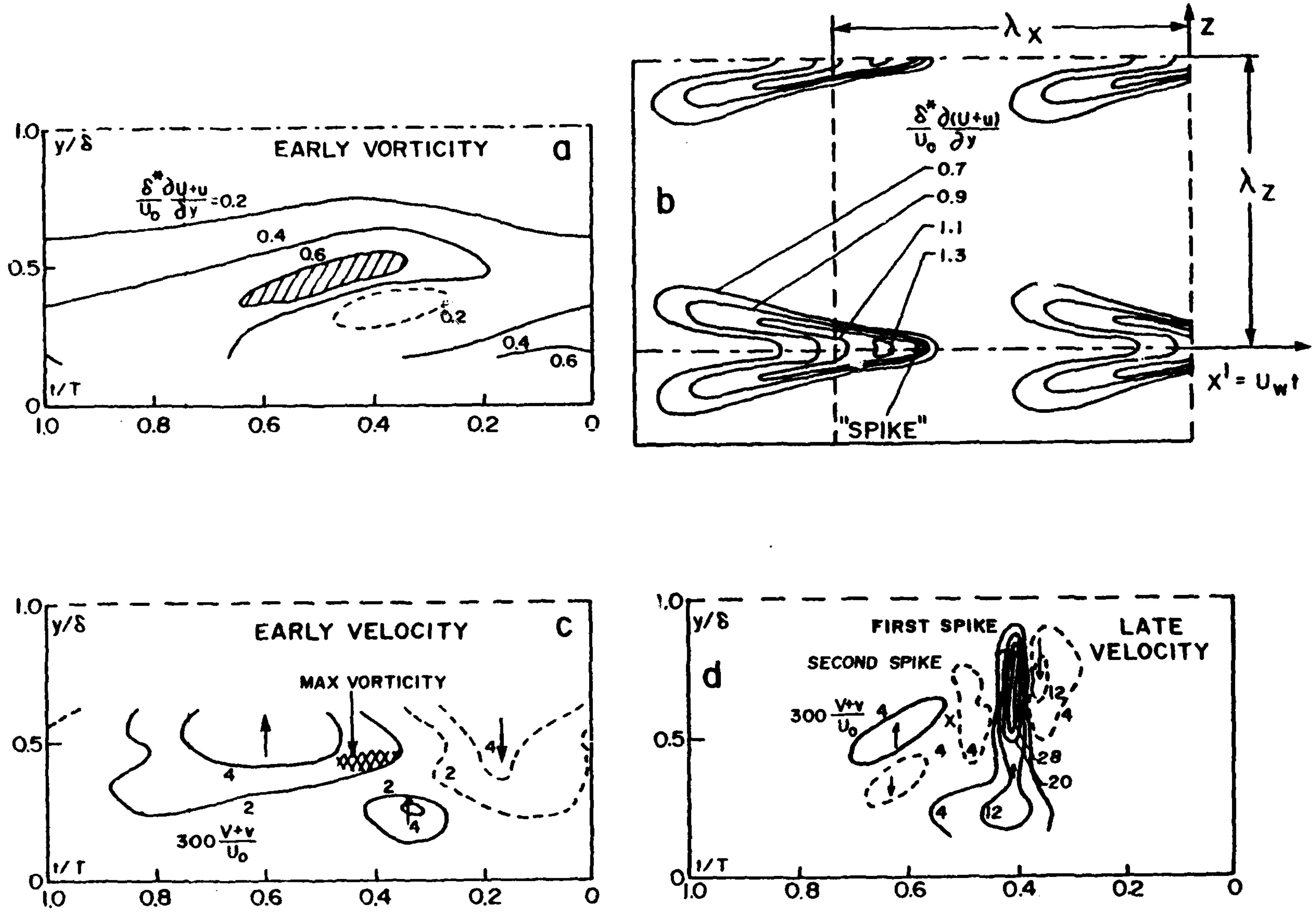

y/δ
EARLY VORTICITY
a
$\frac{\delta^*}{U_0}\frac{\partial U+u}{\partial y}=0.2$
0.4
0.6
0.2
0.4
0.6
t/T
1.0
0.5
0
1.0
0.8
0.6
0.4
0.2
0
λ_x
z
$\frac{\delta^*}{U_0}\frac{\partial (U+u)}{\partial y}$
0.7
0.9
1.1
1.3
b
λ_z
$x^1 = U_w t$
"SPIKE"
y/δ
EARLY VELOCITY
c
MAX VORTICITY
4
2
2
4
4
2
$300\frac{V+v}{U_0}$
t/T
y/δ
FIRST SPIKE
LATE VELOCITY
SECOND SPIKE
d
$300\frac{V+v}{U_0}$
4
X
4
4
12
4
28
20
4
12
t/T

Figure 1

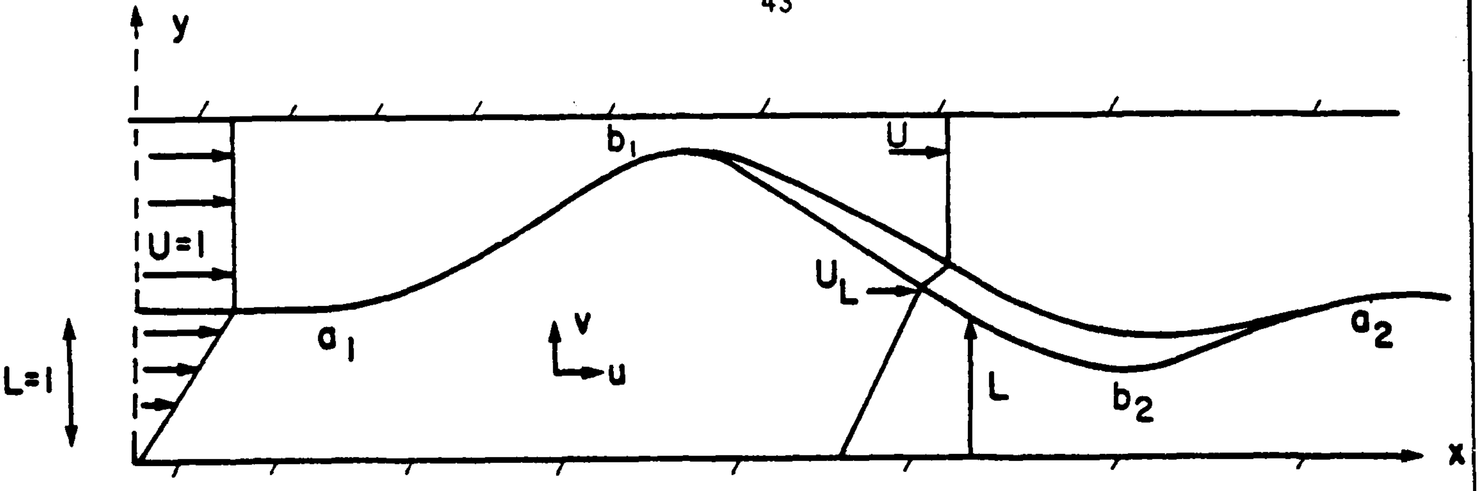
y
U=1
L=1
b1
U
UL
a1
v
u
L
b2
a2
x

Figure 2

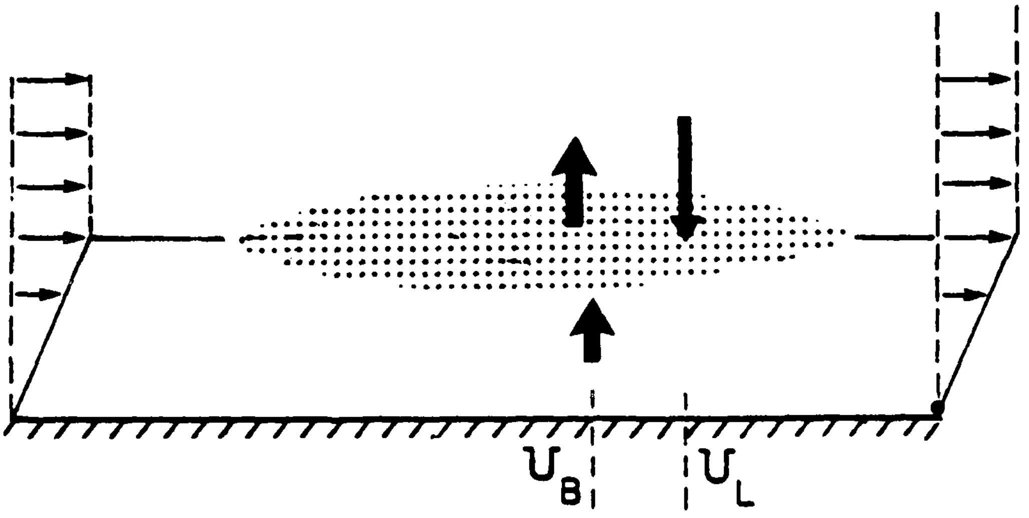

Figure 3

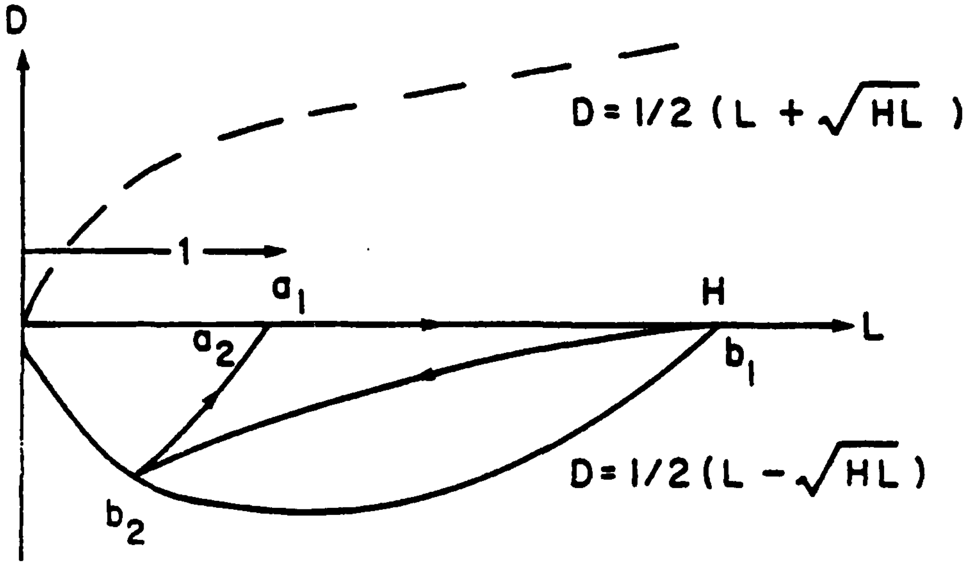
D
L
1
a_1
a_2
H
b_1
b_2
D = 1/2 (L + √HL)
D = 1/2 (L − √HL)

Figure 4

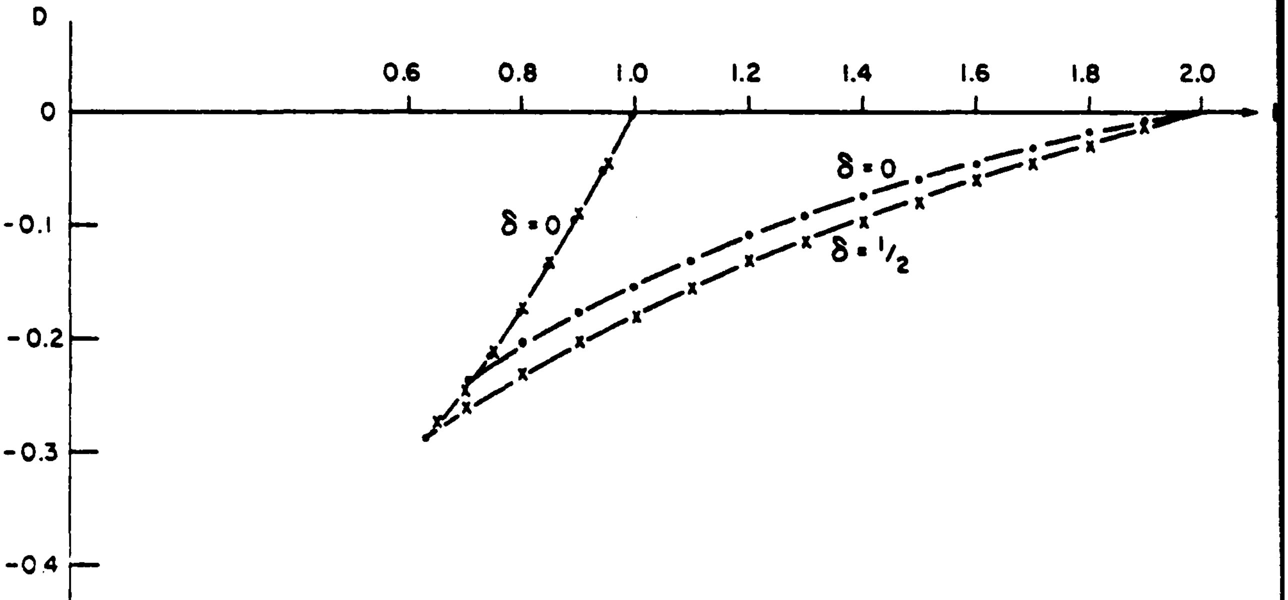

Figure 5

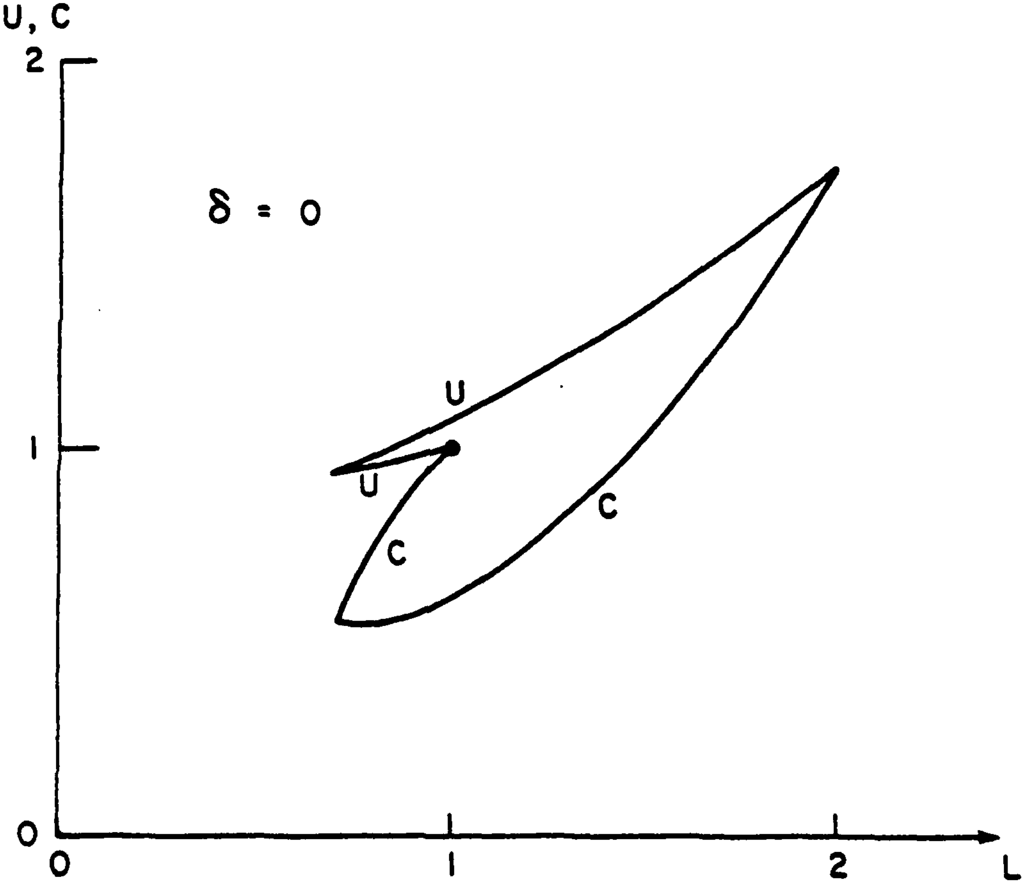

Figure 6

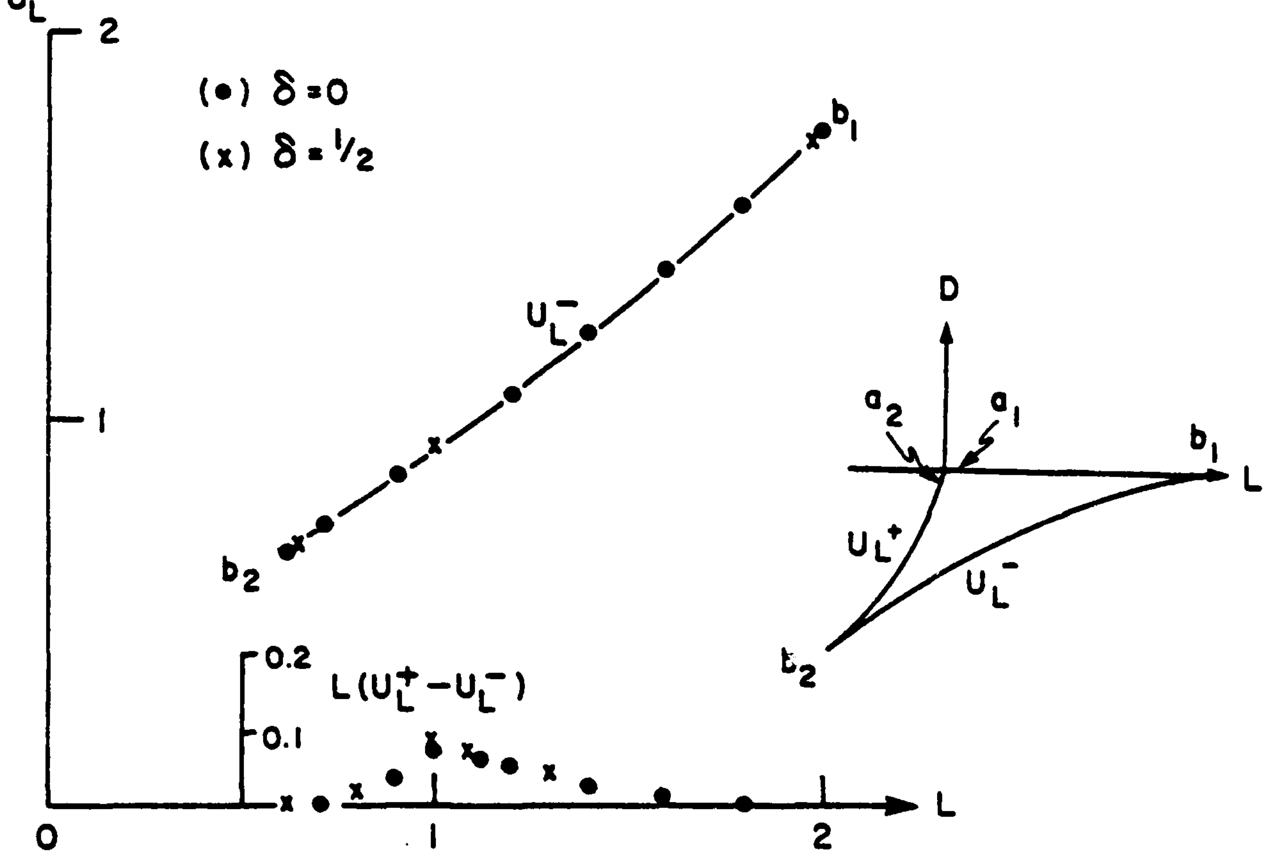
U_L^-
2
1
0
1
2
L
(●) $\delta = 0$
(x) $\delta = 1/2$
b_1
b_2
U_L^-
0.2
0.1
$L(U_L^+ - U_L^-)$
D
a_2
a_1
b_1
L
U_L^+
U_L^-
b_2

Figure 7

AD-A126 396 FINAL TECHNICAL REPORT ON CONTRACT N00014-81-C-0010 1 3/3
OCTOBER 1980-30 SEPTEMBER 1982(U) WOODS HOLE
OCEANOGRAPHIC INSTITUTION MA J A WHITEHEAD MAR 83
UNCLASSIFIED WHOI-83-11 N00014-81-C-0010 F/G 8/3 NL

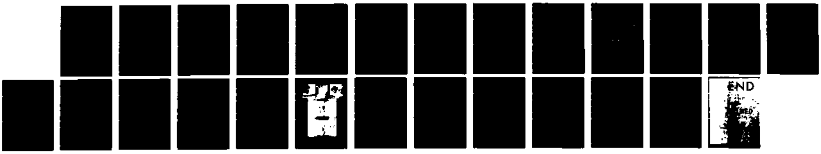

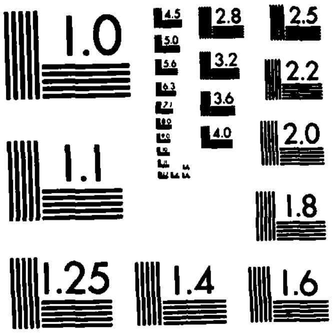
1.0
4.5
5.0
5.6
6.3
2.8
2.5
3.2
2.2
3.6
4.0
2.0
1.1
1.8
1.25
1.4
1.6

MICROCOPY RESOLUTION TEST CHART
NATIONAL BUREAU OF STANDARDS-1963-A

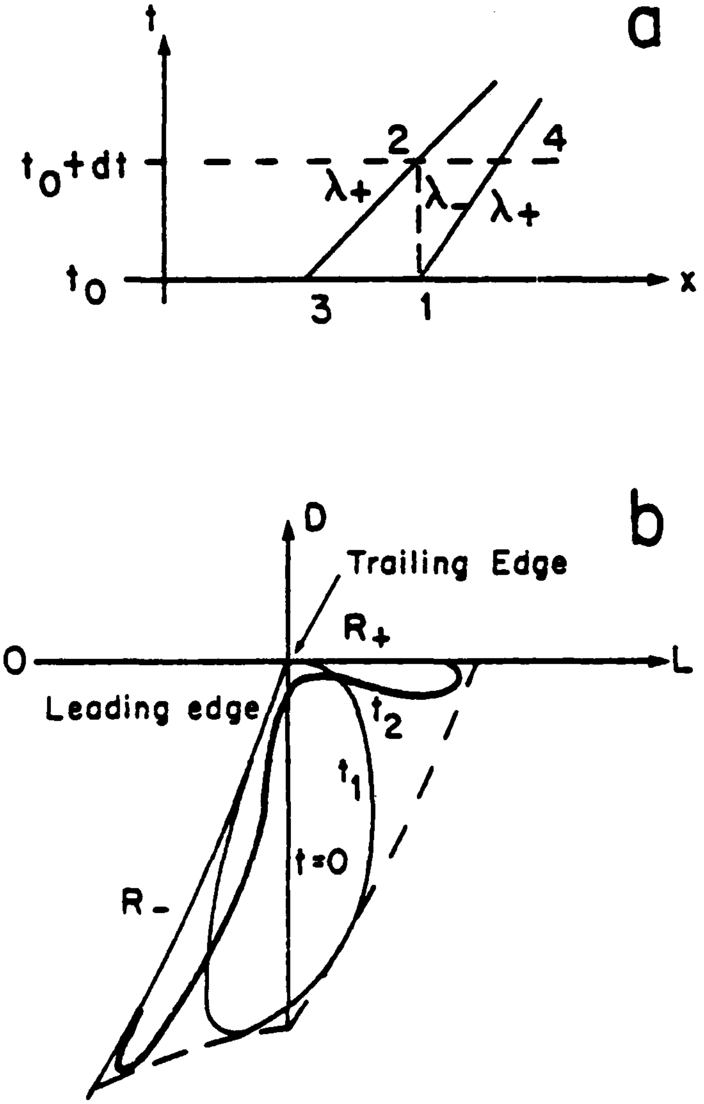
a
t
t_0+dt
t_0
x
2
4
3
1
λ_+
λ_-
λ_+
b
D
Trailing Edge
R_+
O
L
Leading edge
t_2
t_1
t=0
R_-

Figure 8

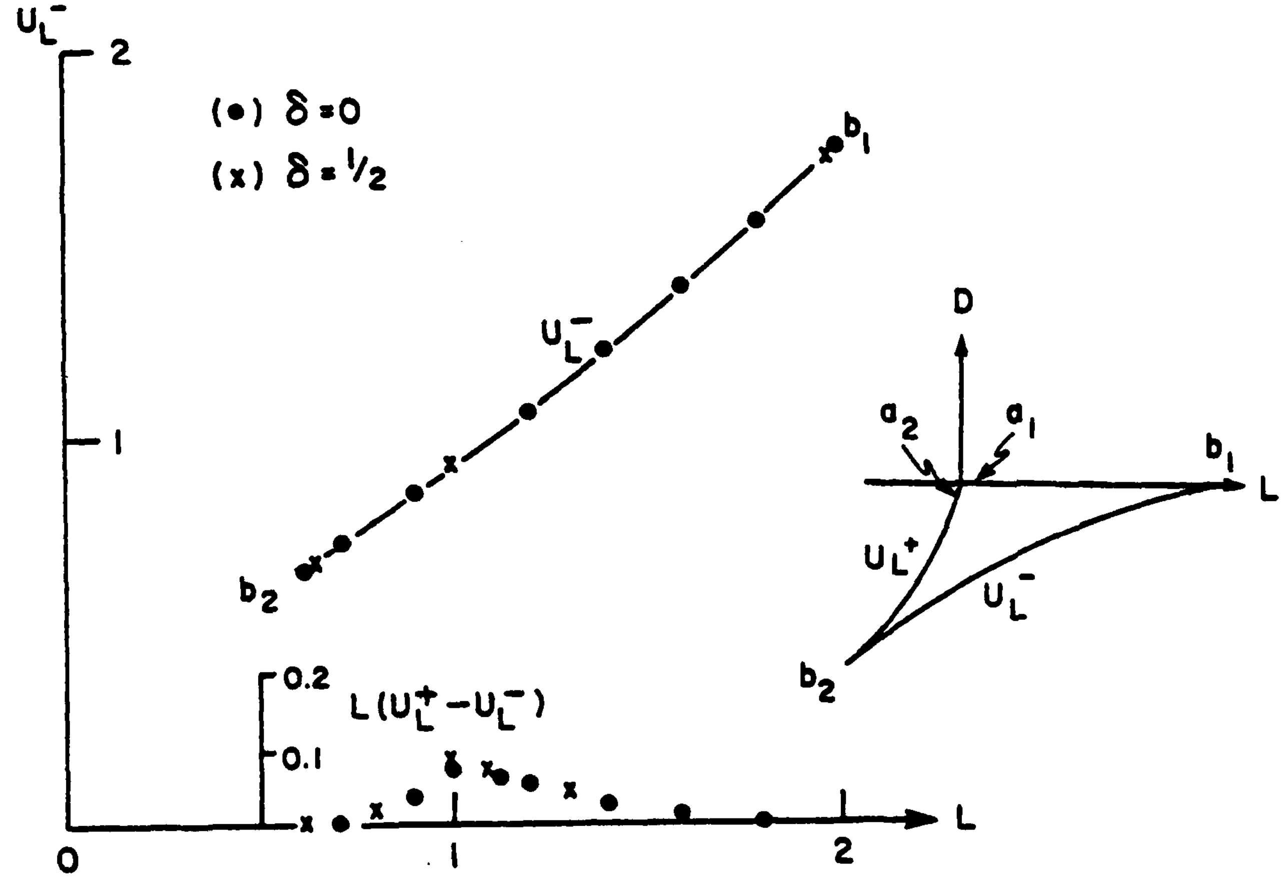
U_L^-
2
1
0
1
2
L
(●) $\delta = 0$
(x) $\delta = 1/2$
b_1
b_2
U_L^-
0.2
0.1
$L(U_L^+ - U_L^-)$
D
a_2
a_1
b_1
L
U_L^+
U_L^-
b_2

Figure 7

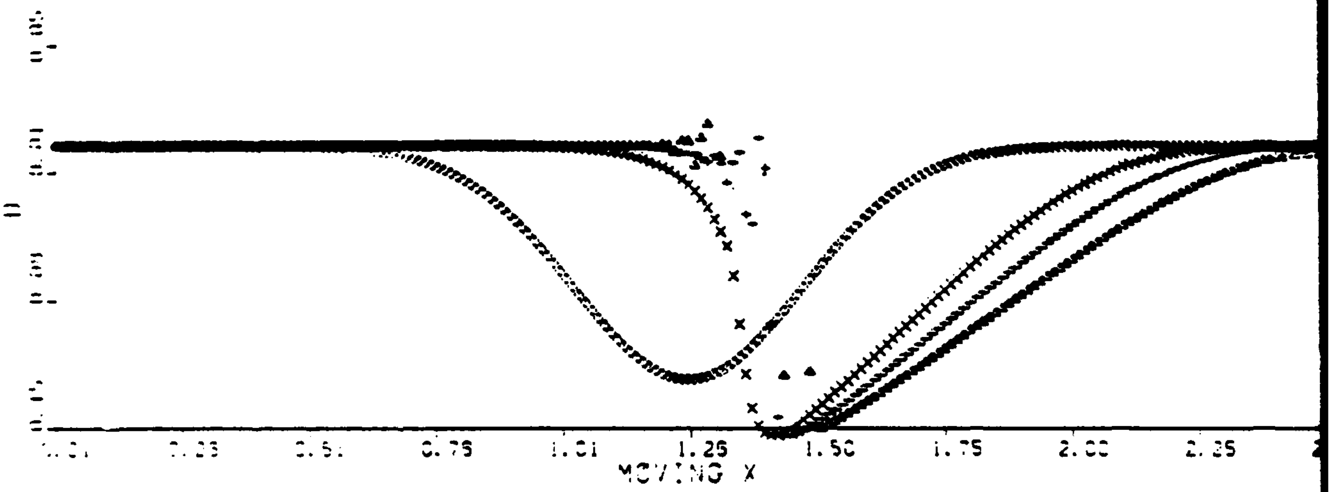

Figure 9a

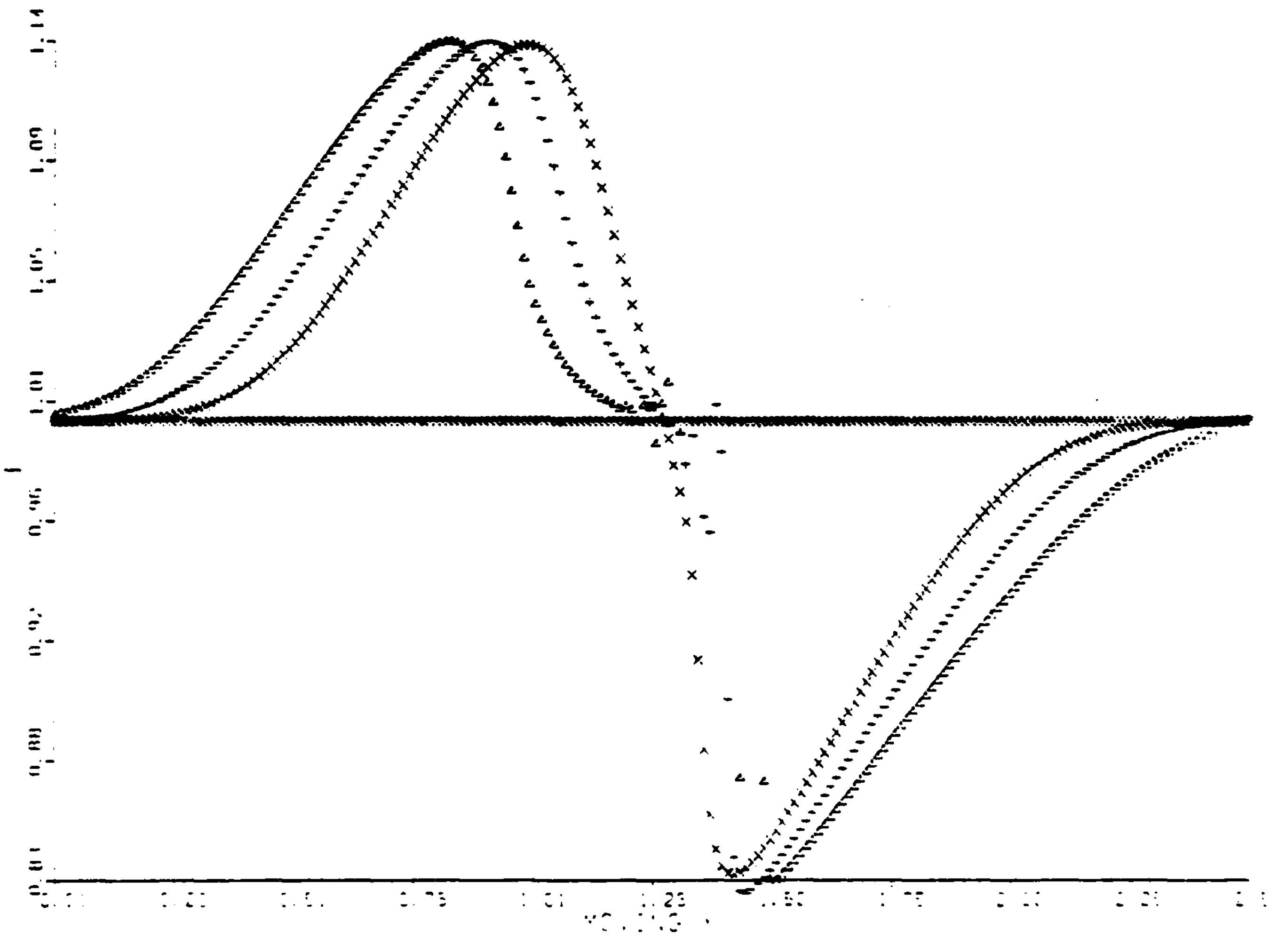

Figure 9b

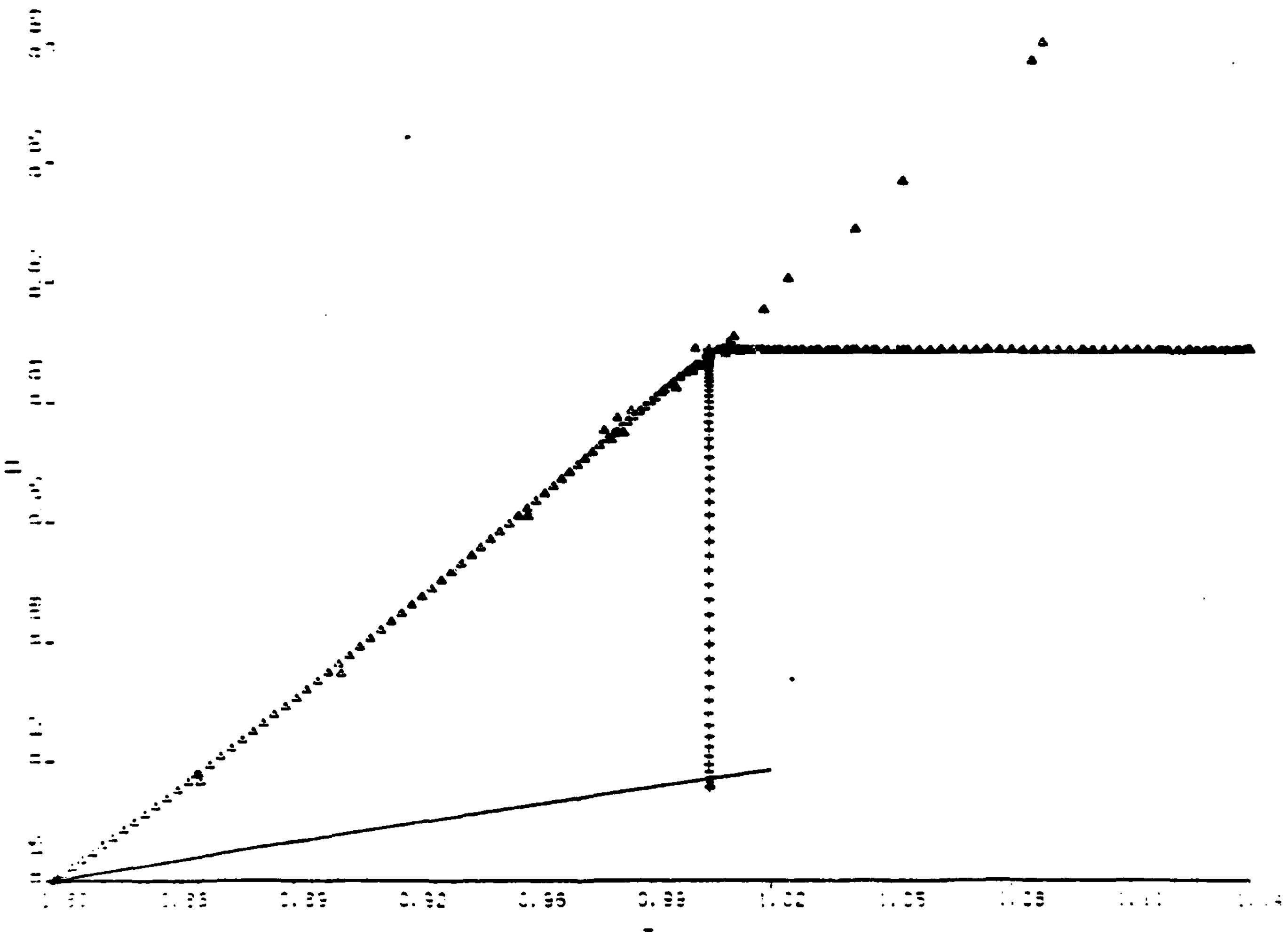

Figure 9c

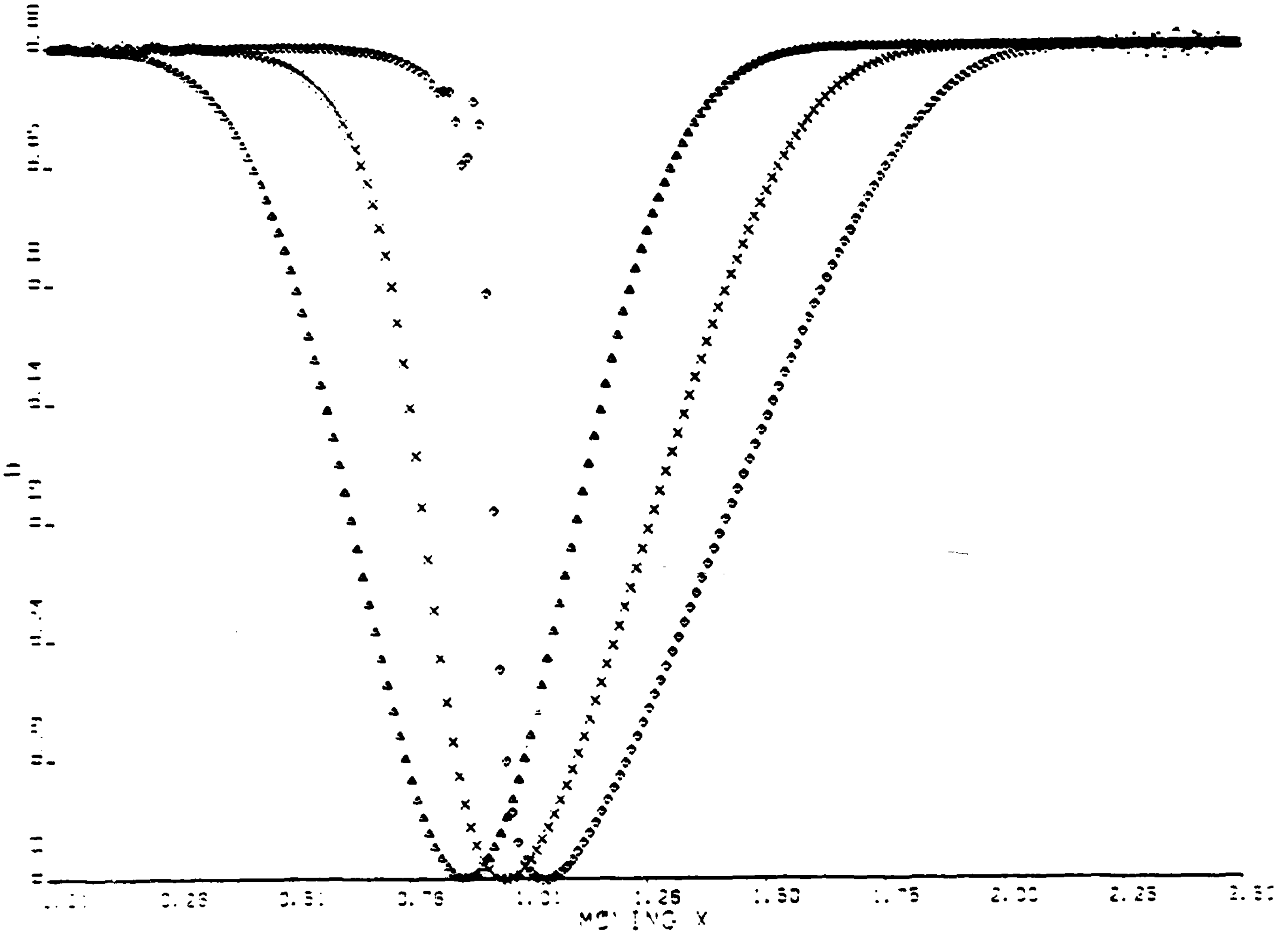

Figure 10a

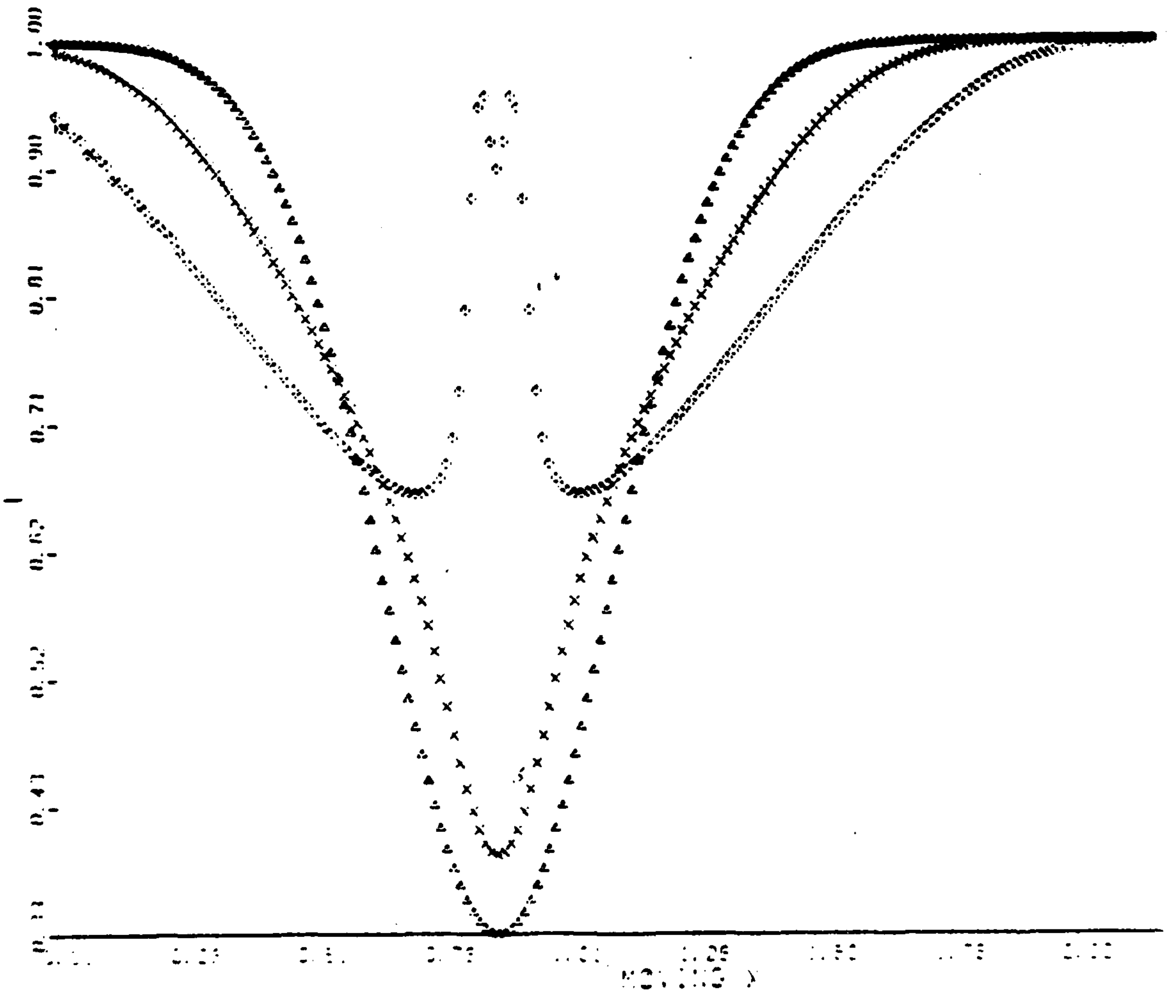

Figure 10b

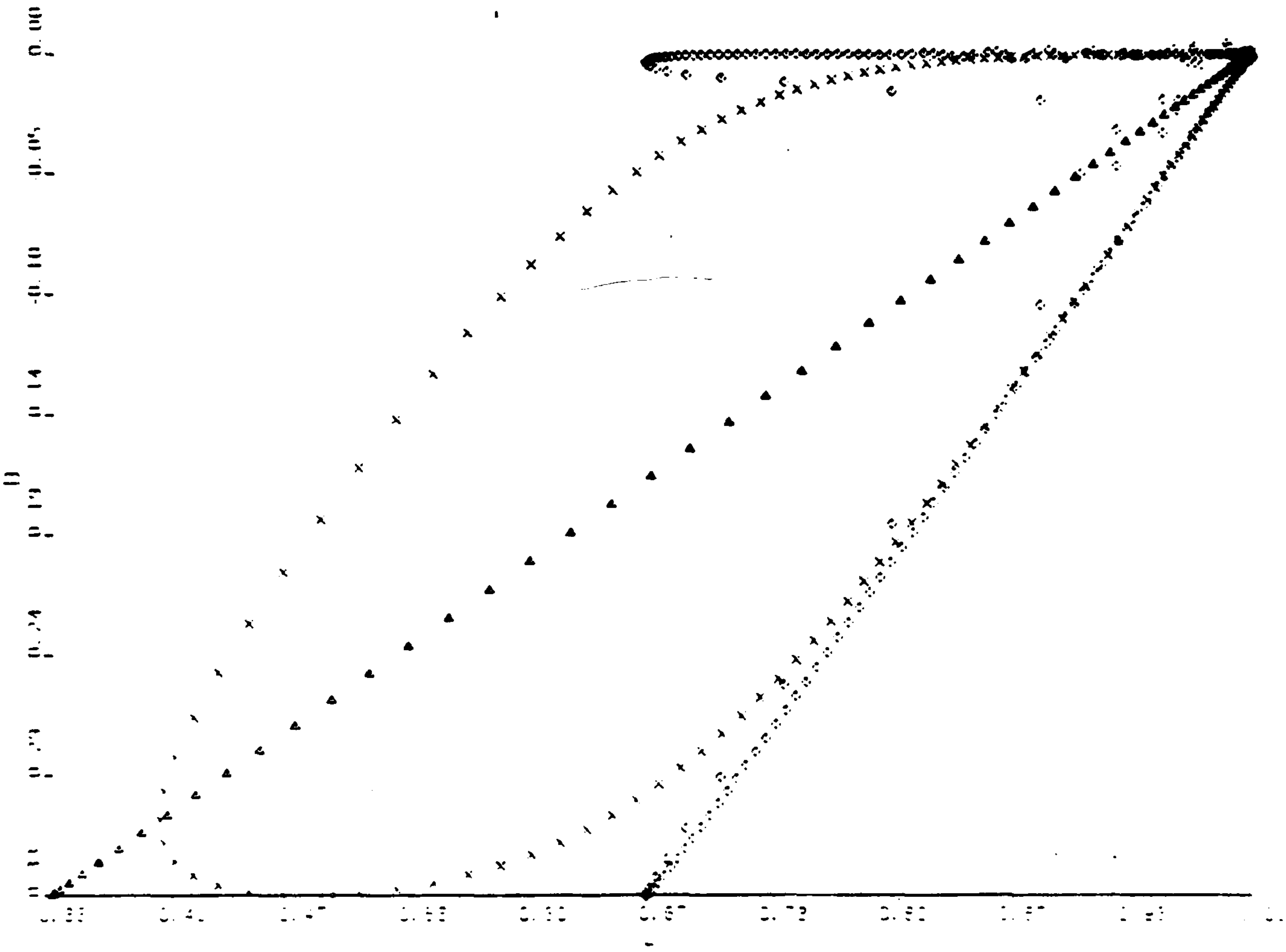

Figure 10c

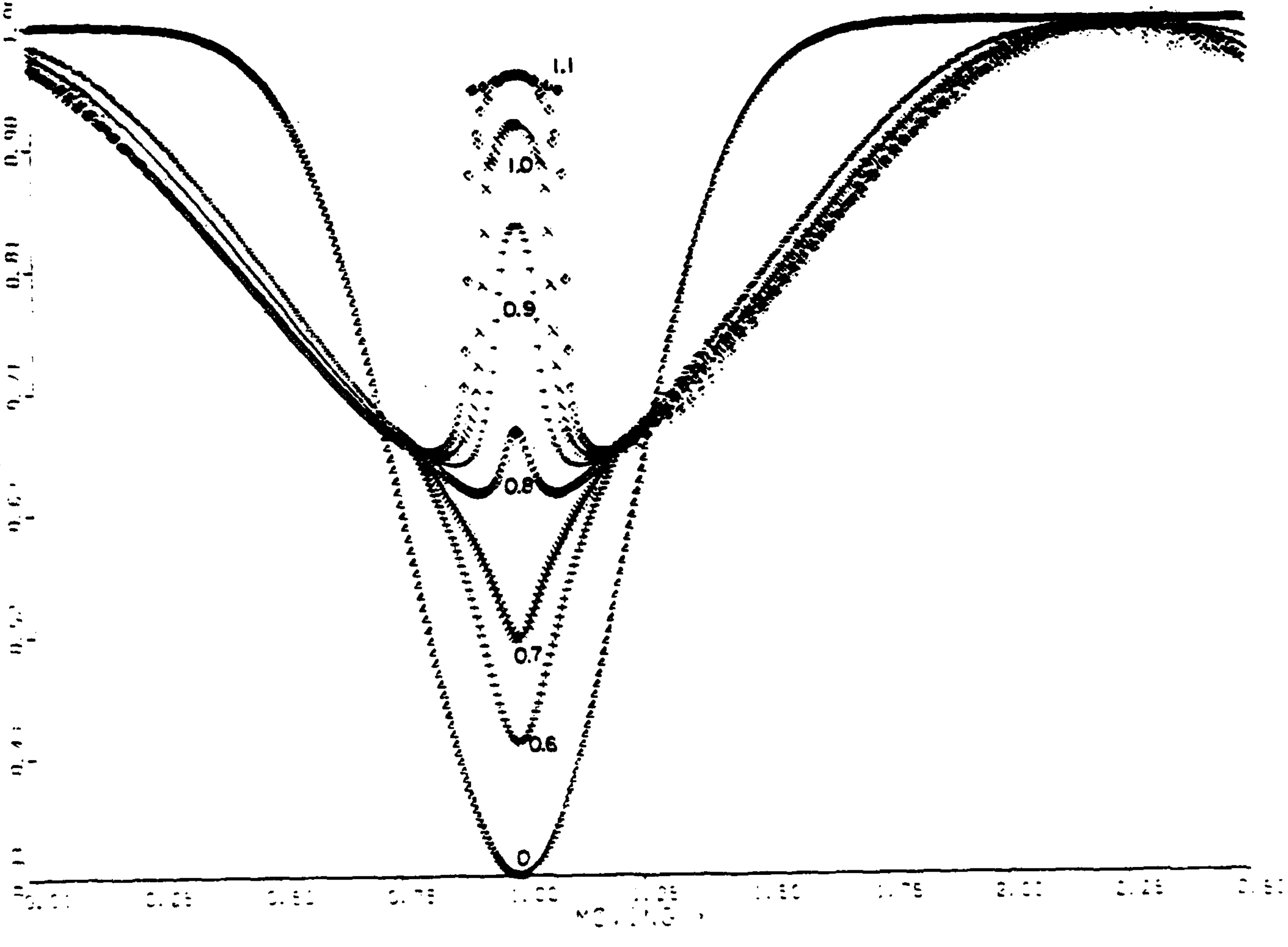
1.00
0.90
0.80
0.70
0.60
0.50
0.40
0.00
0.25
0.50
0.75
1.00
1.25
1.50
1.75
2.00
2.25
2.50
1.1
1.0
0.9
0.8
0.7
0.6
0

Figure 11

Phil. Trans. R. Soc. Lond. A **302**, 583–595 (1981)
Printed in Great Britain

Laboratory models of circulation in shallow seas

By J. A. Whitehead, Jr
Woods Hole Oceanographic Institution, Woods Hole, Massachusetts 02543, *U.S.A.*

[Plate 1]

Three laboratory experiments are described. The first was made to observe the flow field of circulation in a model given by Stommel & Leetmaa (1972). The experiment consisted of a very shallow (1 or 2 cm deep) annulus with an inner heated wall of radius 25 cm and a cooled outer wall of radius 57 cm, all mounted on a turntable. When the Ekman number was large the flow was steady and resembled the solutions for a non-rotating estuary given by Hansen & Rattray (1965), but when the Ekman number was small the flow became time-dependent. Values of shear and stratification obtained from theory indicate that the flowing water probably underwent baroclinic instability. It appears that such instability may develop on real shelves.

The second experiment consisted of a shallow sea of constant depth bounded by a deep ocean through a uniformly sloping continental rise. The experiment is cooled from above and there is a region that exhibits sinking convection cells, which form the coldest water. This water then spills off the right-hand side of the shallow sea (looking downstream for counterclockwise rotation) and forms bottom water in the deep experimental ocean.

The third experiment is a rotating version of the dam-break problem in which a density current is generated after a barrier has been removed. The rotation causes the current to lean against the right-hand wall (looking downstream for counterclockwise rotation) and turbulent eddies are detrained to the side rather than vertically.

1. The Stommel–Leetmaa shelf model

Although there have been many theoretical studies of the dynamics of the oceanic waters on continental-shelf regions, few have been concerned with theories of the general circulation in such regions. One of the first attempts appears to have been an idealized model by Stommel & Leetmaa (1972), which concerns the flows on an infinitely long, straight, constant-depth shelf, subjected to wind stress from above and to fresh water run-off from the continental side. The effects of friction, diffusion, and cross-shelf advection were retained in the governing equations, which were derived by the use of an expansion procedure based on the fact that the ratio of shelf depth to width is very small. Given values of the top wind stress, fresh water run-off, depth and width of the shelf, and 'eddy' properties of the water's viscosity, diffusivity and alongshore pressure gradient, they predicted the cross-shelf density gradient and alongshelf velocity. The numbers believed to be appropriate for the Mid-Atlantic Bight were used to assess the appropriateness of the model to the real shelf, as discussed subsequently by Csanady (1976), Scott & Csanady (1976) and others.

Here I do not continue to discuss applications of this theory to real shelves, but instead observe features of this model through observations of flows in a very shallow annulus experiment in the laboratory. I desired to see if any additional boundary layers or instabilities could be observed, or whether the flow otherwise did not behave as predicted. The dynamics of the experiment differ from the above theories because there is a heat flux rather than a water flux and there are rigid boundary conditions at the top. Hence a brief reformulation will be given.

Formulation of the problem

The model consists of a layer of fluid of constant depth d, breadth L, infinitely long, and subject to a lateral temperature gradient $\partial T/\partial x$ across its breadth as a model of lateral density gradient. The system is rotating at rate $\frac{1}{2}f$ in a field of gravity g. The viscosity ν of the fluid is constant, as is the thermal diffusivity κ and the coefficient of expansion α. The Boussinesq equations will be presented in a dimensionless form by using d as the vertical length scale, L as the horizontal length scale, fd as the horizontal velocity scale, fd^2/L as the vertical velocity scale, $\rho f^2 d$ as the pressure scale (ρ is average density), and by representing the temperature as

$$T' = (x+dT)\,\partial T/\partial x, \tag{1}$$

so T is the dimensionless temperature correction to a linear temperature distribution in the x-direction (across the shelf).

If $d \ll L$ vertical velocities will be much smaller than horizontal ones except near the lateral edges. The Boussinesq equations with all terms of order d/L neglected are

$$-v = -p_x + Eu_{zz}, \quad u = Ev_{zz}, \tag{2 a, b}$$

$$p_z = -Sx, \quad u = PT_{zz}, \tag{2c, d}$$

where a subscript denotes partial differentiation and

$$S \equiv (g\alpha/f^2)\,\partial T/\partial x, \quad P \equiv \kappa/fd^2 \quad \text{and} \quad E \equiv \nu/fd^2.$$

The simplest solutions are antisymmetrical above and below the plane $z = 0$. Pressure at any height z can be found by integrating ($2c$). The x-derivative of pressure at this value of z is

$$p_x = -Sz + C, \tag{3}$$

where C is the lateral pressure gradient at $z = 0$.

The left side of equation ($2d$) is a lateral advection of heat. The right-hand side is the 'short-circuiting' effect first noted by Taylor (1953) for problems where there is advection in one direction and conduction principally in another direction with smaller length-scale.

To model 'wind stress', it will be assumed that the top and bottom boundaries move with equal and opposite velocities. In addition there will be no vertical heat transfer through the boundaries, and hence the boundary conditions are

$$u = \pm U, \quad v = \pm V \quad \text{and} \quad \partial T/\partial z = 0 \quad \text{at} \quad z = \pm \tfrac{1}{2}. \tag{4}$$

Solutions have the form

$$u = (-\tfrac{1}{2}S - V)\,g_1(z) + Ug_2(z), \tag{5a}$$

$$v = +(\tfrac{1}{2}S + V)\,g_2(z) + Ug_1(z) - Sz, \tag{5b}$$

$$T = (\tfrac{1}{2}S + V)\,\frac{E}{P}\,g_2(z) + U\frac{E}{P}\,g_1(z) - \frac{\beta E z}{P\,(\cosh\beta - \cos\beta)}\,(\tfrac{1}{2}S + V + U)\sinh\beta \\ + (\tfrac{1}{2}S + V - U)\sin\beta, \tag{5c}$$

where

$$\beta = (2E)^{-\frac{1}{2}}, \tag{6a}$$

$$g_1(z) = [\sinh\beta(z+\tfrac{1}{2})\sin\beta(z-\tfrac{1}{2}) - \sinh\beta(z-\tfrac{1}{2})\sin\beta(z+\tfrac{1}{2})]/(\cosh\beta - \cos\beta), \tag{6b}$$

$$g_2(z) = [\cosh\beta(z+\tfrac{1}{2})\cos\beta(z-\tfrac{1}{2}) - \cosh\beta(z-\tfrac{1}{2})\cos\beta(z+\tfrac{1}{2})]/(\cosh\beta - \cos\beta). \tag{6c}$$

The flows vary linearly with S, V, and U, and functionally with E. The solutions have very different structure depending upon whether E is large or small. If E is large, the solutions can be reduced to the following polynomials:

$$u = -(S/3!\,E)\,(z^3 - \tfrac{1}{4}z) + 2Uz, \tag{7a}$$

$$v = 2Vz, \tag{7b}$$

$$T = -\frac{S}{EP}\left(\frac{z^5}{5!} - \frac{z^3}{4!\,6} + \frac{z}{4!\,2^4}\right) + \frac{U}{P}\,(\tfrac{1}{3}z^3 - \tfrac{1}{4}z). \tag{7c}$$

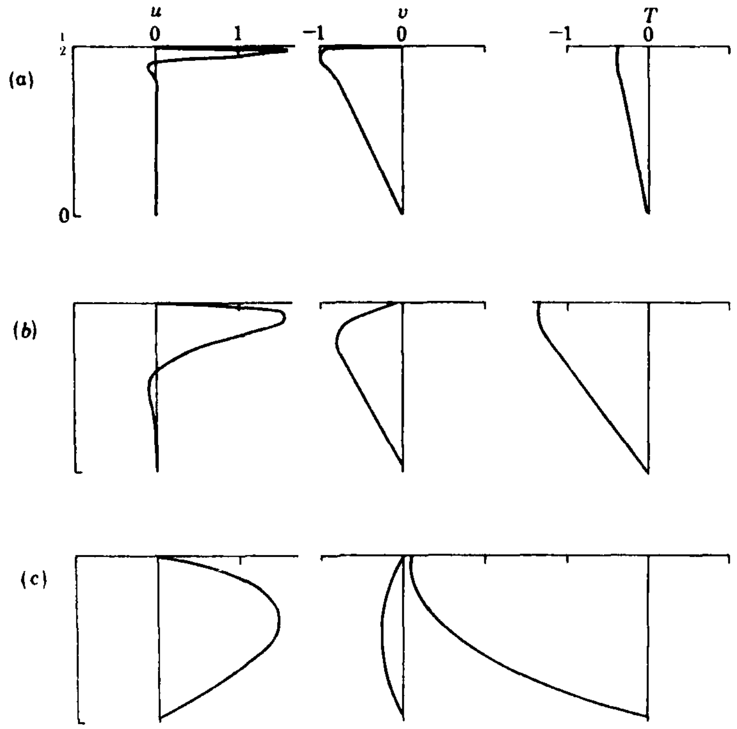

FIGURE 1. Profiles of cross-shelf velocity u, along-shelf velocity v, and temperature T as a function of $\beta = (2E)^{-\frac{1}{2}}$ for no velocity of the boundaries and $S = 1$. (a) $\beta = 64$, $E = 0.00012$; (b) $\beta = 16$, $E = 0.019$; (c) $\beta = 4$, $E = 0.03$.

The solutions for u and T are equivalent to those derived by Hansen & Rattray (1965) as model of estuarine circulation (no rotation). For E small, the solutions can be represented as Ekman layers plus interior flows because the functions (6b) and (6c) approach

$$g_1(z) \simeq e^{\beta(z-\frac{1}{2})}\sin\beta(z-\tfrac{1}{2}) + e^{-\beta(z+\frac{1}{2})}\sin\beta(z+\tfrac{1}{2}), \tag{8a}$$

$$g_2(z) \simeq e^{\beta(z-\frac{1}{2})}\cos\beta(z-\tfrac{1}{2}) - e^{-\beta(z+\frac{1}{2})}\cos\beta(z+\tfrac{1}{2}) \quad \text{for} \quad \beta \gg 1. \tag{8b}$$

For the structure of the solutions to be more clearly visualized, they were calculated by computer from equations (5) and (6) for three values of E, as shown in figure 1. Because the solutions are antisymmetric about zero, only the upper half of the solution is shown. At the top, the Ekman number is small enough for the Ekman layer to be clearly visible near the boundary. In the interior there is a linear stratification and constant shear due to the thermal wind equations (the basic state of the Eady problem). At the bottom, the Ekman number is large enough for the solution to be approaching the limit of Hansen & Rattray.

The experiment

A wide cylindrical annulus was used, rather than a very long, straight channel, to avoid problems with end walls. The tank shown in figure 2 had a Perspex bottom 1.25 cm thick and 114 cm in diameter, lying on 2 inches (*ca.* 5 cm) of insulating styrofoam. The cover could rotate with respect to the bottom tank and was covered by two inches (*ca.* 5 cm) of styrofoam. The depth of the test fluid could be held at 1, 2 or 4 cm, depending upon the height of the cover above the bottom. The inner wall of the annulus was composed of a Perspex disc of 25 cm radius, 1 cm high, upon which was mounted a waterproofed 33 Ω heating wire. Adjacent to the outer wall of the annulus was mounted a copper tube of approximately 1 cm outer diameter. This was flushed by water from a thermostatically controlled bath held at 25.3 ± 0.1 °C. Holes of diameter 2 mm were drilled down through the cover of the annulus to allow access by dye injectors and temperature probes; when not in use the holes were covered with stoppers. The entire apparatus was mounted on the 2 m turntable at Woods Hole Oceanographic Institution.

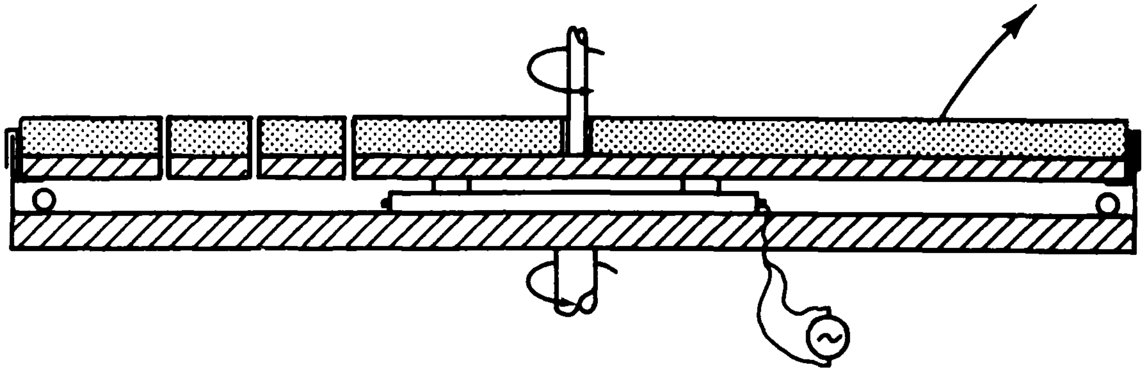

FIGURE 2. Sketch of the cylindrical experimental apparatus. The cross-hatched material is Perspex. The speckled material is styrofoam. The upper lid was free to rotate with respect to the basin. The clear area contains water.

The apparatus was like a large flattened annulus with a width: depth ratio of approximately 30:1 for a 1 cm depth, 15:1 for a 2 cm depth or 7.5:1 for a 4 cm depth. The solution of the basic flow, which was developed in the previous section, is analogous, but different from, the interior and the bottom and top boundary layers for a deep annulus as analysed by Robinson (1959). No solution is developed here for the side-wall boundary layers.

Typical measurements of temperature as a function of radius are shown in figure 3. The solid line gives the predicted profile at midplane as calculated in the next section. The temperature gradient varies with radius because the heat flux per unit area varies. This illustrates one of the most essential features of the Stommel–Leetmaa model – that temperatures at different depths parallel each other in the presence of a continuous change in temperature in the lateral direction.

The data shown here were for zero rotation but measurements at Ekman numbers down to approximately 0.02 were almost identical. However, the objection of the experiments was to observe the small Ekman number limit. They were not very successful in this respect because a time-dependent flow was almost always observed below an Ekman number of 0.02. This is most clearly shown by a series of 21 runs conducted to determine temperature between the hole of 30.4 cm radius and the hole of 50.8 cm radius as a function of rate of rotation. The results are shown in figure 4 for depths of 1 cm (solid circles) and 2 cm (open circles). The temperature difference does not increase substantially for the 13 run with $E > 0.02$, but for the runs with $E < 0.02$ the temperature difference began to increase, but a temporal variation was observed in the signal. The time-scales of the variations are so long that the average of the time-varying signal is not statistically well defined even after 8 h. The extremes of the temperature differences for each sample are shown in figure 4 so that the transitions to a time-dependent state could be illustrated. The values of the temperature differences were divided by a predicted value at zero rotation, which will be called ΔT_p, derived in the next section.

To visualize the flow, the styrofoam cover was suddenly taken off the lid and thymol blue streaks were photographed in the flowing liquid, but heat losses are so great as to render the subsequent data of only qualitative value. The time dependence comes from big eddies that slowly migrate around the tank. The eddies are usually as big as the 'shelf width'.

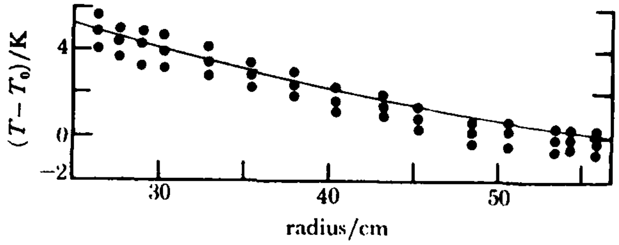

FIGURE 3. Measurements of temperature as a function of radius r at heights 1 mm (lower), 5 mm (middle), and 9 mm (upper) from the bottom of the tank. The apparatus was not rotating for these data, but data with $E = 0.3$, 0.15, 0.03 and 0.02 were almost indistinguishable from these. The solid line is a prediction of temperature dependence at the midplane of the tank.

Quantitative comparison of experiment and theory

The heat flux (Q) per unit length of shelf can be determined by the following integration:

$$Q = \int_{\frac{1}{2}}^{\frac{1}{2}} uT\,\mathrm{d}z. \tag{9}$$

In the two limits of E small and E large, the solutions (7) and (8) can be used in the integral (9) to predict the heat flux. The integrated solutions are

$$Q = -\frac{S^2}{9!\,PE^2} - \frac{4!}{9!}\frac{US}{PE} - \frac{4!}{6!}\frac{U^2}{P} \quad \text{for} \quad E \gg 0.1 \tag{10a}$$

and

$$Q = -\frac{E}{P}\left\{(\tfrac{1}{2}S + V + U)^2 - \frac{1}{2\beta}\left[3(\tfrac{1}{2}S + V)^2 + 4(\tfrac{1}{2}S + V)(U - U^2)\right]\right\} \quad \text{for} \quad E \ll 0.01. \tag{10b}$$

To compare the predictions with the experimental measurements of temperature as shown in figure 3, equation (10a), with $U = 0$, was put into dimensional form, the cross-shelf direction x was replaced by radius r, and the heat flux per unit radius was made equal to $H/2\pi r$.

An ordinary differential equation for T and r results, which can be integrated to give

$$T = \tfrac{3}{2}(9!\,H\nu\kappa^2/2\pi C_p\,\alpha^2 g^2 d^9 \rho)^{\frac{1}{3}}\, r^{\frac{2}{3}} + T_0. \tag{11}$$

The parameters of the experiment were heat flux $H = 55$ W, $g = 980\,\mathrm{cm\,s^{-2}}$, specific heat

$C_p = 4.16\,\mathrm{W\,s\,g^{-1}\,K^{-1}}$, $\alpha = 3\times10^{-4}\,\mathrm{K^{-1}}$, $\nu = 0.01\,\mathrm{cm^2 s^{-1}}$, $d = 1\,\mathrm{cm}$, $\rho = 1\,\mathrm{g\,cm^{-3}}$ and $\kappa = 0.0014\,\mathrm{cm^2 s^{-3}}$. With these values (11) becomes

$$T-T_0 = 12.2-0.837r^{\frac{4}{3}}, \tag{12}$$

where T_0 is the temperature at the outside radius (56 cm). This relation is the solid line in figure 3. The measured temperature distribution is close to that predicted although it is slightly less in the interior, possibly owing to a slight error in the thickness of the test fluid.

The temperature difference between the hole of 30.4 cm radius and the hole of 50.8 cm radius is

$$\Delta T_p = 3.31\,\mathrm{K} \quad \text{for} \quad d = 1\,\mathrm{cm},$$

and

$$\Delta T_p = 0.42\,\mathrm{K} \quad \text{for} \quad d = 2\,\mathrm{cm}.$$

These values were used to normalize the temperatures in figure 4.

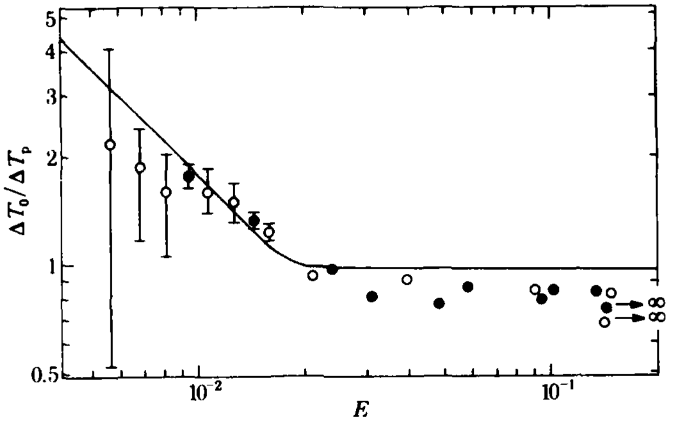

FIGURE 4. Measurements of temperature difference at the midplane between radii of 30.4 and 50.8 cm as a function of Ekman number, with constant heating voltage. The circles are means and the bars denote extremes in the measured ΔT over an eight-hour period.

Since the ratio of (10*a*) to (10*b*) is $(4/9!)^{\frac{1}{3}}E^{-3}$, and since temperature gradient scales as $H^{\frac{1}{3}}$ in (10*a*) and (10*b*), the relation $0.022E^{-1}$ (shown by the solid line in figure 4) is the solution in the small-E limit. The temperature difference was beginning to increase as E decreased in reasonably good agreement with this relation until the fluctuations became large.

Stability of the flow

We conclude that the slow-rotation limit of the theory is realizable and stable, but at high rotation an instability developed. The probable origin of the instability is suggested by the following considerations about the stability of the solution.

To estimate whether the small-Ekman-number limit is baroclinically unstable, a stability criterion derived by Pedlosky (1970, equation (3.11)) for a two-layer fluid was used with solution (5) to calculate the criterion

$$\beta\frac{E}{P}\left[\tfrac{1}{2}S+U+V\right]S\epsilon^2 < 8\left[\left(\frac{32E}{S^2\epsilon^2}\right)^{\frac{1}{2}}+\pi\right]^{-2} \tag{13}$$

for instability, where $\epsilon = d/L$. For our experiments with $U = 0$ and $V = 0$, equation (13) can be put in a more convenient form:

$$S < (4/\pi\epsilon)\left[(\beta Pr)^{-\frac{1}{2}}-\beta^{-1}\right] \tag{14}$$

for instability, where $Pr = \nu/\kappa$ is the Prandtl number.

The following values are typical of our experiment: $Pr = 5.5$, $E = 0.01$ ($\beta = 7.07$), and $\epsilon = 0.04$. These will give $S < 0.60$ for instability. Using $L\partial T/\partial x = 10\,\mathrm{K}$, $L = 25\,\mathrm{cm}$, $f = 1.0\,\mathrm{s}^{-1}$, $\alpha = 3 \times 10^{-4}\,\mathrm{K}^{-1}$, and $g = 980\,\mathrm{cm\,s}^{-2}$, we get a value of S of 0.12 which easily fits the instability criterion.

Hence it is reasonable to assume that the eddies observed here are produced by baroclinic instability. For a real shelf, with $Pr = 1$, $E = 0.01$, and $\epsilon = 0.001$, the criterion (14) (without wind stress) would be

$$S < 298.$$

Using a salinity gradient equivalent to a ΔT of 30 K, $L = 100\,\mathrm{km}$, $f = 10^{-4}$ and $\alpha = 3 \times 10^{-4}$ we get a value of S of 88, so again the criterion for instability is met.

The effect of a rotating lid

Equation (13) implies that we can stabilize the fluid by imposing differential flows in the top and bottom boundaries. This effect occurs because such differential flows do not generate vertical shear (for constant S) but do alter the stratification in the interior for the small-E limit (see equations (5b, c)). The rotating lid was incorporated to see if we could detect such an effect but it did necessitate the removal of some insulation. Of course in this experiment S will change with lid rotation anyway, so in our experiments the radial temperature gradient was measured directly by thermistors implanted in the bottom of the tank. In addition, insulation was removed from the top lid for visualization. Since heat losses were then quite large the observations of whether a flow is stable or not are only qualitative, and a quantitative verification will require a better insulated apparatus. Nonetheless a qualitative verification was obtained. Figure 5 (plate 1) shows three flows: when the lid was rotating faster than the apparatus, at the same speed, and slower. When the lid rotates faster, the flux in the Ekman layers due to differential shear is in the same sense as the buoyancy-driven flow; thus heat transport is aided, stratification is increased, and shear is decreased, resulting in a net stabilization. The dye streaks in figure 5 (a) are laminar except for internal waves that are radiated off the dye inserts. When the lid did not rotate differentially, the experiment was still in an unstable state as shown in figure 5 (b). When the lid rotated slower than the apparatus, the flux in the Ekman layers due to differential shear was opposite to the density-driven flux, i.e. water flows *toward* the centre in the top Ekman layer and *away* from the centre in the bottom one. Large shear may even force a density inversion and gravitational instability. Figure 5 (c) shows very strong turbulence with small eddies that rapidly mix the dye. For these runs the expression

$$\pi^2 \beta Pr (\tfrac{1}{2}S + V)\, S\epsilon^2,$$

which according to (13) must be less than one for instability (for $32E/S^2\epsilon^2 \ll \pi^4$), was respectively of the order of 40, 0.1, and -40. Time dependence rendered these estimates accurate to only a factor of two.

Eleven runs were made with the tank at a depth of 4 cm, and $f = 0.66\,\mathrm{s}^{-1}$, which gave an Ekman number of 9.5×10^{-4}. The velocity of the top lid was left constant for 2 hours, after which streak lines were photographed. The results were that the flow was laminar when $\pi^2 \beta Pr (\tfrac{1}{2}S + V) S\epsilon^2 = 10$, 7, 1.3, and 0.8; the flow exhibited large eddies like the kind in the middle of figure 5 when $\pi^2 \beta Pr (\tfrac{1}{2}S + V)\, S\epsilon^2 = -2$, -5, and -40.

In view of the uncertainty about the estimates of lateral density gradient, it appears that the main prediction of the theory – that the flows are subjected to baroclinic instabilities or actual density inversions when certain critical parameters are exceeded – has been verified. Although it is tempting to report more quantitative details, the effect of heat loss, depth variation up to 1 mm, and influence of the measuring probes may dominate them.

On real shelves (which might have a density flux due to fresh water run off rather than heat) we note that winds would aid the flux of low density water offshore, as does our prograde rotating lid, if they are blowing offshore or to the left facing offshore (in the Northern Hemisphere and on the assumption that low density water is near the coast). Those winds would tend to stabilize the flow. When winds blow onshore or to the right the density flux would be hindered and the waters would be destabilized as in figure 5(*c*).

The effects of a free boundary

If there is a stress-free boundary above the water for small Ekman number, the Ekman layer is changed to a zero-stress Ekman layer. This layer transforms the uniform vertical shear generated by the thermal wind relation to zero and is not capable of advecting as much heat laterally. The solutions of equations (2*a–d*) in the limit of small E, with the boundary conditions

$$\partial u/\partial z = \partial v/\partial z = \partial T/\partial z = 0 \quad \text{at} \quad z = \tfrac{1}{2},$$
$$u = v = \partial T/\partial z = 0 \quad \text{at} \quad z = -\tfrac{1}{2},$$

have the form

$$u = -(S/2\beta)\,e^{\beta(z-\frac{1}{2})}[\sin\beta(z-\tfrac{1}{2}) - \cos\beta(z-\tfrac{1}{2})] - (S/\beta)\sin\beta(z+\tfrac{1}{2})\,e^{-\beta(z+\frac{1}{2})}, \tag{15a}$$

$$v = (S/2\beta)\,e^{\beta(z-\frac{1}{2})}[\sin\beta(z-\tfrac{1}{2}) + \cos\beta(z-\tfrac{1}{2})] - (S/\beta)\cos\beta(z+\tfrac{1}{2})\,e^{-\beta(z+\frac{1}{2})} - S(z+\tfrac{1}{2}) + S/\beta, \tag{15b}$$

$$T = (ES/2P\beta)\,e^{\beta(z-\frac{1}{2})}[\sin\beta(z-\tfrac{1}{2}) + \cos\beta(z-\tfrac{1}{2})] - (ES/P\beta)\cos\beta(z+\tfrac{1}{2})\,e^{-\beta(z+\frac{1}{2})} - (ES/P)(z). \tag{15c}$$

This solution differs from the rigid-lid solutions in two ways. First, heat flux per unit temperature gradient is decreased by a factor of β^{-1} owing to the presence of that factor in (15*a*). Secondly, a net transport along the shelf (around the annulus) is predicted in (15*b*). To test whether transport is observed, the rigid lid was removed from the tank, and the temperature of the bath was set at 5 °C so that the water in the apparatus would remain cold and would not transfer much heat to the atmosphere. The basin was covered with clear cellophane. The voltage of the heater was set at 30 V a.c., so that an r.m.s. wattage of 13.5 W was produced. The apparatus was rotated until the temperature field of the liquid built up to a steady value, after which dye was injected into the fluid. Photographs of the dye streaks were taken every 5 s to record movement of the dye, and a steady flow around the cylindrical tank was observed.

One can predict velocity as a function of heat flux by using solutions (15*a–c*) to predict $\partial T/\partial x$ as a function of heat flux:
$$\partial T/\partial x = (8f^3H\beta/d^3\rho C_p g^2\alpha^2 Pr)^{\frac{1}{3}},$$
where H is heat flux per unit length of shelf, C_p is the specific heat, and α is the coefficient of expansion. The velocity as a function of heat production per centimetre of arc is

$$v = 2(g\alpha H/\rho C_p Pr)^{\frac{1}{3}}\,(2E)^{-\frac{1}{6}}.$$

For the experiment, the appropriate magnitudes are $g = 980\,\mathrm{cm\,s^{-2}}$, $\rho C_p = 4.16\,\mathrm{W\,s\,K^{-1}\,cm^{-3}}$, $\alpha = 3\times10^{-4}$, $H = 0.09\,\mathrm{W\,cm^{-1}}$, and $Pr = 5.5$, and so the velocity as a function of E is given by

$$v = 0.20(2E)^{-\frac{1}{6}}.$$

For this experiment $E = 0.311\times10^{-2}$, and the above E-formula gives a velocity of $0.48\,\mathrm{cm\,s^{-1}}$;

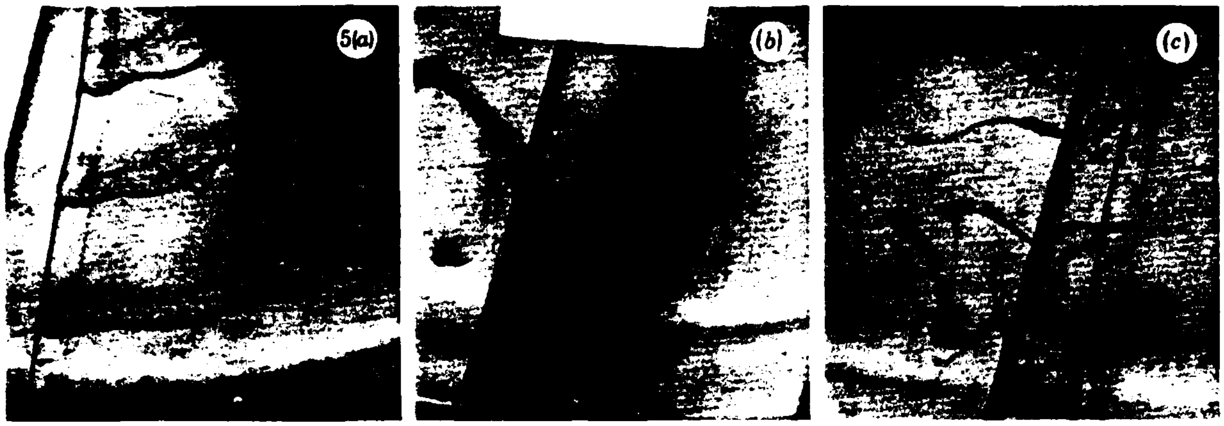

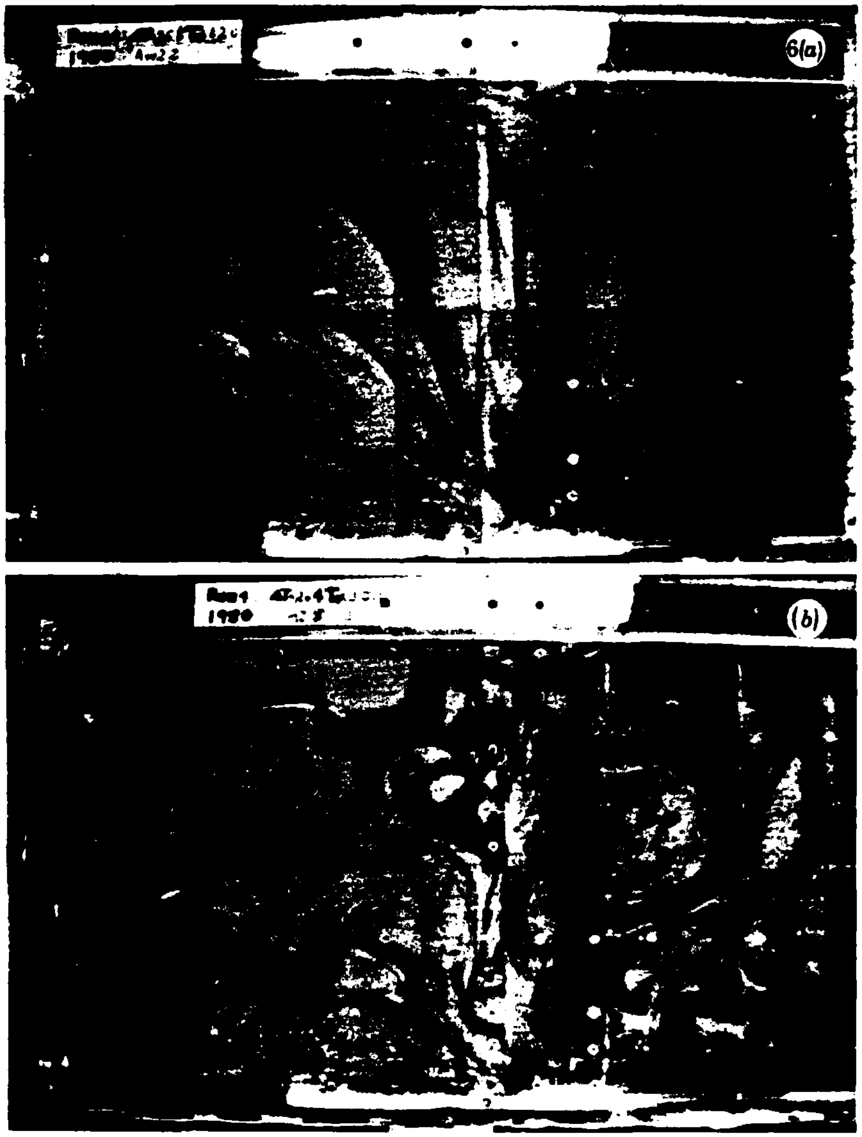

FIGURE 5. Streak lines for the first experiment when the upper lid is rotating (*a*) faster than the tank, (*b*) with the tank and (*c*) slightly slower than the tank. The streak lines on the left are wavy owing to internal lee waves being scattered off the dye probe; otherwise the flow is laminar. The streak lines on the middle reveal large sluggish eddies. On the right the differential shear of the lid is generating a very small stratification that has considerable small-scale turbulence which mixes the dye. The Ekman number is 9.5×10^{-4}.

FIGURE 6. (*a*) Streak lines for moderate rotation. The dark dye comes off wires that are strung across the tank. (*b*) Streak lines for fast rotation. The geostrophic eddies are visible throughout the sheif, some with sinking regions.

the velocity of the dye was about the same. Other runs were done at different rates of rotation, and observed velocities did appear to agree crudely with computed velocities, but there were sufficient heat losses and wind drag to discourage attempts to obtain precise quantitative comparisons.

In summary, even this simplest shelf model can often be unstable. Winds can affect the model by generating circulations that will either increase or decrease heat (or fresh water) transport and thereby alter the stability. Alongshore currents can be generated as predicted.

2. A SHALLOW SEA WITH DENSE WATER FORMATION

If waters in a shallow sea are subjected to much surface cooling and evaporation, they are found to be denser than water in the neighbouring deep ocean. This is due to the effect of surface-evaporative and sensible cooling, both of which decrease temperature, and the first of which increases salinity also. Often this denser water stays confined on the shelf owing to the action of wind set-up or because of topographic barriers. Sometimes the water is observed to spill off the edge of the shelf and irreversibly contribute to the deep waters of the world's oceans. An outstanding and important example of this later class of shelf flows is the flow off the shelf of the Weddell Sea, as discussed by Gill (1973) and Killworth (1979). A recent observation by Foldvic (private communication) of a strong bottom current coming off the Weddell Sea through the Filchner depression emphasizes the importance of shelf regions in generating the thermohaline structure of the oceans.

The main part of the second experiment (built by T. Sugimoto, who also did the bulk of this experiment in consultation with the author) was a rectangular basin mounted on a rotating turntable. In the basin is a square shelf 50 cm × 50 cm × 5 cm deep connected by a narrow (10 cm wide) slope to a deeper basin 30 cm × 50 cm × 15 cm deep. The slope thus emphasizes the dramatic contrast between shelf (which in our model has zero bottom slope even though real shelves do not) and shelf break. The enclosed fluid is cooled through a top lid and heated through an offshore aluminum side wall. This experiment thus also emphasizes winter, or intense evaporation, rather than summer or fresh-water run-off which was emphasized in § 1. Outside the wall is a stirred thermostatically regulated bath. The bottom of the top lid is composed of Perspex plate 6 mm thick above which is a channel 6 mm deep, 56 cm wide, and 91 cm long, through which chilled water is made to flow. The channel is covered above by a 6 mm Perspex plate. Running water is introduced at one end of the lid and removed at the other end, the water coming from a cooled thermostatically controlled bath. The temperature difference between the test fluid and the water in the upper lid was much larger than temperature variation in the tank, so to a first approximation the fluid was cooled uniformly from above. Side walls and the bottom of the test chamber were made of Perspex plate 12.6 mm thick for better insulation.

Photographs of the current pattern were taken by a 35 mm camera and also by a 16 mm ciné camera 1.1 m above the top of the basin. Visualization was with the thymol blue method in which a pH-sensitive indicator is buffered to its transition pH, so that an electric voltage applied between wires results in the fluid near the wires changing from yellow to dark blue. It was possible to trace the movement of the fluid for a few minutes thereafter. Temperature in the basin was measured by a thermistor put through one of 25 small holes in the top lid.

It took over 3 h for the temperature distribution of the test fluid to become steady. Although the current patterns change almost continuously with rate of rotation, they can be classified into the following three groups.

(*a*) Very slow or no rotation. The tank is smaller than the Rossby radius ($[g(\partial\rho/\rho\partial z)\,d^2]^{\frac{1}{2}}f^{-1}$). Vertical circulations predominante so that flow is like a Hadley cell. Water is heated at the offshore wall and flows toward the inner shelf, bending slightly to its right (for anticlockwise tank rotation). The heated water is also being cooled from above so there is a surface-mixed layer with convection rolls aligned in the direction of flow. In the 'sinking' region the mixed layer extends to the bottom. The densest water in the tank is in this region, and it sinks under the surrounding water, makes its way to the shelf break (curving to the right) and plunges off the edge of the shelf break to form bottom water in the model 'ocean'. The sinking region is limited to a narrow inner coastal zone, the width of the zone being less than 2 cm.

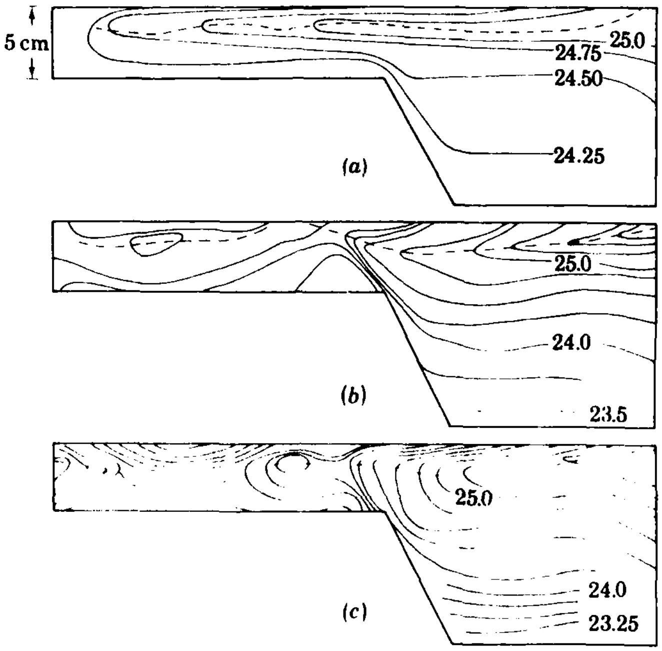

FIGURE 7. A temperature section from shelf to shore for (*a*) no rotation, (*b*) moderate rotation, and (*c*) fast rotation.

(*b*) Moderate rotation (figure 6*a*, plate 1). The tank is approximately the size of the Rossby radius. Horizontal single gyres of basin scale are formed on the shelf. The flow of hot water into the shelf is cyclonic and the lower outflow from the sinking region is anticyclonic. The sinking region is in the right-hand corner (facing offshore). Cold water formed there flows along the shelf break, curving toward the right, hits the right-hand wall and spills off from the shelf in a strong downwelling jet. As the rotation rate is increased, the width of the jet decreases, and curvature of the gyre increases. Also the gyre tends to retreat toward the inner coastal part of the shelf.

(*c*) Strong rotation (figure 6*b*, plate 1). The tank is larger than the Rossby radius. Turbulent eddies are predominant: they fill the shelf as well as the offshore region. Sinking occurs in the centre of some, but not all, eddies. The eddies are mostly cyclonic in the upper layer and anticyclonic in the lower layer but occasionally a gyre is cyclonic from top to bottom. The size of the eddies decreases as the rotation rate is increased. On average the shelf-bottom water flows slowly along the shelf break towards the right-hand side-wall (facing offshore) and flushes out as a downwelling jet at the right-hand wall, but cyclonic eddies on the shelf break also contribute to the flushing of the shelf water. Warm surface water offshore enters onto the shelf intermittently in the upper layer above the shelf break as well as along the left-hand side-wall (facing offshore).

The transition from (*b*) to (*c*) is variable. Sometimes two, three or four gyres are steady, at other times the fluid is very unsteady.

Thermal structures

(*a*) Slow or zero rotation (figure 7*a*). Thermal effluents about 2.5 cm thick extend from the offshore side-wall towards the shelf. They are cooled down rapidly but intrude close to the inner coastal-wall boundary of the shelf by advection. Upper layers are well mixed (convection rolls were clear) but the lower layer is stratified.

(*b*) Moderate rotation (figure 7*b*). Warm offshore water comes into the shelf along both the right-hand and left-hand side-wall boundaries and then circulates. The density structure is basically the same as that for (*a*) except that the width of the density current along the walls decreases. There is a strong jet flowing along the shelf break towards the right-hand side in the lower layer. It hits the right-hand wall (facing offshore) and cascades down the slope.

(*c*) Fast rotation (figure 7*c*). Temporal variability is significant owing to turbulent eddies, and each vertical section differs. However, usually a distinct thermal front is formed at the shelf break, although the front wanders around and varies in association with turbulent eddies.

This experiment, although extremely complicated physically, points out phenomena that may exist on real shelves in winter (or on shelves subjected to intense evaporation). Measurements of the curvature of the circulations on the shelf indicate that the radius of the gyres is roughly proportional to the internal Rossby radius of deformation NH/f, where H is the depth of the shelf and N is the local Brunt–Väisälä frequency. Also, a sizeable percentage of the flux off the shelf occurs near the right-hand wall, through a rotating density current. The magnitude of the temperature difference between the sinking and offshore regions can be reasonably predicted through the use of simple rotating hydraulic formulas (as given in Whitehead *et al.* 1974) of the form $Q = g^* h^2/2f$, where h is the fluid depth of the entire shelf and Q is volumetric flux. Equating $g^* = g\alpha \Delta T$ and $H = \rho C_p \Delta T Q$, where ΔT is the temperature difference between the coldest water and the water offshore, we predict $\Delta T = (2fH/\rho C_p \alpha g h^2)^{\frac{1}{2}}$. This formula was reasonably well obeyed. There is usually a distinct front at the edge of the shelf which hinders sizeable mass flux off the span of the shelf break. It is not known why this front is so persistent. Finally, the sinking regions are only located in a predictable region for small rotation rates (large Rossby radius compared with the shelf). For larger rotation rates the sinking regions must first be located by some remote sensing method. In the laboratory a human eye often suffices but in the real ocean spaceborne or airborne sensors may have to be used. Finally, the elusive chimneys (Killworth 1979) may have been observed here. The general nature of our sinking regions – cyclonic inflow to a sinking region with one or more sinking plumes, and anticyclonic outflow from the water formation region, seems to be similar. By forcing the water to have a convection region we may have produced what may happen not only on shelves but also in deep polar oceans.

3. Rotating gravity current

The third laboratory models were done in conjunction with M. Stern, B. L. Hua & N. Paldor (manuscript in preparation). The purpose was to model a gravity current in a rotating fluid. The work was primarily motivated by a recent theory by Stern (1980) and by the possibility that inertial jets lie along the coasts of some shelves, generated by intense spring run-off or large density contrasts near straits.

Experiments were made in a Plexiglass rectangular tank. Grooves were cut into the sides and bottom of the tank to allow a sliding gate, of 22-gauge (0.80 mm) stainless steel, to divide the tank into two chambers. The procedure was to fill the tank with tap water to a depth of 18.7 cm. A measured amount of salt was added to the water, and the water was mixed thoroughly. The gate was slid into the set of slits to a depth 10 cm above the bottom of the tank, and two pieces of ¼ inch (or *ca.* 0.6 cm) plywood were floated in the shorter chamber on one side of the gate. The tank was covered by a Plexiglass lid, the turntable was brought to the desired rate of rotation, and the salt water was allowed to spin for 15 min to reach a state close to solid-body rotation. The preparation for the experiment was completed by siphoning some coloured water onto the plywood floats in the small chamber until 4 cm of fresh water floated above the salty water.

After the gate was removed, the fresh water was observed to flow over the salt water, and the Coriolis force caused the water to flow as a geostrophic gravity current towards the 'coast' (the right-hand wall looking downstream with the basin rotating counterclockwise). The current was then deflected by the wall and caused to flow downstream next to that wall. The current is similar to a non-rotating density current in that it has a front deeper than the *current* behind, and was observed to move with speed of approximately $1.6(g^*h)^{\frac{1}{2}}$, where $g^* = g\delta\rho/\rho$, $\delta\rho$ is the density difference between the two fluids, and h is the local depth. It differs from its non-rotating counterpart in several ways. The most obvious is that it hugs the right-hand wall. It has a width of approximately $0.4(g^*h')^{\frac{1}{2}}f^{-1}$. It detrains eddies laterally rather than vertically; these eddies lie alongside the more laminar current.

It is anticipated that such currents may be encountered near the mouths of rivers or near straits connecting bodies of water of different densities, in which case measurements of propagation speed and width would be interesting. The observation of a possible gravity current by Mork (this symposium) is promising.

4. CONCLUDING REMARKS

Very shallow shelves (§ 1), shelves with a strong break and sides (§ 2), and coastal jets (§ 3) have been described in this paper. All experiments demonstrated the tendency for baroclinic processes on shelves to form geostrophic turbulence. In the first experiment the cross-shelf density flux was provided by viscous boundary layers. In the second and third by a side-wall. In shallow seas the flushing may be aided or hindered by winds, bathymetry, tides, offshore pressure gradients or other factors, but clearly the role of the eddies must often be addressed. This is one of the challenges for future laboratory studies.

We have purposely not applied these models in detail to specific shelves nor have we hoped to cover comprehensively all the types of shelves in the world. Since there are at least 150 000 km of shelves in the world it is reasonable to expect that there are some shelves modelled well by these few examples, while others (possibly most) are not. A realistic assessment and hints for other models will come as the oceanography of shallow seas matures.

Support for this research was from the Ocean Sciences Division, National Science Foundation, under Grant OCE80-18322 for the first two experiments, and the United States Office of Naval Research for the third under contract N00014-81-C-0010. Thanks are due to T. Sugimoto for allowing the use of his data and to Robert Frazel for skilful laboratory assistance.

References (Whitehead)

Beardsley, R. C. & Festa, J. F. 1972 *J. phys. Oceanogr.* **2**, 444–455.

Brocard, D. N., Jirka, G. H. & Harlemann, R. E. D. 1977 Technical Report 223, Dept of Civil Engineering, Massachusetts Institute of Technology.

Csanady, G. T. 1976 *J. geophys. Res.* **81**, 5389–5399.

Gill, A. E. 1973 *Deep Sea Res.* **20**, 111–140.

Hansen, D. V. & Rattray, M. 1965 *J. mar. Res.* **23**, 104–122.

Killworth, P. D. 1979 *J. phys. Oceanogr.* **9**, 531–554.

Pedlosky, J. 1970 *J. atmos. Res.* **27**, 15–30.

Phillips, O. M. 1966 *Deep Sea Res.* **13**, 1149–1160.

Robinson, A. R. 1959 *J. Fluid Mech.* **6**, 599–620.

Scott, J. T. & Csanady, G. T. 1976 *J. geophys. Res.* **81**, 5401–5409.

Stern, M. E. 1980 *J. Fluid Mech.* **99**, 687–704.

Stommel, H. 1962 *Proc. natn. Acad. Sci. U.S.A.* **48**, 766–772.

Stommel, H. & Leetmaa, A. 1972 *Proc. natn. Acad. Sci. U.S.A.* **69**, 3380–3384.

Taylor, G. I. 1953 *Proc. R. Soc. Lond.* A **219**, 446–468.

Whitehead, J. A., Leetmaa, A. & Knox, R. A. 1974 *Geophys. Fluid Dyn.* **6**, 101–125.

MANDATORY DISTRIBUTION LIST

FOR UNCLASSIFIED TECHNICAL REPORTS, REPRINTS, AND FINAL REPORTS PUBLISHED BY OCEANOGRAPHIC CONTRACTORS OF THE OCEAN SCIENCE AND TECHNOLOGY DIVISION OF THE OFFICE OF NAVAL RESEARCH

(REVISED NOVEMBER 1978)

1 Deputy Under Secretary of Defense
(Research and Advanced Technology)
Military Assistant for Environmental Science
Room 3D129
Washington, D.C. 20301

Office of Naval Research
800 North Quincy Street
Arlington, VA 22217
3 ATTN: Code 483
1 ATTN: Code 420C
2 ATTN: 102B

1 CDR Joe Spigai, (USN)
ONR Representative
Woods Hole Oceanographic Inst.
Woods Hole, MA 02543

Commanding Officer
Naval Research Laboratory
Washington, D.C. 20375
6 ATTN: Library, Code 2627

12 Defense Technical Information Center
Cameron Station
Alexandria, VA 22314
ATTN: DCA

Commander
Naval Oceanographic Office
NSTL Station
Bay St. Louis, MS 39522
1 ATTN: Code 8100
1 ATTN: Code 6000
1 ATTN: Code 3300

1 NODC/NOAA
Code D781
Wisconsin Avenue, N.W.
Washington, D.C. 20235

1 Mr. Michael H. Kelly
Administrative Contracting Officer
Department of the Navy
Office of Naval Research
Eastern/Central Regional Office
Building 114, Section D
666 Summer Street
Boston, MA 02210

FILMED

5-83

DTIC